Tools for In-situ Manipulation and Characterization of Nanostructures

Kristian Mølhave
Ph.D. Thesis, August 2004

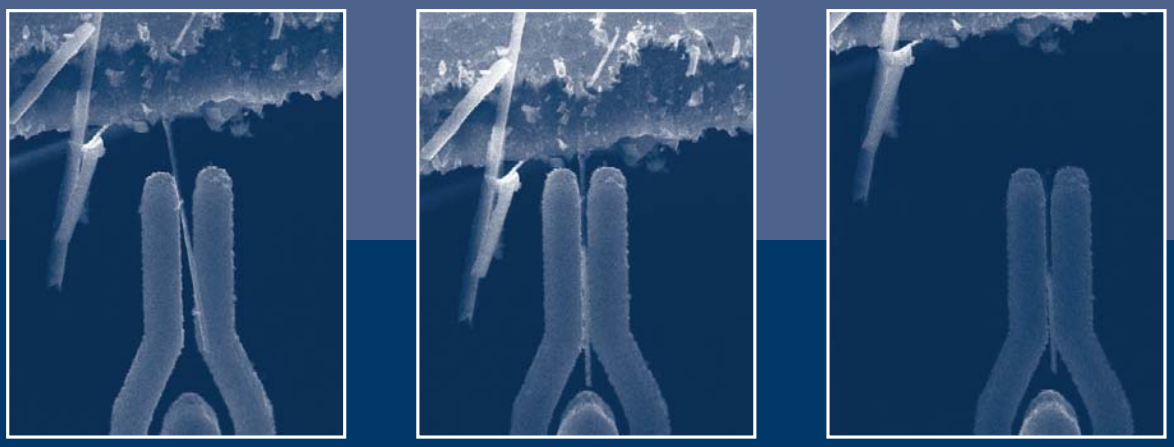

MIC - Department of
Micro and Nanotechnology
Technical University of Denmark

DTU

ISBN: 87-89935-84-5

For construction and characterization of prototype devices with nanometer-scale parts, this Ph.D. project developed an in-situ scanning electron microscope (SEM) laboratory with a set of novel tools for three-dimensional nanomanipulation. Together the developed set of tools comprise a nanolaboratory which in many ways can accomplish the same tasks as an electronic workshop - but using nanoscale components that are some 10000 times smaller.

The developed nano-toolbox contains microfabricated grippers that have been used successfully for pick-and-place manipulation of nanowires and grippers with integrated force-feedback. Environmental electron beam deposition (EEBD) was developed as a method for soldering electrical nanoscale circuits and constructing three-dimensional nanostructures. To characterize nanostructures in a transmission electron microscope (TEM), a method using micro-cantilever chips was developed and used to study Joule heating effects in carbon nanotubes.

Published by:
MIC - Department of Micro and Nanotechnology
Technical University of Denmark
Ørsteds Plads, building 345 east
DK-2800 Kgs. Lyngby

Tools for In-situ Manipulation and Characterization of Nanostructures

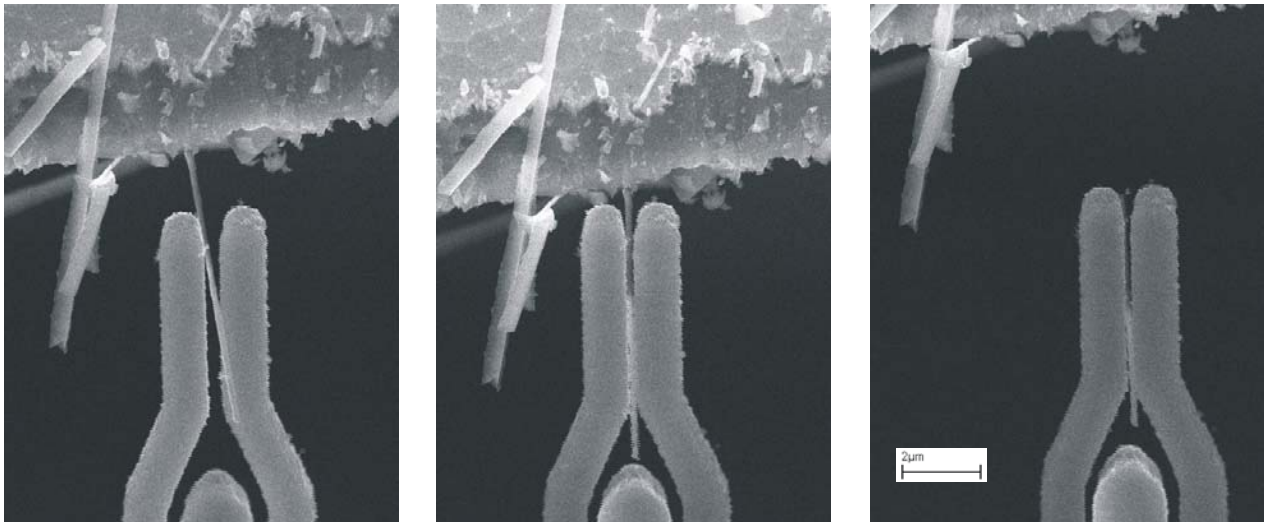

Ph.D. Thesis
By
Kristian Mølhave

August 2004

ISBN: 87-89935-84-5

MIC
Department of Micro and Nanotechnology
NanoDTU
Technical University of Denmark

Contents

Preface **vii**
0.1 Included Papers . . . ix
0.2 Additional Output from the Ph.D. Project . . . x

1 Introduction **1**
1.1 A Perspective on Nanomanipulation . . . 1
1.1.1 Nanocomponents and Methods . . . 2
1.1.2 Nanomanipulation Systems . . . 3
1.2 The Present Work . . . 4

2 Nanomanipulation Systems **7**
2.1 Introduction to Electron Microscopy . . . 7
2.1.1 Electron Optics and Scattering . . . 9
2.1.2 Scanning Electron Microscopy . . . 10
2.1.3 Transmission Electron Microscopy (TEM) . . . 13
2.1.4 Summary . . . 13
2.2 Tools for Nanomanipulation . . . 14
2.2.1 Manipulation Tools . . . 14
2.2.2 Characterization Tools . . . 16
2.2.3 Actuation Systems for In-situ Nanomanipulation . . . 17
2.2.4 Summary . . . 20
2.3 Developed Nanomanipulation Systems . . . 21
2.3.1 Optical Manipulation Station . . . 21
2.3.2 In-situ SEM Systems . . . 22
2.3.3 The TEM-Chip system . . . 24
2.3.4 Conclusion . . . 27

3 In-situ SEM Pick-and-place Nanomanipulation **29**
3.1 Grippers for Micro- & Nanomanipulation . . . 30
3.1.1 Nanotweezers . . . 33
3.1.2 Choosing the Actuation Principle . . . 33
3.1.3 Summary . . . 36

3.2 Introduction to Pick-and-place Nanomanipulation 36
3.2.1 Picking Strategies 38
3.2.2 The Place Procedure 41
3.3 Electrostatic Tweezers 43
3.3.1 Processing Limits 43
3.3.2 Modelling the Gripper Design 44
3.3.3 Finite Element Simulation of Grippers 49
3.3.4 Realized Designs and Characterization of Actuation 49
3.3.5 Summary 54
3.4 Pick-and-Place Manipulation of Nanowires 54
3.4.1 Picking Up Nanowires 55
3.4.2 Placing Nanowires 58
3.4.3 Summary 59
3.5 Electro-Thermal Grippers with Piezoresistive Force Feedback 62
3.6 Summary and Outlook 64
3.6.1 Outlook 64

4 Environmental Electron Beam Deposition **67**
4.0.2 Background 67
4.1 Initial Study of EBD 71
4.1.1 Making Nanotweezers by EBD 71
4.1.2 Soldering Nanotubes by EBD 74
4.1.3 Summary 74
4.2 A Simple Model of EBD 74
4.2.1 Rate Equation Model 75
4.2.2 Limitations to the model 77
4.2.3 Summary 78
4.3 Experimental Setup 78
4.3.1 The ESEM source system 79
4.3.2 A Simple Electron Beam Lithography System 80
4.3.3 Summary 83
4.4 Solid Gold Structures Created by EEBD 83
4.4.1 Deposition Rate 83
4.4.2 The Shell Structure 83
4.4.3 Summary 90
4.5 Feasibility Study of EEBD 90
4.5.1 Additional Depositions 91
4.5.2 Line Depositions 93
4.5.3 EEBD Soldering of Carbon Nanotubes 94
4.5.4 Summary 96
4.6 Conclusion and Outlook 97
4.6.1 Outlook 98

5 Studies of Carbon Nanotubes **99**
5.1 High Bias Voltage and Thermal Effects in MWNT 100
5.1.1 Conductance of MWNT 101
5.1.2 MWNT Annealing and Oxidation Effects 104
5.1.3 Summary 105
5.2 Scanning Micro Probe Measurement of Nanotube Conductance . . . 106
5.2.1 Measurements in Air 106
5.2.2 In-situ SEM Measurements 108
5.2.3 Summary 109
5.3 TEM investigation of MWNT Shell Burn Experiments 110
5.3.1 Setup and Probe Preparation 110
5.3.2 Experimental Results and Discussion 111
5.3.3 Summary 121
5.4 Electron Irradiation Induced Destruction of Carbon Nanotubes . . . 121
5.4.1 TEM observations of Nanotube Irradiation Damage 123
5.4.2 Electron Irradiation Induced Chemical Reactions with Nanotubes 125
5.4.3 Can TEM Cause Etching of Nanotubes ? 125
5.4.4 Nanotube Damage in SEM 128
5.4.5 InP Nanowire Damage in TEM 130
5.4.6 Summary 131
5.5 Conclusion and Outlook 131
5.5.1 Outlook 132

6 Summary **133**

A Article [1]
Electro-thermally Actuated Microgrippers with Integrated Force Feedback **135**

B Article [2]
A Simple Electron Beam Lithography System **143**

C Article [3]
Constructing, connecting and soldering nanostructures by environmental electron beam deposition **151**

D Article [4]
Solid Gold Nanostructures Fabricated by Electron Beam Deposition **161**

E Article [5]
Soldering of nanotubes onto microelectrodes **169**

F Article [6]
Towards pick-and-place assembly of nanostructures **175**

G Article
Pick-and-place nanomanipulation using microfabricated grippers **181**

H Article
Transmission Electron Microscopy Study of Individual Carbon Nanotube Breakdown Caused by Joule Heating in Air **191**

Bibliography **209**

Preface

This thesis presents the results achieved during my three year Ph.D. study mainly carried out at the Nanohand project at MIC, the Department of Micro and Nanotechnology at the Technical University of Denmark, under supervision of Peter Bøggild.

The project work has to a large extent been done in close collaboration with numerous people and other laboratories, who have been an invaluable help:

The EEBD study was mainly done at Haldor Topsoe A/S together with Anne Marie Rasmussen, Anna Carlsson, Charlotte C. Appel, Michael Brorson, Claus J. H. Jacobsen, Sven Ullmann. Our initial study of EEBD was performed at Risø National Laboratory together with Jørgen B. Bilde-Sørensen. EBD studies were also done at Polymercentret, DTU, with Keld West. We thank I. Maximov and L. Montelius for allowing us to use their SEM for the initial work on depositing nanotweezers tips at Lund University.

The TEM analysis with the TEM-Chips were done at IPL, DTU, where Andy Horsewell and Flemming Grumsen generously let us use their TEM. The cryogenic measurements of TEM-chips were made at Copenhagen University with Jesper Nygård and Thomas Sand.

The nanowire samples were supplied by Erik P. A. M Bakkers (Philips Research Laboratories, Eindhoven), and nanotube samples were supplied Richard Czerw, Wake University. During the project I have visited several laboratories which provided valuable experience that helped improving the systems I was building. I thank Rodney Rouff (Northwestern University), John Ballato (Clemson University), Richard Superfine and Sean Washburn (University of North Carolina) for inviting me to visit their groups. A three month stay at AMiR/Oldenburg, where I worked on pick-and-place manipulation, was both productive and enjoyable thanks to the close collaboration with Axel Kortschack and Thomas Wich.

During the three years, I started two projects that lasted for about a year each, which are beyond the scope of this report: A project on planar waveguide chips for optical measurements on nanostructures was done at COM, DTU, together with Karsten Rottwitt and Morten Dyndgård. Another project led to the development of a piezo driven rotational actuator, "The Nanoarm", for in-situ nanomanipulation. Jesper Mygind at the Department of Physics, DTU, helped us with amplifiers.

The processing of the microfabricated grippers was done in collaboration with

Capres A/S, Torben M. Hansen, Maria Dimaki, Ramona Mateiu, and the laboratory technicians at MIC. Since I have not been doing cleanroom processing myself, the project would not have been the same without them.

A special thank to Ole Hansen for valuable discussions and the people at MIC who were always ready to help. The Nanohand team at MIC, primarily Kjetil Gjerde, Jakob Kjelstrup-Hansen, Søren Dohn, Dorte Nørgaard Madsen, Ramona Mateiu, Maria Dimaki, Torben M. Hansen, and especially Peter Bøggild for never failing enthusiasm.

The major part of the project was funded by the STVF talent project "NanoHand" grant, while my work at the University of Oldenburg was funded by the ASSEMIC EU-project.

Updated errata and pdf file of this thesis is available on:

www.kristian.molhave.dk.

This version was published after the defense with additional publications and minor corrections.

Submitted July 1st 2004.
Kristian Mølhave
MIC- Department of Micro and Nanotechnology, Technical University of Denmark
DTU - Building 345 east
DK-2800 Kgs. Lyngby
Denmark

0.1 Included Papers

Part of the work presented in this thesis has been published or submitted to refereed journals. The thesis could have been written as a continuous text based on both published and unpublished results. To save the reader for repetition of the detailed discussion of the articles s/he may have read already, the following articles are briefly summarized in the report and are included as appendices to the thesis:

- [1] Electro-thermally Actuated Microgrippers with Integrated Force Feedback
  J. Micromech. Microeng. 15 1265–1270 (2005)
  K. Mølhave and O. Hansen

- [2] A Simple Electron Beam Lithography System
  Ultramicroscopy 102 215–219 (2005)
  K. Mølhave, D. Nørgaard Madsen, and P. Bøggild

- [3] Constructing, Connecting and Soldering Nanostructures by Environmental Electron Beam Deposition
  Nanotechnology 15 1047–1053 (2004)
  K. Mølhave, D. Nørgaard Madsen, S. Dohn and P. Bøggild.

- [4] Solid Gold Nanostructures Fabricated by Electron Beam Deposition
  Nano Letters 3 (11) 1499-1503 (2003).
  K. Mølhave, D.N. Madsen, A.M. Rasmussen, A. Carlsson, C.C. Appel, M. Brorson, C.J.H. Jacobsen, and P. Bøggild

- [5] Soldering of Nanotubes onto Microelectrodes
  Nano Letters 3 (1) 47-49 (2003).
  D.N. Madsen, K. Mølhave, R. Mateiu, A.M. Rasmussen, M. Brorson, C.J.H. Jacobsen, and P. Bøggild.

- [6] Towards Pick-and-place Assembly of Nanostructures
  Journal of Nanoscience and Nanotechnology 4 (3) 279-282 (2004).
  K. Mølhave, T.M. Hansen, D.N. Madsen, and P. Bøggild.

Additional publications from the Ph.D. project submitted after the defence

- Pick-and-place nanomanipulation using microfabricated grippers
  Nanotechnology 17 2434–2441 (2006)
  K. Mølhave, T. Wich, A. Kortschack, and P. Bøggild.

- Transmission Electron Microscopy Study of Individual Carbon Nanotube Breakdown Caused by Joule Heating in Air
  Accepted by Nano Letters 2006
  K. Mølhave. S. B. Gudnason, A. Tegtmeier Pedersen, C. Hyttel Clausen, A. Horsewell, and P. Bøggild

0.2 Additional Output from the Ph.D. Project

In addition to the included papers, I contributed to the papers and proceedings listed below that have been published during my Ph.D. project. These are not included in this report (several relate to my previous work at Aarhus University on quantum optics and ion traps). During the Ph.D. project, part of the time should be used on teaching/supervision. Apart from supervising projects, I also started up the Science Show, an outreach project from DTU based on students who go out to schools to present natural sciences in a new and exciting way. The project currently has more than 20 members; receives substantial annual funding by DTU to cover the students' salaries; and has been seen by more than 5000 people since it started. See www.scienceshow.dk for more information. I was awarded the McKinsey&Company Initiative Award 2003 for starting the Science Show.

- [7] Direct Measurement of Resistance of Multiwalled Carbon Nanotubes Using Micro Four-Point Probes
  Sensor Letters.3, 300–303 (2005)
  Søren Dohn, Peter Bøggild and Kristian Mølhave.

- [8] An approach to a multi-walled carbon nanotube based mass sensor
  Microelectronic Engineering 73-74 670-674 (2004)
  Ramona Mateiu, Zachary J. Davis, Dorte N. Madsen, Kristian Mølhave, Peter Bøggild, Anne-Marie Rassmusen, Michael Brorson, Claus J.H. Jacobsen, Anja Boisen.

- Nanoscale Soldering of Positioned Carbon Nanotubes Using Highly Conductive Electron Beam Induced Gold Deposition
  IEEE Proceedings (2003.)
  D.N. Madsen, K. Mølhave, R. Mateiu, P. Bøggild, A.M. Rasmussen, C.C. Appel, M. Brorson, C.J.H. Jacobsen.

- Soldering of Carbon Nanotube Bridges using Electron Beam Deposited Gold
  MRS Proceedings (2003).
  S. Dohn, K. Mølhave, D.N. Madsen, R. Mateiu, P. Bøggild, A.M. Rasmussen, M. Brorson and C.J.H. Jacobsen

- Assembly of carbon nanotubes on microelectrodes by nanomanipulation
  K. Mølhave, R. Mateiu, M. Dimaki, T.M. Hansen, D.N. Madsen, P. Boggild.
  Proceedings of 7th International Conference on Nanometer-Scale Science and Technology and 21st European Conference on Surface Science (NANO-7/ECOSS-21)

- Customizable nanotweezers for manipulation of free-standing nanostructures
  Proceedings of the 2001 1st IEEE Conference on Nanotechnology. 87-92

P. Bøggild, T. M. Hansen, K.Mølhave, A. Hyldgård, M. O. Jensen, J. Richter, L.Montelius, F. Grey.

- Non-stationary Coulomb crystals in linear Paul traps
  J Phys B 36 (3): 525-532 (2003).
  M. Drewsen, I.S. Jensen, N. Kjærgaard, J. Lindballe, A. Mortensen, K. Mølhave, D. Voigt.

- Stability of Coulomb crystals in a linear Paul trap with storage-ring-like confinement.
  Phys. Rev. E 66, 015401 (2002).
  N. Kjærgaard, K. Mølhave, and M. Drewsen

- Coulomb crystals in a pulse-excited linear Paul trap
  AIP Conf. Proc. 606, 145 (2002).
  N. Kjærgaard, K. Mølhave, and M. Drewsen

- Ion Coulomb crystals and some applications
  AIP Conf. Proc. 606, 135 (2002).
  M. Drewsen, L. Hornekær, N. Kjærgaard, K. Mølhave, A. Thommesen, Z. Videsen, A. Mortensen, and F. Jensen

Chapter 1

Introduction

1.1 A Perspective on Nanomanipulation

In his famous speech "There is plenty of room at the bottom" in 1959, Richard Feynman discussed how to manipulate and control things on a molecular scale in order to achieve electronic and mechanical systems with atomic sized components. He concluded that the development of technologies to construct such small systems would be interdisciplinary, combining fields such as physics, chemistry and biology, and would offer a new world of possibilities that could radically change the technology around us. A few years later, in 1965, Gordon Moore [9] noted that the number of transistors on a chip had roughly doubled every other year since 1959, and predicted that the trend was likely to hold as each new generation of microsystems would help to develop the next generation at lower prices and with smaller components. To date, the semiconductor industry has been able to fulfil Moore's Law. The impact on society and our lives of the continuous downscaling of systems is profound, and continues to open up new frontiers and possibilities. However, no exponential growth can continue forever, and the semiconductor industry will eventually reach the atomic limit for downsizing the transistor. Today, as that limit still seems to be some 20 years in the future, the growth is beginning to take new directions, indicating that the atomic limit might not be the limiting factor for the technological development the future. The semiconductor devices show an increased diversification, dividing for instance processors into very different systems such as processors for cheap disposable chips, low power consumption portable devices or high processing power devices. Microfabrication is also merging with other branches of science to included for instance chemical and optical micro systems. This diversity seems to increase on all levels in technology. As the components become so small that quantum effects become important, the diversity must be expected to further increase as completely new devices and possibilities begin to open up that were not possible with the bulk materials of the today's technology. The visions of Feynman are today shared by many others:

when nanotechnology is seen as a general cross disciplinary technology, it has the potential to create a coming "industrial" revolution that will have major impact on society and everyday life, comparable to electricity and information technology.

1.1.1 Nanocomponents and Methods

As an emerging technology, the methods and components of nanotechnology are under continuous development and each generation is providing a better foundation for the following. With regards to the methods, the Scanning Tunneling Microscope (STM) [10] and Atomic Force Microscope (AFM) [11] were developed in the 1980's and opened up completely new ways to investigate nanoscale materials. An important aspect was the novel possibility to directly manipulate nanoscale objects. Transmission and scanning electron microscopes (TEM and SEM) had been available since the 30's [12][13], but mainly offered the possibility to passively image rather than actually interact with the sample.

Several unique nanoscale structures were also discovered around 1990: the C_{60} buckyball molecule [14] and later the carbon nanotube [15]. In recent years, more complex nanostructures such as semiconductor nanowire heterostructures have also proven to be useful building blocks or components in nanodevices [16][17]. The applications of such nanocomponents span all aspects of technology: Electronics [18], optics/photonics [19], medical, biochemical [20] as well as better and smarter materials. But to date few real products are available with nanoscale components, apart from traditional nanoscale products, such as paint with nanoparticles or catalytic particles for chemical reactors. Prototype devices have been created from individual nanocomponents, but actual production is still on the verge. As when integrated electronics were developed [9], nanotechnology is currently in the phase where component production methods, characterization methods, tools for manipulation and integration are evolving by mutual support and convergence.

A main problem is reliable integration of the nanoscale components into microsystems since the production methods are often not compatible. For fabrication of devices with integrated nanocomponents, the optimal manipulation technique is of course to have the individual components self-assembling or growing into the required complex systems [21][22]. Self assembly of devices in liquids is an expanding field within nanotechnology but usually requires the components to be covered in various surfactants, which usually also influence the component properties. To avoid surface treatments, nanotubes and whiskers/wires can be grown on chips and microsystems directly from prepatterned catalytic particles [23][24][25]. Although promising for future large scale production of devices, few working devices have been made by the method to date.

The prevailing integration technique for nanowire/tube systems seems to be electron beam lithography (EBL) of metal structures onto substrates with randomly positioned nanowires deposited from liquid dispersions [26]. By using flow alignment

or electrical fields, the wire deposition from liquids can be controlled to some extent [27]. The EBL method has allowed for systematic investigations of nanowires' and tubes' electrical properties, and creation of high performance electronic components such as field-effect transistors and chemical sensors [28]. These proof of principle devices are some of the few but important demonstrations of devices nanotechnology might offer. In addition nanomechanical structures have also recently been demonstrated, such as rotational actuator with a carbon nanotube axis built by Fennimore et al. [29].

A more active approach to creating nanowire structures is to use scanning probe microscopy (SPM) to push, slide and roll the nanostructures across surfaces [30][31]. SPM manipulation has been used to create and study nanotube junctions [31] and field effect transistors [32]. The ability to manipulate individual nanoscale objects has hence proven very useful for building proof-of-principle devices and prototypes, as well as for characterizing and testing components. The self-assembly method is likely to be important for future large scale production, but nanomanipulation will probably be a key technique to use for testing individual structures and developing prototypes before processes are made to mass-produce devices. Such techniques could hence become important factors in the self-sustaining development of nanotechnology.

1.1.2 Nanomanipulation Systems

To monitor the manipulation process, in-situ SEM or TEM manipulation seems preferable. AFM (or STM) does have the resolution to image nanoscale objects, even down to the sub-atomic scale [33], but the imaging frame rate is usually slow compared to SEM or TEM and the structures will normally have to be planar. SEM offers the possibility of high frame rates; almost nanometer resolution imaging of three-dimensional objects; imaging over a large range of working distances; and ample surrounding volume in the sample chamber for the manipulation setup. TEM has a much more limited space available for the sample and manipulation systems but can on the other hand provide atomic resolution. For detailed studies of the nanowires' structure, TEM is a useful tool, but for the assembly of nanoscale components of a well defined structure, such as batch fabricated nanowires and nanotubes, the SEM resolution should be sufficient to complete the assembly task.

As the STM and AFM techniques opened up completely new fields of science by allowing the investigator to interact with the sample rather than just observe, development of nanomanipulation tools for SEM and TEM could probably have a similar effect for three-dimensional manipulation. Recently, commercial systems for such tasks have become available such as the F100 Nanomanipulator System from Zyvex in October 2003 [34]. Several research groups have also pursued developing such systems [35][36][30].

To date the tools used for in-situ SEM nanomanipulation have almost exclusively been individual tips (AFM cantilever tips or etched tungsten tips), sometimes

tips used together with electron beam deposition have been used to create nanowire devices [37]. Despite the availability of commercial microfabricated grippers in the last couple of years, little has been reported on the use of such devices for handling nanostructures. Some electrical measurements and manipulation tasks have been performed in ambient conditions with carbon nanotube nanotweezers [38][39].

1.2 The Present Work

The three year Ph.D. project aimed at developing an in-situ SEM nanomanipulation setup with tools for prototyping and research applications. In this thesis focus will be on investigating and characterizing nanowires and nanotubes, since these rod-shaped components can be complex individual nanosystems such as the nanowire heterostructures developed by the groups of Lieber [16] and Samuelson [21].

At the project start, the actuation systems to move tools with nanometer precision were available commercially. The microfabrication facility at MIC also meant that we were able to design and fabricate unique tools to use in such a setup. Our research group, the Nanohand project, had previously gained experience in the fabrication and use of microcantilever chips for measuring the conductivity of surfaces. By changing the design of the chips, microfabricated grippers could be made that might be able to manipulate objects in the in-situ setup. The existing microcantilever systems developed at MIC, the four point probes and piezoresistive AFM cantilevers, could also become useful tools within the setup for characterization of nanostructures. After integrating the nanowires/tubes in a microsystem, it would be preferable to be able to investigate the structure of the device with high resolution. A special method was developed using microcantilever chips for TEM studies, so-called *TEM-Chips*.

Chapter 2 introduces the SEM and TEM instruments, as well as the standard chips available at MIC by the beginning of this project. Then, the developed SEM manipulation systems and the TEM-chip system are described. In Chapter 3, the development of microfabricated grippers for nanomanipulation and how the devices were used for successful manipulation of nanowires is described. Chapter 4 describes how electron beam deposition (EBD) can be used to directly solder and construct nanostructures. The study was done using an environmental electron microscope. The environmental EBD (EEBD) was found to give unique opportunities, such as the possibility to create structures with a solid polycrystalline gold core under suitable conditions. Finally chapter 5 describes how the "TEM-Chips" were used to investigate carbon nanotubes.

The developed concept for an in-situ nanolaboratory is a versatile system where each part can have several different applications:

- The microfabricated gripper could be the assembly tool as well as a device platform onto which nanowires can be placed. Such nanowire devices can then be

characterized in both TEM and by other methods (cryogenic or optical measurement etc.). Microgrippers could also find applications such as manipulation of micrometer sized samples for microscopy in general.

- The electron beam would be used for imaging during manipulation. With EBD, the beam can also be used to solder and bond nanostructures together and even to directly construct nanostructures. EBD is for instance used to make nanoscale tips on the microfabricated grippers.

- The nanowires/EEBD structures can be used for electrical as well as structural components (such as tweezers tips).

With sufficiently small gripper tools for the in-situ nanomanipulation system, pick-and-place assembly of nanodevices might be feasible. Electron beam deposition could be used as a soldering tool for fixing the components and ensuring electrical contact. Such a scheme is resembling the automated pick-and-place of macroscopic electronic components onto printed circuit boards, but applied to objects that are 10000 times smaller.

Chapter 2

Nanomanipulation Systems

Design of an in-situ electron microscope nanomanipulation system requires an understanding of how to achieve optimal images with the microscope. The first section reviews transmission (TEM) and scanning electron microscopy (SEM), which are both used for experiments in this work. The manipulation system consists of a manipulation tool and an actuation unit to move the tool. Section 2.2 reviews the tools for manipulation and characterization of nanostructures that were available at MIC when the project started, as well as the actuation units capable of moving the tools with nanometer precision (Chapter 3 describes the development and use of microfabricated grippers for manipulation). Finally, the developed setups for nanomanipulation are described.

2.1 Introduction to Electron Microscopy

For manipulation and imaging of nanoscale objects, optical microscopy has limited resolution since the objects are often smaller than the wavelength of the light. The achievable resolution for a wavelength λ is often given by the diffraction limit δ [40] as

$$\delta = 0.61\frac{\lambda}{NA}, \tag{2.1}$$

with numerical aperture NA, which can be approximated[1] by the the angle of incidence $NA \approx \alpha \approx r_a/r_{wd}$ where r_a is the radius of the objective lens aperture and r_{wd} the working distance. Optical microscopes can often reach a resolution of about δ =200 nm. For nanomanipulation this is unfortunately not sufficient to distinguish for instance a single one nanotube from two adhering to each other, since they have diameters $\lesssim$ 100 nm. One can achieve a considerable improvement in resolution with instruments such as the transmission electron microscope and the scanning electron

[1] Since $\alpha \ll 1$for the present purposes, $\sin\alpha \approx \tan\alpha \approx \alpha$.

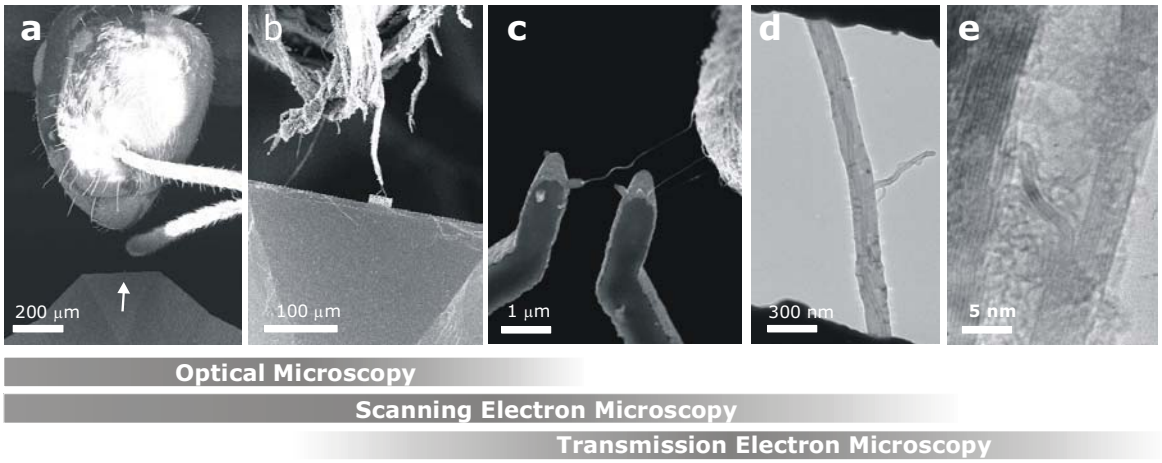

Figure 2.1: The different methods for microscopy used in this thesis each cover a range of magnification roughly indicated by the bars. The resolution of optical microscopy is limited to about 200 nm. a) SEM image of the head of an ant facing one of the microfabricated grippers. The gripper is barely visibly at the tip of the arrow. b) SEM image of a gripper approaching a large bundle of carbon nanotubes. c) Closeup in SEM of the gripper and nanotubes. d) TEM image of a carbon nanotube suspended between two grippers. e) TEM closeup of the shells of carbon atoms in a carbon nantoube. On the nanometer scale this particular carbon nanotube does not show a well defined carbon shell structure.

microscope that use electrons with De Broglie wavelength much smaller than that of visible light. Figure 2.1 gives an overview typical magnifications achievable by the different electron microscopes compared to a light microscope. Electron optical systems use electrical and magnetic fields to control the electron beam. Although the law of refraction in optics is exchanged with the Lorentz force in electrodynamics, the electron optical system has similar diffraction limits as optical systems, since they depend on the wave nature of the beam.

The De Broglie wavelength λ of an electron with momentum p is

$$\lambda = \frac{h}{p} = \frac{h}{\sqrt{2m_e E_b}}, \tag{2.2}$$

where h is Plancks constant. The electron has rest mass m_e and energy $E_e = m_e c^2 = 511$ keV. If an electron with charge q_e is accelerated from rest by an electrical potential U, to the electron beam energy $E_b = q_e U$, it will have a wavelength of 1 nm at 1 eV decreasing to 1 pm at 100 keV where it will be travelling with 50% the speed of light.

This chapter will briefly review fundamental issues for electron microscopy that are similar for SEM and TEM: the limitations imposed by the electron optical beam system in the microscope column; the interaction of the electron beam with the sample; the standard image formation method in SEM and TEM. These issues are essential

to understand the results and limitations reached in the experiments throughout the thesis. For further details, please refer to reviews of electron microscopes and their applications, such as Goldstein et al. [41] that contains a thorough review of SEM, while Goodhew and Humphreys [42] is a more general introduction to both SEM and TEM.

2.1.1 Electron Optics and Scattering

The electron optical system

For high resolution imaging, a well focused beam is required, just as in optical microscopy. Due to the short wavelength of electron beams with keV energies, as given by Eq. (2.2), the properties of the electron optical system and the electron emitter mainly defines the limits on the achievable beam diameter. The current density in the electron beam can be approximated by a Gaussian distribution of current density j [A/m^2] as function of radius, r, from the beam center

$$j(r) = j_0 e^{-\left(\frac{r}{r_0}\right)^2}, \tag{2.3}$$

with radius determined by r_0, giving a the full width half maximum $FWHM = 2\sqrt{\ln 2} r_0$. Integrating $I_b = \iint j(r) r dr d\theta$ gives the total beam current

$$I_b = j_0 \pi r_0^2. \tag{2.4}$$

The electron optics impose a limit on the achievable beam current density and radius by the brightness of the electron emitter β_e, which is conserved throughout the system [43]. Brightness, β, is a measure of the current per area normal to the beam direction and per element of solid angle [44]. At the center of the Gaussian beam,

$$\beta = \frac{j_0}{\pi \alpha^2} \tag{2.5}$$

and the brightness is related to the current density in Eq. 2.3. The emitter brightness β_e is determined by the type of electron emitter and the beam energy E_b [45]

$$\beta_e = \frac{j_e E_b}{\pi \Delta E} \tag{2.6}$$

with emission current density for W-filament sources about $j_e \sim 3$ A/cm^2, for LaB_6 sources about 100 A/cm^2, while field emission guns (FEG) can reach 10^5A/cm^2. The energy spread of the electrons from the sources are about $\Delta E \sim 1$ eV and slightly lower for FEGs. Due to conservation of the brightness in the system, the beam diameter depends on current as

$$r_0 = \frac{1}{\pi}\frac{r_{wd}}{r_a}\sqrt{\frac{I_b}{\beta_e}}. \tag{2.7}$$

The ideal beam probe size determined by the conservation of brightness cannot be obtained in a real system. Effects such as aberration will make the minimum achievable beam diameter larger. Equation 2.7 however seem to adequately describe the beam diameter for the present discussion [46][47]. Apart from the additional beam widening contributions, the image detection method imposes limits on useful values for the parameters in Eq. 2.7 which differ for SEM and TEM.

Electron Range

The electron optical system sets limitations to the achievable primary beam current and radius. The expected image resolution set by the primary beam cannot be reached if the signal detected for imaging is caused by electrons scattered far in the sample. The trajectory of an electron penetrating a bulk solid is a complex trajectory due to multiple elastic and inelastic collision events. As the primary electron (PE) penetrates into the sample it will gradually change direction and loose energy in collisions. The mean free path due to elastic and inelastic collisions, λ_{mfp}, depends on the atomic number of the material and the PE energy. At 100 keV $\lambda_{mfp} = 150$ nm for carbon and 5 nm for gold [42]. For samples thinner than λ_{mfp} the main part of the PE will pass relatively unaffected through the sample, which is the basis for TEM.

SEM can be used for thicker specimens. The electrons that escape from the sample in a new direction compared to the PE due to elastic collisions are called backscattered electrons (BSE). For samples thicker than λ_{mfp}, the volume interacting with the scattered PE defines the range of the electrons in the material, and this is considerably larger than the minimum achievable primary beam diameters. The electron range is about 1 μm at 10 keV for carbon, decreasing with higher atomic number for the material. Both the high energy PE and BSE generate secondary electrons (SE) by inelastic scattering events. The SE are generally defined as having energy below 50 eV while the BSE have energies up to the PE energy. The range of SE is typically 1 nm for metals and about 10 nm for insulators [41]. The short range of the SE make the yield of SE highly dependent on the energy lost by the PE within the SE range from the surface, and this makes high Z substances efficient generators of SE. The main emission of SE takes place in the region where the PE strikes the surface and within the SE escape depth from this region.

2.1.2 Scanning Electron Microscopy

In a scanning electron microscope a beam is scanned over the sample surface in a raster pattern while a signal is recorded from electron detectors for SE or BSE. The

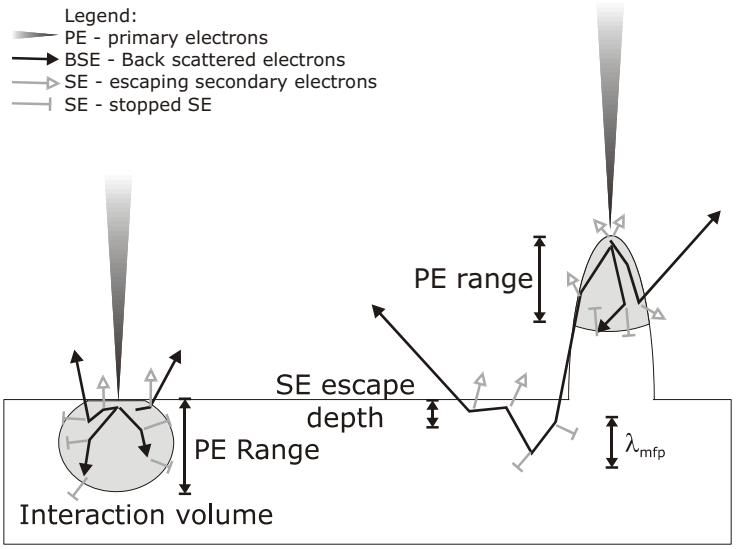

Figure 2.2: Overview of electron electron scattering processes in bulk and tip-shaped specimens. The PE are scattered within the interaction volume, defined the electron range in the material. The range is longer than the mean free path λ_{mfp}. The SE have a very short range, and only those created within that range from the surface can escape the material. This defines the SE escape depth.

PE energy is kept relatively low ($1 - 30$ keV) to limit the interaction volume in the specimen that will contribute to the detected signal. Especially low energy PE will provide high sensitivity to surface composition as they cannot penetrate far into the sample. Fig. 2.3a-b show the effect of PE penetration depth of a carbonaceous nanostructure with a gold core, where only the surface is visible at low PE energies, while the carbon becomes increasingly transparent and the core visible at high PE energies.

The low energy SE can easily be attracted and collected by a positively charged detector and are hence an efficient source for an image signal. The standard SE detector is an Everhart-Thornley (ET) detector where a positively charged grid attracts the SE and accelerates them to sufficiently high energies to create a light pulse when striking a scintillator. The light pulse is then amplified by a photomultiplier. Despite the complex construction, the ET detector is remarkably efficient, but requires large r_{wd} for effective collection of the SE by the charged grid. Another SEM detector used in this work, is the in-lens detector, where SE passing through the column aperture are accelerated towards a solid state detector. The in-lens detector complements the ET by being more efficient at short $r_{wd.}$.

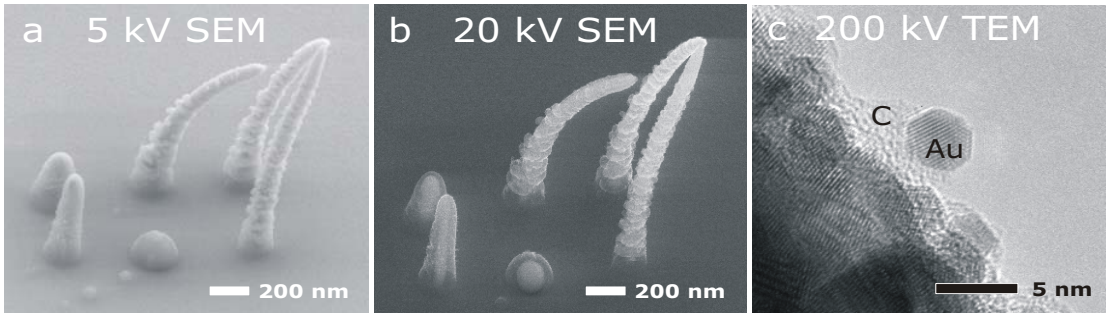

Figure 2.3: The electron range increases with beam energy. The internal structure of the EEBD deposits can be examined at high electron beam energies in SEM. At 5 kV with shallow penetration depth, the surface of the tips is clearly visible while at higher energies a core of more dense material becomes increasingly visible. At 100 keV and above, TEM images can achieve atomic resolution where the lattice planes in nanocrystals such as the gold nanocrystal in (c). The gold crystal is embedded in amorphous carbon with no clear lattice pattern.

The Optimal SEM Image for Nanomanipulation

As the typical SEM image is created from the secondary electrons collected from the sample, compromises must always be made to obtain the optimal imaging conditions regarding resolution and contrast. The contrast in a SEM SE image depends on the variations in SE yield from the different surface regions in the image and the signal to noise level. The resolution depends on the beam diameter and is at least some nm larger due to the SE range.

The optimal solution is always to use as good an emitter as possible (high β_e in Eq. 2.7). The SEM instruments at MIC, Lund, and the ESEM at Haldor Topsøe, all use FEG sources. Working at short r_{wd} gives a narrow beam (Eq. 2.7), but will usually shield the standard ET detectors from attracting sufficient secondary electrons. Nanomanipulation often requires working with high resolution between two large manipulator units which further limits the efficiency of signal detection. The manipulation equipment must be designed to make the end-effector and samples meet at short r_{wd}, and without obstructing the electron path towards the detector. A short r_{wd} also gives a short depth of focus, which can be a help during nanomanipulation because it makes it possible to judge the working distance to various objects by focussing on them. The operator can use this to get an impression of the height of the objects in the setup. Generally, for nanomanipulation, the above considerations indicate an inlens detector often can be advantageous.

Reducing the beam current to narrow the electron beam necessarily limits the number of detected electrons and make the signal-to-noise ratio low, unless one makes very slow scans to increase the number of counts[2]. When used for in-situ nanomanip-

[2]The signal to noise ratio S/N for Poisson distributed count measurements n is $S/N = \sqrt{n}$ and high counts are necessary to reduce noise in the images.

ulation one needs a fast scan rate to follow the moving tools (preferably at rates approaching live video) and this requires high beam currents. The acceleration voltage is also important, and too high PE energy can make the sample transparent (such as the carbon coating in Fig. 2.3b) while low energy usually make the image susceptible to drift due to charging and similar effects.

2.1.3 Transmission Electron Microscopy (TEM)

When the specimen thickness is about the mean free path, λ_{mfp}, TEM can be used to achieve high resolution images such as the image in Fig. 2.3c where the atomic lattice of a gold nanocrystal is visible. Since the detected electrons are transmitted PE where the energy can be in the 100 keV range, the resolution is not limited by the issues regarding secondary electrons. The electron beam optics can be optimized for higher current densities (Eq. 2.5) at higher energies compared to SEM. To achieve optimal imaging conditions for the thin TEM samples, the working distance has been made short. In most TEMs, the space for the sample holder is only about $(5\text{ mm})^3$ between the two objective lenses for the incoming and transmitted beam. Before reaching a CCD camera, the transmitted beam is sent through several magnification lenses to achieve the high magnification (500.000X is not unusual).

The image formation in TEM can be based on several principles, but practically all images used in this work were made by phase contrast imaging, here called High Resolution TEM or HRTEM. At sufficiently high brightness, electron sources can produce coherent electron beams due to the point-like emitter surface area and small energy spread [48]. The coherent electron beam can be considered as a spherical wave propagating from the emitter and out through the electron optical system, much like a laser beam would propagate through an optical system. The HRTEM images are based on the interference of the electron wavefront after it has passed through the sample and reaches a CCD detector to give a phase contrast image of the sample. The image will have a resolution determined of course by the wavelength of the electrons (Eq. 2.2) but mainly by the imperfections of the electron optics which also perturbs the wavefront. The optimal imaging condition is for a sample thickness about λ_{mfp}, where the wavefront is only slightly perturbed by passing through the sample. Both the TEM at Haldor Topsøe and at IPL that we have used for this project are capable of resolving individual shells of a carbon nanotubes as discussed in Chapter 4 and 5. The fine-tuning of the electron optical system to the required resolution can be achieved in about 30 min.

2.1.4 Summary

SEM seems to offer a suitable environment for nanomanipulation of nanowires and nanotubes. The resolution can be of the order nm, and there is a large space available

for the sample and manipulation system in the vacuum chamber. For optimal resolution and contrast, the available detection methods and the need for a short working distance should be considered when building the setup. It is important to remember that a good SEM image usually requires careful balancing of all the issues mentioned in Sect. 2.1.2. Failure to design an experimental setup to satisfy proper imaging conditions can end up wasting days with the manipulation equipment to accomplish what might have been achieved in a fraction of the time if proper imaging conditions had been obtained.

TEM provides higher resolution, capable of imaging atomic lattice patterns in HRTEM images. Compared to SEM the sample space is very limited and manipulation setups difficult to construct, although commercial systems are available [49]. In this project a microchip based system is developed for combined electrical and TEM characterization of nanostructures (Sect. 2.3.3).

2.2 Tools for Nanomanipulation

The main part of the nanomanipulation experiments in literature has been done using tips on AFM cantilevers or STM tips; even for three-dimensional in-situ SEM manipulation. AFM and STM are very well developed technologies with high resolution and possibilities for doing manipulation, but mainly limited to planar surfaces. This project aims at developing microfabricated grippers in the hope that they will offer a wider range of possibilities for three-dimensional manipulation, though this will also require an increase in complexity of the manipulation method. This is the subject of chapter 3, which starts with a literature review of nano/micro grippers and tweezers. In this project STM tips are also used for manipulation of samples that adhere too strongly to be manipulated by grippers (see Chapter 5). Such tips and other alternatives to grippers for manipulation are briefly reviewed below.

Apart from imaging, both AFM and STM can also be used for measuring the electrical properties of the samples. AFM can also provide detailed information about the forces between the tip and object. For the in-situ laboratory both electrical and force measurements would be very valuable. At MIC various cantilever chips have been developed that might be useful for such measurements. These are described in Sect. 2.2.2 followed by a description of the actuation systems used for the manipulation systems in this work.

2.2.1 Manipulation Tools

The manipulation techniques not involving grippers/tweezers can be divided in methods for moving and methods for fixing objects. A wealth of techniques are available for handling of samples under ambient and liquid conditions, such as micropipettes

and optical tweezers [50], but these are beyond the scope of this work where the focus is on SEM compatible methods.

SEM Compatible Manipulation Methods

- Tip manipulation: Sharp tips such as AFM tips [51][52] or STM tips [53] have been used to manipulate carbon nanotubes onto microchips. Nanotubes have also been attached to existing AFM cantilever tips to make higher aspect ratio AFM tips or for measurements of the mechanical properties of the nanotubes [54][52]. In ambient conditions, we have used etched tungsten tips to move nanotubes onto microcantilevers by the naturally present adhesion forces, which are mainly capillary forces (See Sect. 5.3). For in-situ SEM manipulation, our experience, as well as the published results [51][52][53], show that the tip manipulation technique usually requires some sort of soldering or gluing method to attach the nanotubes to the tips (see below). Tungsten STM tips with coarse micrometer-sized apices are easily etched from cheap tungsten wire in a few minutes [55] making them favorable for many applications, since they are much cheaper than any probe made by microfabrication.

- Electrostatic attraction: By applying a voltage to a metallic tip coated in a thin insulating layer, electrostatic attraction can be used to move objects around. Tsuchiya et al. built a small sub-millimeter model of a house with prefabricated thin-film elements by this technique [35].

- Dielectrophoresis: Application of an alternating electrical field between two electrodes has mainly been used to attract or repel carbon nanotubes in solution, but can also be used to move nanoobjects in vacuum [56].

Methods for fixing objects

Micrometer and nanoscale objects can be fastened by several methods. Some method for fixing the object can be required to pick up an object by in-situ SEM tip manipulation and particularly to fix it when placing it again.

- Glue: Kim et al. and other have used acrylic glue to attach nanotubes to AFM tips and micropipettes [38].

- Electron beam deposition: EBD may be used in situ to "solder" the nanotube/nanowire onto the desired location and thereby increase the surface adhesion [53].

- Laser soldering: A focused laser beam has been used to melt materials locally to solder micro objects [35].

- Thermal soldering: Electro-thermal heating could be used to fix the objects, like the laser soldering. Grippers have been developed with interchangeable end-effectors fixed to the actuator by thermally activated glue [57].

2.2.2 Characterization Tools

Several of the microcantilever structures that were developed at MIC at the beginning of the NanoHand project can be as tools in the in-situ SEM setup for characterizing nanostructures. Microfabricated conductance probes which have been extensively used in this project are described below. In addition, a short description is given of piezoresistive cantilever (PRC) force sensors which seem to be potentially useful for measuring the mechanical properties of nanostructures in the in-situ SEM setup.

Conductance Probes

Probes for measuring surface conductivity on the micrometer scale by microfabricated cantilevers had prior to this project bee developed by researchers at MIC [58]. The conductance probes are now commercially available from the company Capres A/S [59]. The process for making the conductance probes is briefly described in Ref. [60], while Ref. [58] provides an detailed discussion. The process was also used to make the electrostatic grippers (Chapter 3), the chips nanotubes were soldered to (Chapter 4), as well as the conductance probes and the TEM-chips used for electrical measurements on carbon nanotubes (Chapter 5). The most essential step in the fabrication process to consider for the present work, is the anisotropic gold coating of the under-etched cantilever electrodes. The gold coating on the chip is shown in Fig 2.4 together with a SEM image of such a probe contacting a nanowire in the in-situ SEM setup. The gold coating on the sidewalls of the cantilevers can vary in thickness and uniformity from device to device. The total resistance including leads and contact resistance of one cantilever electrode to a gold surface is usually about 90 Ω.

PRC Force Sensors

The BioProbe group at MIC had developed piezoresistive cantilevers (PRC), initially intended for AFM measurements, and later re-designed to make cantilever probes for biochemical experiments with surface coatings [61][62]. The PRC probes are potentially useful for measuring forces in the nanomanipulation setup. SEM compatible AFM systems are available, but expensive and cumbersome to operate. The PRCs offer a convenient way to do force measurements, requiring only electrical connections and an actuator to position it. Unlike a conventional AFM, the PRC probe can easily be rotated or mounted to measure on three-dimensional structures in the SEM.

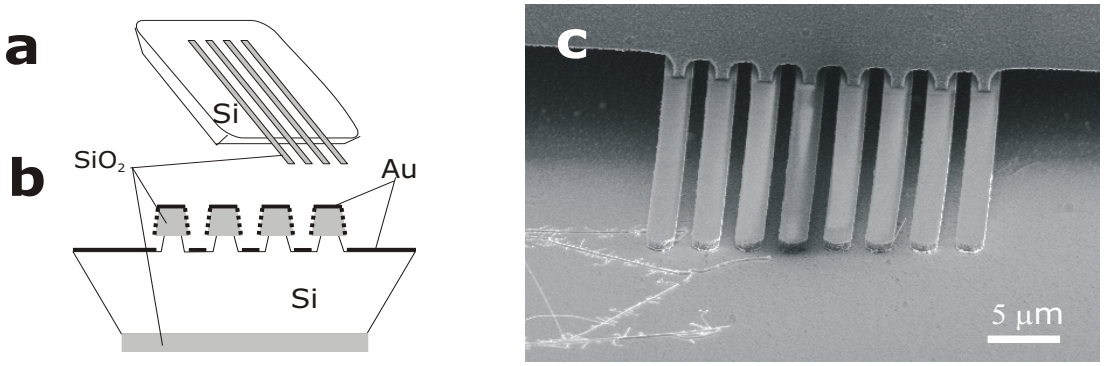

Figure 2.4: The conductance probes. a) By microfabrication processes [58], a SiO_2 cantilever array system is made. b) The cantilevers are underetched by isotropic RIE and metallized by anisotropic metal deposition (usually 10 nm Ti / 100 nm Au). The underetch prevents the cantilevers from short-circuiting. Depending on the RIE conditions, the cantilever sidewalls will be slightly inclined and to some extent become metallized as well. c) SEM image of such a probe contacting InP nanowires in the in-situ SEM setup. The darker of the cantilevers is positively biased with 20 V.

The individual PRC probes are not well calibrated for precise measurements of forces. Each PRC probe could be calibrated by measuring it response when pressed against cantilevers with well-known properties. For a good calibration, several cantilevers with a well defined geometry and material properties were needed, and this can easily be tested by measuring the resonance frequency of the cantilever. Various standard AFM cantilevers were acquired to be used as a calibration standards. Unfortunately, the AFM cantilevers turned out to have poorly defined resonance frequencies and rather variable thickness. To solve this problem, I designed a chip called the "Xylophone" which has cantilevers of various lengths and width, fabricated by the standard four point process without the metallization step. Such Xylophone cantilevers generally had fundamental and 1st harmonic resonance frequencies within a few percent of the values predicted from the physical properties of SiO_2 and the geometry as measured in the SEM. Though the xylophones seem to be appropriate for calibrating the PRCs, the system has not been extensively tested, and has not been used for the work presented in this thesis. It is planned to continue this work and create a calibrated PRC setup for nanomanipulation, which could be a very useful tool in the in-situ SEM setup for measuring the mechanical properties of nanostructures.

2.2.3 Actuation Systems for In-situ Nanomanipulation

For in-situ nanomanipulation, a tool and a sample will have to be positioned in the region with optimal SEM resolution, and then to be moved with a sufficiently high precision over a range large enough to accomplish the required manipulation task. For the present experiments, the required precision is of the order $\lesssim$ 100 nm, since

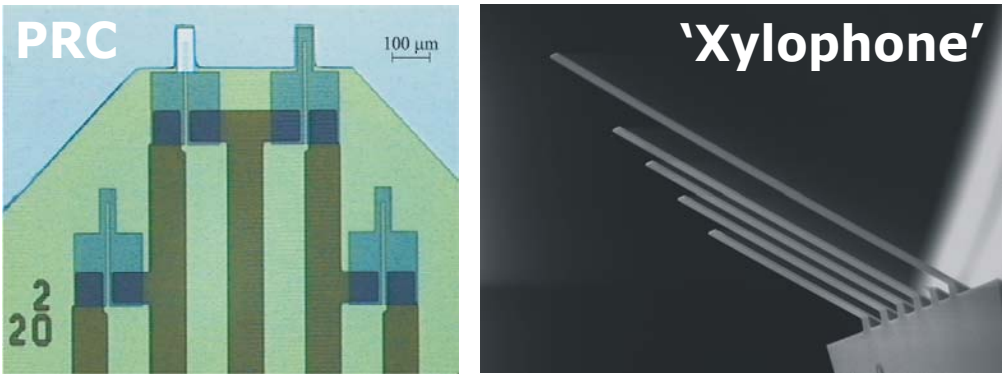

Figure 2.5: a) The piezoresistive cantilever (PRC) developed by the Bioprobe group (image from [61]). b) The "Xylophone" for calibration of the PRC.

that is a fraction of the gaps between the cantilevers made by the four point process (grippers or conductance probes) and also the typical diameter of the nanowires. The required actuation range must be judged from the individual task, but several millimeters is a minimum requirement for systems that must be mounted in a SEM without excessive demands on the mounting alignment.

For AFM and STM systems, it is normally essential to avoid both drift and vibrations in the system. In the present systems, the direct user control and fast frame rate makes drift a less critical issue than in STM and AFM, while vibrations can severely reduce the effective resolution. An effective measure to reduce both drift and vibrations is to mount everything with screws and use very thin and flexible wires for electrical connections (such as Litz wires).

Two actuation units are required, one for the tool and one for the sample. The stage in most SEMs is often of such high quality that it can be used as one of the actuation units. The stage often also provides more than x, y and z in the degrees of freedom, which gives extra flexibility when designing the setup. The SEM stages will be mentioned along with the appropriate setups in the following section. The actuation units do not have to be equally good. One can be slow and coarse, and used for slowly bringing either the sample or tool into the imaging region so it can be accessed. To avoid time-consuming sessions and wasted SEM time, at least one of the manipulators should be able to move fast, precisely, reliably, and with intuitive control through the user interface.

The second manipulation unit will have to be inserted into the sample chamber. Since it must be SEM compatible it should have non-magnetic elements and low outgassing rates. Piezoactuatated slip-stick drives seem to fulfill the requirements well [63] and several systems are available commercially [64][65]. The slip-stick drive principle is explained in Fig 2.6. For fine positioning, DC voltages are applied to the piezo element, which makes the actuator move within the range of the piezo element

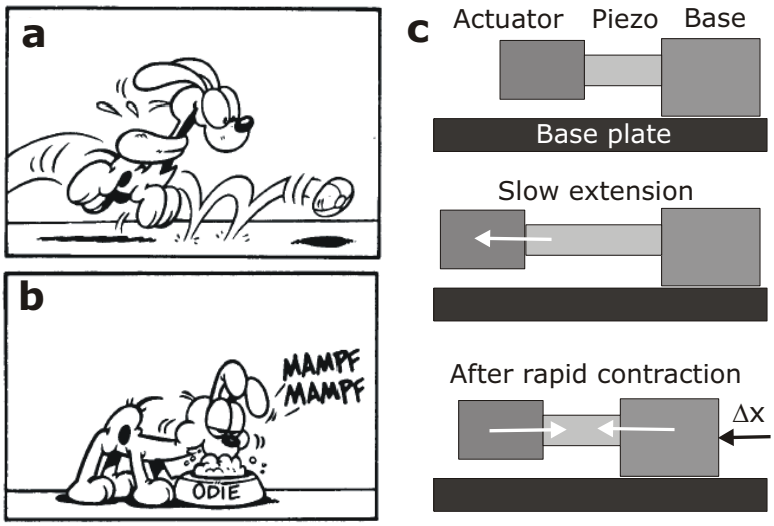

Figure 2.6: Two use either a coarse or fine positioning method is natural. a) Coarse positioning provides long range but low precision, while fine positioning (b) provides high precision and short range. (adapted from [63] and Garfield by Jim Davies). c) The slip stick principle: Slow actuation of the piezo element leads to fine positioning. A combination of rapid contraction and slow extension can make the actuator move in coarse steps Δx because the force on the base becomes larger than the static friction force between the base and base plate. Reversing the direction is done by using slow contractions instead.

(usually of the order 1 μm).[3]

Before the project was initiated three NanoMotor units from Klocke NanoTechnik [64] was acquired for the actuation system. The NanoMotor setup consists of three linear actuators mounted to provide x,y, and z actuation with a range of 20 mm on each axis. The actuators units are based on the slip-stick principle [67][68]. The effective precision of the system is highly dependent on the vibration level in the setup. In the SEM at MIC, which is placed inside the cleanroom facility, the observed vibrations were often considerable (of the order 10-30 nm). I built the three units into the system shown in Fig 2.7a with protective plates that made handling it easier and safer.

By the end of the project, while working at AMiR at Oldenbrug University together with Axel Kortschack and Thomas Wich, we tried using the actuation system developed by Axel Kortschack [66]. The system is colloquially called R2-D2, since it is able to move in x-y and rotate when placed on a supporting plate. The R2D2 unit

[3]To achieve a longer range of fine positioning, I designed a 2-degree-of-freedom actuation system based on mulitlayer piezo-benders with a finepositioning range of about 100-300 μm and circular coarse positioning range within a radius of about 10 cm. The system is based on a rotational slip-stick principle and performed well in both ambient and SEM conditions. This project is however beyond the scope of this report.

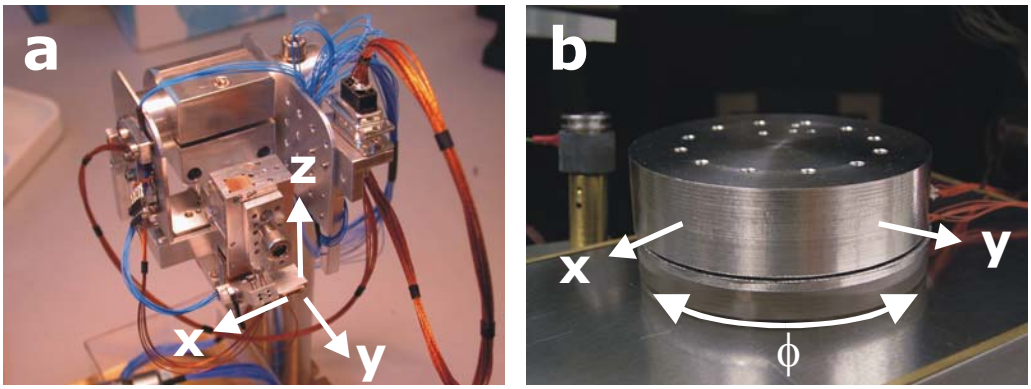

Figure 2.7: Actuation systems. a) The "NanoMotor" setup. Three Klocke Nanomotor units are mounted in xyz configuration giving a range of 20 mm in all axes. The nanomotor has been mounted within protective plates that serve as convenient breadboards for fixing plugs and wires. b) The R2D2 unit developed by Axel Kortschack [66]. When placed on a planar support in can move in xy and rotate as indicated.

is shown in Fig 2.7b. Unlike the nanomotor system that has to be mounted on a rod and has a limited range of actuation, the R2-D2 can move as far as the supporting plate reaches. The ability to rotate makes it possible to mount many probes that extend over the edge of the unit, and the required tool can then be selected by rotating the unit. The limited range of the nanomotor makes it difficult to mount even two probes simultaneously. Since the R2-D2 unit cannot adjust the height in its present configuration, this must be accomplished by the sample holder.

2.2.4 Summary

Alternatives to nanomanipulation with grippers were briefly presented. Then the microcantilever tools developed at MIC prior to the project start, that could find applications for characterization of nanostructure in the in-situ SEM setup were described: The conductance probes and force sensing PRC. Two actuation systems were used for in-situ nanomanipulation together with the SEM sample stages. Both systems relied on piezo driven slip-stick actuation and were capable of moving with sub micrometer precision and low levels of vibration. The nanomotor has a range of 20 mm in each of the x,y, and z axis and hold on or two tools. On the other hand, the R2-D2 can move in x and y only limited by the supporting surface and has the ability to rotate which makes it possible to change between several tools mounted on the R2-D2.

2.3 Developed Nanomanipulation Systems

In this section the optical manipulation systems are described, followed by the SEM systems and finally the TEM-chip system.

The use of microfabricated tools increases the cost and complexity of the individual tool or probe, such as the conductance probes compared to using etched tungsten tips (STM tips). But this apparent increase in complexity of the tool leads to a considerable reduction in the requirements on the manipulation system. If for instance four point measurements of conductance should be accomplished with tungsten tips, it would probably require four independent xyz-manipulators [69]. Such a setup would be very sensitive to drift and vibrations and probably very time consuming to operate. By using a single conductance probe, such measurements can be achieve by a single xyz-manipulator. The microgripper and PRC are likewise chips that only require one manipulator to function. This makes it necessary to have two manipulators in our nanomanipulation systems: one for the tool and one for the sample, since both will have to be moved into the focus region of the microscope with micrometer precision.

2.3.1 Optical Manipulation Station

The in-situ SEM systems offer the high resolution, but an having access to an optical manipulation system in ambient conditions gives definite advantages:

- Much easier to access, since the equipment does not have to be SEM compatible or cleaned to prevent outgassing.
- Manipulation can be done by simple and cheap mechanical xyz-stages rather than expensive remote controlled in-situ systems.
- It can often be used for preparing samples, test devices and testing systems before they are inserted into the SEM.

A dedicated optical manipulation setup can hence often complement the in-situ system in many ways. Since the objects are often smaller than the diffraction limit (Eq. 2.1), a single nanowire will appear as a slightly blurred rod-shaped object. By manipulating the object it will often become clear if more wires are present. To achieve as high resolution as possible, the numerical aperture of the objective has to be large. This often means a short r_{wd}. In the laboratory we had good experience with a Mitutoyo objective with a 13 mm r_{wd}. This is substantially larger than the standard objectives for the available Zeiss microscopes (1.3 - 5 mm). Peter Bøggild in 2001 constructed a "4 point probe station" with such an objective lens system connected to a video camera and Labview controlled frame grabber. Apart from scanning conductance measurements, the station turned out to be very suitable for manipulation

of sub-micron objects. Jakob Kjelstrup-Hansen and I built a comparable system, but with the possibility to control the atmosphere since the humidity turned out to be an important factor when doing manipulation in ambient conditions (see sect 5.3.1).

The main source of vibrations in a setup are caused by the operator physically touching the setup. To reduce the vibration level during manipulation, Burleigh micromanipulator stages were used. The position is coarse adjusted manually by micrometer screws, while fine positioning is actuated by piezo elements driven by an external control to avoid touching the setup (with a range of 75 μm). These setups have proven very useful for preparing probes with nanotubes on micrometer wide cantilevers, such as those used in chapter 5.

In addition to these dedicated manipulation stations, a standard Zeiss Axiotech microscope has been used to do many sample preparation tasks. The working distance is 1.3 mm, so the manipulation setup will have to be carefully designed to be useful with such limited space. Most of the TEM-Chips discussed in Chapter 5 were prepared under the Zeiss microscope, using a standard probe station stage (Quater XYZ-300) to move the tool (an etched tungsten tip).

2.3.2 In-situ SEM Systems

The main issues to consider when building an in-situ nanomanipulation setup is described in Sect. 2.1.2 and Sect 2.2.3. The in-situ nanomanipulation systems were developed during 2001-2004, for solving various tasks and using the available electron microscopes for those task. The following section describes each system and the advantages and disadvantages as we have experienced them. The summary concludes the general features and issues to consider when designing an in-situ nanomanipulation system.

MIC-SEM (High vacuum)

Images of the setup built for the LEO 1550 FEG SEM are shown in Figure 2.8. The stage of the Leo-1550 is of outstanding quality for nanomanipulation. The joystick control is intuitive and compensates for the magnification of the image, which makes it easy to control the stage even at the highest resolution. The stage is actuated by small electromotors and spring loaded clogs. The stage makes it possible to mount a large holder with many samples, so new probes and samples can be brought into view by rotating the stage. This saves time by avoiding venting and pumping to change samples. Manipulation is often easier to do by using the stage rather than the NanoMotor. The SEM has an in-lens detector,which makes it possible to work at very short $r_{wd} \sim 2 - 3$ mm.

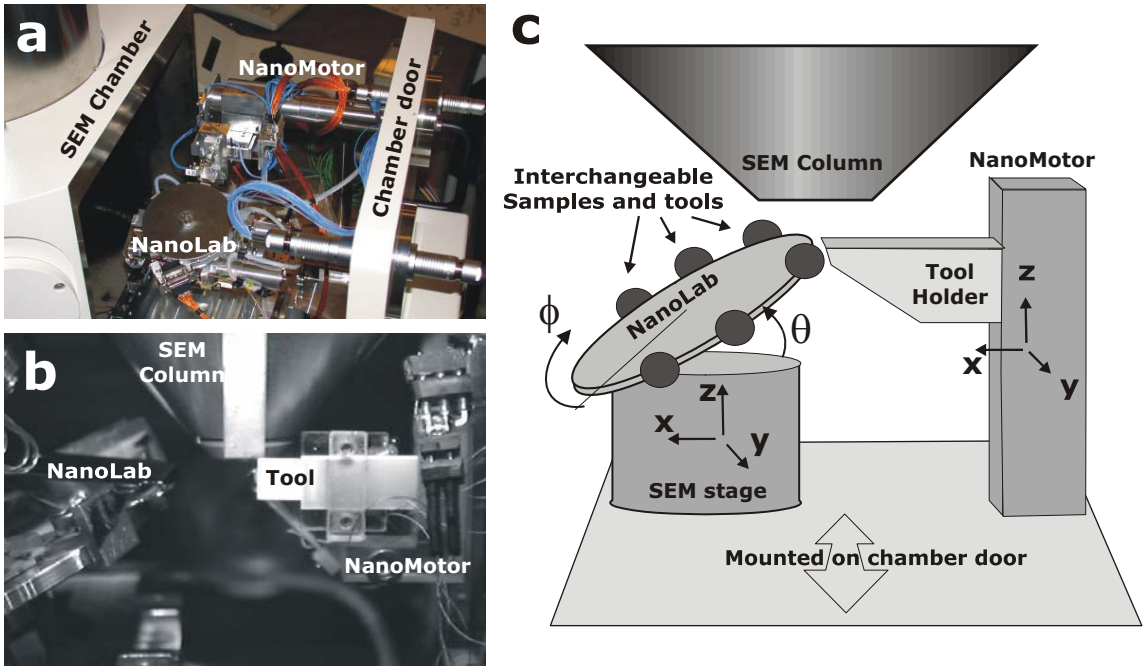

Figure 2.8: The setup in the MIC-SEM. The nanomotor and LEO sample stage are both mounted on the SEM door for easy access. The stage can move in xyz, rotate ϕ and tilt θ. a) The "NanoLab" is mounted on the stage with several different tools and samples fixed on the edge, so they can be rotated into contact with the probes on the nanomotor. b) Chamber scope view of the setup. c) Schematic view of the setup. The θ tilt of the NanoLab gives ample space for the detectors while ensuring a short r_{wd}. One or two tools can usually be mounted on the NanoMotor.

HT-ESEM (controlled atmosphere)

The Philips XL-30 FEG environmental SEM (ESEM) makes it possible to do SEM, while gasses with pressure in the range 0.1-10 Torr are present in the sample chamber [70]. The resolution is somewhat limited in environmental mode due to scattering in the gas [71]. The stage is controlled by the user interface of the SEM control program. The stage was usually positioned as required and the manipulation was done by the NanoMotor. The environmental mode makes the ESEM interesting for studying the difference between manipulation in ambient conditions and in vacuum, but in this work the focus is on electron beam deposition under environmental conditions (chapter 4).

AMiR-SEM

The Zeiss DSM 950 electron microscope at AMiR, Oldenburg, was equipped with a W-filament, which limited the resolution somewhat compared to the above FEG SEMs. For high frame rates and moderate resolution, the W-filament source has an

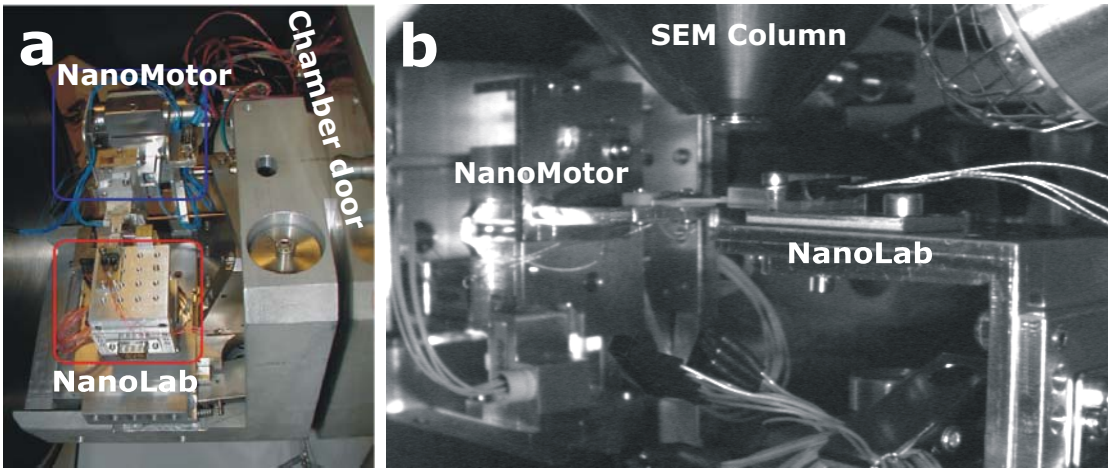

Figure 2.9: View of the ESEM setup from the chamber scope. The nanomotor is in the back holding a horizontal probe towards the ESEM nanolab in the front.

advantage since it can give higher beam currents than the FEG. This made the setup useful for live video recording of manipulation experiments with a reasonable frame rate and signal-to-noise ratio. For high resolution imaging an attached scan system [72] could improve the resolution considerably.

The stage was controlled manually by micrometer screws. After some adjustments and cleaning, it turned out to be highly reliable and intuitive to use. In fact it was to some extent easier than the joystick controlled Kleindieck manipulator also tested in the setup, and the nanomotor used in the other SEM setups. For the pick-and-place operations presented in chapter 3, the R2-D2 unit was used. The software for that device is still under development, so it was mainly used for bringing the probe into the imaging region, so the manual stage could be used to carry out the manipulation tasks.

2.3.3 The TEM-Chip system

Despite the superior resolution, the very narrow sample space of a TEM has so far limited the possibilities for in-situ TEM nanomanipulation in practice. AFM and STM systems are commercially available from companies such as Nanofactory Instruments [49]. In this project I have designed microfabricated cantilever electrode chips compatible with both standard TEM probe holders and a custom made in-situ probe holder with electrical connections. In this TEM-chip system, nanostructures can ex-situ be manipulated onto the chips, for then ex- or in-situ to be subjected to electrical or mechanical experiments. The changes taking place in the nanostructure can then be followed by TEM analysis between or during the experiments.

The cantilever chips were fabricated by the conductance probe process (Fig 2.4)

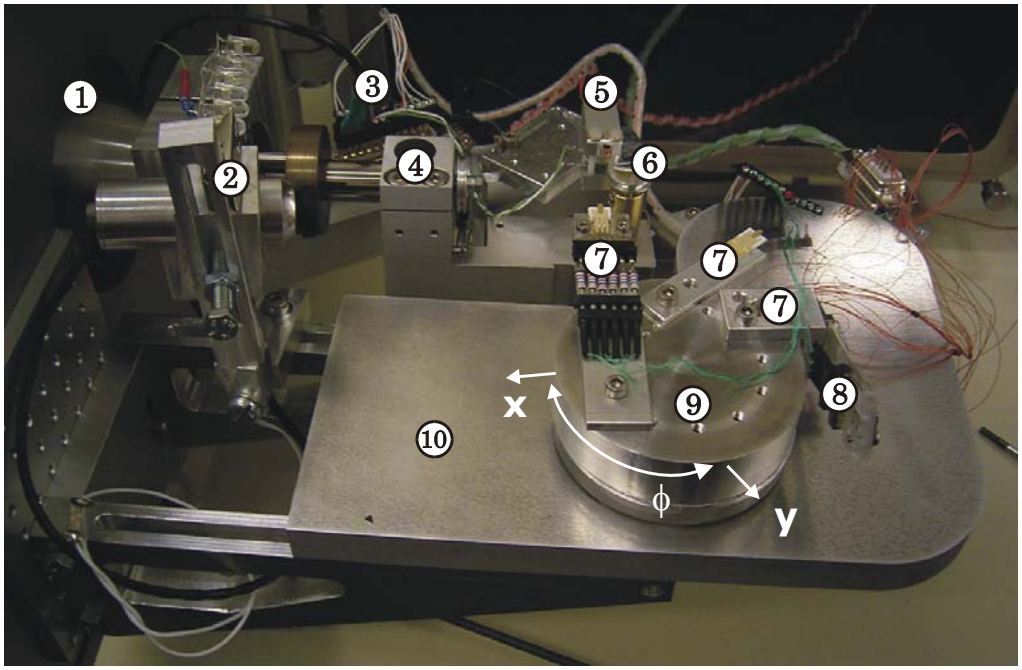

Figure 2.10: The AMiR-SEM setup.The whole system is mounted on the door (1) for easy access when the chamber is open. A small camera (2) was built in with IR-LEDs for illumination, to provide an overview image of the chamber. Electrical connections from the feedthrough were distributed to the system from a plug securely fixed on the door (3). The original manually controlled sample stage (4) was used for the sample (6) which could move in xyz, rotate and tilt. A piezo and Peltier temperature controlled source for EBD was mounted behind the stage (5). A large platform (10) was supporting the R2-D2 (9) which had several different tools extending over the edge, such as a gripper (7) and PRC mounted in a piezo-bender (8).

and made to fit into a standard TEM sample holder (Outer Ø < 3 mm). To reduce the risk of loosing a probe in the TEM, they were glued to a 0.5x2 mm slot nickel TEM grid (standard Cu grids were too soft to sustain prolonged use).

The system can be compared to the thin film TEM grids by Kasumov et al. [73]. Kasumov uses FIB to make a sub-micron gap in a Si_3N_4 thin film on a TEM grid with a metal coating reaching the edge of the slit. Nanotubes are dispersed onto the device until contact is achieved, and in this way measurements on individual nanotubes can be made. The TEM-Chips system appear to offer more possibilities in terms of varying the design of the cantilevers, to make for instance multi-point conductance measurements. Batch microfabrication also seems preferable to expensive FIB treatment of individual devices. The present use of optical manipulation equipment for placing nanotubes on the TEM-Chips, make it easier to ensure that the electrical measurements are done on one specific tube than if tubes were just dispersed onto the device.

Kasumov et al. [73] did measurements down to 100 K on their samples. Only

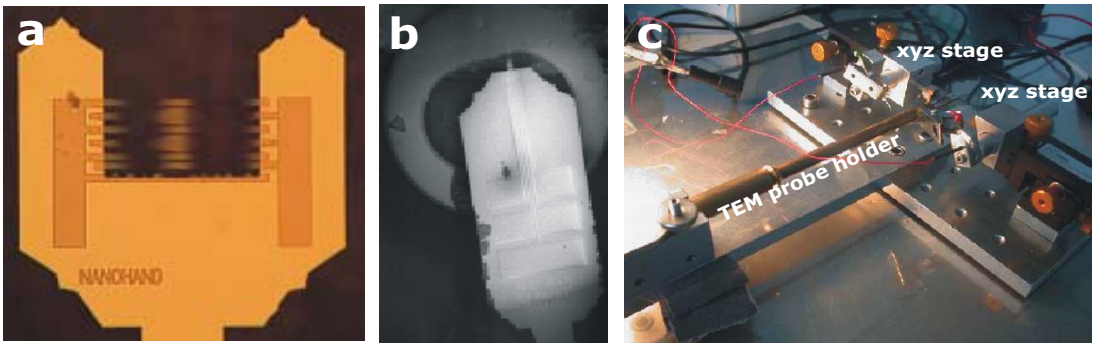

Figure 2.11: The TEM-chip system. a) Chips were developed to fit directly into a standard TEM probe holder. For easy handling, the chips were glued to a standard Ni-TEM grid (Ø 3mm). b) In some TEM probe holders there is also space to use the larger chips with the standard layout used for the conductance probe process (Fig. 2.4), when glued to a TEM grid. c) For electrical measurements, I constructed a mobile probe station with two xyz-stages to contact the chips electrically with metal needles. The TEM probe holder could be inserted directly into the probe station without touching the TEM chip.

one TEM-chip has been tested at cryogenic temperatures and contact was lost at 150 K. Such measurements are often essential to understand the electrical properties of a devices and further experiments are planned to improve the reliability of the cryogenic contact in the TEM-Chip device.

Another comparable device is the micromachined grippers made by Hashiguchi et al. [74], which have been used to retrieve DNA from solutions by dielectrophoresis, for then to analyse the DNA in TEM.

The TEM beam is intense and can dissipate up to mW's of power. The silicon based probes can therefore be heated considerably up in the TEM. The cantilevers should be as short as possible to avoid bending during heating due to the different thermal expansion coefficients of the SiO_2 and metal coating. For electrical measurements during manipulation or between TEM investigations, either a probe station or wire bonds can be used to contact the chip. To quickly contact the device for reproducible and reliable electrical measurements between TEM analysis (see Chapter 5), a small portable probe station was constructed, where electrical measurements could be made on the TEM-Chips without removing them from the standard TEM probe holders.

The In-Situ TEM probe holder

Although no direct nanomanipulation system has been made for the TEM in this project, the microfabricated grippers could in principle be used to stress or bend a nanowire placed across the gripper gap. To do such an experiment in-situ, electrical connections are needed to the chip in the TEM. I constructed a probe holder were in-

situ electrical contact to the chips can be made by wedge bonding wires between the chip and holder. It has been tested and approved for use in the TEM. It is planned to do in-situ shell-burn experiments on carbon nanotubes with this probe, as those done under ambient conditions in chapter 5, to follow the process in detail when done in vacuum. In-situ electrical contact to the probes also open up new experimental possibilities, such as actuating grippers to deform structures bridging the gripper gap and follow the changes in their structure and electrical properties.

2.3.4 Conclusion

In the SEM, a short r_{wd} will usually provide high resolution and limit the drift due to stray fields, which is important for these setups with many electrically driven devices. It is also important to leave enough space open for the detector to work efficiently and prepare the setup so samples are angled correctly in relation to the detectors. The other factors described Sect. 2.1.2 and Sect 2.2.3 are also worth keeping in mind while designing a setup.

Using microfabricated tools for nanomanipulation and characterization, requires at least two manipulation units: one to move the tool and one to move the sample. Several in-situ SEM manipulation setups were developed to solve the different tasks in chapter 3, 4 and 5.

For high resolution imaging and electrical characterization of nanotubes and nanowires, the "TEM-Chip" system was developed. Chips with microfabricated cantilever electrodes were made, fitting into both standard TEM probe holders and into a dedicated probe holder for the TEM-chip system, where electrical connects are available for in-situ TEM experiments.

Chapter 3

In-situ SEM Pick-and-place Nanomanipulation

This chapter will present the design of microfabricated grippers and their use for pick-and-place nanomanipulation of nanowires. The grippers were designed to pick a nanowire up from a suitably prepared substrate, move it to the target sample and release it at a well-defined position. Such grippers could find applications not only for making prototype nanowire devices, but also for handling microscope samples in general. Micromanipulation is a mature field in micro-biology for manipulation of cells and other micrometer-sized objects. Electrostatic grippers and nanotweezers have been used in ambient and liquid conditions, as demonstrated by the DNA manipulation by Watanabe et al. [75] and gripper cell-manipulation by Jericho et al. [76]. It is plausible that gripping tools could become useful even for liquid applications. The focus in this work is on in-situ SEM manipulation, where an obvious manipulation application is handling of TEM samples, such as TEM lamella (also called TEM coupons) or nanowires/tubes and related heterostructures. These TEM samples are usually fabricated on surfaces of wafers and cannot readily be inserted in TEM for analysis. As discussed in Sec. 2.1, the TEM samples have a thickness of the order 100 nm. The TEM lamella are usually some micrometers wide and long, while the nanowires generally have diameters between 10-100 nm and lengths of the order a few μm. Hence micrometer scale end-effectors are required on the grippers to handle such samples. Examples of manipulation of nanowire TEM samples with grippers will be examined at the end of this chapter. In order to place a grabbed object at the target position, it might be required to use electron beam deposition or some other means for to fasten it (see Sect. 2.2.1 and Chapter 4).

The first section will give a brief literature review of various grippers and the fundamental design considerations for the present project, such as choice of electrostatic and electrothermal actuation principles, which are related to the choice of microfabrication processes. Section 3.2 investigates the main strategies for pick-and-place operations to identify the optimal methods for grabbing a nanowire object as well as

the requirements of the grippers in terms of gripping force and the significance of the spring constant of the gripper arm. Section 3.3 describes the design of electrostatically actuated grippers and characterization of the fabricated devices. In section 3.4 a description is given of how the electrostatic grippers were used for in-situ SEM nanomanipulation with successful pick-and-place operations of silicon nanowires. Results comparable to those described in this chapter are presented in the included article [6]: "Towards Pick-and-place Nanomanipulation".

However, the design of the electrostatic grippers however have some inherent limitations, and the final section is a review of the results presented in the included paper [1] "Electro-thermally actuated microgrippers with integrated force feedback". The article describes the design and test of grippers which not only provide higher gripping forces but also provide a feedback signal to estimate the applied gripping force.

3.1 Grippers for Micro- & Nanomanipulation

Several research groups have been developing grippers for micromanipulation over the last years. Grippers have also become commercially available from the companies Nascatec and Zyvex (from October 2003) by the end of the Nanohand project. In literature, the terms *microgripper* and *micromanipulation* cover several orders of magnitude in terms of the scale of the grippers, as well as the objects to be manipulated by the grippers, from the millimeter to sub-micrometer range. In this thesis, the term *grippers* will be used for all microfabricated devices. The grippers can be refined to what will be termed *nanotweezers*, if tips with sub-micron diameters are made by either attaching/growing additional structures, such as carbon nanotubes, or by electron beam deposition (EBD, see Chapter 4).

Grippers are based on a variety of actuation principles:

- Electrostatic: Hinged or flexible actuator electrodes are electrostatically attracted to driver electrodes when a bias voltage is applied between them. The structures can be shaped as long thin cantilevers (such as the Nanohand grippers in Fig. 3.1a) or as more complex systems such as the large comb-drive structures used for actuation of the Nasqatec grippers in Fig. 3.1b.

- Electro-thermal: Actuation can be achieved by heating a part of a flexible structure relative to another part by passing a current through it. The principle is used in the Zyvex grippers in Fig 3.1c with a "traditional" two beam actuator design. Jonsmann et al. [77] have also developed thermal actuator designs based on a topology optimization algorithm, which calculates the optimal design for a specific set of device specifications. Figure 3.1d shows an example of one of the resulting complex optimized designs for an x-y actuator.

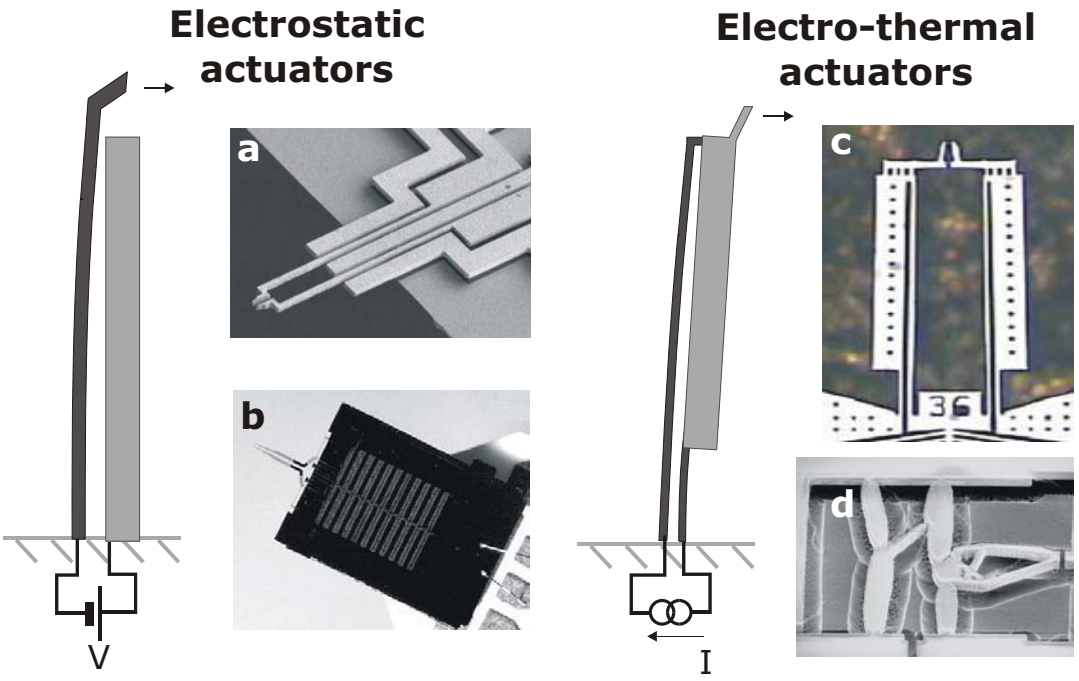

Figure 3.1: Representative grippers based on electrostatic and electro-thermal actuation principles. A simple electrostatic actuator consists of a flexible cantilever that can be electrostatically attracted to a nearby electrode by applying a bias voltage between the two. a) A typical electrostatic actuator developed in this project with a 1×1 μm cantilever cross-section. Such devices are discussed in Sect. 3.3.2. b) Images of the commercially available Nascatec gripper (Image from Nascatec.com). The gripper arm is about 1 mm long and actuated by a large electrostatic comb drive on the chip surface. c) Electro-thermal actuator from Zyvex (Image from Zyvex.com). The gripper length is about 1 mm. Passing a current through the structure heats the thin beam to a higher temperature than the wide beam, resulting in actuation due to the difference in thermal expansion. A variation of this design is the basis for the electro-thermal actuators discussed in Sect. 3.5. d) Electro-thermal actuators have also been designed by a topology optimization algorithm to improve the actuation range and applicable force [77].

- Piezoelectric: Piezoceramic elements are difficult to miniaturize, but grippers have been microfabricated with an attached millimeter-sized piezo element for actuation [76].

- Bimetallic or shape memory alloy: By heating a cantilever consisting of two material layers with different thermal expansion coefficients, the cantilever will bend and close the gripper gap [78]. Another possibility for thermal actuation is using shape memory alloys (SMA) [79].

The typical characteristics of several grippers are listed in the table below, including typical devices made in this project at the bottom.

Actuation	Length (μm)	Gap (μm)	Actuation (μm/arm)	Force (μN)	Reference
Electro-thermal	∼1000	10-500	25	550	Zyvex model BB
Electro-thermal	∼1000	7-18	8	210	Zyvex model SM
Electro-thermal	500	?	30	15000	[77]
SMA	3900	1000	180	17000	[79]
Bimetal	1500	?	∼200	250	[78]
Electrostatic	1200	150	?	?	Nascatec
Electrostatic	500	10	10	0.013	[80]
Nanotwewzer	10	2	1	0.01	[38]
Electrostatic	100	2	1	∼1	This work
Electro-Thermal	100	2	1	∼10	This work

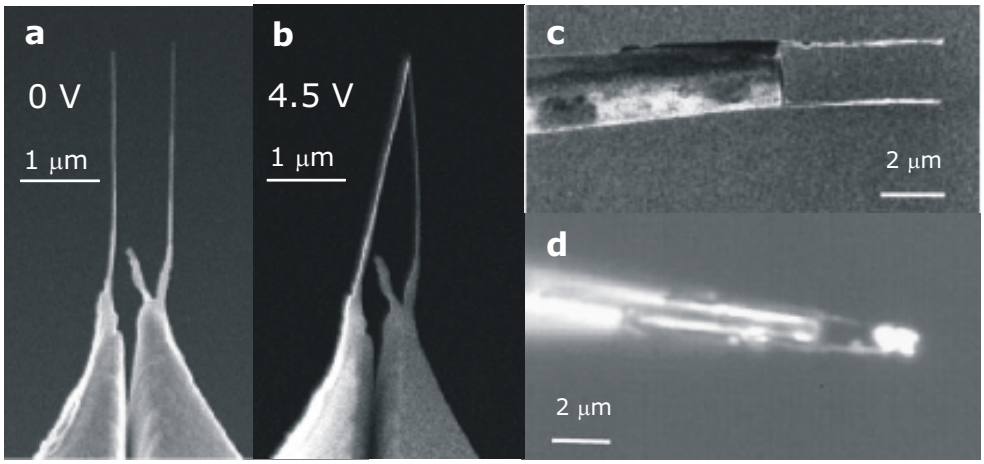

Figure 3.2: Examples of carbon nanotube nanotweezers. a,b) Akita et al. [81] divided an AFM tip by FIB and attached nanotubes to make a pair of nanotweezers that close at 4.5 V. c,d) Kim et al. [38] deposited two gold electrodes on a tapered micropipette and then attached carbon nanotubes. The pair of nanotweezers closes at about 10 V. The device was used for grabbing different nanomaterials, as shown by the optical image in (d) and for measuring the electrical properties of the grabbed objects. SEM inspection however showed that often several particles were grabbed.

3.1.1 Nanotweezers

Kim et al. [38] produced nanotweezers by attaching nanotubes to a micropipette with two gold electrodes on the side. The tweezers gap could be closed by applying a voltage of about 10 V. Once closed, the nanotubes would adhere to each other, but the tweezers could be reopened by applying the same potential to both nanotubes relative to a nearby surface. The gripping force was estimated to be $\geqslant$10 pN. The tweezers were used to pick up nanoobjects such as polystyrene nanospheres and GaAs nanowires. The tweezers could then be used to measure the two-point conductance of the grabbed objects. The operations were performed under ambient conditions in an optical microscope. A later SEM analysis showed that the objects picked up under the optical microscope often turned out to consist of several adhering particles.

Later Watanabe et al.[75] used such nanotweezers to contact DNA and carbon nanotube rings for electrical measurements while imaging with an AFM. To control the adhesion of the tips to the sample and substrate, they used different resonance frequencies to excite vibrations in different directions and parts of the nanotweezers. In this way they were able to grab, move and release DNA samples.

Another method for making carbon nanotube nanotweezers was demonstrated by Akita et al.[81]. Focused Ion Beam (FIB) milling was used to divide a conducting AFM tip in two halves with each their separate electrical contact. Carbon nanotubes were attached by electron beam deposition and the device could be opened and closed as the device by Kim et al. [38].

3.1.2 Choosing the Actuation Principle

The carbon nanotube based nanotweezers by Kim et al. [38] demonstrated the feasibility of nanomanipulation using tweezers. It seems desirable to be able to batch fabricate the grippers or tweezers if they are to be used often, rather than make each device individually. Using carbon nanotubes as tweezers' tips, where the actuation voltage is applied to the tubes can be problematic since the actuation voltage will be applied directly to the grabbed object. Many nanoscale objects cannot sustain bias voltages of the order of several Volts. In addition, electrical measurements of the grabbed object will influence the force applied to the sample with unpredictable effects for contact resistance and the object properties.

For the Nanohand project we decided to develop microfabricated grippers. This would ensure batch fabrication with a reasonable output of devices that can be used with a minimum of preparation time for the individual gripper. The microfabrication method also allows the design of more complex structures than what can be assembled manually. For nanoscale manipulation tasks, the grippers would probably also have to be microfabricated to achieve the necessary precision of the gripper end-effector that closes around the object, in terms of surface roughness and alignment.

By choosing electrostatically actuated grippers, it is possible to use indirect actu-

ation, in the sense that the driving voltage is applied to static electrodes, while the actuated electrodes can be grounded or used for electrical measurements independently of the driving voltage. Though electrothermally actuated grippers generally appears to be capable of applying larger gripping forces, this actuation principle has some disadvantages: In all designs of thermally actuated grippers it seems that a considerable fraction of the driving voltage (due to the heating current) will be present at the end-effector and this will make indirect actuation difficult to achieve. The increased end-effector temperature will also influence the grabbed objects properties such as its conductivity, and potentially also damage it. The electrostatic actuation principle also made it possible to process the grippers together with the four point probes by the existing microfabrication process the group was using already (see Sect. 2.2.2).

Development of a new microfabrication process and the processing of wafers are very time consuming and being able to rely on established processes was a considerable advantage. For research and test purposes where usually only a few devices are needed, it is a clear advantage to be able to have a wide variety of probes on a wafer and to be able to change the design often. As defined in the Nanohand project description, the microfabricated grippers should be fabricated based on the existing process used for making four point probes. This made it possible for us to process wafers with devices for the entire Nanohand team and also collaborate with the company CAPRES A/S on joint fabrication of wafers, which considerably eased the fabrication workload. The main work in this thesis has hence been on electrostatically actuated grippers microfabricated by the standard conductance probe process (Fig 2.4).

For everyday handling of objects, force feedback is an essential requirement for successful pick-and-place manipulation. Few grippers can today provide a gripping force feedback signal. Millimeter-sized piezoresistive [78] and optical sensors [82] have been attached to millimeter sized grippers to provide such feedback. However, it seems that no microfabricated gripper structures, that have the precision required to work with nanoscale materials, have been reported with force sensitivity. By the end of the project a new process sequence developed by Ramona Mateiu was used for processing solid metal cantilever devices [8]. This opened up the possibility to make thermally actuated grippers as well, and I developed a gripper capable of providing both higher forces than the electrostatic grippers but also capable of giving a force feedback signal from the gripping force. The thermally actuated grippers are described in the included article [1]. The choice between the two developed grippers is hence depending on the limitations of the grabbed object in terms of temperature and the measurements one would like to make on the object.

If smaller end-effectors should be required for the manipulation tasks, it is possible to add nanoscale tips to the microfabricated grippers end-effectors to create indirectly actuated nanotweezers. In this manner one could hope to achieve the full gripping

force of the large actuator structure combined with the precision of the nano-scale tips. Instead of attaching carbon nanotubes by gluing [38] or EBD [52], the EBD method can be used to make the entire tip. The standard four point microfabrication process also allowed gripper designs with gaps down to 1 μm, which was suitable for EBD of nanotweezers tips. The next chapter in this thesis describes our investigation of EBD for such purposes.

It is instructive to remember the wealth of gripping tools in everyday life - from the tiniest tweezer to hydraulic powered grippers. In this project a few gripper designs are developed and tested. But success is highly dependent on the compatibility of the gripper design with the manipulation task. Applying a tiny tweezers for heavy duty work is not feasible in every day life - on the nanoscale we can attempt to avoid such situations by making estimates of the forces involved, but many of the properties are not well known and surprises must be expected for pick-and-place operations that have never been done with such objects, grippers and conditions before. Sample preparation must be expected to be a very important factor, in order to obtain samples that are actually possible to release and pick up. The preparation of such substrates and refinement of grippers designs to suit different types of substrates is a continuing effort, while this project mainly demonstrates that in-situ SEM pick–and-place manipulation is actually possible.

3.1.3 Summary

Grippers have been made by several research groups and companies, using a wide variety of actuation principles and designs. Electrostatic nanotweezers have been demonstrated, but only with actuation voltage applied to the tweezers tips which can possibly interfere with measurements on the gripped object. In this project the emphasis has been on developing an electrostatic microfabricated gripper with indirect actuation, where the driving voltages is applied to static electrodes that deflect the grounded actuator electrodes. Electro-thermally actuated grippers capable of providing a force feedback signal of the gripping force were also developed.

3.2 Introduction to Pick-and-place Nanomanipulation

In any pick-and-place operation, it is essential to control the balance between the forces acting between the object and the surface, $F_{surface}$, and the forces acting between the object and the tool, F_{tool}. When picking up an object, F_{tool} must overcome $F_{surface}$, and when placing the object, the balance must be reversed. In everyday life, the gravitational force is often an essential factor in the force balance, and is conveniently used to overcome F_{tool} when releasing a grabbed object. For nanoobjects, the surface forces become much more important than gravitational force and this makes control of the force balance difficult. To make an object start sliding along a surface, the force applied to the object tangentially to the surface must be larger than the static friction force. The static friction force is also termed "stiction" [83]. Because the static friction force usually is directly proportional to the gripping force [83], it is a convenient way to control F_{tool} if the friction force is the major contributor to F_{tool}. Adhesion is another important effect in manipulation, and relates to the energy gained by bringing an object in contact with a surface. Ideally, the adhesive forces do not affect friction and stiction, because the contact area to the underlying substrate is maintained when an object is sliding parallel to a surface, but the adhesive forces are important if objects are being picked up from a surface. Overcoming the contribution of the adhesion forces to $F_{surface}$ is among the main challenges of micro- and nanoscale pick-and-place manipulation.

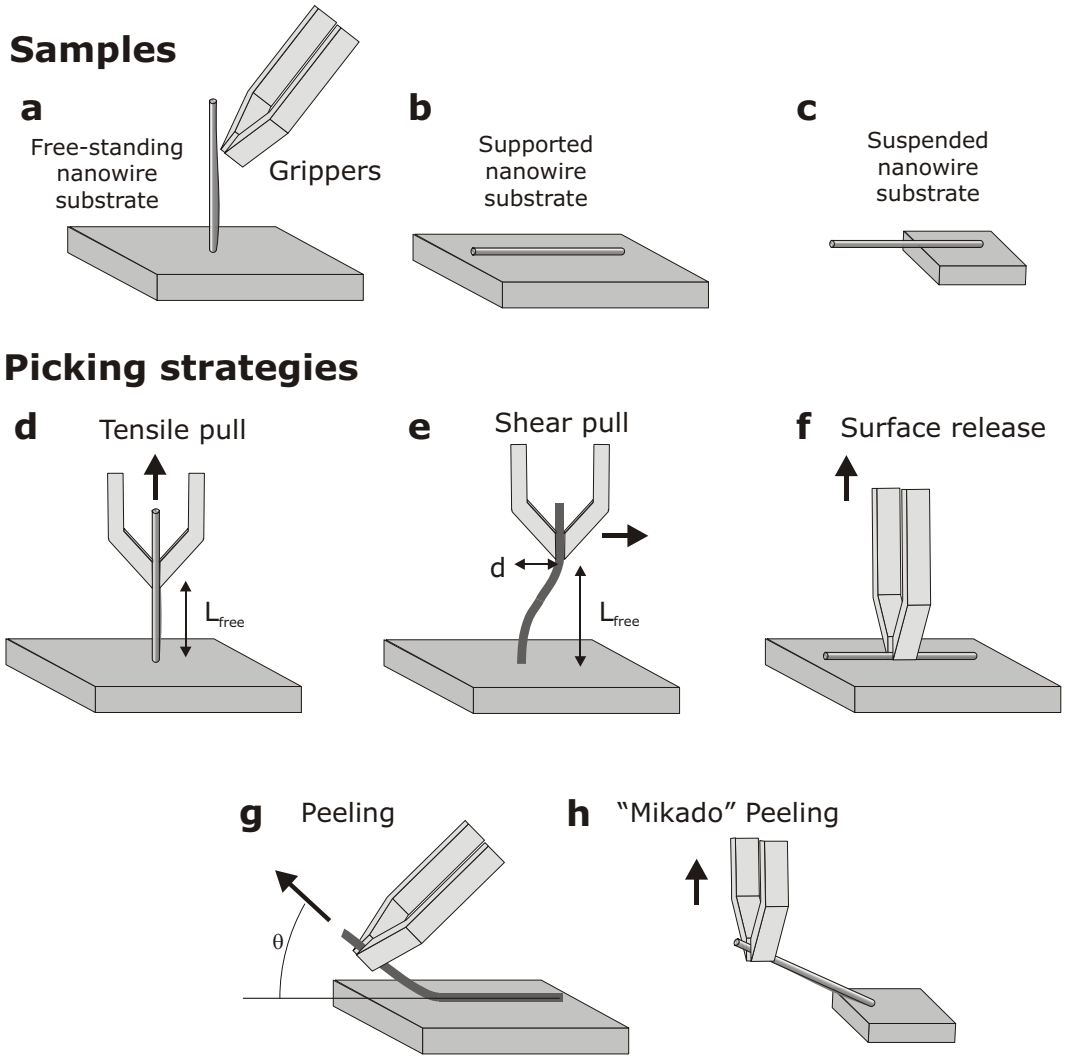

Figure 3.3: Samples and strategies for picking up a nanowire. Substrates with nanowires (a) standing up from the substrate, (b) deposited on planar surface, or (c) extending over edges. Picking nanowires can be done by pulling along (d) or sideways (e) to the axis of a standing wire. Wires lying on substrates can be lifted perpendicularly to the substarte (f) or peeled (g). Wires extending over an edge make it possible to use several strategies (h).

3.2.1 Picking Strategies

There are several approaches to use a gripper for picking up a nanowire from a substrate. Figure 3.3 shows some fundamental strategies depending on how the nanowire is placed on the sample substrate (fig 3.3a-c). Different demands must be expected on the gripper to complete the various pick-operations. Estimates will be presented below for the required gripping force in the different cases, to facilitate suitable preparation of nanowire substrates and optimal gripper designs for the chosen strategy. The calculations are based on a "typical" silicon nanowire with a radius r_0 =50 nm and a gripper with a two 1μm×1μm surfaces contacting the wire.

The Static Friction Force

The static friction force is the limiting factor that prevents the wire from sliding through the gripper. Amontons law of friction also holds for many cases on the nanoscale [83]. If the gripper and nanowire surfaces are assumed to be smooth, the friction force, F_f, is proportional to the normal force, F_N, on the sliding interface,

$$F_f = \mu F_N, \tag{3.1}$$

with μ representing either the static or dynamic friction coefficient. The static friction coefficient of common bulk materials is in the range $\mu \in [0.1; 1]$. A wider range of values have in some cases been observed for nanoscale friction [83]. A conservative estimate of the friction coefficient $\mu = 0.1$ will be used for the present purposes. The required gripping force is hence ten times the required force needed to pull the nanowire to complete the pick operation. It must be remembered that a wide range of effects such as surface roughness, contamination, and charging of the nanowire and gripper surfaces must be expected to have considerable and unpredictable influence on this value.

Tensile gripping

When pulling a nanowire standing perpendicularly to the substrate in a direction along the nanowire axis (fig 3.3d), the force required to break it is

$$F_{yield} = \sigma_{yield} \pi r_0^2. \tag{3.2}$$

The lowest yield stress, σ_{yield}, of either the substrate or nanowire should be used. For silicon $\sigma_{yield,\mathrm{Si}} = 7$ GPa, giving $F_{yield} = 55$ μN for the nanowire. The force will have to be applied through the static friction force between the gripper and the nanowire, which then must be of the order F_{grip}=μF_{yield} =0.5 mN. The wire will maximally be elongated by a few percent before breaking, so it will be apparent after retracting the gripper a few percent of L_{free}(Fig 3.3d), whether the gripper simply slides along the wire or the applied force is sufficient to break the wire.

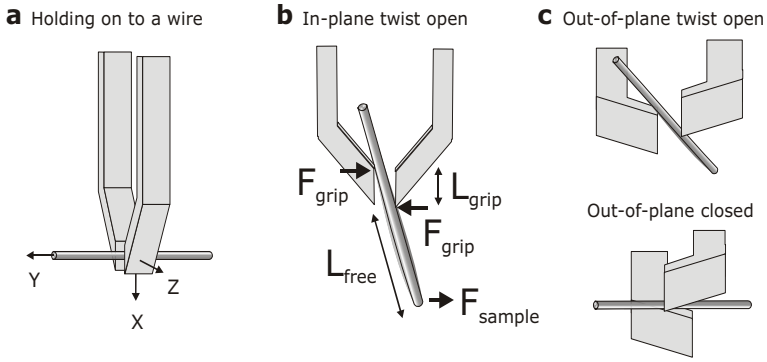

Figure 3.4: The mechanics of holding on to a nanowire. a) The nanowire can rotate and slide in the xy-plane if the applied forces can overcome the static friction force. Applying forces to the wire in the y-z plane can make the gripper twist out-of-plane open. b) For shear gripping, the applied moment to the nanowire will make the gripper open. c) For low aspect ratio grippers, out-of-plane twisting of the gripper can make it open up. It is possible that it can close in a out-of-plane-closed manner.

Shear Gripping

By bending a wire it is possible to break it at the base where the strain is concentrated. By "shear gripping" (Fig 3.3e), where the gripper moves parallel to the nanowire substrate, the free-standing nanowire is bent in two points where the surface stress is concentrated and eventually can reach the yield stress to make it break.

The flexure formula [84] gives the maximal stress as function of the bending moment

$$\sigma_{\max} = \frac{MR}{I}, \tag{3.3}$$

where R is the maximal distance from the beam neutral axis. For the circular nanowire, $R = r_0$, the moment of inertia is $I = \frac{\pi r_0^4}{4}$, and the moment is $M = F_{sample} L_{free}$. The force due to deflection F_{sample} can be calculated from the distance, d, the gripper has moved the wire tip sideways and the spring constant of a clamped-clamped wire $F_d = 3\pi r^4 d \frac{Y}{L_{free}^3}$. The deflection $d_{\max}$ required for breaking the wire becomes

$$d_{\max} = \frac{1}{12} \frac{\sigma_{\max}}{Y} \frac{L_{free}^2}{r_0}, \tag{3.4}$$

which for a nanowire with $L_{free} = 10$ μm and Yongs modulus of silicon Y =190 GPa gives $d_{\max} = 6$ μm. To complete this operation, the gripper must be able to apply the required moment $M_{\max}$

$$M_{\max} = L_{free} F_{sample,\max} = \frac{\pi}{4} r_0^3 \sigma_{\max}, \tag{3.5}$$

which in this case is 70×10^{-13} Nm. Applying such a moment requires to two grippers to press the wire with a gripping force $F_{grip} = M_{\max}/L_{grip}$ where L_{grip} is the length of the gripper contact surface with the nanowire (Fig 3.4b). The required force is $F_{grip} = 7$ μN. By shear gripping we have reduced the required force by almost an order of magnitude compared to tensile gripping. However, if the wire does not point directly along the gripper x-axis (Fig 3.4a), the forces are likely to cause the wire to slide out of the gap in the process. If the wire is perpendicular to the gripper plane, it can twist the gripper open as shown in Fig 3.4c. For a typical microfabricated cantilever, the spring constant will be of the order 1 N/m giving a deflection of at least 7 μm when applying the moment. This is a large distance compared to the 1 μm $\times 1$ μm surface area considered here, and the operation is likely to twist the gripper open as shown in Fig. 3.4c. When twisting open, it is possible that the gripper close around the wire in a twisted manner, which might change both the forces and the adhesive and friction properties of the interface (Fig. 3.4d).

Lifting a Nanowire lying parallel to the substrate

When attempting to lift a nanowire up perpendicularly to the surface (Fig. 3.3f), the adhesive forces must be overcome. The scenario requiring the maximal force is when the entire wire must be lifted up simultaneously. The Van der Waals (VdW) force per unit length of a cylindrical rod is [85]

$$f_{vdw} = -\frac{A_H \sqrt{r_0}}{8\sqrt{2} D^{5/2}}, \tag{3.6}$$

with Hamaker constant, A_H, which usually lies in the range 10^{-19}-10^{-20} J. For the interface distance, D, the typical Lennard-Jones distance of about 0.2 nm can be used [86] giving 2 μN per μm length of nanowire.

An estimated VdW force for a rigid 10 μm nanowire will be 20 μN, requiring a 200μN gripping force. If the wire has a sufficiently low spring constant, the wire end extending out of the gripper will tend to deflect and be peeled off as the wire is lifted up. This, and if the wire is allowed to rotate in the gripper to release one end first, will reduce the required force. The estimated force is also uncertain since a wide variety of forces such as capillary and electrostatic forces can be expected to influence the process. Another aspect to consider is the use of the gripper in close contact with the surface. The gripper will have to have extremely sharp end-effectors to grab the thin wire, and also be placed so that it does not touch the surface, which would make it difficult to actuate. The nanowires lying on surfaces hence seem to be difficult to pick up.

Peeling a Nanowire lying parallel to the substrate

A detailed discussion of peeling can be found in Kaelble [87]. If the wire is assumed to be unable to slide or stretch, but able to bend, the force required to peel at an angle θ to horizontal is given by

$$F_{peel} = \frac{\Delta U/\Delta x}{1 - \cos\theta}, \tag{3.7}$$

where the adhesive peeling force, $\Delta U/\Delta x$, is the adhesion energy per unit length of wire [85]

$$\Delta U/\Delta x = -\frac{A_H\sqrt{r_0}}{12\sqrt{2}D^{3/2}}, \tag{3.8}$$

with the same constants as the VdW force above, this can be estimated to be $\Delta U/\Delta x = 0.2$ nN or about 1 eV/nm. The peeling force can be as low as half the adhesive peeling force at θ=180° where the wire is peeled to make a U bend, but also infinitely high if the peeling is attempted by simply pulling straight at the wire (since it is assumed to be unable to slide).

If the wire is rigid and extending over the edge of the substrate, peeling at θ=90° can considerably reduce the required force to release the wire (Colloquially called "mikado"-peeling in Fig. 3.3h). The required force to lift the rigid wire becomes (see Fig. 3.3h)

$$F_{rigid} = \frac{L_{surface}^2 f_{vdw}}{2L_{free}} \tag{3.9}$$

If $L_{free} = 10 \times L_{surface} = 10$ μm and the VdW force is as before, the force becomes F_{rigid} =0.1 μN and the gripping force 1 μN. Peeling seem to offer the lowest requirements for gripping force of the possible picking strategies.

3.2.2 The Place Procedure

The place operation requires some specific steps when moving and placing an object. The following will describe the steps together with the requirements they impose on the gripper design based on the forces involved. A typical scenario would be to pick up a nanowire from a prepared substrate to place it on either a microchip surface or TEM grid for later TEM analysis.

- Moving: When gripped, the electrostatic forces due to charging in the SEM can result in loss of the wire. The wire should be in electrical contact with the grounded grippers to avoid excessive charging. The sample and target substrates should both be well grounded. The manipulator should move from the sample to target substrate with low vibration levels and frequencies, since vibrations could excite a resonance in the grippers and result in loss of the grabbed object [75].

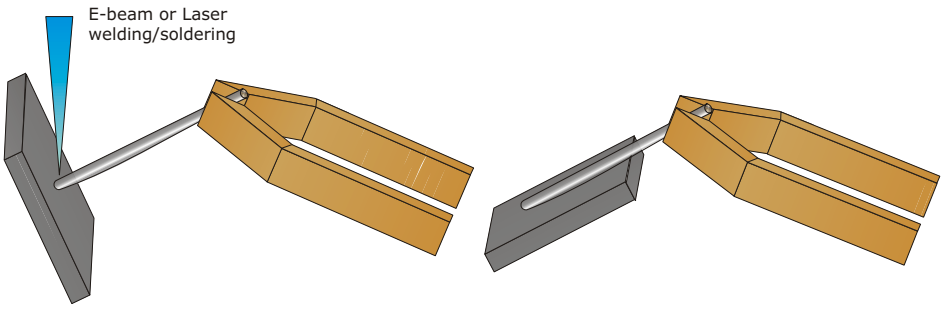

Figure 3.5: Placing a nanowire. a) In the energetically unfavorable position at some angle to the surface, EBD or some other method is required to fix the wire. b) If the wire should end up lying on the surface, the surface forces should make it adhere strongly.

- Releasing: Depending on how the wire should be placed on the target substrate different methods seem necessary to complete the operation: If the placed wire should end up standing perpendicularly to the substrate, as in fig 3.5, the energetically unfavorable position will makes it necessary to fix the wire to the substrate with the correct angle to the substrate to avoid it ending up lying on the substrate. The gluing methods reviewed in Sect 2.2.1 could probably be used as well. Using electron beam deposition to solder nanotubes is described in Chapter 4. Preparing the substrate with narrow holes, or edges the nanowire could adhere to, should also increase the success rate for such an operation. If the wire is to be placed on a surface as in fig 3.5, the surface forces should be capable of holding it in place during release, provided the surface has a high adhesion energy to the wire compared to the gripper surface. This should be achieved in most cases since the free length of the wire can be much longer than the gripped part. If the wire is being placed on conducting electrodes, applying a bias voltage might assist in placing the wire successfully.

Summary

The forces required to complete the pick-up operation in vacuum with nanowires by different picking-strategies were examined. Peeling of nanowires extending over the edge of the substrate surface seems to be the method giving the lowest requirement on the gripping force the gripper should be able to apply, which should be of the order 1 μN for the given example.

3.3 Electrostatic Tweezers

The microfabrication of electrostatic grippers with the standard conductance probe process (Fig 2.4) defines certain limitations to the design and applicable voltage which are reviewed below. Then the basic design is presented and a simple model for the actuation is examined. The simple model was compared to finite-element simulations to evaluate its precision and the model and simulations were used as guides for developing the gripper design. Finally the model and simulation to measurements of real devices are compared and the device reliability is discussed. The analysis and characterization focusses on the actuation as function of bias voltage, which can be easily measured in an optical microscope. The gripping force is also an important factor, which will be estimated at the end of this section.

3.3.1 Processing Limits

The cantilever chips are fabricated by the process briefly described in Ref. [60] while a detailed discussion of the limitations can be found in Ref. [58]. The cantilever structures, as seen in Figure 3.6, are etched from a 1 μm thick silicon oxide layer and covered with a thin layer of metal (typically 100 Å Ti/800 Å Au). The gold covers the sides of the cantilevers to some extent. The sidewall gold covering can vary from wafer to wafer, but will be assumed to be uniform and conductive in the following. The process requirements and limitations influence the design of the devices. The cantilever chips can usually withstand voltages up to 30 V. Ideally, process allows any planar multielectrode geometry with a line width down to 750 nm and cantilever lengths up to about 100 μm. Such limitations seemed reasonable for fabricating grippers since the aspect ratio (ratio of cantilever thickness to width, T/w) can be larger than one, making the tweezers more flexible for in-plane bending for closing the gap than out-of-plane bending (Fig 3.4c). However, such narrow line width processing pushes the available UV-lithography technology to the very limit [58]. With time it became apparent that the yield of devices matching these specifications was limited. Eventually we had to increase the minimum line width to 2 μm to ensure successful fabrication. The increased line width gives a lower aspect ratio and is not optimal for gripper structures, as they will easily bend out of the plane compared to the in-plane actuation (Fig. 3.4c). The processing of the wafers has been done by laboratory technicians, Maria Dimaki, and in the beginning of the project also in collaboration with the company CAPRES A/S.

3.3.2 Modelling the Gripper Design

To achieve indirect actuation, a typical gripper consists of three to five cantilevers. Figure 3.6 shows a SEM image of a typical five-electrode gripper chip with two long thin and flexible gripper arms and three wide and rigid driver electrodes. By applying a voltage between the narrow flexible gripper electrodes and the wider "driver" electrodes, the electrostatic attraction causes the grippers gap to open or close, depending on whether the inner or the outer driver electrodes are biased. Because no voltage difference has to be applied between the grippers arms, the electrostatic fields near the grabbed object can be reduced significantly, thus reducing the risk of unwanted electrostatic forces on the object. For the same reason the gold covered surface of the chip itself is also grounded.

There are other possibilities for gripper designs than the straight actuator electrodes. Comb-drives are often used for electrostatic actuation, to provide a linear relation between applied voltage and actuation. The cantilever based design in the present project however limits the efficiency of comb-drive structures as the comb will bend at an angle to the actuator electrodes when actuating. Calculations show that cantilever actuators based on comb-drives do not deflect linearly with applied voltage [88]. Various designs, such as combdrives and meander structures were simulated using the MEMS simulation program CoventorWare, but no significant advantages were found in the complex designs compared to a simple straight cantilever actuator. The gripper design and following discussion is hence based on a simple straight cantilever actuator.

The design of the gripper is hence limited to determination of the optimal length, electrode gap and cantilever width. The simple model and the simulations were based on an idealized gripper as shown in fig 3.7. The real device will deviate from the idealized model in surface roughness and dimensions depending on the specific processing conditions. The aim of the modelling presented below was hence to be able to design devices with a reasonable actuation range at low driving voltages given the process limitations -not to make precise measurements of electrostatic actuation.

The end-effector of the actuator, as shown in Fig. 3.7, is not affected by the electrostatic forces and will have an actuation, A, depending on the actuator's end deflection $g(L)$ and angle θ as

$$A = g(L) + L_+ \sin\theta \tag{3.10}$$

The force F and torque M applied by the actuator on the end-effector (Fig 3.7) will result in a gripping force F_{grip}

$$F_{grip} = F + \frac{M}{L_+} \tag{3.11}$$

and any applied gripping force will influence the cantilever deflection. The end effector is disregarded and the gripping force is assumed to be zero in the following models.

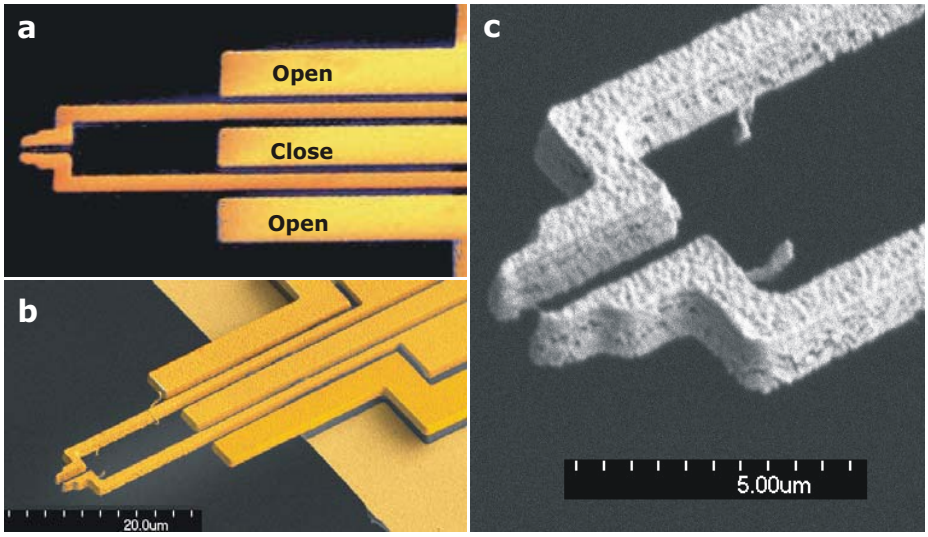

Figure 3.6: Typical layout for electrostatic tweezer with 5 electrodes considered in this work. a) The outer two electrodes will open the gripper gap when a voltage is applied relative to the gripper arms. Correspondingly, the center electrode will close the gap. b) When viewed at an angle, the uncoated parts of the gripper below the electrodes become visible. c) Close-up of a pair of end effectors. The gold coverage on the side of the cantilevers can vary from device to device and the surface cannot be expected to be very uniform or planar on the sub-micrometer scale. For modelling the device, a uniform sidewall gold coverage will be assumed.

Theory of Electrostatic Actuation of Cantilevers

The cantilever deflection is governed by the differential equation [84]

$$\frac{d^2y}{dx^2} = \frac{M(x)}{YI}, \tag{3.12}$$

where Young's modulus of the cantilever material is denoted Y, the moment of inertia $I = \frac{Tw^3}{12}$. The moment acting on the cantilever at point x is given by

$$M(x) = \int_{x'=x}^{L} f(x')(x' - x)dx' \tag{3.13}$$

with the electrostatic force per unit length, $f(x)$. The electrostatic force is the negative gradient of the capacitive energy of the cantilever, giving a force per unit length

$$f(x) = -\frac{1}{2}V^2\frac{d}{dy}c(y) \tag{3.14}$$

with applied voltage V, and $c(y(x))$ the capacitance per unit length that depends on the deflection $y(x)$ of the beam at position x.

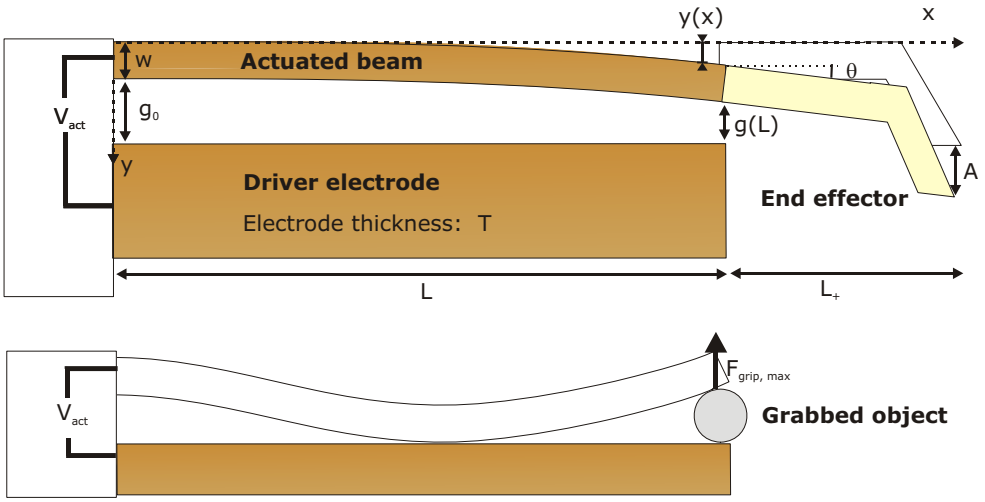

Figure 3.7: The actuator dimensions and actuation. The upper illlustration of the gripper show the dimensions used in the calculations. The lower illustration show how a gripping force can keep the end of an otherwise pulled-in actuator at the starting position while the cantilever is pulled-in. This can provide an estimate of the gripping force by considering the beam deflection.

The above leads to a differential equation describing the cantilever deflection $y(x)$ as function of voltage V

$$\frac{d^2y}{dx^2} = -\frac{1}{2}\frac{V^2}{YI}\int_{x'=x}^{L} \frac{dc(y(x'))}{dy}(x'-x)dx' \tag{3.15}$$

This nonlinear differential equation does not have an analytical solution in general in general, and the capacitance can only be calculated analytically for a few simple geometries. By making suitable approximations, we can solve the equation and understand the main effect of essential design parameters such as the cantilever dimensions.

Two analytical solutions for the capacitance of simple systems are useful [89]:

- The parallel plate capacitor: This model neglects fringing fields and is a good approximation when the gap is much smaller than the thickness of the cantilevers. The capacitance per unit length is $c_{pp} = \varepsilon_0 T/g(x)$ (see Fig 3.7) giving a force
$$f_{pp} = \frac{\varepsilon_0}{2}V^2 T\frac{1}{g\,(x)^2}. \tag{3.16}$$

- Two parallel cylindrical electrodes: An analytical solution exists for the capacitance which accounts for the fringing fields [89]. For an actuator with a quadratic cross section, the actuator geometry is relatively comparable to cylindrical rods if the thickness, width, and diameter are equal, $T = w = d$. The

capacitance per unit length is

$$c_{pc} = \frac{\pi\varepsilon_0}{\ln\left(\frac{g(x)}{d} + 1 + \sqrt{\frac{g(x)^2}{d^2} + 2\frac{g(x)}{d}}\right)}, \tag{3.17}$$

and the corresponding expression for f_{pc} is lengthy.

The parallel plate and cylinder model forces are equal if $T = w = g = 1$ μm. The parallel plate model overestimates the force by 10% if the distance is reduced to $g = 0.5$ μm. Knowing the approximate correction of the fringing fields is of the order 10% when the gap is half closed for this design, the simpler parallel plate model will be used in the following.

Low bias actuation

Consider the electrodes with a low applied bias voltage applied to them, making $y \ll g_0 \approx g(x)$. In this limit the electrostatic force can be considered a uniformly distributed force. The actuation can be calculated from the Eq. (3.12) by integrating and applying appropriate boundary conditions for the clamped cantilever[1]

$$y = \frac{1}{2}\frac{\varepsilon_0}{YI}V^2\frac{T}{g_0^2}\left(\frac{1}{24}x^4 + \frac{1}{4}L^2x^2 - \frac{1}{6}x^3L\right). \tag{3.18}$$

The actuation at $x = L$ becomes

$$y(L) = \frac{1}{16}\frac{\varepsilon_0}{YI}\frac{TL^4}{g_0^2}V^2 \tag{3.19}$$

$$= F_{pp}/k_{dist}, \tag{3.20}$$

with total force on the cantilever $F_{pp} = Lf_{pp}$ and spring constant of the tip for a distributed force

$$k_{dist} = 8YI\frac{1}{L^3}. \tag{3.21}$$

For a 50 μm long cantilever with a cross section of 1x1 μm the actuation is $y(L) = 0.1$ μm at 10 V bias. Equation (3.19) is a lower estimate of the actuation since the force is increasing nonlinearly as the gripper actuates.

[1] The standard cantilever beam equations for uniform force distribution are $y''''(x) = f_{pp}/(IY)$, $y'''(x) = (x - L)\, f_{pp}/(IY)$, and Eq. (3.12) $y''(x) = \left(\frac{1}{2}L^2 - xL + \frac{1}{2}x^2\right) f_{pp}/(IY)$ with boundary conditions $y(0) = 0$ and $y'(0) = 0$.

High Bias and the Pull-in Effect

As the cantilever is deflected to narrow the gap, a point will be reached, where the attractive non-linear electrostatic force increases at a rate higher than the linear spring constant can counter balance it. This is the pull-in effect, that limits range within which the actuator can be moved controllably. Once the pull-in voltage is reached, the gripper becomes unstable and is pulled into close contact with the driver electrode. To obtain a simple analytical relation to estimate the pull-in voltage and actuation range, a simple standard model of the pull-in phenomena will be used [90][91]. The model considers the gripper to consist of two parallel plates, one fixed and one movable suspended by a spring. The gripper actuators can only be considered parallel at very low bias voltages, and the simple model will be compared to finite element simulations to evaluate its precision. Consider the net force on the actuator, F_{net} ,at equilibrium [84]

$$F_{net} = -\frac{\varepsilon_0 TLV^2}{2g_L^2} + k_{dist}\left(g_0 - g_L\right) = 0, \tag{3.22}$$

where the actuator is approximated with a parallel plate capacitor with distance g_L held by a spring constant k_{dist}. For such a system, a perturbation of the gap by δg_L will change the net force

$$\delta F_{net} = -\frac{\partial}{\partial g_L} F_{net}|_V \, \delta g_L \tag{3.23}$$

$$= \left(\frac{\varepsilon_0 TLV^2}{g_L^3} - k_{dist}\right) \delta g_L. \tag{3.24}$$

Stability requires $\delta F_{net} \leq 0$. At the limiting pull-in voltage V_{pi} the requirement is $V_{pi}^2 = k_{dist} g_{L,pi}^3 / \left(\varepsilon_0 TL\right)$. Using Eq. 3.22 the pull-in limit of stability is at

$$g_{L,pi} = \frac{2}{3} g_0 \tag{3.25}$$

$$V_{pi} = \sqrt{\frac{8 k_{dist} g_0^3}{27 \varepsilon_o TL}} \tag{3.26}$$

Our actuation range is only 1/3 of the initial gap size if we want to avoid pull-in. The above equation only applies if no object is grabbed. If an object is grabbed hindering the end-effectors to move inwards, the pull-in will make the middle of the gripper arm flex in to touch the driver electrode, and this will take place at a higher voltage. If electrical contact is achieved when the gripper arm pulls-in and touches the driver electrode, one can imagine several undesirable events: The arm to either discharge and destroy the gold covering, to solder itself to the driver electrode, or to start vibrating as it is rapidly discharged and charged by the bias voltage. To what extent this will result in permanent damage of the gripper functionality, will be examined when characterizing the fabricated grippers.

3.3.3 Finite Element Simulation of Grippers

Several devices were simulated in the finite element analysis program CoventorWare in order to estimate the analytical model limitations. The program also allows simulation of more complex structures such as comb-drives, or added meander sections to the cantilever structure to decrease the spring constant and thereby lower the actuation voltage, but these designs did not show significantly changes in the actuation behavior compared to the straight actuator designs. The main focus was hence on the straight cantilever actuators. In the simulations, various mesh densities were tested to find the mesh size influence on the simulation results. Mesh sizes of 0.5 μm with "Manhattan parabolic cells" gave results matching those with finer mesh densities and were used for all simulations. The simulations were made for cantilever beams with dimensions in the range L = 40, 50, 60 μm, w = 1, 2 μm, and g_0 = 1, 2, 3 μm. An example of such a simulation is shown in Fig. 3.8a. Comparing the analytical model above with the simulations in Fig. 3.8b, the actuation is about twice as large for the simulated devices at high bias voltage. The increased actuation in the simulations compared to the model must be expected since the model neglects the increasing non-linear force as the gap decreases. The pull-in voltage is on the other hand described reasonably well by the rather crude pull-in model Eq. (3.25) with less than 10% deviation between the simulated results and the analytical model. The pull-in range is usually about $y = 0.5g_0$ in the simulations while the model only allowed for $y = g_0/3$. Within its limitations, the simple model seems to be suitable for order of magnitude estimates of the gripper actuation when designing the grippers.

3.3.4 Realized Designs and Characterization of Actuation

A wide variety of gripper designs were produced during the project, partly because the process line width specifications were changed to increase the yield of working devices. When the cantilever and electrode spacing are allowed to be 1 μm wide, the model and simulation make a cantilever length of about 50 μm appropriate if one would like to be able to close the 1 μm gap at reasonably low voltages at about 20 V. From Eq. 3.19 the actuation scales as

$$y(L) \propto \frac{L^4}{w^3 g_0^2} \tag{3.27}$$

When the process line width was increased to 2 μm, the cantilever length had to be increase to about 100-150 μm to achieve a reasonably low actuation voltage when closing the gap. Such grippers push the processing to the limits, since surface stress in the cantilevers will make them bend out of the plane. As the actuator and driver electrodes often bend similarly out of the plane, even 150 μm long devices can often be used. To evaluate whether the grippers actuate as expected from the above model and simulations, the fabricated grippers were tested in the 4-point station (Sect 2.3.1).

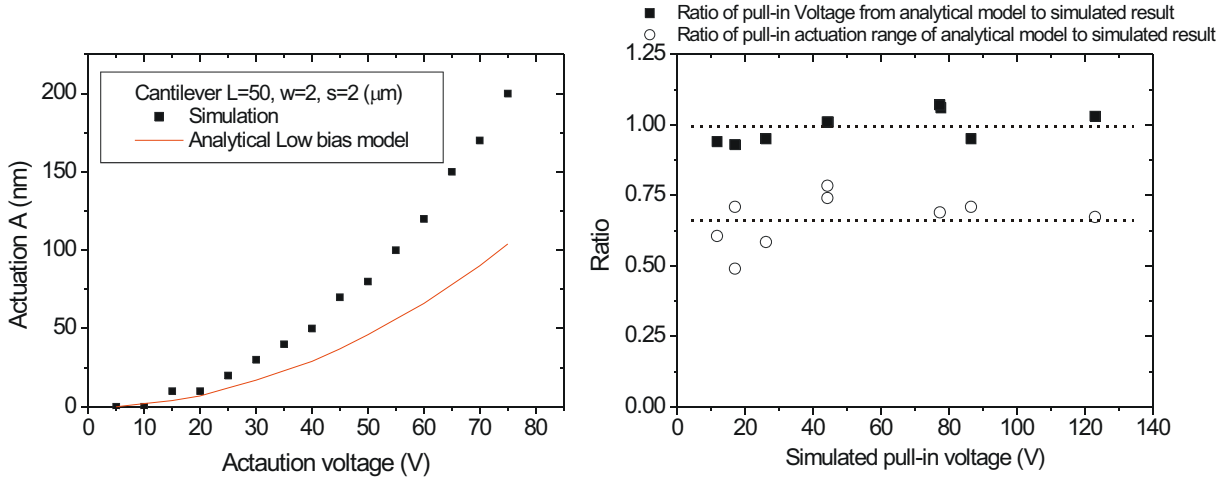

Figure 3.8: Comparison of the finite element simulations and analytical model of the electrostatic actuator. a) The actuation as function of bias voltage for a device 50 μm long with 1 μm wide cantilevers and electrode gap. As expected, the analytical model describes the actuation at low voltages and underestimates at higher voltages. b) The ratio of values from simuations and analytical models for the pull in voltage and pull-in range. The simple analytical model seems to describe the pull-in voltage to within 10% of the simulated value but underestimates the pull-in range by about 25 %..

Experimental Setup

The Labview controlled system developed by P. Bøggild has an integrated image analysis program that allows accurate detection of the gripper position and also controls a Keithley 2400 Sourcemeter to provide the bias voltage. As shown in Fig. 3.9, a region of interest can be selected in a live video image from the high magnification microscope (video field of view down to 50 μm). The pixel values in the image are summed over either the x- or y-axis depending on the gripper orientation, in order to produce a graph which for two cantilevers contains two peaks 3.9. The peak positions are fitted by a Labview peak detection routine, giving a precision of the order of a few nanometers under optimal conditions, despite the low optical resolution. The peak positions are stored in a file together with the voltage for further analysis.

The grippers were fabricated; glued to ceramic substrates to make handling of the small chips easier; and wedge bonded for electrical contact. If pull-in is reached when actuating the gripper, the bias voltage will be short-circuited and the thin gripper arm can be damaged severely. Experience has shown that these damaging discharge effects can be reduced by adding a 100 kΩ protective resistor to the wires leading to the chip, provided the resistor is close to the gripper, to minimize the capacitance of

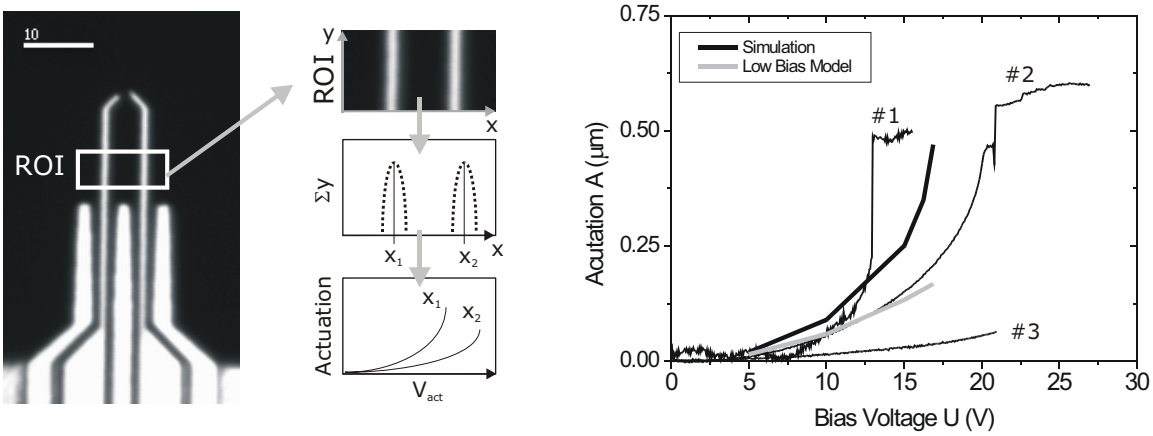

Figure 3.9: Measurement of actuation. In the Four point station (Sect. 2.3.1), a region of interest is selected in the video image. The pixel values are summed along the y-axis to give a graph with two peaks corresponding to the cantilever positions. Plotting the peak positions as function of applied voltage gives the actuation curve for each actuator in the for the device. Measurements on three devices (50 μm long and both gap and width are 1 μm) are shown together with the simuation and model predictions.

the leads with high voltage between the resistor and gripper[2]. It seems that about half the devices can reproducibly be actuated to pull-in and will release when the bias voltage is removed, while the other half will remain stuck to the driver electrode after pull-in. A "stuck" gripper can usually be released again by pushing it against an external object, and this will often restore the functionality of the device.

Reproducibility of Actuation

Figure 3.9 shows simulated actuation curves together with the measured curves on three different grippers with a length of 50 μm. The variation in actuation of the real devices is quite large.

Figure 3.10 shows four actuation curves (opening and closing of two actuators) measured on the same gripper with the dimensions (in μm) $L = 100$, $L_+ = 30$, $w = g_0 = 2$. This is one of the grippers actuating most reproducibly. When closing, the two gripper arms actuate reasonably identically, but when opening, arm 2 actuates almost twice that of arm 1. Practically all devices show deviations between the actuation of very identical gripper arms that is at least comparable to this device.

[2]The resistor should ideally be placed on the chip. From experience it seems that even a few centimeters of wire between the resistor and chip has sufficient capacitance to store an energy at 30 V bias that can severely damage the actuator.

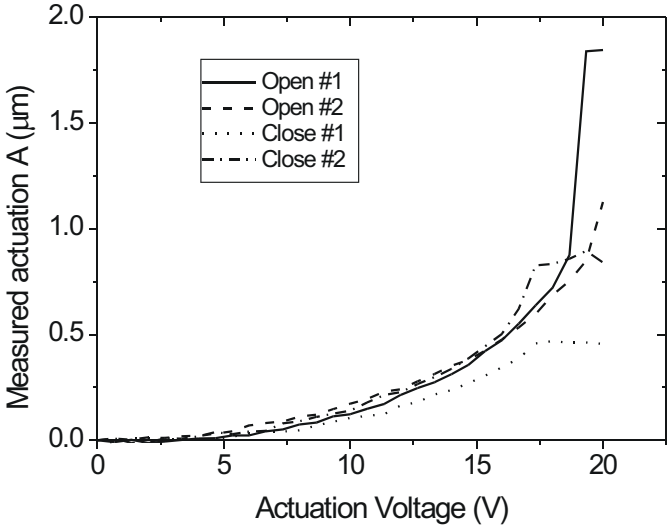

Figure 3.10: Measured actuation when opening and closing the two gripper actuators in one device. This is one of the good devices in terms of reprodubile actuation.

Given the non-linear behavior of the actuation as the pull-in voltage is approached, and spring constant of the cantilever with the cantilever width, very small deviations in the gap and width of the cantilevers can easily cause such deviations.

Given the wide variation in actuation even on a single device, the yield of functional devices depend strongly on the specification of "functional": Many devices will be able to show some kind of actuation, but very few will be operating within the range of actuation predicted by the model and the simulations. Even for successfully processed wafers, inspection in an optical microscope will often show that some devices have defects such as pin-holes or poorly etched regions. In addition 1-2 percent of the devices will be lost during handling (being released from the wafer, glued and bonded). Electrical testing will find short-circuits due to small fabrication defects not easily visible in the microscope, or debris created during the release from the wafer (some debris can be blown off by a nitrogen jet, and more sticky debris can often be successfully removed by a "vacuum cleaner" made from a Ø1 mm soft plastic tube connected to a vacuum pump). The ratio of devices showing some actuation on one or both gripper arms can in well processed wafers be quite high (more than 50%), but devices matching the simulated behavior was typically only a few percent of the devices on the wafer.

The grippers' end-effectors often stick together after the processing. Such sticking grippers cannot be actuated electrostatically and strongly reduce the number of

functioning devices. The sticking grippers can often be released if moved in contact with a solid object. This is a time-consuming operation for each device, but can considerably increase the yield of functional devices.

With the large variation in device functionality, the modelling and simulations seem to provide reasonable estimates of the gripper behavior. For future work, the processing of the devices should be carefully optimized for production of grippers.

Gripping Force and Compliance

For the manipulation tasks discussed in section 3.2, the gripper force and gripper compliance (the spring constant of the gripper) is also important considering the forces required to complete the task.

An estimate for the absolute maximal gripping force $F_{grip,\max}$ can be calculated from the pull-in of the actuator where a point gripping force at the tip of an actuator keeps the tip at the initial position as shown in fig 3.7. Given the uncertainty of the actuators' actual behavior, detailed simulations of the forces involved during pull-in would not provide much more information than an estimated value. If the cantilever is touching the driver electrode, the bias voltage must be assumed to be zero. An order of magnitude value can be found from the force required to deflect a beam of about half the length of the full actuator length by g_0 as shown in Fig. 3.7b:

$$F_{grip,\max} \approx 3YI\frac{g_0}{\left(\frac{L}{2}\right)^3}, \tag{3.28}$$

which for $L = 50$ μm, $T = w/2 = g_0 = 1$ μm gives $F_{grip,\max} = 1$ μN. If the cantilevers are not short-circuited, higher forces can be achieved by applying a voltage. For grippers capable of opening, the applicable force can also be increased when grabbing objects larger than g_0 as the actuator will deflect more to grab these.

It is a fundamental problem with the electrostatic cantilever actuators that the grippers must have a low spring constant to achieve a useful range of actuation at low voltages, but such low spring constant also limits the applicable gripping force. The w^3/L^3 dependence of $F_{grip,\max}$ and L^4/w^3 dependence of the actuation $y(L)$ in Eq. (3.27) make the gripper length and width important parameters for the design.

With a gripping force of the order 1 μN the grippers seem to be capable of peeling nanowires as described in section 3.2.

3.3.5 Summary

A simple analytical model of the electrostatic gripper actuation was compared to finite-element simulations by the program CoventorWare. The simple analytical model can be used to predict low bias actuation and also seems to describe the pull-in voltage reasonably well. The finite element simulations are useful when testing more complex structures such as comb drives, however, various structures were tested and did not show improved performance over the straight cantilever grippers, so the investigation was focused on the straight cantilever actuators. The actuators are in practice capable of actuating about half the gap width before pull-in occurs. The gripping forces are expected to be of the order μN, but depend strongly on the length of the gripper, the size of the object, and the realized actuation of the individual device. The measured actuation of processed devices show a large variation for similar devices, and even for two cantilevers on the same device. The present fabrication process limits the thickness of the grippers and this gives a low aspect ratio, which is likely to cause out-of-plane bending (Fig 3.4c). For many pick operations we must expect the out-of-plane bending to be pronounced. Despite the shortcomings, the devices do work reasonably as intended and are among the smallest microfabricated grippers made to date.

3.4 Pick-and-Place Manipulation of Nanowires

From the description of picking strategies in section 3.2 and the gripping force of the order 1 μN estimated in the previous section, the preparation of the sample for picking by peeling seems to be an essential issue. Carbon nanotubes were generally observed to adhere strongly when manipulated in the SEM. The larger silicon nanowires available from Philips Research laboratories did not appear to adhere as strongly and were chosen as the sample for the manipulation experiments. Attempts of tensile or shear gripping of the wires directly from the substrate did not succeed as expected, since the gripper does not have sufficient gripping force to do so. To prepare samples for peeling, the front edge of a used gripper chip was lowered into the standing nanowire sample. This would make several nanowires break off and extend over the edge of the chip where they could be easily approached and also mounted on a grounded gold surface to reduce charging. The pick-and-place manipulation is presented below in two sections describing first the picking process and then the placing of a nanowire. The in-situ SEM nanomanipulation setups in the MIC-SEM and AMiR-SEM described in the previous chapter were used for pick-and-place nanomanipulation with the electrostatically actuated grippers.

3.4.1 Picking Up Nanowires

The image sequence in Figure 3.11a–f shows a gripper picking up a silicon nanowire extending from the gold surface of the chip. The operation was done in the MIC-SEM setup and the gripper had an actuation range of 300 nm at a voltage of 30 V. The silicon nanowire had a diameter smaller than 100 nm and was initially extending over the edge of a gold-coated Si substrate.

To investigate whether the applied gripping force or the adhesion between the wire and the grippers is dominating the pick-up process, the grippers were first moved while touching the wire (Fig. 3.11b,c), then closed around the wire (Fig. 3.11d) and subsequently reopened (Fig. 3.11e). Although the nanowire adhered to the grippers, during these operations, the adhesive forces were not sufficient strong to move the wire considerably or pull it off. But closing the grippers again and pulling (Fig. 3.11f) made it possible to pick up the wire. The wire was later lost from the gripper when it was attempted to place it on a cantilever, probably because a part of the target chip appeared to be considerably charged by the electron beam. Proper grounding of all parts is essential, and even then, insulating parts should be avoided in the vicinity of the gripper, to avoid disturbing electrostatic forces.

The adhesion forces between the gripper and the wire can be sufficiently large to attach it to the gripper. The sequence in fig. 3.12 shows another example of a nanowire being picked up from a similarly prepared substrate. However, in this sequence, the bias closing the gripper was removed after gripping was achieved, and the nanowire was observed to remain in the gap by adhering to one of the end-effectors.

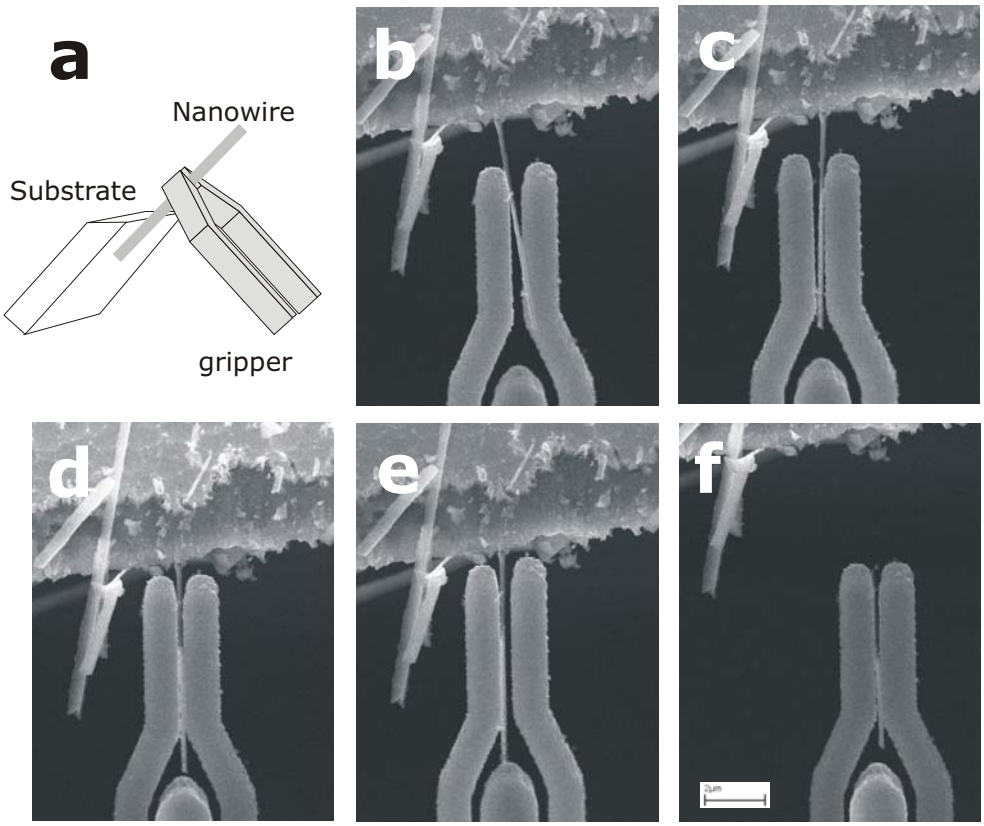

Figure 3.11: Picking up a silicon nanowire extending over the edge of a substrate. a) Illustration of the setup. The SEM images are top-views of the setup. The wires located on the upper silicon surface of the substate were usually adhering so strongly to the substrate, that they could not be removed. Wires extending from the edge of the gold surface were generally much easier to both move and remove. b) The gripper moved into contact with the wire. c) Moving the wire and sliding the gripper along it could not release the wire. d) The gripper was closed around the wire and reopened (e) without removing the wire. f) The wire could only be peeled from the substrate, when the gripper was closed.

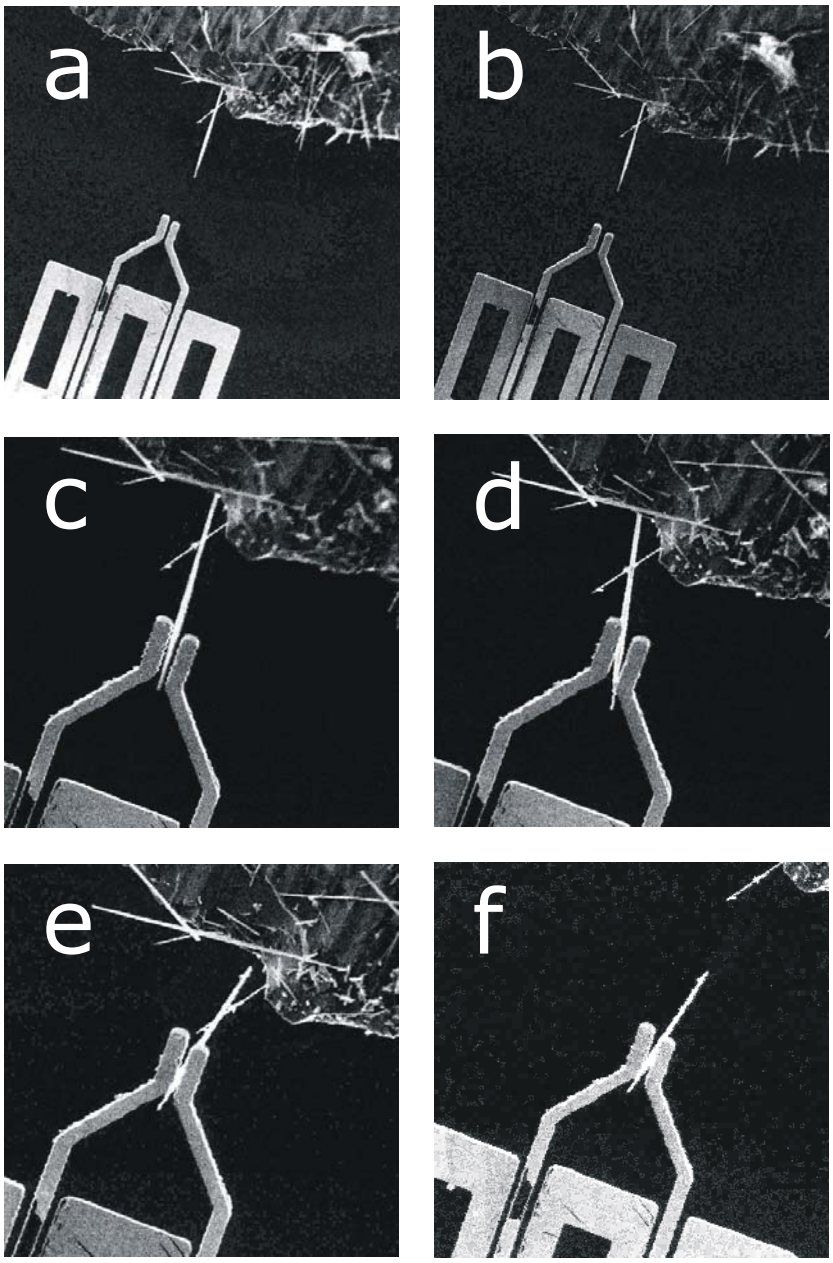

Figure 3.12: SEM image sequence by A. Kortschack and T. Wich showing the pick up of a nanowire. (a) Gripper approaching, the gripper arms are 2 μm wide. (b) Gripper opening at 15 V. (c) The nanowire was slowly moved from a position above the gripper into the opened gap. (d) The nanowire is adhering to the gripper but not enough to break it free. (e) The gripper was closed by 15 V bias and the nanowire could be broken free from the substrate. (f) Once grabbed the gripper could be opened and the nanowire was observed to adhere to the left gripper arm.

3.4.2 Placing Nanowires

To place a grabbed nanowire accurately, the forces between the substrate and the nanowire must be increased to the point where the nanowire can be released from the gripper as discussed in section 3.2. The observation that the nanowires supported by the silicon surface of the substrate adhered strongly, made it obvious to try placing a grabbed nanowire on this surface. Such a place-operation was performed in the AMiR-SEM and is shown in Fig. 3.13. A grabbed nanowire was picked up and held by the gripper, which then twisted and closed around the nanowire (as in Fig 3.4c). The nanowire was moved to contact the substrate in Fig. 3.13c (the height of the substrate in the left hand side of the image is higher than the height of the gripper, while the right is lower). It was the impression that the wire adhered well already upon the initial contact to the surface, but to be on the safe side, the contact point was exposed to the electron beam for 60 seconds, to improve the mechanical strength. The EBD rate was however very low in this setup, and there was no obviously visible change in the structure. The release from the gripper was successful and the nanowire remained at the position it was placed (Fig. 3.13d).

To investigate the strength of the nanowire's mechanical connection to the substrate, it was attempted to break the nanowire free from the substrate again. The grippers could be moved in under the wire (Fig. 3.13e), indicating that it was standing out from the surface and not supported along the entire length. The wire did not seem to move at all, even when lifting the gripper up with one end-effector stuck under the wire as in Fig. 3.13f.

It seemed that the wire was so well attached to the substrate that attempts to break it off would probably do more damage to the gripper than the wire. The microrobot was rotated to use another larger cantilever tool capable of applying larger forces (one of PRCs, see section 2.2.2), Fig. 3.13g. With the larger cantilever it was possible to break the nanowire off the substrate. In the image Fig. 3.13g, taken just before the wire broke, the radius of curvature at the fixed end of the nanowire is about r_{curv} = 6 - 7 μm. With a nanowire radius of about $r_0 = 0.27$ μm this gives an approximate yield stress [84]

$$\sigma_{yield} = \frac{r_0}{r_{curv}} Y \tag{3.29}$$

of 7 - 8 GPa, if the Youngs modulus 190 GPa of silicon is used. This is in agreement with the 7 GPa yield stress of bulk silicon. The rather thick "nanowire" used in this experiment was one of the thickest that have been used. Generally the nanowires are observed to withstand bending with radii of curvature down to a few microns. In Fig. 3.13g, the nanowire itself is bending, rather than rotating as a rigid wire around the point where it is fixed to the substrate. This indicates that the contact to the substrate is as strong as the wire material itself. A residue of the wire or EBD is left after it has broken off, indicated by the arrow in Fig. 3.13h. It was not clear if a piece of the wire was still attached at the contact point or the residue is due to the

EBD. If electron beam deposition was soldering the wire to the substrate, it resulted in this case in a mechanically very strong solder joint with a yield stress comparable to silicon.

The possibility to use the grippers to move nanowires samples from their substrate to TEM grids was also investigated. In the image sequence shown in fig 3.14, a grabbed bundle of silicon nanowires is placed onto a copper TEM grid. The nanowires were slowly moved into contact with the TEM grid (fig 3.14a-c). When one of the wires touched the grid, the contact point was irradiated for 60 seconds, to increase the adhesion to the grid. The bias voltage was than turned off, and the grippers were withdrawn (fig 3.14d). This was however not sufficient to release the wires from the gripper. In Fig 3.14e the grippers were opened further up by applying bias to the outer driver electrodes, and this apparently altered the force balance enough to release the wires (fig 3.14f) that remained stuck to the TEM grid. The nanowires were later inspected in an optical microscope, where they appeared to be in the same position. Some days later, when the grid was inserted into the TEM for detailed analysis, the wires had unfortunately disappeared for unknown reasons. Despite the unfortunate loss of the wires, it is worth noting that in this case EBD was not required to make the wires adhere and stick to the grid well enough for the grid to be handled by a pair of tweezers by hand when removed from the SEM and observed under a light microscope. In a future study it would be interesting to investigate the strength of the EBD soldering by a combination of EBD, nanowires, and piezoresistive cantilevers for force measurements.

3.4.3 Summary

Several in-situ SEM pick-and place operations of silicon nanowires were demonstrated. Successful picking of the nanowires required the sample to be prepared with wires extending from the edge of a grounded gold substrate where they could be peeled off. Placing of nanowires onto silicon substrates was demonstrated, where the wires apparently adhered strongly, and onto a TEM grid. EBD is possibly a useful tool for making mechanically strong contacts to the target substrate when placing a grabbed object. In the present experiments, the wires possibly adhered strongly to the surfaces even before EBD was applied. In the discussion of EBD in the following chapter, it will be demonstrated how EBD can be used to solder carbon nanotubes during nanomanipulation.

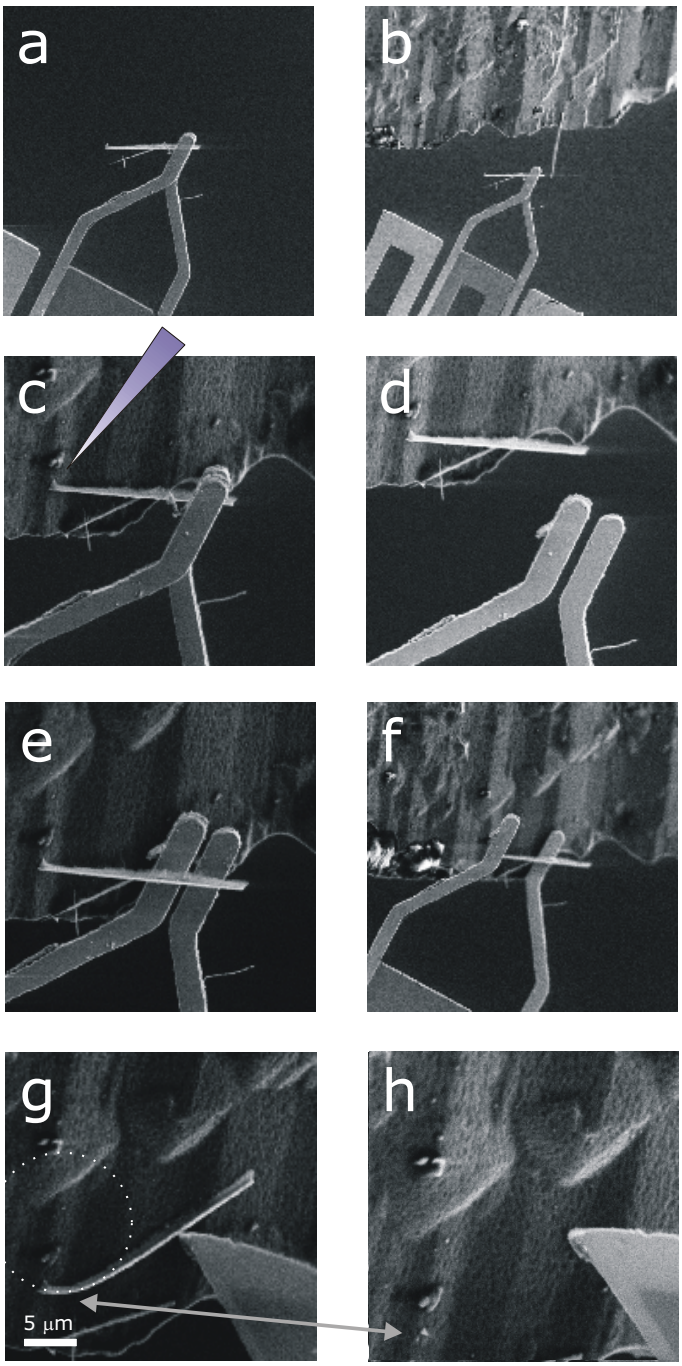

Figure 3.13: The SEM image sequence shows placing of a nanowire (a-d) and subsequent test of the yield strength of the nanowire attachment to the substrate (e-h). (a) The nanowire was picked from the substrate as described in Fig 3.12.

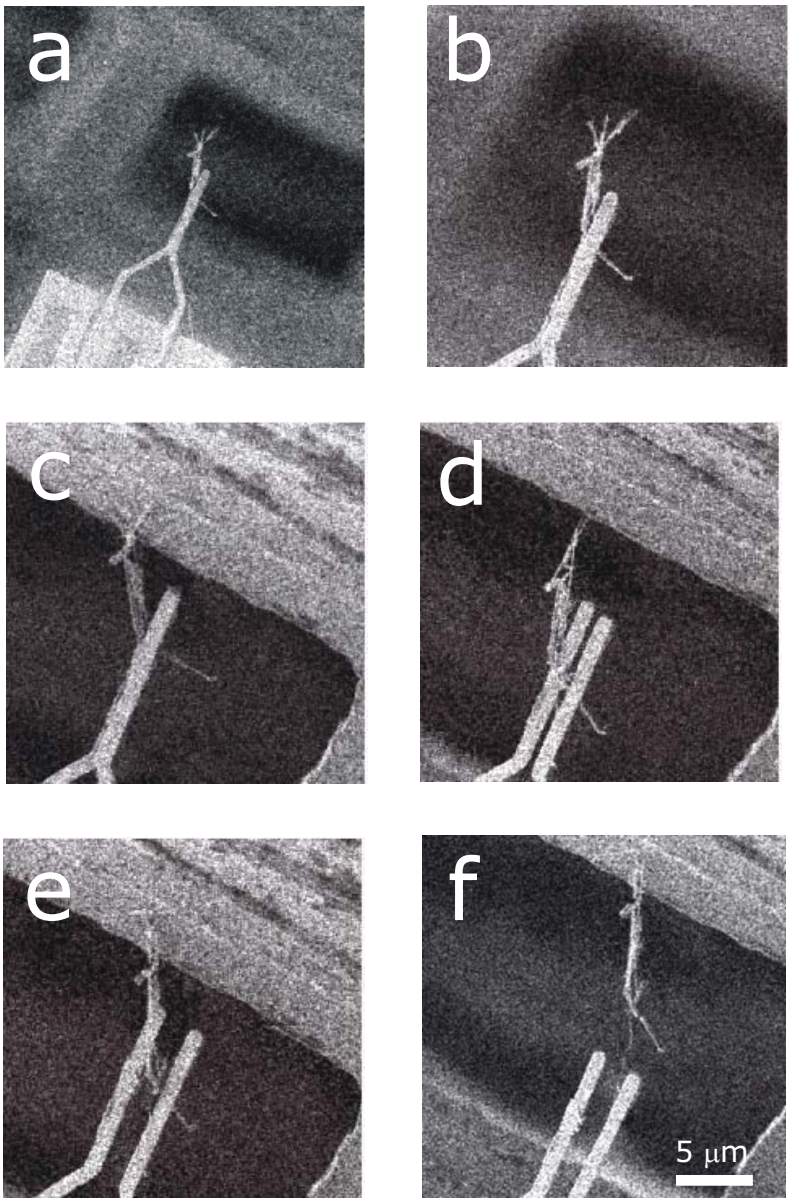

Figure 3.14: Frames from a SEM video sequence of a nanowire bundle being placed on a TEM grid.

3.5 Electro-Thermal Grippers with Piezoresistive Force Feedback

The pick-and-place results achieved with the electrostatically actuated grippers demonstrate the feasibility of in-situ SEM pick-and-place manipulation. The gripping force applicable by those devices seem to be the main limiting factor for successful manipulation. In the presented design, the electrostatic actuators are necessarily made of cantilevers with a low spring constant to achieve a reasonable actuation range at low bias voltages.

Thermal actuators are generally capable of applying higher gripping forces, since the actuating structure can be a rigid body where the thermal expansion coefficient is important for the actuation. The review of grippers in the first section of this chapter also show this tendency. In addition to achieving a higher gripping force, an electrothermal gripper should also make it possible to create a design where the applied gripping force can be measured by piezoresistive changes in the actuating elements of the gripper.

In the included article [1] "Electro-thermally Actuated Microgrippers with Integrated Force Feedback.", the design and test of prototype devices is presented. The device is shown in Fig. 3.15c,d together with two related devices which inspired the design (Fig. 3.15a,b). The Zyvex gripper (Fig. 3.1c) is based on a traditional two beam actuator (Fig. 3.15a). Actuation is achieved by passing a current through the connected thin and thick beams, which heats the thin beam to a relatively higher temperature than the thick beam, making the actuator bend towards to colder tick beam. A higher actuation range has been demonstrated by the design of Kolesar et al. [92] where two thin flexible beams is used to carry the current (Fig. 3.15a), thereby reducing the temperature of the cold beam and increasing the actuation range.

The present device uses three identical beams connected by an end bar, shown in Fig. 3.15b. Depending on how the bias voltage is applied, the thermal actuator design can be used to both open when heated or, as shown in Fig. 3.15c, to close when heated. Closing in the cold state is important if the materials to be manipulated cannot withstand high temperatures and will also make electrical measurements on the grabbed object possible without voltage applied to the actuator structure (indirect actuation). A reasonable range of actuation of about 3 μm was measured on the prototype devices. The design allows for several approaches to implementation of piezoresistive detection of forces while actuating, where each implementation would be suitable for different applications. Figure 3.15e shows a typical Wheatstone bridge circuit for sensitive detection of changes in resistance. The actuator can for instance be connected as a Wheatstone bridge circuit as shown in Fig. 3.15c. Measurements on the prototype device are presented in the graph in Fig. 3.15f. The measured sensitivities were considerably lower (a factor of 15) than the values estimated from a simple analytical model. The discrepancy is likely to be caused by out-of-plane

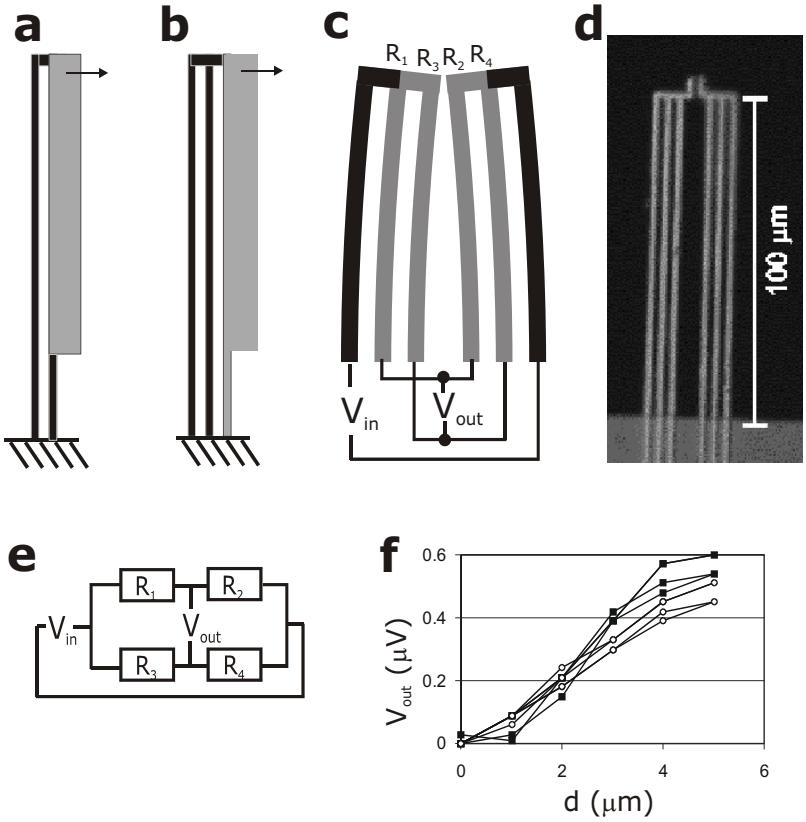

Figure 3.15: Thermal gripper with piezoresisitive force feedback. a) The standard thermal actuator, which is also used by Zyvex (see Fig. 3.1). b) A three-beam design by Kolesar et al. [92]. c) The device design, capable of both opening or closing in the heated state depending on how the driving voltage is applied, and also capable of providing a piezoresistive force feedback signal. d) Optical image of a fabricated device. e) A typical Wheatstone bridge circuit. The resistor numbers correspond to those in (c). f) Measurements of the piezoresistive signal when opening and closing the gap by deflecting each of the actuators in (c) (square and circle mark each actuator).

bending of the beams due to the low aspect ratio. The sensitivity in the present prototype device is comparable to other reported piezoresistive sensitivities [78], where silicon was used for the sensors, which has an about 20 times higher piezoresistive coefficient than the gold the present devices were made of.

The current prototype devices have a low aspect ratio, and this makes them unsuitable for manipulation. The performance of the tested devices make it worth to consider developing a new process to make high aspect ratio cantilever structures that can be used to process well-functioning electrothermal grippers with piezoresistive force feedback and higher gripping forces than the present electrostatic actuators. Such a process would also be suitable for making electrostatically actuated grippers with a high aspect ratio and hopefully improved performance as the out-of-plane

bending is reduced.

3.6 Summary and Outlook

Based on a survey of existing gripper designs for micro and nanomanipulation, it was decided to develop microfabricated electrostatically actuated grippers based on the existing fabrication processes used for making conductance probes (Fig 2.4).

The requirements for such grippers in terms of gripping forces were studied by investigating several scenarios for picking up nanowires. A model for the electrostatic gripper actuation was developed and compared to finite-element simulations, to aid the design process. Grippers were fabricated and their performance compared to the model and simulations. The yield of well-functioning grippers was unfortunately rather low. However, grippers were shown to be able to perform reasonably as expected, and the devices are among the smallest microfabricated grippers to date. The achievable gripping force was analyzed and it appeared that they would be suitable for peeling nanowires extending over the edge of a substrate since that was expected to be the nanowire sample that required the lowest gripping force to successfully pick up a nanowire.

The grippers were successfully used for in-situ SEM nanomanipulation. Silicon nanowires were picked by the peeling method and placed on both silicon substrates and TEM grids. Electron beam deposition seemed to be a potentially helpful tool when placing nanowires to ensure strong adhesion to the target substrate.

Finally microfabricated electrothermal actuators were presented which provide a unique combination of being able to both open and close in the heated state, as well as providing higher gripping forces and a force feedback signal.

3.6.1 Outlook

With further development, the pick-and-place method, possibly aided by electron beam deposition or other methods to fix the placed objects, could become a versatile in situ method for integrating nano- and microstructures. Compared to manipulation with STM or AFM tips, the grippers could offer better control of the forces in a pick-and-place manipulation process. Indirect actuation of the gripper compared to the direct application of the bias voltage to the nanotweezers tips, also seem to be an advantage that leaves more options open for measurements of the properties of grabbed objects.

Based on the presented results, it seems worth pursuing the development of a dedicated fabrication methods for thermal and electrostatic grippers, which especially means higher aspect ratios and yield of well functioning devices. If more reliable grippers with higher gripping forces are developed or acquired commercially, the pick-and place methods could be developed to the point where it can become a routine method

for research and prototyping purposes in the near future. Looking back, it took decades to develop the devices for surface mounted circuit boards and the technology to mass-produce these. Considering the increasing availability of nanomanipulation systems with gas injection for methods such as EBD (available from at least both Zyvex and LEO) and the commercially available grippers (Zyvex, Nascatec), the development of automated pick-and place assembly on the nanoscale seems to be on its way.

Chapter 4

Environmental Electron Beam Deposition

The highly focused electron beam in the SEM is used for imaging nanostructures, but it can also be used to make nanoscale deposits. In the presence of carbonaceous or organometallic gasses in the SEM chamber, electron beam deposition (EBD) can be used to construct three-dimensional nanostructures or solder/glue nanostructures. In the NanoHand project one of the main goals was to investigate if EBD could be used for:

- Soldering of nanotubes and wires with conductive material.
- Fast and reproducible EBD of nanoscale tips on the grippers to create nanotweezers tips on microgrippers.

4.0.2 Background

It was apparent with the first electron microscopes in the 50's, that the presence of an electron beam slowly coated the sample with a carbonaceous substance [13]. Even earlier, it was observed that electron radiation decomposed organic vapors present in the vacuum chamber, such as oil vapors unavoidable in diffusion pumped vacuum systems or outgassing from the sample itself [93][94]. When the background gas is decomposed by irradiation through various ionization and dissociation processes, the gas turns partly into volatile compounds re-emitted into the chamber and partly into solid amorphous carbon. The material properties range from diamond-like-carbon (DLC) to polymers depending on the exact deposition conditions [95].

The reactions taking place during EBD are not well characterized. Both ionization and dissociation are expected to contribute [100]. The cross-section for both dissociation and ionization are peaked at low electron energies ($\sim$50 eV), indicating that secondary electrons are likely to be the main cause of deposition rather than the

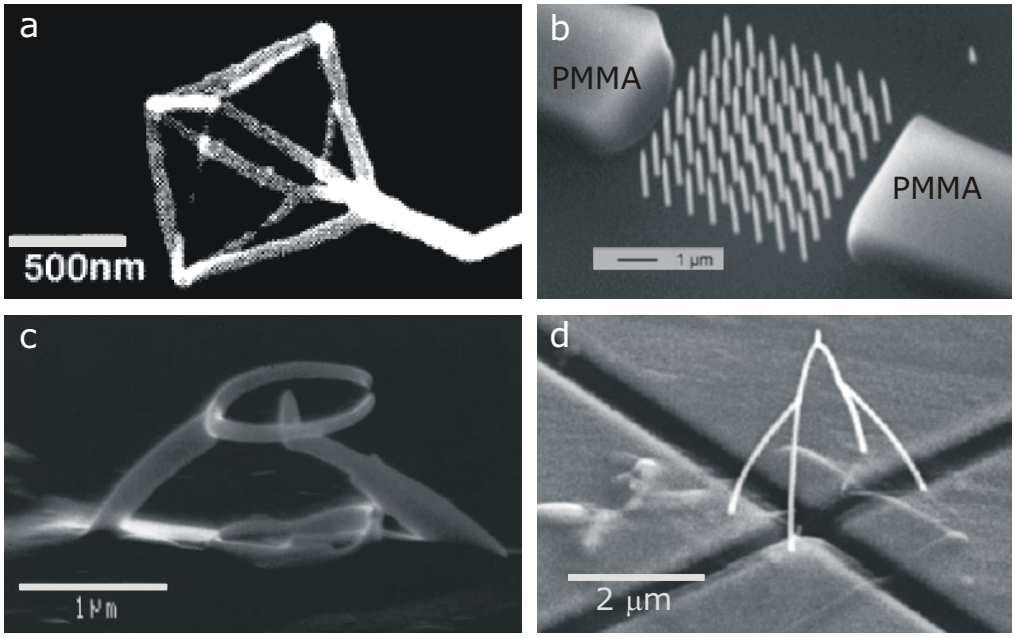

Figure 4.1: Three-dimensional EBD structures. (a) Carbonaceous ochtaedra by Ooi et al. [96]. (b) Array of metal containing EBD tips make a photonic band gap structure between polymer (PMMA) waveguides, by Koops et al.[97]. (c) Field emission anode and cathode made by platinum containing EBD by Koops et al.[98]. (d) Thermal sensor structures by Edinger et al. [99] Four point measurement of the central arch resistance makes it possible to measure temperature induced changes in the platinum containing resistor.

primary electrons (PE). By focusing the PE beam in a fixed spot, a thin needle-shaped deposit will grow up towards the electron beam. The tip width can be considerably wider than the PE beam diameter and typically of the order 100 nm. The width is determined by the scattering of the PE in the tip structure which in turn also creates SE escaping through the tip apex and sidewalls causing a wider deposit [100].

With many potential applications micro- and nanotechnology, the EBD technique has received increasing attention since the 80's as a method for creating submicron structures. Comparing EBD to electron beam lithography (EBL), the EBD process must be considered "slow" while EBL is "fast" since the required irradiation dose is many orders of magnitude smaller for EBL. The use of EBD in commercial production of nanostructures is today limited to "supertips" for AFM cantilevers with extreme aspect ratios that cannot readily be achieved by other methods [101]. For research purposes, where high throughput is not a requirement, the technique appears convenient in many applications. Apart from depositing structures, it has also been used to solder nanocomponents. Both single and multiwalled carbon nanotubes (SWNT and MWNT) have been soldered to AFM cantilevers for stress-strain measurements [54][52] and to micromechanical actuators [51].

A large fraction of the EBD publications have been focussing on the use of metal containing precursor gasses. Koops et al. [102] and Matsui et al. [103] pioneered the extensive use of metal containing source gasses to make deposits with high metal contents. They also began scanning the beam in patterns to make three-dimensional structures. Figure 4.1 shows several illustrations of complicated three-dimensional structures made by both carbonaceous and metal-containing EBD. Another intriguing possibility is to use EBD to make catalyst particles for subsequent growth of nanowires and tubes as demonstrated in Ref. [104].

Compared to the planar and resist-based EBL, the EBD method is slow and difficult to scale to large productions, but on the other hand offers the possibility to create elaborate three-dimensional structures, which cannot readily be made by EBL. For our nanomanipulation setup, the EBD method appears to be a versatile tool capable of constructing nanotweezers tips, contacting nanowires to create composite electronic nanostructures, and soldering nanostructures such as carbon nanotubes to microelectrodes.

For electronic applications one would like to achieve as high a conductivity as possible of the deposited material. Metal-containing EBD materials usually contain metallic nanocrystals in an amorphous carbon matrix with a conductance considerably lower than that of the pure metal. The metal content and conductivity of the EBD material can be increased to approach that of bulk metals by several methods:

1. Heating the substrate has been shown to increase the metal content of the deposit. Koops et al. [105] have observed an increase from 40 wt. % at room temperature to 80 wt.% at 100°C.

2. Using a carbon free precursor gas, such as PF_3AuCl, Hoffman et al. [106] made gold deposits with a conductivity of 22 $\mu\Omega$cm which is only 10 times the bulk value of Gold.

3. Introducing an additional gas such as water vapor while using an environmental scanning electron microscope (ESEM). Folch et al. [107] investigated EBD in an ESEM with Dimethyl-Gold-Hexafluoroacetylacetonate as precursor gas. Using Auger electron spectroscopy analysis they found that the gold content of tips could be increased to 50% by using 10 Torr $80\%Ar/20\%O_2$ as ESEM gas.

This chapter presents our investigation of electron beam deposition as a method for constructing, contacting and soldering nanostructures. The main results have been published in the attached papers [2]-[6]. The first section presents our initial studies of how EBD based on carbonaceous background gas can be used to create delicate nanostructures and to perform complex manipulation tasks. However, the background gas was an unstable source for the deposition experiments, and a system was built with a more reliable integrated organometallic source. A simple model for the deposition process is reviewed to estimate the achievable growth rates and basic

flow rates required by the source system for efficient deposition. To achieve a high conductance of the deposited structures we chose to focus on the EBD method using ESEM, since the differential pumping system in the instrument protects the SEM electron gun from the precursor gasses. We call the ESEM EBD for environmental EBD -or EEBD. The ESEM is also an interesting instrument for nanomanipulation, since the environmental gas can often reduce problems with charging[1]. The experimental setup for the ESEM investigation is then described, including a brief review of the simple electron beam lithography system I developed to control the electron beam during EBD (see the included article [2] for details). The following sections present the experimental results: the internal morphology of the tip deposits was examined by HRTEM and STEM, and it was discovered that it is possible to create desposits with a solid gold core under certain deposition conditions. These results were published in the included paper "Solid Gold Nanostructures Fabricated by Electron Beam Deposition" [4]. The main results of that paper are summarized in Sect. 4.4. In order to achieve reliable deposition of three-dimensional structures by slowly scanning the electron beam, a detailed study was made of the deposition process as function of scan rate. The electrical properties was also investigated since the gold core make the method an attractive tool for creating conductive structures and connecting nanostructures electrically. This work was published in the included article "Constructing, Connecting, and Soldering Nanostructures by Environmental Electron Beam Deposition"[3]. The results are reviewed together with the main results from the included paper "Soldering of carbon nanotubes onto microelectrodes" [5]. The ESEM study was done together with primarily D. N. Madsen (R. Mateiu and S. Dohn also contributed) in close collaboration with the company Haldor Topsøe A/S, who generously provided the ESEM and TEM expertise.

[1]The ESEM also provides a nanomanipulation environment where capillary forces might be controlled during manipulation and both high temperatures and light can be used while imaging in ESEM mode. These aspects are beyond the scope of this thesis.

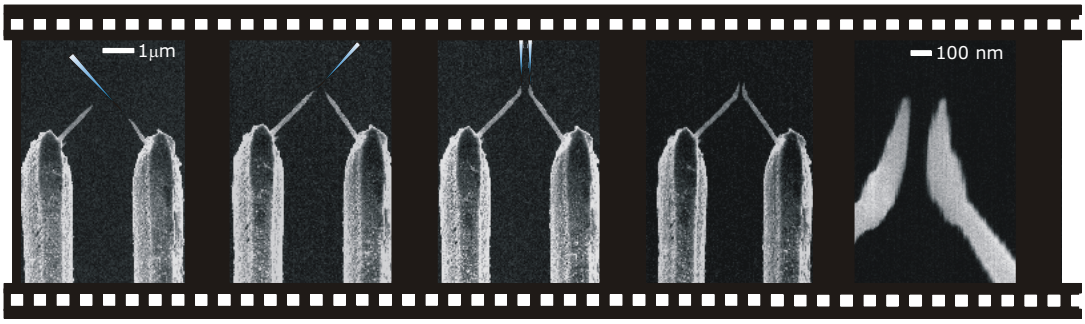

Figure 4.2: EBD of a pair of nanotweezers using carbonaceous background gas as precursor. A fixed electron beam was used to grow nanotweezers tips on an electrostatic microgripper by sequentially rotating the gripper in different directions relative to the electron beam [108]. The trinagles indicate the direction of the beam. (Images adapted from [108], and the experiment was done by P. Bøggild)

4.1 Initial Study of EBD

Before making dedicated systems for organometallic EBD, we gained experience with the EBD method by using the carbonaceous background gas as source. The results from these initial studies demonstrate that EBD has the potential to become a very useful technique for the nanomanipulation setup.

4.1.1 Making Nanotweezers by EBD

When the NanoHand project started, Peter Bøggild and Torben M. Hansen used EBD to make nanoscale carbonaceous tips on micro four point probes. They were using the SEM at the Division of Solid State Physics at Lund University, which turned out to have a background gas giving high deposition rates, unlike the SEM at MIC which rarely displayed any noticeable EBD rates[2].

In these experiments, the deposition rate varied substantially with the instrument history - and sometimes deposition was not possible at all. But when deposition was possible, delicate three-dimensional nanostructures could be deposited. Figure 4.2 illustrates how nanotweezers tips were deposited on the two middle cantilevers of a small cantilever probe, which then could be used as an electrostatic microgripper. Bøggild and Hansen created gaps as small as 25 nm in this manner [60]. The gap between the nanotweezers tips can be made smaller by imaging the tweezers structure at high magnification, which causes a slow deposition to widen the tweezers tips until the imaging is stopped when the desired gap width has been reached. The method was also used to make nano four point probes with four EBD tips extending from

[2] All our observations indicate that deposition from a gas naturally present in the chamber is hindered by frequent exposure of the chamber to ambient air. In addition, the LEO SEM at MIC is not pumped by a diffusion pump which is known to cause a carbonaceous background gas.

the micro four point probe to give a probe spacing of 300 nm. The probe was made conducting by anisotropic gold coating, but the coating was found to be fragile due to poor adhesion to the EBD tips.

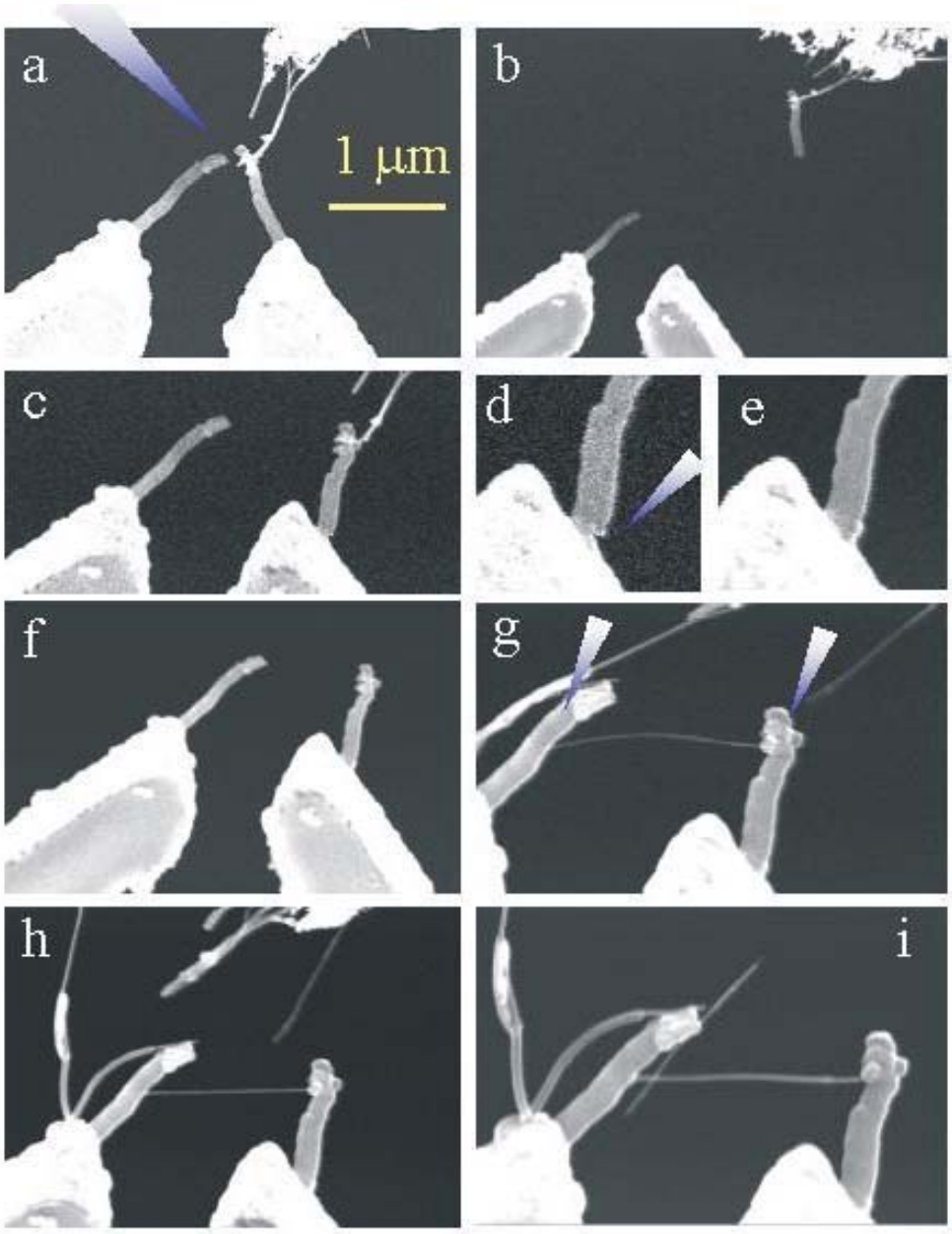

Figure 4.3: Demonstration of the versatility of EBD in the nanomanipulation setup at MIC, using the background gas as precursor gas. (a) A MWNT was soldered to a pair of carbonaceous EBD tips deposited in Lund on a microgripper. The MWNT was brought in contact to one tweezer tip and soldered by 30 s EBD (the beam is indicated by the triangle). (b) By pulling the nanotube away, the tweezers tip breaks off. (c) The tip is brought back in contact with the microgripper. (d-e) The tip is soldered to the gripper by a 30 s EBD that filled the gap. (f) When the MWNT is pulled away again, it breaks off at the nanotweezer tip, and the tweezers have been repaired. (g) A MWNT is soldered to the side of the tweezers and a thin tube is pulled across the gap and soldered to create a nanotube bridge. (h-i) more tubes could be added by further soldering, but electrostatic forces due to charging by the electron beam made it difficult to control the position.

4.1.2 Soldering Nanotubes by EBD

At the MIC SEM, EBD was only rarely possible and usually only with very limited deposition rates. Serendipitously, it was possible to demonstrate the versatility of EBD soldering for nanomanipulation tasks as shown in Fig. 4.3 on a day where the deposition rate was much higher than normal. Though promising, the results cannot not be reproduced since precursor sources are not allowed in the instrument, and the use of EBD is anyway limited to gluing as long as the deposited material appears to be highly insulating.

4.1.3 Summary

Electron beam deposition was found to be a versatile tool to include in the nanomanipulation setup. EBD could be used for both constructing new nanostructures such as nanotweezers and for soldering existing nanostructures such as carbon nanotubes to other micro- and nanostructures. However, the material deposited from the SEM background gas at Lund and at MIC did not appear to be conducting, and this limits the applicability of EBD for electrical devices. To make nanoscale conductance probes, it is possible to coat the nanotweezers tips by anisotropic gold deposition, but the gold does not adhere well to the EBD material.

The soldering experiments at MIC demonstrated that the soldering was mechanically so strong that the nanotubes often broke before the soldering joint. The method is however unlikely to make reproducible results as long as it depends on the unstable background gas of the SEM. Since it is not allowed to insert gas sources into these SEM instruments, the following investigation was focused on using the ESEM with more controlled gas sources.

4.2 A Simple Model of EBD

To achieve a higher degree of reproducibility of the deposition process, an organometallic source system was built for the ESEM at Haldor Topsøe A/S. This section reviews a simple model of the EBD process and the requirements for the source system.

To accurately model the EBD process, one has to resort to Monte Carlo simulations that can incorporate the different scattering effects taking place during the process. Extensive work done has been done on models for the deposition of amorphous carbon tips by Silvis-Cividjian [100]. However, the study presented here deals with deposition of organometals, and there is very little available knowledge on:

- The radiation induced chemistry of the metal containing precursor gas. A wealth of reactions are possible, but limited data is available for the conditions and substances used for EBD.

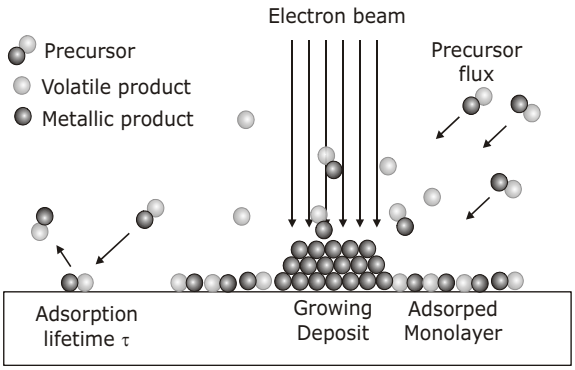

Figure 4.4: The surface ad- and desorption processes during EBD used in the rate equation model.

- The chemical content of the produced amorphous carbon in the deposit. We were not able to perform successful Raman spectroscopy on the sub-micron sized deposits.
- The current density in the ESEM electron beam.

Not knowing the chemical details of the deposition process, the exact product of the deposition, or the electron beam, it is not possible to do a detailed Monte Carlo modelling of the process. A simple model is reviewed below to provide an understanding of the basic requirements and limitations for the EBD process.

4.2.1 Rate Equation Model

Electron beam deposition of planar layers on surfaces can be reasonably described by a simple rate equation model [109]. The model shows the fundamental limitations for growth rate and its dependence on beam current and precursor gas flow. The model calculations and most experiments in this thesis, are based on the precursor gas dimethyl gold acetylacetonate, here abbreviated to DGAA. The vapor pressure of the precursor gas determines the flux of precursor molecules to the surface. The flux rate of molecules F [$\mathrm{m^{-2}s^{-1}}$] of an ideal gas at rest is

$$F = \frac{P}{\sqrt{2\pi m k_B T}}, \tag{4.1}$$

with pressure P, atomic weight m, Boltzmans constant k_B and temperature T. For DGAA which has a vapor pressure of 1.3 Pa at 25 °C, this gives a flux rate $F = 10^{18}$ $\mathrm{cm^{-2}s^{-1}}$

The cross-sections for electron beam induced ionization and dissociation of the precursor gas to form the deposits are generally not known. Cross-sections are usually of the order $\mathrm{Å}^2$ and peak at low energies, corresponding the low energy of the

secondary electrons which are probably the main cause of the deposition. The adsorption of molecules on the target surface and highest density of SE near the surface make it reasonable to assume that the deposition rate dN_{dep}/dt depends on the surface density of adsorbed precursor molecules N_{pre}, the beam current density J, and the effective cross section σ_0 as

$$\frac{dN_{dep}}{dt} = N_{pre}\sigma_0\frac{J}{q_e} \tag{4.2}$$

The surface density N_{pre} of the adsorbed precursor molecules in Eq. (4.2) is the source for the deposited material and depends on both the deposition, ad- and desorption processes as sketched in fig. 4.4. With maximum surface density N_0 (e.g. one monolayer[3]), adsorption probability a and lifetime τ (s), a rate equation can be written for the precursor surface density as [109]

$$\frac{dN_{pre}}{dt} = aF(1 - \frac{N_{pre}}{N_0}) - \frac{N_{pre}}{\tau} - \frac{N_{pre}}{q_e}\sigma_0 J \tag{4.3}$$

The steady state adsorbate density, $\overline{N_{pre}}$, is then

$$\overline{N_{pre}} = \frac{aF}{\frac{aF}{N_0} + \frac{1}{\tau} + \sigma_0\frac{J}{q_e}} \tag{4.4}$$

If each deposition event on average results in a cubic unit cell of deposited material with volume V, the vertical growth rate R [nm/s] is

$$R = V\sigma_0\frac{J}{q_e}\overline{N_{pre}} \tag{4.5}$$

$$= V\frac{aF}{q_e\frac{\tau aF/N_0+1}{\sigma_0 J\tau} + 1} \tag{4.6}$$

The dependence on precursor flux falls into two cases:

1. $\tau aF > N_0$ when a monolayer is always present and increasing the flux rate F has little effect on the growth rate R, since the surface is saturated

2. $\tau aF < N_0$ when less than a monolayer is present, and increasing F will increase the growth rate R.

Increasing the electron beam current will in this model always increase the deposition rate. The rate increases relatively linearly with the electron flux, until it begins to saturate when the source gas flux becomes the limiting factor for the growth rate.

[3]Generally, more than one monolayer cannot be expected unless the target is cooled compared to the source, to give condensation of the source gas.

Scheuer et al. [109] have measured the EBD deposition cross section of $Ru_3(CO)_{12}$ to be of the order $\sigma_0 = 0.2$ Å^2 and $\tau = 1$ s. Using these values, a rough estimate of the growth rate can be calculated. For the estimate, we assume a monolayer is present ($\tau aF = N_0$); a sticking efficiency of $a = 100\%$; the vapor pressure flux of DGAA; an electron beam diameter of 20 nm, which is comparable to the minimum observable resolution in the ESEM; a total beam current of 0.2 nA, which was the standard setting for most ESEM experiments; and finally that the unit cell volume V for deposition is that of gold. With this set of values, the deposition rate becomes $R = 100$ nm/s. The used values make $\sigma_0 \frac{J}{q_e} \gg \tau aF/N_0$ so the deposition is not limited by the electron beam current but by the gas flux which would have to be 10 times higher to reach saturation. The beam radius will have to be increased to $r = 0.5$ μm to reach the electron flux limited region and this radius is much larger than the observed resolution in all presented experiments. Its is important to secure as high as possible flux of precursor gas in the experiments, since this is the main limiting factor in the model whereas the focus of the electron beam is expected to be less important due to the high current density.

4.2.2 Limitations to the model

The rate model is suited for describing deposition of planar layers, but for the case of deposition of tip structures in a real system, several other effects influence the deposition rate:

Scattering of primary electrons in the deposited structure. BSE and SE are emitted through the sidewalls and apex of the structure in a non-uniform way, and the PE/BSE scattering make SE generation take place in a larger region than the PE beam radius, which considerably limits the minimal radius for tip structures. Figure 2.2 illustrate these effects. Simulations are needed to make proper estimates of the influence of scattering, but qualitatively it should cause a lower vertical growth rate as less electrons must be expected to emerge through the upper surface of the structure.

The PE beam is not uniform as considered in the model. A Gaussian distribution of the PE beam can be expected, and for ESEM, the scattering of the electron beam in the environmental gas creates an low current density "electron skirt" around the PE beam. This should be considered both for the possible contamination in the larger region irradiated with low current density, but also for reducing the current in the primary beam and thus the growth rate.

It was assumed that the source supply precursor gas with the vapor pressure gas flux rate. The rate could be considerably lower if the source material does not have enough surface area to sustain the gas flow or the distance to the source is too large. The fact that many organometallic compounds, including DGAA, decompose in contact with water could also reduce the source gas flow.

Not all irradiation induced events will result in deposition of material.

Substantial amounts of material could be volatile or negatively ionized and carried away in the ESEM environment. Electron attachment is taking place in the ESEM and is known to influence the detection of secondary electrons [71]. This could reduce the supply of precursor gas and hence the deposition rate.

Surface diffusion of the precursor gas will influence the supply rate. When depositing in only a small area, surface diffusion of adsorbed molecules from the surrounding area can considerably increase the supply of precursor molecules. This is usually the explanation given why many EBD experiments observe that the tip deposition is faster in the beginning; for then to decrease to a steady state growth rate, when a tip structure is formed which limits the supply by surface diffusion. This could increase the rate at the very beginning of the deposition.

The predicted vertical growth rate from the model must be an upper estimate on the achievable rate, since beam scattering in the gas and tip structure and limitations to the gas flux rate in the ESEM is expected to reduce the steady state growth rate.

4.2.3 Summary

Little data is available on the precursor gasses for EBD especially for electron irradiation in an ESEM environment. A simple rate equation model gives an estimated deposition vertical growth rate of 100 nm/s for the precursor gas DGAA. This estimated growth rate is expected to be an upper limit. Especially the flow rate of precursor gas should be as high as possible in the experiment since this is the limiting factor for the deposition rate.

4.3 Experimental Setup

The deposition setup was installed in a Philips XL30 ESEM equipped with a field emission electron gun. The ESEM makes it possible to use various gasses in the sample chamber of the microscope since the apertures between the sample chamber and the gun column are connected to a differential pumping system. Pressures up to 10 Torr are possible in the sample chamber. The standard Everly-Thornhart detector would not work under such conditions since it would create a discharge in the low pressure gas. Instead a "*gaseous secondary electron detector*" is used, as shown in fig. 4.5, which measures the current of a weak cascade discharge in the gas, which is seeded by the emission of electrons from the sample. Without precursor gas present in the chamber, the deposition rate was negligible in the high vacuum mode as well as in the gas mode of the ESEM. All experiments were performed at room temperature. The TEM analysis of the deposited tips was made together with A. Carlsson using a Philips CM200 FEG UltraTwin at Haldor Topsøe A/S.

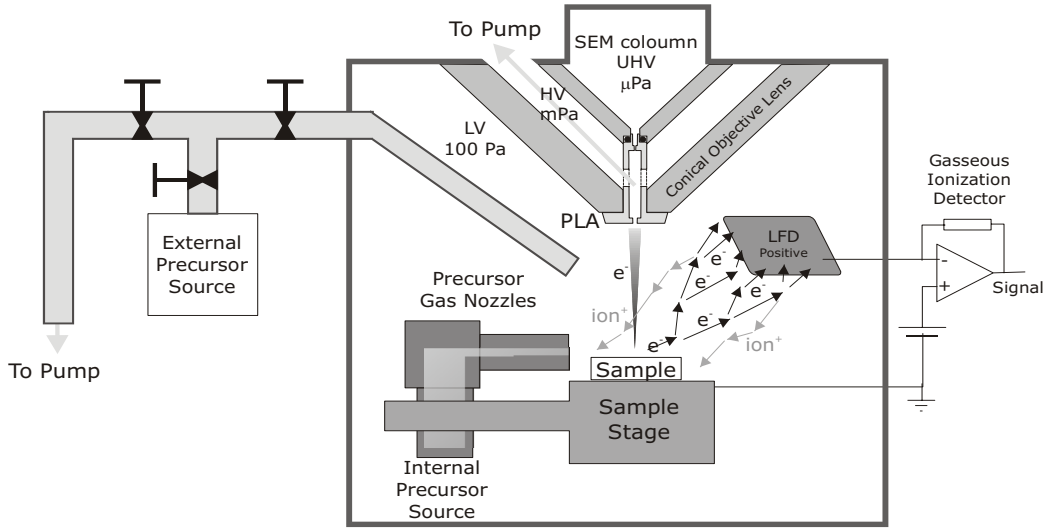

Figure 4.5: Schematic view of the ESEM deposition setup. Ultra high vacuum (UHV) is maintained in the column to protect the field emission gun by two pressure limiting apertures (PLA) separated by a differential pumping system. The sample chamber can be at pressures in the mPa-hPa range (<10 Torr). The differential pumping system also protects the UHV region from the precursor gas for the EBD experiments. In environmental mode, the gasseous ionization detector is used, which measures the current in a weak cascade discharge to the positiviely charged large field detector (LFD). The discharge creates a low density current of positive ions from the detector. Both precursor sources placed inside and outside the chamber were tested in the experiments. The external source could be turned off by a valve and evacuated by a pump when changing the source material.

4.3.1 The ESEM source system

Our choice of precursor gas was guided by the work of Folch et al. [107], who used Dimethyl-gold-hexafluoro-acetylacetonate (a liquid with a vapor pressure of 100 Pa). To avoid handling high vapor pressure liquid organometals, we preferred to use the compound Dimethyl-gold-acetylacetonate (DGAA[4]) . DGAA is a white powder with a vapor pressure of 1.3 Pa (0.01 Torr) at 25 °C. It sublimates at $25°C$ [110].

For the majority of the deposition experiments, the in-situ source system shown in Fig. 4.5 was used. The precursor flux is directed towards the deposition target by a nozzle ending about 1 mm from the deposition target. The DGAA was placed in a small aluminum cylinder screwed onto the nozzle (10 mm long, 1 mm diameter bore). By neglecting the limitations by the gas flow conductance of the nozzle and the diffusive flow through the ESEM gas we can set an upper limit on the mass loss rate from the source by the vapor pressure flux rate, giving $\Delta m/\Delta t = 4$ μg/s. With this loss rate, the source containing about 50 mg DGAA should last about 3 hours. This is comparable to the lifetime we observe in our experiments, which is of the order

[4] $(CH_3)_2Au(C_5H_7O_2)$; CAS number 14951-50-9.

5-10 hours. It is our impression that freshly crushed DGAA crystals decompose on the surface and the outgassing rate is reduced over the source life time, since plenty of DGAA appears to be left in the source when the deposition rate becomes low. Freshly crushed crystals were always used when starting an ESEM session. Each data series presented in this thesis is based on data from within one single session. Since the source gas pressure wasn't measured, it has not been attempted to study the effect of varying the source gas flow rate.

Apart from the directed flow from the source nozzle, the deposition process will also have a contribution from the DGAA supplied by the sample chamber background gas. A 1 m^2 gold monolayer weighs only 4 mg, which is a fraction of the material contained in the source chamber. The SEM chamber must be expected to be covered in a monolayer of DGAA in a few minutes. Since it takes $20 - 30$ min to flush the chamber for background gas and do the initial focusing to prepare for experiments, an equilibrium background pressure of DGAA must be present during experiments. The actual vapor pressure at the beam target in the chamber will depend on the distance to the source nozzle, whether flow is ballistic or diffusive, as well as the background DGAA pressure in the chamber. The highest deposition rates were observed within 1 mm from the source nozzle. Several centimeters away from the nozzle and behind the nozzle, tips could also be deposited, but at lower growth rates. This indicates that both direct flow from the nozzle and the chamber pressure of DGAA contributed to deposition.

At the end of the project an external source system shown in Fig. 4.5 was tested. The external source was connected to the chamber through steel tubes and directed towards the sample by tubes in-side the chamber. This setup allowed the source to be turned on only when deposition was needed to avoid unnecessary deposition when imaging the sample.

In the ESEM, the environmental gas is typically water vapor or nitrogen. The pressure range is from 0.1 to 10 torr, though the contrast is very poor at the pressure limits and optimal around 0.8 Torr. The optimal setting was used in all measurements, unless pressure changes are specifically stated. For water vapor at the standard pressure of 100 Pa (0.8Torr), the molecular flux is two orders of magnitude higher than the precursor flux calculated above. The water vapor supply should hence be sufficient for water to participate in every irradiation induced reaction of DGAA at all pressures in the environmental mode.

4.3.2 A Simple Electron Beam Lithography System

For deposition of three-dimensional structures a system was needed to controllably scan the electron beam while depositing. Neither the MIC SEM or the ESEM had electron beam lithography equipment or provided external control of the electron beam such as an external electrical connection to the $x - y$ scan coils. In the ESEM the software for X-ray analysis allowed a certain degree of control over slow line

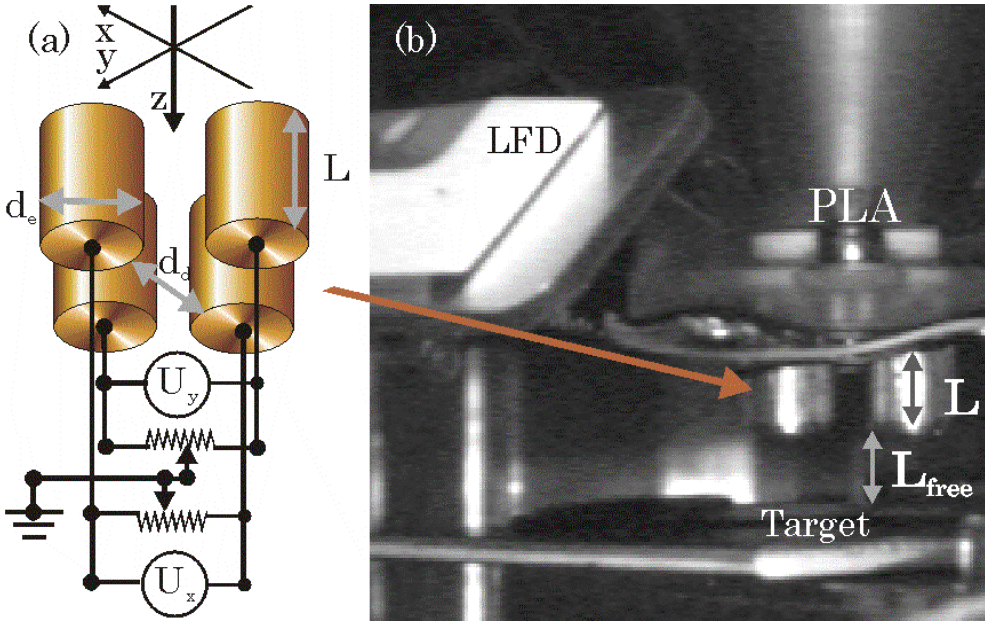

Figure 4.6: The EBL system made from four cylindrical parallel rods. a) the system geometry. b) Image of the system inserted into the ESEM chamber, where it is clipped onto the pressure limiting aperure (PLA). In the foreground, the Large field detector (LFD) plate is visible (see Fig. 4.5)

scans, but not with the precision required for creating reproducible complex three-dimensional nanostructures, such as free standing tips on microgrippers. To have full control over the beam in the microscopes an expensive add-on EBL system could have been acquired. Instead, I developed a simple electrostatic quadrupole scan system that amply suited our requirements. The EBL system is presented in the included article "A Simple Electron Beam Lithography System" [2]. The following is a brief review of the system.

The system should able to scan in two directions to allow three-dimensional structures to be deposited and the scan range should be of the order 10-100 μm to make the system suitable for creating nanostructures contacting micrometer sized electrodes. The scan speed should be comparable to the growth rate (1-100 nm/s), which is low compared to standard EBL systems. Finally, it had to be portable and easy to install and remove, since the setup cannot be mounted permanently in the microscopes.

The developed system is a general-purpose portable electron beam lithography system consisting of an electrostatic deflector plate system mounted where the electron beam exits the column and enters the specimen chamber, see Fig. 4.6. For the ESEM, the system is designed to be mounted onto the pressure limiting aperture in a few minutes. With bias voltages applied to the electrodes directly from a standard two-channel DAQ card in a portable computer, the system can deflect the beam in two directions with nanometer precision. To achieve a high resolution, the aber-

rations and astigmatism induced by the deflection system should be minimized. A highly linear electrical field was achieved by using a deflector geometry adapted from the linear Paul trap or quadupole mass spectrometer with four parallel cylindrical electrodes equally spaced around the electron beam [111]. If a voltage $\pm\frac{1}{2}U$ is applied to two diagonally opposed rods with diagonal distance d_d, while the other two are kept at ground potential, the electrical field at the center is constant $E = U/d_d$. The deflecting force on an electron $F = q_e U/d_d$, is acting over the length of the electrodes l over a time $T = l/v$ for the beam with kinetic energy $E_b = \frac{1}{2}m_e v^2$.The deflection D of the beam at the end of the plates D is

$$D = = \frac{1}{2}\frac{F}{m_e}T^2 \tag{4.7}$$

$$= \frac{1}{4}\frac{q_e U}{E_b}\frac{l^2}{d_d}. \tag{4.8}$$

If we use typical values such as $d_d = 5$ mm, $K = 5$ keV, $U = 50$ V, $l = 5$ mm, we find $D = 12$ μm, which is in accordance with the range we would like to achieve. After passing the deflection system, the transverse velocity of the beam dD/dt will increase the deflected distance if the target is at a distance l_+ below the lower edge of the deflection system. The total deflection of the beam becomes

$$D_{total} = \alpha\frac{qUl}{2E_b d_d}\left(\frac{1}{2}l + l_+\right) \tag{4.9}$$

$$= C\frac{U}{V}, \tag{4.10}$$

where α is a first order correction coefficient to account for edge effects due to the finite length of the rods. The correction coefficient α is expected to be about 1. If needed, α and higher order corrections can be found by finite element simulations of the electrical field in the device. The deflection distance D is proportional to the ratio of deflection to acceleration voltage, U/V, with C denoting the proportionality constant.

The system performed as expected from Eq. (4.9) with linear deflection due to the applied voltage. If a conservative limit of 10 nm is chosen for the acceptable increase of the beam diameter due to the system induced aberrations, the achievable scan range is about 50 μm for the tested system. Commercial systems can typically scan a larger range, but the range and precision achieved by the present system is more than sufficient for the present experiments. Given the low cost and the fact that the scan range needed for many research EBL and EBD applications are of the order some micrometers (typically to make contacts to larger structures defined by optical lithography), the present system could probably be used for many of such applications.

4.3.3 Summary

Dimethyl-gold-acetylacetonate (DGAA) was chosen as the precursor gas. Both an internal and an external source system were developed during the project. The external source system was capable of turning the source off when deposition was not needed, and this was used to decrease unwanted deposition when imaging the sample. However, the simpler internal source system was used for most of the EEBD experiments. A simple low cost electron beam lithography system was developed and used to control the electron beam during deposition of three-dimensional structures.

4.4 Solid Gold Structures Created by EEBD

A TEM study was done on the internal structure of the deposited tips, showing a layered shell structure with different material composition. The results were presented in the included article [4] and the following is a brief review of those results.

4.4.1 Deposition Rate

From the rate equation model (Sect. 5.4.4), we should expect a constant growth rate of the tip structure with rates up to 0.1 μm/s, and possibly an increased growth rate at the beginning of the deposition due to surface diffusion. Figure 4.7 shows the resulting height of tips as function of time. The tip height grew with a constant rate of about 1-1.5 μm/min or about 15-20 nm/s, which is comparable to EBD growth rates reported in literature [105][112], but a factor of 10 below the estimated upper limit (Sect. 5.4.4). The considerably lower value was expected considering the many limitations to the model that made it overestimate the rate. The scattering of the measurements is too large to make any firm conclusion on whether the initial rate decreases with time as surface diffusion to the tip apex becomes limited[5].

4.4.2 The Shell Structure

After the first deposition experiments in the ESEM, it was apparent from TEM analysis that the deposited tips had an internal shell-like structure, which to our knowledge had not previously been observed in EBD tips[6]. The shell structure in the deposited tips consisted of different material layers each characterized by a certain range of gold/carbon content ratio. Above a certain threshold water vapor pressure

[5] Surface diffusion could be reduced in the ESEM compared to SEM, because the beam skirt irradiates the surroundings and decompose the precursor before substantial amount can diffuse towards the main beam region. Pre-scanning of a region is one of the techniques commonly used in SEM to reduce contamination by surface diffusion [94].

[6] Folch et al. [107] who first studied EEBD used Auger electron analysis, which only probes the outermost atomic layers within the SE escape depth and hence cannot detect the shell structure.

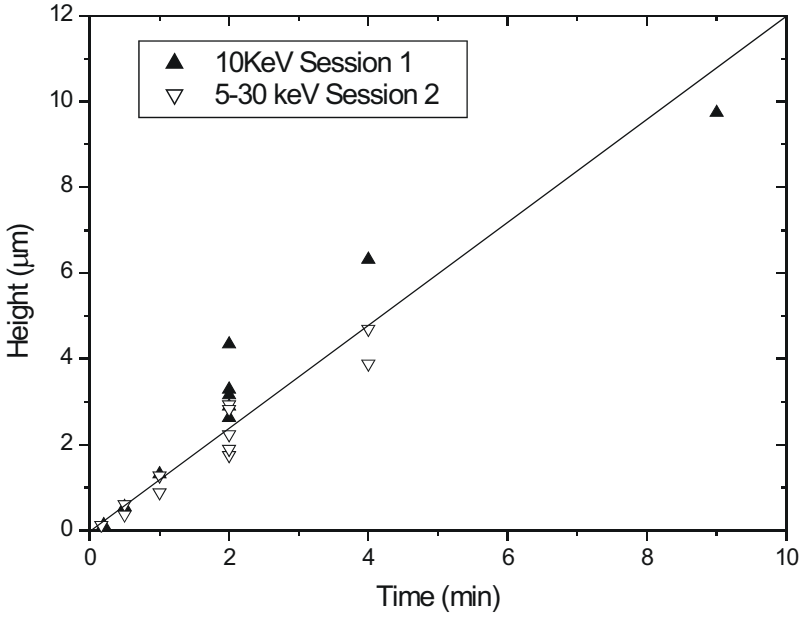

Figure 4.7: The tip height as function of deposition time. The curve is almost linear, and reasonably reproducible from session to session, compared to the variation within one session. Energies between 5 and 30 keV were used in session 2 without showing any clear dependence of the rate on energy.

and a certain threshold of electron beam current, the deposited tips contained a solid polycrystalline gold core. The results are described in detail in the included paper [4] "Solid Gold Nanostructures Fabricated by Electron Beam Deposition". This section will briefly review the main results.

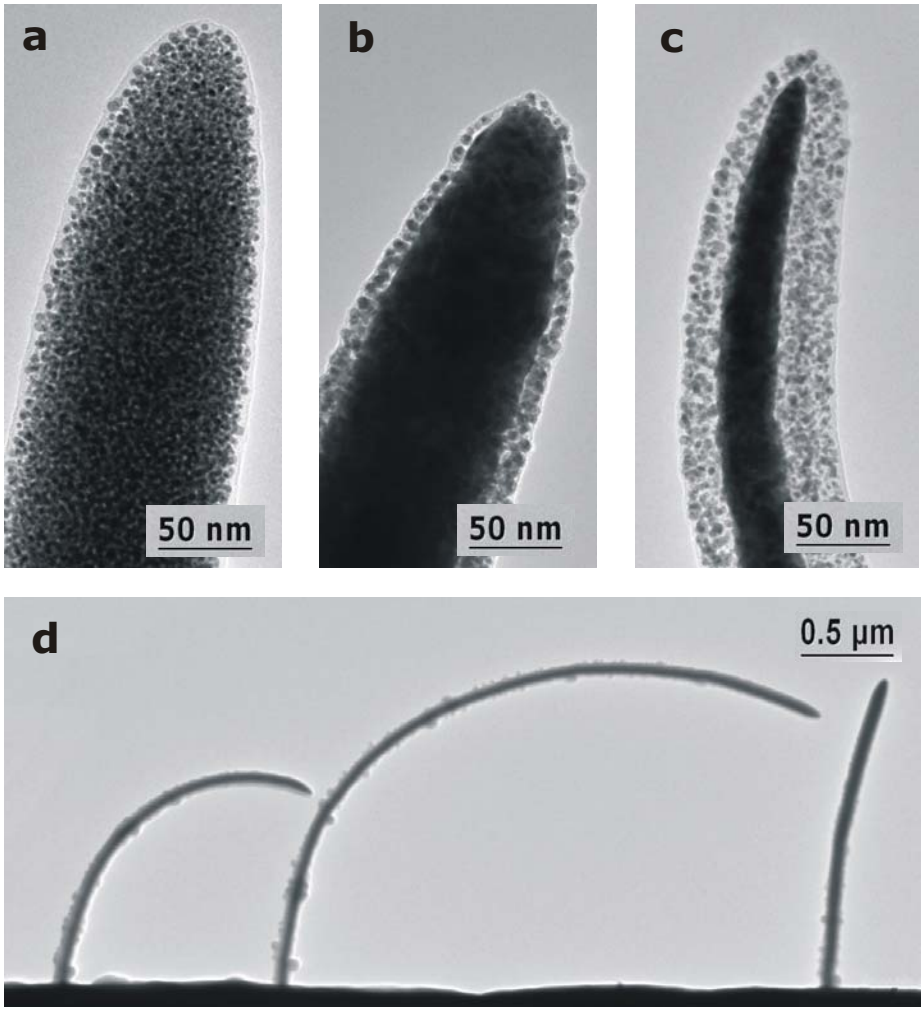

Figure 4.8: TEM images illustrating how the morphology of EEBD tips using DGAA as precursor depends on the deposition conditions. (a) Apart from water vapor, all other tested environmental gasses (N_2; O_2/Ar; H_2/He) resulted in tips containing gold particles embedded in an amorphous carbon containing matrix. (b) When using water vapor as environmental gas, a dense gold core becomes increasingly pronounced as the vapor pressure and beam current is increased. In (b), the beam current is 0.2 nA, and in (c) 0.02 nA. (c) A contamination layer almost void of gold can be deposited on the tip by scanning the beam while imaging. So-called proximity contamination can also occur if depositions are done later within a range of a few μm from the tip. The contamination layer is thicker on the side facing later depositions. (d) Electron irradiation in SEM or TEM causes the contaminated tips to bend irreversibly towards the side with the thickest contamination layer. The tips were deposited from left to right and thus bent towards the last deposition.

Three distinct types of layers have been identified: a core, a crust, and a carbonaceous contamination layer. Fig 4.8 show the apices of three tips with different morphologies, all were deposited by a 10 keV beam. All tips deposited in N_2, in $60\%He/40\%H_2$, and in $80\%Ar/20\%O_2$, consisted of 3-5 nm gold nanocrystals embedded in an amorphous carbon matrix; This composite structure is similar to what is observed in EBD tips in SEM [112]. When water was used as the environmental gas, the tips contained a central core of dense gold surrounded by a crust with material similar to that of the tip shown in Figure 4.8a. Sometimes an outermost layer with very low gold content was observed. Such low gold content contamination layers seemed to be caused by later contamination of the deposited tip. Contamination occurs on tips that have been imaged intensively while the source was present. Another source of contamination is what we term "proximity contamination", which occurs if a later deposition was made in vicinity of the tip. Proximity deposition has also been observed in EBD by Utke et al. [113]. Such nearby depositions seem to coat the tip in an asymmetric contamination layer, as shown in Fig. 4.8c, thickest to the side facing the later deposition. If tips with asymmetric contamination layers are irradiated by electrons in SEM or TEM, the layer make the tip bend irreversibly to the side with the thickest layer, as shown in Fig. 4.8d.

EDX spectra and the observed crystal lattice spacings of the nanocrystals confirm that the material in the tips is carbon and gold. The deposits with $60\%He/40\%H_2$ and $80\%Ar/20\%O_2$ environmental gas were made so the atomic density of oxygen or hydrogen was as high as under the depositions using water where a gold core were observed. That no core was observed when using the other gasses strongly indicates that water is essential for the formation of the core.

The structure of the crust material is comparable to what would be expected if DGAA is decomposed to an amorphous carbon matrix containing gold nanocrystals. If such crystals have a diameter of 3 nm as in the crust material, the gold spheres must be spaced by 1 nm to give the C:Au ratio of DGAA. The exact composition of the amorphous carbon matrix cannot be predicted since we do not know the amount of H or O included in the amorphous carbon, or to what extent it is polymerized, graphitic (sp^2 bonds), or diamond-like-carbon (sp^3 bonds).

The underlying processes causing the creation of the core is not well understood. Both water and irradiation have been reported to influence the diffusivity of gold, but under conditions not well comparable to the present EBD process [114][115]. In the gold cores, crystalline domains can often be found over areas much larger than the typical diameter of nanocrystals in the crust, and sometimes even comparable to the core diameter. An example of such a large crystal domain is shown in Fig. 4.9. Both the large crystal domains and the high mass thickness that blocks the TEM beam in the core, indicate that the core consists of polycrystalline solid gold. This conclusion is also supported by the high conductance of EEBD structures with gold core, which is described later in Sect 4.5.2.

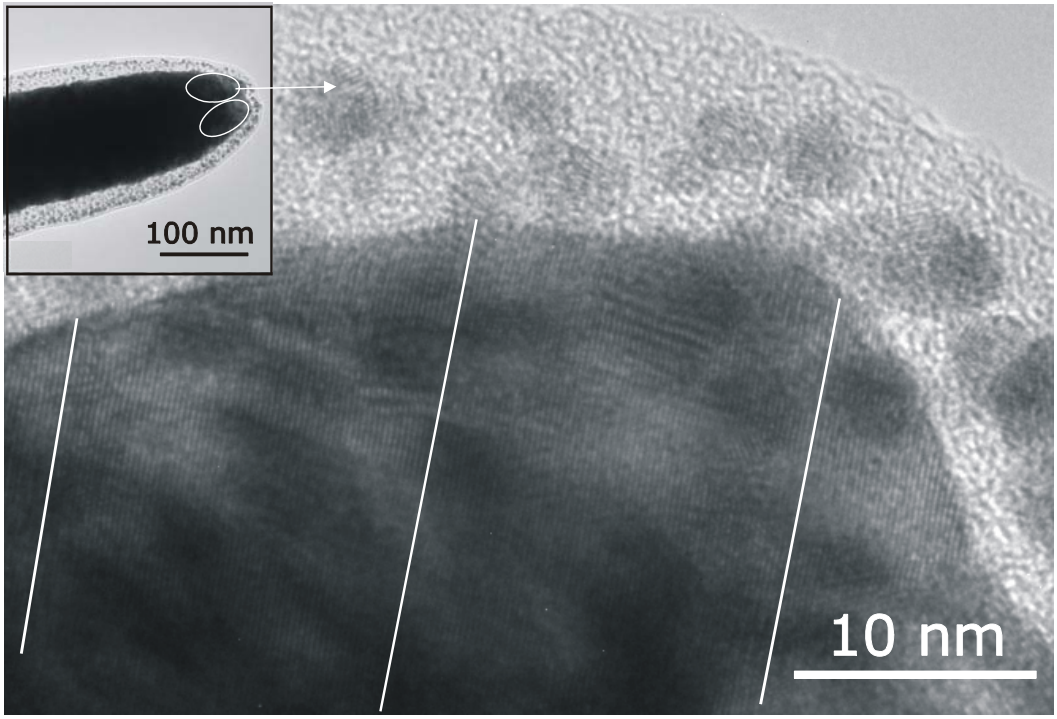

Figure 4.9: Large monocrystalline domains are observed within the gold core. The inset shows a TEM image of a tip apex, which is divided into two large crystal domains as indicated by the encircled regions. The upper region is shown in the main HRTEM image, with the crystal plane orientation along the white lines. Often crystalline domains with dimensions comparable to the core diameter are observed.

The results indicate that high current densities and water vapor are required to create the gold core. The dependence of the core diameter on the beam current and water vapor pressure was studied. The results are shown in Fig. 4.10. All measurements are relying on the experimenter's ability to focus the beam optimally and this will influence the measurements, especially due to low image contrast when the parameters are far from the optimal conditions 0.2 nA and 0.8.Torr water vapor pressure.

At low and high beam currents the image contrast was low which made it difficult to achieve optimal focusing. Poor focus might be the cause of the short tips with a wide crust radius at highest and lowest beam currents. The diameter of the gold core on the other hand seems to be proportional to the square root of the beam current, indicated by the thin line in Fig 4.10c. Since the beam diameter also scales with the square root of the beam current in Eq. 2.7, this could indicate that the beam diameter could have a direct influence on the creation of the core. According to FEI/Philips [46], the ESEM operated in high vacuum mode should have beam diameters two orders of magnitude smaller than the observed core diameters, but

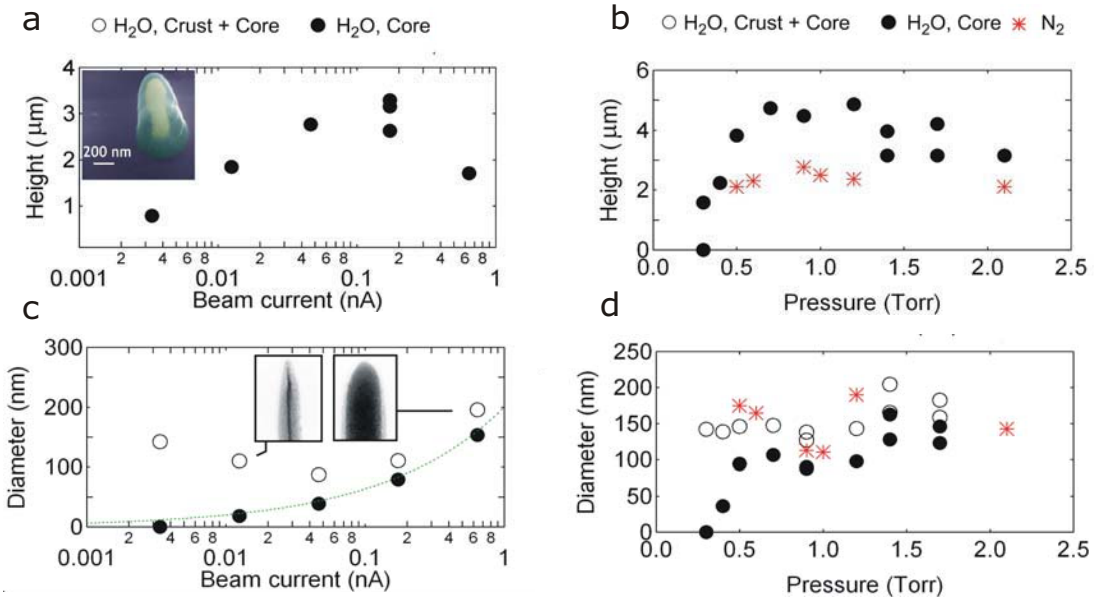

Figure 4.10: The tip height and width as function of beam current and environmental gas pressure. Tip height vs beam current (a) and pressure (b). Outer crust diameter and core diameter as function of beam current (c) and pressure (d).

follow Eq. 2.7. Whether the environmental gas could make the beam diameter scale similarly with current is not known, and the present results are probably be highly dependent on the operators ability to focus properly.

At low currents with core diameters about 20 nm, the core does not consist of a continuous solid material, but rather a region with a higher density of gold nanocrystals. Qualitatively, the data indicate that a minimum beam current density is required to create the solid gold core, while measurements of the beam diameter are needed to clarify the reason for the empirical square root relation for the core diameter dependence on beam current.

The tip structure also depends on the water vapor pressure. Below 0.5 Torr, the core diameter was observed to rapidly decrease. This could in principle be caused by the lower contrast at low pressures, which made focussing difficult. However, the tip crust diameter seems relatively constant, indicating that beam broadening probably isn't pronounced and the water vapor pressure is an controlling factor for the formation of the gold core. Direct measurements of the beam diameter would be relevant to do in a future study to be able to identify the mechanisms behind the apparent correspondence to Eq. 2.7 for the dependence on beam current, and the threshold for core formation at 0.5 Torr water vapor pressure.

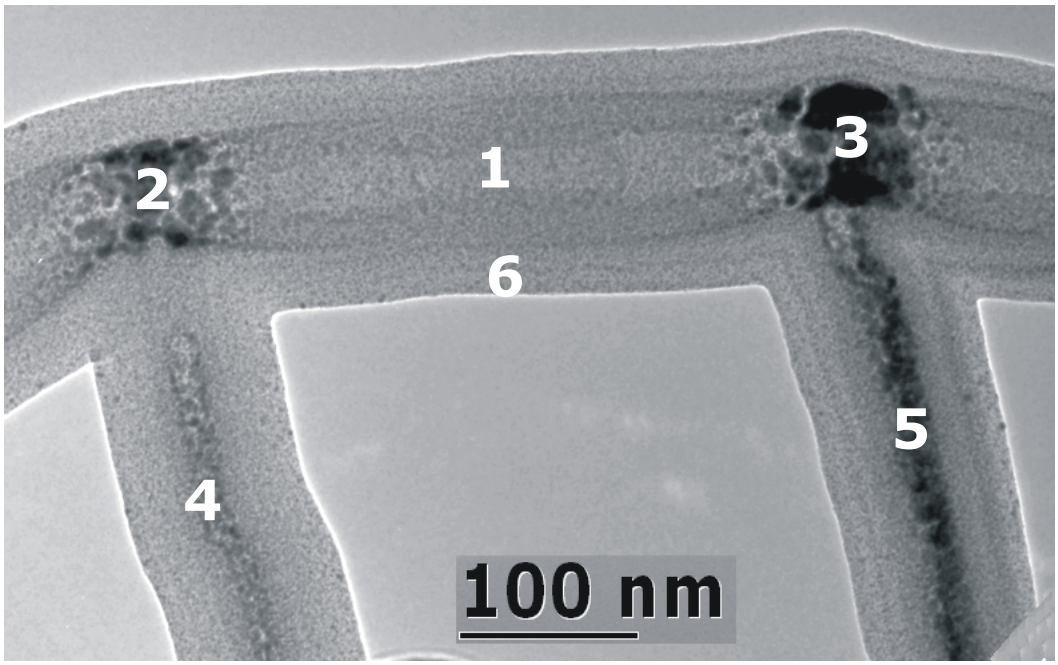

Figure 4.11: TEM image of a MWNT (1) used as starting point (2,3) for two scanned EEBD lines (4,5). The tube is deformed (collapsed or contracted) at the starting point where a thick gold layer surrounds the tube. Both tube and deposits are coated in a carbonaceous contamination layer (6).

TEM Study of EEBD Soldered Carbon Nanotubes

The gold core in the deposit makes the EEBD method interesting for applications such as soldering nanocomponents together. To investigate the structure of such a soldering joint, the beam was scanned across a MWNT on a TEM grid. A TEM image of the resulting structure is shown in Fig. 4.11.

The EEBD wire appears to contain a gold core and to be firmly attached to the MWNT, which was noticeably deformed at the joint. Both the MWNT and the gold wire were covered by a low gold-content contamination layer that probably was caused by both ESEM imaging at high magnification and proximity contamination from the deposition of the lines. The EBD process could be called a nano-soldering technique rather than welding since the soldered components do not coalesce as in welding, but the EEBD soldering can strongly deform the soldered MWNT as seen in Fig. 4.11.

4.4.3 Summary

When water is used as environmental gas it was observed to be possible to deposit structures with solid polycrystalline gold cores. The formation of a gold core depends on the ESEM deposition parameters. The current series indicate that a minimum current density is required to form the gold core and narrow cores are formed at low beam currents. Gold cores have been observed with diameters from about 10 to 150 nm (Fig. 4.10c). When the cores are thinner than about 20 nm they appear as regions with a high density of crystallites rather than solid cores. A minimum water vapor pressures of about 0.5 Torr is required to form the core as well. When used MWNT as a soldering method, TEM images of the deposits show gold cores in close contact to the tubes, and the tubes being both deformed and contaminated by the process.

4.5 Feasibility Study of EEBD

It is possible to deposit well controlled three-dimensional EBD structures by scanning the beam slowly. Slow scan speeds result in almost vertical depositions, while high speeds makes horizontal deposits. The variable deposition rate and manual scans in the Lund SEM made it difficult to realize precise three-dimensional structures by this method in that instrument. As shown previously in Fig. 4.2, when depositing nanotweezers in the SEM at Lund University, well defined structures could be made by using a fixed electron beam position and rotate the sample to get the desired angle of the deposit, but that is a very time consuming method.

With the reasonably reproducible EEBD deposition rate, it was tested whether tweezers tips by using the line scan function in the ESEM software. Figure 4.12a show an example of such a structure. The software did not allow to set any specific scan rate and scan time, and this made it very difficult to achieve aligned tips, but the process was considerably faster than using the cumbersome rotation of the device used to make the tips in fig. 4.2. Several structures comparable to the example in Fig. 4.12a could be made in one hour. But apart from the limited precision of the scan, additional unwanted deposits occurred, such as the deposits under the main tips in Fig 4.12a. We then tested the EBL system described in section 4.3.2 and found it capable of creating elaborate structures with well defined scan rates. An example of a cork screw structure is shown in 4.12b and c.

With the EBL system we made an investigation of he feasibility of the gold core deposition for research applications and the results are presented in the included paper [3] "Constructing, contacting and connecting nanostructures by Environmental Electron Beam Deposition" and included paper [5] "Soldering of nanotubes on microelectrodes". The following is a brief review of the main results.

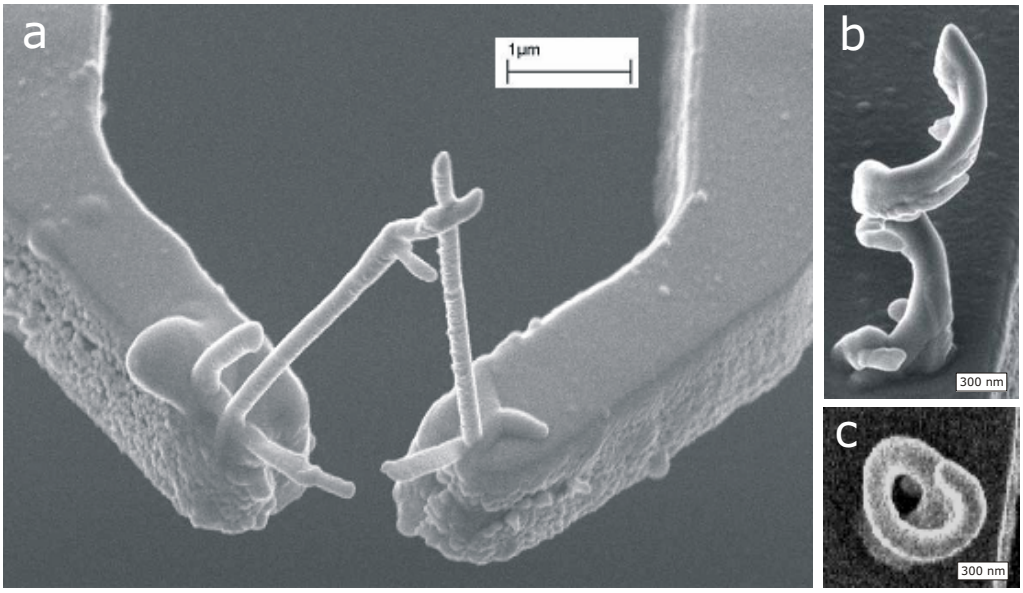

Figure 4.12: Three-dimensional structure created by slowly scanning the electron beam during deposition. (a) Nanotweezer structure made by linear scans using the ESEM EDX system. The EDX system make it difficult to determine the scanned distance and hence the tip height. An additional deposition was attempted to reach equal height of the two arms. Branching of the deposits is seen at each starting point for depositions. Side view (b) and top view (c) of corkscrew structure deposited using the EBL system (Sect. 4.3.2). At high scan rates, the x-y beam scan resulted in circular two-dimensional structures, and the three-dimensional structure is likely deformed by contamination bending.

4.5.1 Additional Depositions

As mentioned above, a contamination layer can be deposited on existing structures by imaging or by proximity contamination from nearby depositions. Sometimes the deposited structure itself also have unwanted additional structures growing out from it or parallel to it, such as the small tips below the main nanotweezers structure in Fig 4.12a. We term these effects *additional depositions* and a summary of these are given in Fig 4.13.

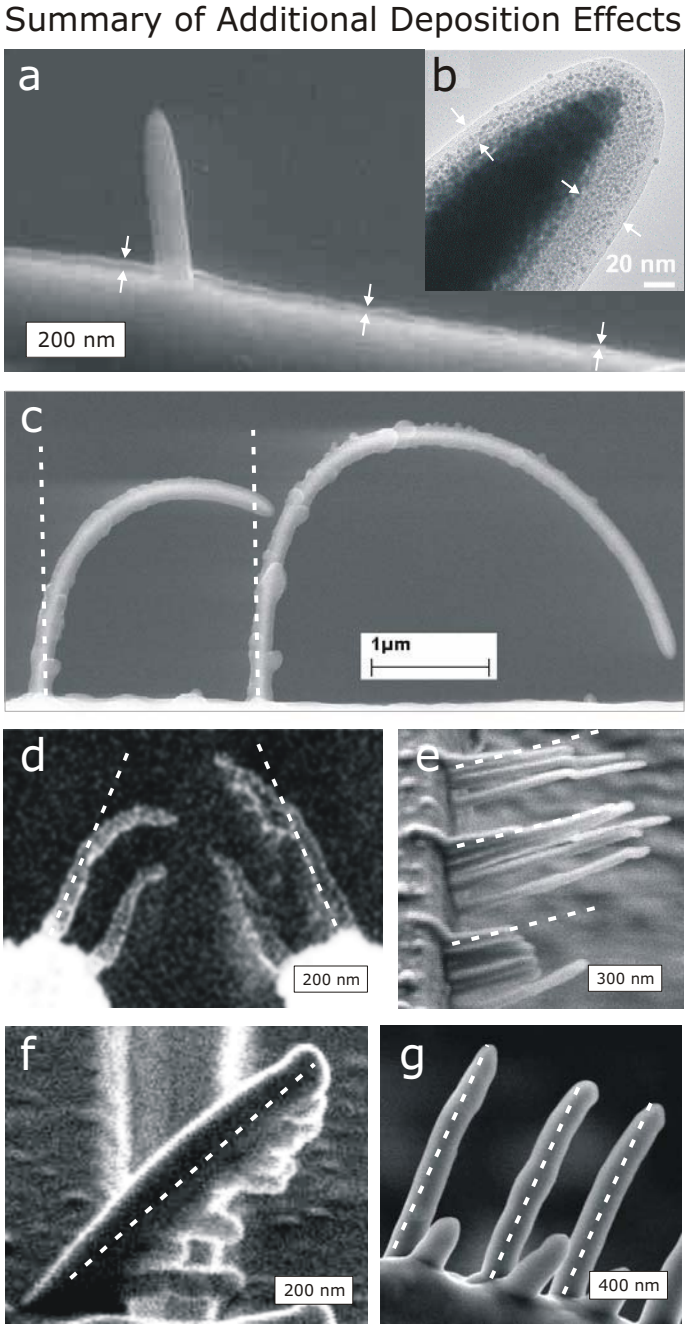

Dotted lines indicate the intended structures.

a) SEM image showing an EEBD proximity contamination layer on the substrate. The layer is thicker close to the tip deposition site, as indicated by the arrows.

b) TEM image of a typical asymmetrical proximity contamination layer with low gold content.

c) Contamination layer bending. Electron irradiation make the tips bend to the side with the thickest layer during SEM investigation.

d) Parallel growth of EBD tips. Made by background gas EBD in Lund. Below the intended line deposition, additional lines can be deposited.

e) Parallel lines made by EEBD.

f) Branching of the main EEBD deposit. The branches grow out at lower angles than the main structure.

g) Branching during EEBD. This deposition was made using $Mo(CO)_6$ as precursor.

Figure 4.13: Summary of the typical additional depositions observed in three-dimensional structures made by EBD and EEBD. The intended structures are indicated by dashed lines.

We have observed the additional depositions in both ESEM and SEM deposits and found that they can be divided into sub-categories: contamination layers (Fig 4.13a,b), contamination layer bending (Fig 4.13c), parallel growth (Fig 4.13d,e), and branching (Fig 4.13f,g). The additional depositions can often be damaging to the functionality of the intended structures, contamination layers could cause insulating layers on intended conductive surfaces and branching deposits could short-circuit the intended structures.

In some cases the additional depositions could be used intensionally: contamination bending could be used to deform structures into new shapes. To what extent this process could be controlled reliably is an open question. Ooi et al. [96] have suggested parallel deposits could be used to form parallel structures. Our experiments indicate that the reliability of this method would be questionable, and the process would have to be optimized for such type of deposition (though it is presently not clear what is required for that). Branching can also be seen in some other structures reported in literature [116], but this effect has as the other additional depositions gone largely unnoticed.

How much of the contamination layer is due to later imaging and how much stems from the beam skirt during nearby depositions is not clear in the present data. Imaging with the source gas present does cause a considerable part of the deposition and preliminary experiments using the external source (Fig 4.5) that can be closed when deposition is undesired, show that the thickness of contamination layers can be reduced, thereby also reducing the deformation effect during subsequent imaging.

We have not identified parameters that reliably control the creation of additional deposits, but it is our impression that a high source gas pressure probably tends to favor their creation - a source with controllable source gas pressure is needed should one want to test this. This is in accordance with the observations of branching FIB deposits [117].

4.5.2 Line Depositions

To deposit nanotweezers tips reliably, a study was made of the effect of the beam scan velocity in the deposited structure. As in earlier experiments (Fig 4.7), the vertical growth rate, v_v, was found to be reasonably constant with a value of $v_v = 9 \pm 3$ nm/s for all acceleration voltages and beam scan rates. With a constant vertical growth rate, the angle θ to horizontal of the deposited line is expected to follow

$$\theta = \arctan(v_v / v_s) \tag{4.11}$$

The expected dependence of the angle was found to be in good agreement with the measurements, considering an estimated uncertainty of $\pm 10^\circ$. The angle of the deposits can hence be controlled from vertical to about 10° above horizontal by the scan rate. At scan rates higher than 30 nm/s, the diameters of the deposited lines

was observed to decrease from the base of the tips to the apex. The tip diameter seems to reach a lower limiting value of about 60 nm and when this value is reached deposition seems to stop. The length of deposited three-dimensional structures is therefor quite limited when depositing almost horizontal structures at high scan rates. For comparison, Shimojo et al. [118] observed an 8 nm linewidth at high scan rates in a TEM EBD experiment, and [119] observed at 5 nm line width limit for carbonaceous EBD in a SEM. In future studies, it could be interesting to investigate if the EEBD linewidth could be reduced by using for instance higher electron beam energies.

To test the reliability of the deposition of almost horizontal lines, bridges were deposited to make bridges between microcantilevers 1.5 μm apart. About one third of the bridges made electrical contact between the cantilevers and gold cores were observed in the bridges deposited using water vapor as the environmental gas.

The deposited bridges made it possible to measure if the presence of the gold core had an effect on the electrical properties of the EEBD material. Only one bridge deposited in nitrogen achieved making contact between the cantilevers (200 MΩ detection limit). The nitrogen bridge had a resistivity about 2 MΩ - three orders of magnitude higher than those deposited in water vapor which had resistances of the order of 1 kΩ. The bridges could sustain high powers up to 100 μW and currents up to 0.6 mA The current density in the core reached 10^{12} A/m^2 (assuming the crust is highly resistive as the nitrogen deposited bridge). The lowest resistivity was about an order of magnitude higher than that of bulk gold.

The electrical properties of EEBD bridges with gold cores are comparable to those of gold nanowires on surface investigated by Durkan and Welland [120] and the EBD results achieved by Utke et al. [121]. Such electrical properties make the EEBD gold nanowires comparable to e.g. multiwalled carbon nanotubes [122] and gold wires made by electron beam lithography [120].

4.5.3 EEBD Soldering of Carbon Nanotubes

The highly conductive gold deposition was used to solder MWNT to microcantilever electrodes, as shown in Fig. 4.14. The line width of the gold core in such depositions can be down to 20-30 nm. The resistances across such bridges were usually in the range 10 kΩ and this is what would be expected from the MWNT itself (compare to the electrical measurements on MWNT in chapter 5). The low resistances indicating that EEBD is a potentially useful technique for nanoscale soldering, but was observed to deform and potentially damage the MWNT in Fig 4.11.

To investigate the properties of EEBD soldered MWNT, a bridging MWNT was stretched by deflecting one of the microcantilevers with an etched tungsten tip, while simultaneously measuring the resistance of the device, as shown in Fig 4.15. This measurement enabled a measurement of the piezoresistive strain-induced changes in electrical resistance of the device as well as setting a lower estimate on the solder bond strength.

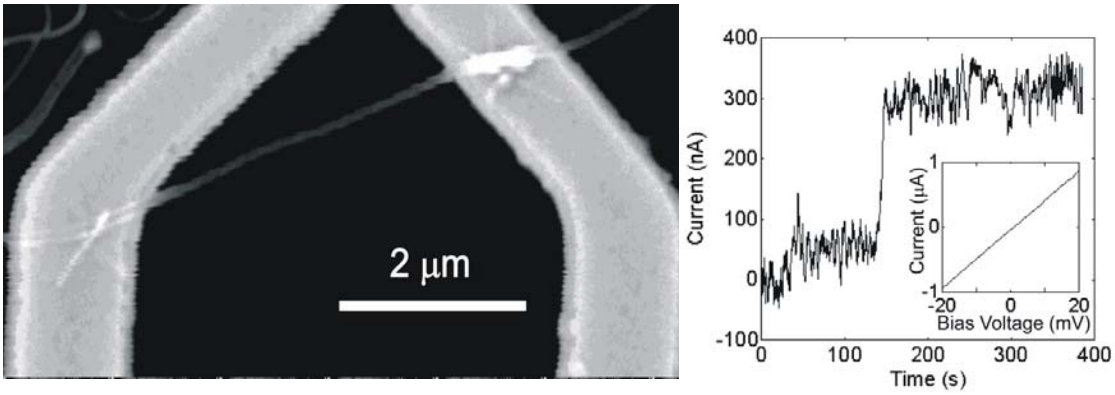

Figure 4.14: Conductivity of an EEBD soldered carbon nanotube. The ESEM image shows a MWCNT soldered to two microcantilevers by two cross-shaped deposits. With a 10mV bias voltage, the current increases in steps as function of time during soldering on each cantilever. As the second soldering bond is completed the current jumps to a stable high value. The inset shows the linear low bias IV characteristic of the device, which has a 20 kΩ resistance. These measurements were done by D.N. Madsen and R. Mateiu.

The deflection of the cantilever pulled by the nanotube can be used to estimate the tensile stress and strain in the tube. The measurement gives an estimate of the Youngs modulus of the nanotube of 30 GPa (based on the total tube cross section). Nanotubes have been measured to have Youngs modulus up to about 1 TPa for defect free arc-grown tubes [52], but measurements have also shown lower Youngs modulus of tubes, comparable to 30 GPa [123].

The strain induced change in conductivity is 1% at 4% strain. Piezoresistive measurements on SWNT have shown much higher piezoresistive sensitivity [124][125], while measurements on carbon fibers seem to give sensitivities comparable to this measurement [126].

The tensile strength of the soldering can be estimated by considering the contact area of the gold core soldering, which is of the order 0.1 μm^2. The observation that the tube only appears to move between the cantilevers and not on their surface indicates that the surface contact area might be larger. With an estimated maximal force of 20 μN, the largest shear force on the soldering joint is about 200 MPa. This is comparable to the yield strength of gold.

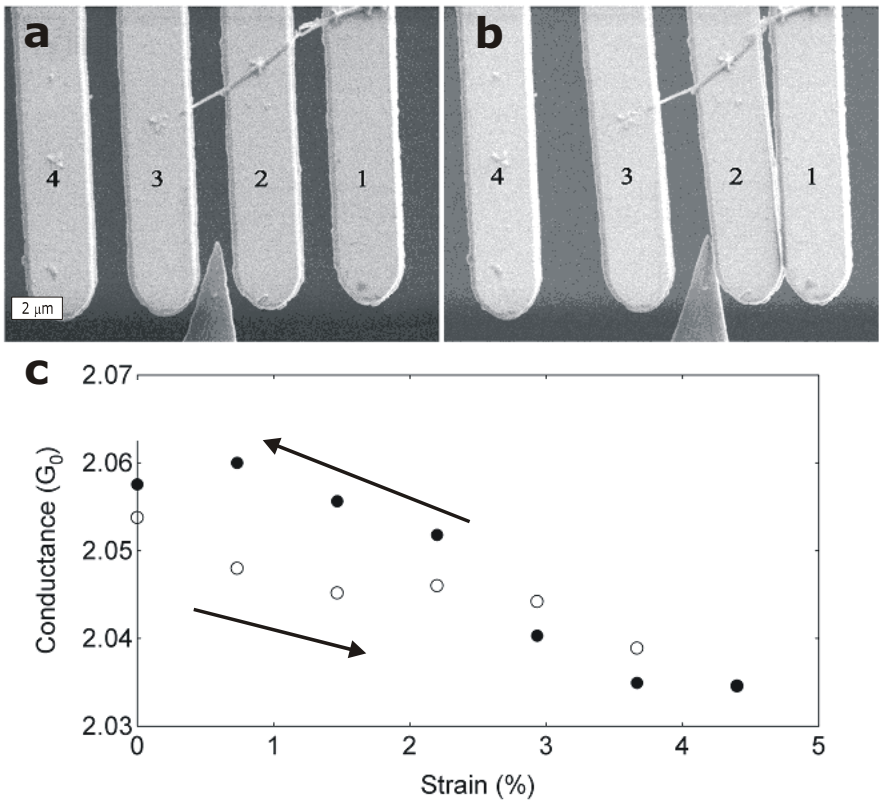

Figure 4.15: Piezoresistive properties of a soldered MWCNT. (a-b) A carbon nanotube was soldered to two microcantilevers to form a conducting bridge. By deflecting one cantilever with an STM tip mounted on the nanomotor, the strain induced change in resistance of the MWCNT bridge could be measured (c). The measurements were made in the MIC SEM setup for improved image quality by S. Dohn.

4.5.4 Summary

The EEBD technique can be used to solder carbon nanotubes to create highly conductive devices with resistances comparable to what is expected from the nanotube itself. The high conductivity indicates the contact resistance of the soldering is negligible compared to the intrinsic nanotube resistance. The soldering seems to be mechanically stable with yield strengths in the range of that of bulk gold. The device has not been tested to failure to determine the ultimate strength of the soldering. Severe contamination is observed on all devices and future studies should try improving the setup by using shutters to turn the source on and off to only have source gas present when needed. The measured piezoresistivity is much lower than what has been measured in SWNT, but comparable to measurements on carbon fibers. Whether the low sensitivity is due to the properties of the CVD grown MWNT or the contamination and deformation by the soldering process is not know.

4.6 Conclusion and Outlook

The EBD method provides the unique possibility of directly forming electrical and mechanical interconnections between free-standing carbon nanotubes and other micro- and nanostructures as demonstrated by the work done using the carbonaceous background gas as precursor.

The discovery of the highly conductive solid gold core in the *environmental electron beam deposited* (EEBD) structures makes the EEBD method a potentially very useful technique for creating, contacting and soldering nanostructures, with uses in many areas of nanotechnology.

The essential parameters required for creating the gold core have been investigated, and it was found that the gold core diameter increases with the square root of the beam current. We also found that a vapor pressure above 0.5 Torr is required, but it cannot be ruled out that this was due to low image contrast causing a wider beam.

Apart from the intended structure, additional depositions such as contamination layers, parallel deposits and branches have been observed in both EBD and EEBD. Preliminary experiments have shown that being able to turn the precursor supply off when not needed seemed to limit the contamination effect when imaging. It is not clear what conditions could limit the creation of proximity contamination due to nearby depositions as well as the parallel deposits and branches, though a high precursor gas pressure might favor these effects.

Soldering of carbon nanotubes to microcantilevers was demonstrated with depositions containing gold cores. The observed resistances of the devices were comparable to what would be expected from the nanotube itself, indicating a low contact resistance.

A strain measurement on a soldered nanotube showed piezoresistivity comparable to that of carbon fibers but lower than those reported on SWNT. TEM images of nanotube-gold core soldering joints show that the gold core connections deform or collapse the nanotube in the joint, which may damage the graphitic layer-structure of the nanotube close to the solder material. To what extent this and the contamination layers affected the measured electrical properties of the nanotube in the piezoresistive measurements remains to be investigated.

Although time did not permit refinement of the EBL system to create tweezers structures and solder bonds "by the click of a mouse", the systems software could be extended to included such features. The presented analysis of the deposition as function of beam scan rate show that the EEBD method can be used to create nanotweezers tips, especially if the tips are made at angles higher than about 45° to horizontal.

4.6.1 Outlook

The presented study has demonstrated the versatility and limitations to the EEBD method. Several questions remain unanswered by the study and new questions have appeared. A list of the possible future investigations could be

- What is the effect of contamination layers and soldering deformation on the physical properties of the soldered nanowires and MWNT?
- What are the mechanical properties of the deposited tips and each of the types of layers (core crust and shell). Can the tips be used for conductive probe tips in AFM or scanning four point nano-probes or will contamination layers prevent electrical contact?
- What are the mechanical properties of the EEBD structures ?
- Measurements in a setup with controlled source gas pressure and beam diameter should be able to provide data for better models of the deposition process and a better understanding of the apparent square root dependence of core diameter with beam current.
- Fujita et al. [119] did not observe limits to the length of lateral thee dimensional deposits. If this could be achieved in EEBD the technique would be more useful. They also observed a line width of only 5 nm for carbonaceous structures, which is considerably thinner than the 60 nm limit observed in the present experiments. It would be interesting to find the factors determining the line width.
- Could EEBD gold dots be used as catalytic particles for nanowire growth as Lau et al. [104] used Co deposits for nanotube growth? If this is possible a whole new range of devices with integrated nanowires on microfabricated devices should become possible, since EEBD can be done on any surface, after the microstructure has been processed.

Chapter 5

Studies of Carbon Nanotubes

Applications of the tools and systems developed in the previous chapters range from preparation of microscope samples, such as TEM lamella, to complicated integration of nanostructures in prefabricated microsystems. While manipulation and soldering techniques open up new possibilities for handling and characterizing nanostructures, these techniques can also potentially damage the nanostructure. To characterize the created devices or the nanowires themselves, TEM offers unsurpassed resolution to observe the internal structure. The TEM-Chip system was presented in Chapter 2.

In this chapter, the emphasis is on high bias voltages measurements of multiwalled carbon nanotubes (MWNT) produced by chemical vapor deposition (C-MWNT). The first section presents a brief review of MWNT conduction, and explains why C-MWNT are relevant to study. Since the measurements are done at high bias voltages the effects of heating nanotubes are also described. The measurements were initially done by scanning micro four point probes in ambient air under an optical microscope by Søren Dohn[1] [7]. At high bias voltages, the measurements could be interpreted as sequential breakdown of carbon shells in the C-MWNT, that eventually led to the nanotube being cut in two pieces. The limited microscope resolution made it impossible to observe where and how the nanotubes failed. I attempted to reproduce the measurements in SEM in an attempt to observe the changes taking place in the nanotubes with higher detail. However, the C-MWNT apparently failed in one single step in the vacuum environment. Section 5.2 compares the measurements with scanning probes in ambient conditions and in the SEM manipulation system. I then turned to the TEM-Chips to be able to apply the bias voltages in ambient air and subsequently analyze the effects on the C-MWNT with TEM. All TEM measurements were done together with three students, Anders Tegtmeier Pedersen, Casper Hyttel Clausen, and Sven Bjarke Gudnason, for their mid-term project. The TEM measurements are presented and discussed in Sect. 5.3. Finally, Sect. 5.4 presents the results on electron beam irradiation induced damage of nanotubes. Investigations

[1] During his M.Sc. project at MIC [127], where I was co-supervisor.

have shown that electron irradiation with energies below 80 keV should be harmless to carbon nanotube structures [128]. During the TEM study we discovered that both TEM and SEM irradiation could damage the nanotubes severely, despite the electron beam energies being within ranges that are normally considered harmless to MWNT. Using a cold finger in the TEM reduced the rate of irradiation induced damage to a level where monitoring the nanotube experiments were not affecting the electrical measurements. The TEM and SEM induced damage seemed to be caused by the presence of water vapor. Because SEM and TEM are standard methods for characterizing nanotubes, these results are important for future work, since it will set limits on the water vapor pressure and electron doses singlewalled carbon nanotube (SWNT) and MWNT can be exposed to without being damaged.

5.1 High Bias Voltage and Thermal Effects in MWNT

The MWNTs used for the many of measurements reported in literature have been produced by arc discharge (A-MWNT), and such nanotubes are known to have a much lower defect density than the C-MWNT [129]. A-MWNTs have been shown to be ballistic conductors on the micrometer scale even at room temperature [130] and have also been observed to withstand extremely high current densities $>10^9$ A/cm^2 [131], suggesting they could find applications as interconnects in microsystems. Many of the "exotic" nanoscale effects such as ballistic conductance in A-MWNT are limited by the higher defect density in C-MWNT. However, from a technological perspective, the C-MWNT are interesting, since they can be grown from catalytic particles directly on microsystems [25][132]. This could make integration of C-MWNT in mass-produced microsystems much easier than A-MWNT which cannot be grown directly in a desired place. Despite the high defect density, C-MWNT have been shown to sustain high current densities ($>10^7$ A/cm^2 [133]) and high density (10^{11} cm^{-2}) transistor arrays have been made with highly defective C-MWNT [134].

When high bias voltages are applied to A-MWNTs deposited from a dispersion onto gold electrodes on a planar substrate, Collins et al.[122] have found it to be possible to remove the outermost carbon shells sequentially - a process that is termed "shell burn" in the following. Their results were based on electrical measurements in vacuum and air, combined with SEM observations of the A-MWNT as they were sequentially thinned down. In a later paper by Bourlon et al. [26], the results by Collins et al. are reproduced, but this time with EBL defined contacts and AFM images. De Pablo at.[135] also used AFM to correlate the position of electrical breakdown with defects in nanotubes. The SEM and AFM observations only provide images of changes to the outer diameter of the nanotube and not the changes to the internal shell structure. Nakayama et al. [136] observed by TEM that MWNT were thinned down to have pointed ends by shell burn experiments in vacuum. Poncharal et al. [137] have also been investigating A-MWNT at high bias. Their method is based on

lowering a bundle of pristine A-MWNTs into liquid mercury. This enables them to observe the change in conductance as the contact length of the metal to the nanotube is varied. They have also done this as in-situ TEM experiments. Unlike Collins et al. [122] they did not observe sequential shell burn in their experiments. Once a too high bias voltage was applied to a nanotube, the outer shell turned into amorphous carbon and the electrical contact was lost. Poncharal et al. suggests that the treatment used to make a dispersion of A-MWNT by Collins et al. created defects in the A-MWNT and influenced the measurements.

By their TEM images of the individual nanotubes, Poncharal et al. provide compelling evidence that their observations should be related to a pristine multiwall structure, and that the sequential shell burn observed by the other groups could relate to defects caused by the treatment of the nanotube sample. From these observations, it seems interesting to make shell burn experiments on pristine C-MWNT to see if sequential shell burn is possible (as Collins et al.) or whether these nanotubes will fail in one single step (as Poncahral et al.).

The present work has focused on studying a C-MWNT sample supplied by Richard Czerw from Wake University. The nanotubes were produced by a ferrocene/xylene CVD process [138]. This C-MWNT sample consists of mats of relatively aligned MWNT. Compared with the other MWNT samples we have tested, this sample appeared to contain more uniform nanotubes in terms of length and diameter, which would hopefully lead to more reproducible results. With this sample it was also easier to manipulate individual nanotubes when preparing the TEM-chips, since these nanotubes appeared to have lower inter-tube adhesion forces and were relatively thick (diameters 50-100 nm).

The shell burn experiments require an understanding of the conductive properties of carbon nanotubes; the oxidation effects taking place as the nanotube is heated by the dissipated power at high bias voltages; and finally the irradiation effects that could influence the measurements done in SEM and TEM. These effects are reviewed in the following.

5.1.1 Conductance of MWNT

Each shell of a MWNT can be regarded as single walled tube made from a rolled up graphene sheet. Planar graphene is a semi-metal with an in-plane resistivity of 5×10^{-5} Ωcm, while the resistivity perpendicular to the graphene planes is of the order 10^{-3}-10^{0} Ωcm [139].

The periodic boundary conditions imposed on the electronic wave function along the circumference of a graphene shell will alter the electronic structure of the NT shell compared to planar graphene. A review of the electronic properties of carbon nanotubes can be found [140]. Depending on the chirality a nanotube shell can have metallic or semiconducting properties along the nanotube axis. Statistically, two out of three shells can be expected to be semiconducting in a MWNT. The band gap for

a semiconducting shell is [141]

$$\Delta E_{sc} = 2\frac{\gamma_0 a}{D}, \tag{5.1}$$

where $\gamma_0 \approx 2.45$-2.90 eV is the energy overlap integral for tight binding calculations, $a = 0.142$ nm is the C-C bond length in graphene, and D the diameter of the shell. At room temperature, the thermal energy $k_B T$ is larger than the band gap for semiconducting nanotube shells with diameters $\gtrsim$30 nm. Only more narrow shells would display signs of semiconducting behavior at room temperature. For metallic shells, two states cross the Fermi level, and a sub-band structure similar to that of the semiconducting shell is present with a sub band gap 3 times larger. At low temperatures, only the two states at the Fermi level will contribute to the conduction, each with a conductance quantum [142]

$$G_0 = 2\frac{q_e^2}{h} \approx (13\ \mathrm{k}\Omega)^{-1}, \tag{5.2}$$

giving a conductance of an ideal nanotube shell of $G = 2G_0$ [137]. At room temperature, the sub band states of metallic shells must participate in the conduction unless the shell diameters are much smaller than 100 nm and the tube diameter used in this work.

Conductance of C-MWNT

Generally, C-MWNT are not considered defect free. Dai et al. [129] measured the resistivity of C-MWNT to be diffusive rather than ballistic, and of the order 10-100 $\mu\Omega$m (1-10$\times 10^{-3}$ Ωcm), which is at least 20 times larger than expected for the graphene in-plane resistivity. The term *defects* is here meant to cover imperfections such as

- Interstitials (incomplete shells included in the shell structure)[143].
- Various types of topological defects such as faults and kinks in the shell structure, and vacancies, such as Stone-Wales defects where carbon atoms are missing within a shell.
- Catalytic particles or gasses absorbed or included in the shell structure from the growth of the nanotubes can act as scattering centers and also as donors changing the Fermi energy [144].
- Molecules adsorbed on the nanotube surface are known to act as dopants and scattering centers, which influence on the electrical properties [145]. Often pristine nanotube samples are hole doped, which increases the conductance of semiconducting shells.

Zhou et al. [146] have developed a model based on thermal activation of conduction channels giving a linear dependence of doped MWNT conductivity with temperature. Their measurements on C-MWNTs show that the conductance is increasing and highly linear in the range 50-800 K. They note that it is probably the widest observed linear temperature dependence of conductance reported for any material to date. However, Jang et al. [147] have measured the temperature dependence of the conductivity of C-MWNT depending on the degree of disorder in the shell structure, and use a model for heterogeneous material conductivity to explain their observations of both positive and negative temperature coefficients, which are not always linear. The influence of defects on the electronic structure of a shell has also been studied by Raitkin et al. [148], who concluded that a high defect density can lead to an increased gap compared to the value of Eq. 5.1 by effectively increasing the value of γ_0.

Given the wide variety of defects and the different types of effects they have on the electrical properties of a nanotube shell, it seems difficult to even estimate the properties of a C-MWNT without extensive studies of the individual nanotube under investigation. For a rough estimate, the C-MWNT in the present work can be assumed to be a (solid) graphite rod with a length about 1-10 μm. The resistance of a 1 μm long 100 nm diameter nanotube is between 50 Ω and 12 kΩ depending on whether the highest resistivity obtained by Dai et al. [129] or that of graphene resistivity is used. In the following, conductances will be measured in units of the conductance quantum, G_0, which appear to be a reasonable scale for the present nanotube conductance. One should keep in mind, that the transport mechanism is not likely to be ballistic on the length scales and temperatures investigated here.

Some measurements have been reported on the conductance of C-MWNT and its dependence on the applied bias voltage. Lee et al. [133][149] have measured the IV characteristic of a C-MWNT in air to have increasing conductance with increasing bias until a saturation effect limits the current at bias voltage of 1-10 V. Oxidation of the outer shells due to Joule heating of the nanotube at the high bias voltage is mentioned as a possible explanation for the current limit. A lasting decrease in device conductance is observed when the current saturation has been reached. For measurements in vacuum, Qui-Hong et al. [150] also measured increasing conductance of C-MWNT, with increasing bias and saturation starting around 3-5 volts. Qui-Hong et al. explains the increasing conductance by annealing effects in the nanotube due to joule heating by the dissipated power, since the conductance increases in subsequent scans. Here, the current saturation is explained by the onset of electron-phonon scattering and Bragg-reflection. Altough there is some variation in the IV curves reported in the mentioned literature, the IV measurements on C-MWNT generally seem to show nonlinear increasing conductance with bias voltage.

5.1.2 MWNT Annealing and Oxidation Effects

The effect of heating nanotubes in air or vacuum must be considered to explain the changes taking place in C-MWNT at high bias voltage and current. For a MWNT bridging two cantilever electrodes, the temperature rise depends on the dissipated power and the thermal conductance of the nanotube. Since MWNT have been measured to have thermal conductivity in the range 25-3000W/Km, a very simple model [151][152] will be used for estimating the temperature at the middle of the bridge:

$$\Delta T = \frac{L}{8\kappa A} P, \tag{5.3}$$

where L is the bridge length, A the cross-sectional area, κ the thermal conductivity and $P = UI$ the dissipated power in the bridge with bias voltage U and current I. For a 1 μm long 100 nm diameter nanotube with a dissipated power of 1 mW, the temperature rise is between 5 K and 600 K given the wide range reported for the thermal conductivity.

In thermogravimetric experiments where the mass of a sample is measured as it is slowly heated in a controlled atmosphere, carbon sooth begins to oxidize at around 350 °C in air, while carbon nanotubes generally have higher oxidation temperatures, starting around 600 °C [153]. The higher temperature needed for oxidation of nanotubes is often explained by the absence of dangling bonds and protection of inner shells by the outermost one, so oxidation is required to take place shell by shell. Heating an impure nanotube sample in air is often used as a way to clean the sample for carbon sooth. When heating nanotubes in air, TEM studies have shown that pits tend to form in the shell structure [154]; once oxidation has opened a shell at a certain point, the dangling bonds are attacked and so is the underlying shell.

Defects in nanotubes will also be attacked during oxidation, and nanotubes have been observed to oxidize faster at kinks and at points with high strain due to bending. Lu et al. [155] observed MWNT to be completely oxidized in 10^3 s at 700 °C and about 60 s at 1200 °C. In those measurements, the oxidation time τ had an Arrhenius dependence [156],

$$\tau \propto e^{-\frac{E_A}{RT}}. \tag{5.4}$$

The activation energy was found to have a value $E_A = 122$ kJ/mol, in agreement with measurements on graphite oxidation where $\mathrm{E}_A = 100 - 300$ kJ/mol [155].

For nanotube samples containing regions in the shell structure with amorphous carbon, annealing is a common technique used to graphitize such amorphous carbon into a proper shell structure[157][158]. As the temperature of a sample is increased in inert gasses, such as nitrogen and helium, various thermal processes take place. At about 1000°C carbonization is beginning to take place, turning organic material into amorphous carbon. At 1500-3000°C graphitization is occurring. As with the oxidation, increasing temperature is expected to increase the reaction rate. The rate is however slow and hours are often needed to achieve a reasonable effect [157].

Stable field emission has been observed with MWNT reaching 2000°C in vacuum [151], indicating that MWNT can sustain very high temperatures.

If catalytic particles are present within the nanotubes, these must be expected to change shape, move, melt, or evaporate depending on the reached temperature. By in-situ TEM studies, Ichihashi et al. [159] observed Fe catalytic particles move through amorphous graphite nanorods at 650°C with a velocity of 5 nm/s, leaving behind a tubular track of graphite. Indium metal particles have also been observed to move by electromigration on a carbon nanotube surface when a current is passed through the nanotube [160]. By annealing, Kim et al. [161] have observed Fe catalytic particles to both move, change phase, and alter the innermost carbon shell structure. From TEM images, the internal structure of the C-MWNTs in our sample appear comparable that of the nanotubes used by Kim et al..

When high currents are passed through a nanotube, electron scattering near defects will heat the defect sites up to higher temperatures than the surrounding nanotube material [135]. For shell burn experiments in air, the nanotubes must be expected to begin oxidizing slowly at defect sites where amorphous carbon is present at temperatures as low as 350°C. At temperatures around 700°C the oxidation rate will be considerably faster and begin to cause increasingly deep pits and even cut nanotubes at kinks and large defect sites. Temperatures can easily reach 600°C in nanostructures heated by moderate powers in the mW range (Eq. 5.3), and the nanotubes must be expected to burn in seconds or minutes, depending on the temperatures achieved in the experiment. If the nanotubes are oxidizing at this rate, annealing effects will not have time to take place, but catalytic particles are expected to be able to move and possibly change the nanotube structure in the relatively short time interval.

5.1.3 Summary

MWNTs are potentially very interesting components in a variety of applications from high current carrying leads to field emission tips. The reviewed measurements have shown MWNT to have extremely high current carrying capabilities and thermal stability. The conclusions regarding the electrical properties of MWNT from different groups are often not in agreement. The preparation methods and specific details of the experiment are apparently very important in determining the behavior of the individual devices. There are still many open questions and even contradictions especially when comparing results from different groups, and new publications on the subject are appearing continuously. The possible effects taking place in carbon nanotubes at high temperatures have been reviewed and it was concluded that burning near defect sites would probably be the primary thermally induced effect in Joule heated nanotubes.

Given the wide variety of results on MWNT electrical conduction, the TEM-Chip system offer the possibility to both obtain high resolution images of the individual

nanotube being investigated and observe the details of the changes in the structure due to the high bias voltages. Ideally, the measurements should include not only TEM images, but also measurements of the resistance as function of temperature, Hall resistance measurements to determine the density of carriers, and gate voltage dependence of conductance in a field effect device to determine the sign of carriers. Such measurements are beyond the scope of the present investigation, but are planned for future TEM-chip studies.

5.2 Scanning Micro Probe Measurement of Nanotube Conductance

Micro conductance probes (Sect. 2.2.2) were used to directly measure the electrical properties of carbon nanotubes without the need for electron beam lithography to define contacts. The results are reported in detail in Søren Dohns masters thesis [127] and in the manuscript [7]. Each nanotube sample was prepared in an optical manipulation station by pulling a C-MWNT from the substrate with an etched tungsten tip or microcantilever probe, and then placing it on a silicon oxide surface. The nanotubes can be aligned on the substrate by pushing them gently around with the W-tip.

5.2.1 Measurements in Air

When the scanning conductance probe (with two or four cantilevers) was moved down on the nanotube, contact was usually not achieved until the probe had been nudged around while pressing down on the nanotube. Once contact had been achieved the measured resistance would be very sensitive to vibrations and drift in the setup. Generally, resistances of the order kΩ were measured on the nanotubes by both four and two point measurements with a resistance per length of the order 1-4 kΩ/μm. The measurements indicated a difference between measured conductances of different nanotubes that was larger than the measurement error, and the measurements hence seemed to primarily measure the intrinsic properties of the individual MWNT rather than the contact resistance.

Figure 5.1 shows a sequence of a typical IV characteristics on a C-MWNT acquired by a Labview controlled Keithley 2400 source meter. The inset in the figure show an optical image recorded during such a measurement, where the limited resolution makes it difficult to distinguish between a single or a bundle of MWNT. When preparing the sample it often becomes clear whether more nanotubes are present, since they tend to separate as they are moved around.

The C-MWNT were found to have a conductance of the order $0.2 - 1\ G_0$ as expected, and a zero-bias resistivity of 1.3-3.3 kΩ/μm. The first sweep of bias voltage generally gave a non linear IV characteristic, where the conductance increased with

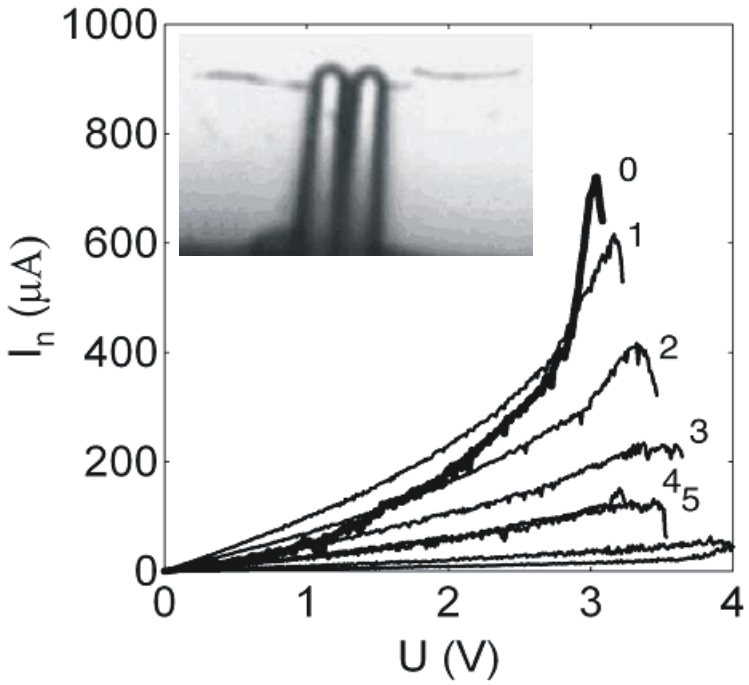

Figure 5.1: Typical shell burn measurement series with two-point conductance probe in air. The inital IV sweep (0) is more non-linear than the subsequent sweeps. As the sweep reaches a relatively constant threshold voltage about 3 V, the current saturates and then rapidly decreases. Subsequent sweeps show stepwise decrease of the zero-bias conductance, G_{0V}. The inset shows an image from the optical microscope of a tube that had previously been burnt in two pieces and the tip of the two-point conductance probe. Images adapted from [127].

voltage, until about 1.5-3 V where the current would saturate. If the sweep was continued beyond the current saturation point, the current would begin to decrease rapidly until the nanotube burned into two pieces. If the voltage sweep was stopped at the point where the current had begun to decrease in the IV curve, G_{0V} would be lower in the following IV curve.

The program controlling the voltage sweep would stop the sweep if there was a decrease of current by more than a predefined percentage level. For about one third of the nanotubes, this method made it possible to decrease the conductance sequentially in several steps until they eventually burned into two pieces. The sequential conductance decrease could be interpreted as a sign of sequential burning of the shell structure as observed by Collins et al. [122]. They base their conclusion that individual shells burn partly on the observation of stepwise decrease on current, and it is worth noting that no clear step-shaped pattern was observed in the present measurements. However, a continuous current decrease resembling the present measurements, has also been observed in the shell burn experiment by Bourlon et al. [26] which to some extent reproduces those of Collins et al.

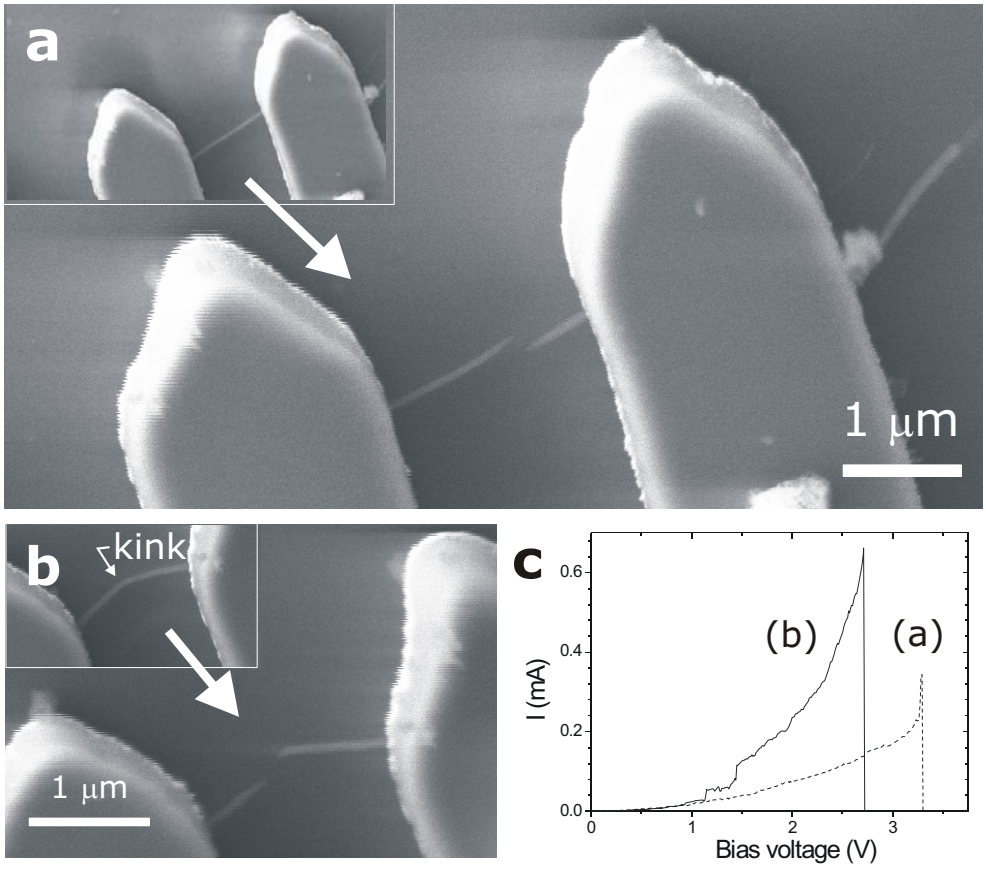

Figure 5.2: In-situ SEM measurements of MWCNT conduction until breakdown. a) Images show the C-MWNT before and after a bias voltage sweep. b) Another C-MWNT that failed at the kink in the middle of the gap. c) IV curves from the MWNT, acquired during the bias voltage scan. They are representative of the curves acquired in SEM.

5.2.2 In-situ SEM Measurements

In order to study how and where the nanotubes failed or burned, experiments similar to those made by Dohn in air, were attempted with the in-situ SEM setup at MIC (Sect 2.3.2). Based on the results by Collins et al. [122] the effect of performing the experiment in vacuum, rather than under ambient conditions, was anticipated to be an observation of slightly higher bias voltages before failure.

In the SEM it was considerably more difficult to achieve good contact to the nanotubes than in air. The nanotubes did not adhere well to the underlying surface and had a tendency to move around when touched by the probe. It was practically impossible to achieve contact to the nanotubes if they were not well aligned with the probe tips, and the probe had to be moved around while pressing down on the

nanotube to achieve contact. Conductances of the order of G_0 could be achieved on most nanotubes, but the IV measurements had a considerable noise level compared to the measurements in air, which is understandable given the difficulty in achieving a stable contact. The nanotubes generally burned in a single event, too fast to observe any time resolved decay of current with the Keithley Sourcemeter, and sequential change in conductance of the nanotubes by repeated application of high bias voltages was not observed. This is in contrast to the results by Collins et al. [122], who were able to make sequential reduction of conductance of MWNT in vacuum.

The images in Fig. 5.2 show two C-MWNT before and after applying a high bias voltage together with the acquired IV curves. The nanotubes had a tendency to burn at kinks (Fig. 5.2b) and possibly also near included catalytic particles. After the nanotube has burnt into two pieces, the remaining ends are usually deflected as if the nanotube had been under stress when it was intact, and this might have increased the rate of oxidation [155].

5.2.3 Summary

Sequential reduction in the nanotube conductivity was observed by scanning conductance microprobe measurements in air for about every third of the tested C-MWNT. The current saturation was observed when applying bias voltages of about 1.5-3 V. The resolution in the optical microscope was however not sufficient to resolve if any changes were taking place within the nanotube before breakdown. The vibration level and drift in the setups, especially in the SEM setup, was a potential problem because the scanning conductance microprobe measurements were very sensitive to motion of the probe. When applying a high bias voltage in vacuum, the data acquisition was unable to resolve the time dependence of the rapidly decreasing current ta breakdown, which appeared to fail in a single step. The image resolution in the SEM experiments was not sufficient to reveal of the nanotube burned near internal catalytic particles or defects, but the nanotubes typically failed at kinks if such were present.

5.3 TEM investigation of MWNT Shell Burn Experiments

The limited resolution and high noise of the SEM experiments, led to the development of the TEM-Chip system to achieve high resolution images of the nanotube structure during the shell burn experiments. If the TEM-Chip investigation of the shell burn process is feasible, more detailed studies should be initiated to thoroughly characterize the behavior of different types of MWNT, since proper modelling of these complex nanosystems seem to require detailed knowledge of the dependence on the internal structure of the individual tube.

5.3.1 Setup and Probe Preparation

The setup for the TEM-Chips was described in Sect. 2.3.3. Individual C-MWNT bridges between microcantilevers were made by manipulation with an etched tungsten tip in an optical manipulation setup (Sect. 2.3.1).

The bridge resistance was often in the 100 kΩ range when the nanotube was initially placed on the cantilevers. Temporary condensation of water onto the chip surface usually resulted in bridge resistances below 50 kΩ for about every other tested nanotube. The capillary forces during drying of the chip can apparently pull the nanotube into close contact with the cantilever surface. The temporary condensation can be achieved simply by breathing on the chip. Once a bridge has been made, the device is extremely sensitive to electrostatic discharges. Outmost care must be taken to ensure proper grounding during handling of the device.

The TEM investigation was done in a Philips EM 430 operating at 100 keV. The TEM analysis was made at low beam currents, with short exposure times on the bridging MWNT, and liquid nitrogen cooling of the TEM cold finger to avoid damaging it (see Sect. 5.4). No major influence was observed on the electrical properties of the TEM-chip devices by the TEM investigation.

The experiments were made using an improved computer programs to control the IV acquisition. In the initial program used for the scanning conductance probe measurements, the acquisition did not provide information about the possible time dependence of the conductance. A new program was made that stopped the voltage sweep (IV curve) during a shell burn experiment when predefined voltages was reached or current saturation occurred ($dI/dV = 0$). When the sweep was stopped, the current was recorded as function of time (It-curve) until the user chose to continue the voltage sweep or to start from zero bias voltage in a new sweep.

5.3.2 Experimental Results and Discussion

This section will first describe a typical TEM image sequence for shell burn experiments performed in air to provide an overview of the general effects that have been observed. Then an overview is given of the electrical measurements that have been done, in order to find the general characteristics of the C-MWNT sample. Finally the acquired IV and It curves are discussed, and the shell burn experiments performed in air are compared to similar experiments performed in a nitrogen flow.

Shell Burn Performed in Air

Figure 5.3 shows a typical sequence of the progressive burning of a nanotube in air, where shell burn experiments have been performed between each TEM image. The nanotube clearly becomes thinner in the middle part of the bridge and also severely damaged in the vicinity of a large catalytic particle. It is assumed that all observed particles in the C-MWNT are catalytic Fe particles, although this has not been verified by EDX or similar measurements. Another catalytic particle is visible within the interior cavity of the nanotube in the upper part of the image. This particle does not cause damage to the nanotube and only moves slightly in the images. The catalytic particles in the nanotube interior generally move and deform very much as described in the work by Kim et al. [161].

The graph in Fig 5.4a shows the distribution for the tested devices of gap length between the cantilevers, L_{gap}, and C-MWNT cross sectional area (neglecting the narrow inner hole). The length of the cantilever gap span the range 0.7-8 μm. Howver, the length between contact points of the nanotube located on top of the cantilevers, L_{tube}, could be larger than the gap length as shown in the inset in Fig 5.4a. It does however seem that the nanotubes probably make contact close to the edge of the gap, since the measured resistance is reasonably linear with gap length for the investigated nanotubes. The measured resistance as function of length seems to be linear through origo, indicating a negligible contact resistance. Fitting gives a contact resistance of 0.5 kΩ which is less than 10 % of the measured resistances and the cantilevers alone contribute with about 90 Ω to that value. The observations indicate that the nanotubes are diffusive conductors with resistance $R = \rho L/A$ and the measured resistivities are scattered in the range 20-100 times the in-plane resistivity of graphite ($\rho_{graphite}$ =5*10^{-5} Ωcm), which is comparable to the results by Dai et al. [129].

Most nanotubes burned somewhere in the visible region of the gap, indicating that heating was mainly taking place in the suspended part of the nanotube rather than at the contact point. This is in agreement with the expectation of low contact resistance and diffusive transport. Ballistic conductance would imply that most heat was dissipated at the contacts and little if any dissipation would be in the nanotube [162].

Fig 5.4c shows that the nanotubes burned at a bias voltage about 2 V, almost

independent of gap length. Since it is independent of length, it is not likely to be related to an electrical breakdown phenomena in the nanotubes which would normally be determined by the electrical field in the nanotube ($E = V/L_{gap}$) reaching some limiting value. The constant saturation value taken alone could be taken as indication of a breakdown phenomena at the contacts at 2 V, but this is in contradiction with all the above observations indicating Ohmic behavior of the nanotube. Although the 2V limit seems to be very constant, it could be a fortuitous coincidence of nanotube length, diameter and conductance, making the nanotubes burn at this voltage, but this is unlikely given the wide spread in the tube dimensions as shown in Fig 5.4a. The peak current density reaches 10^6-10^7 A/cm^2 for all nanotubes comparable to the current density observed by Lee et al. [133]. Measurements on the same nanotube with different gap lengths should be done to study if the saturation voltage is indeed independent of length.

By plotting the peak power dissipated in the nanotube in Fig 5.4d, it is apparent that the peak power is quite different for the studied C-MWNT, but seems to be limited to about 1 mW. The wide scattering in peak power is in sharp contrast to the relatively constant peak voltage[2].

[2] A corresponding scattering is found in the data if the peak power×area is plotted. This should give an indication of the peak temperature proportional to length from Eq. 5.3.

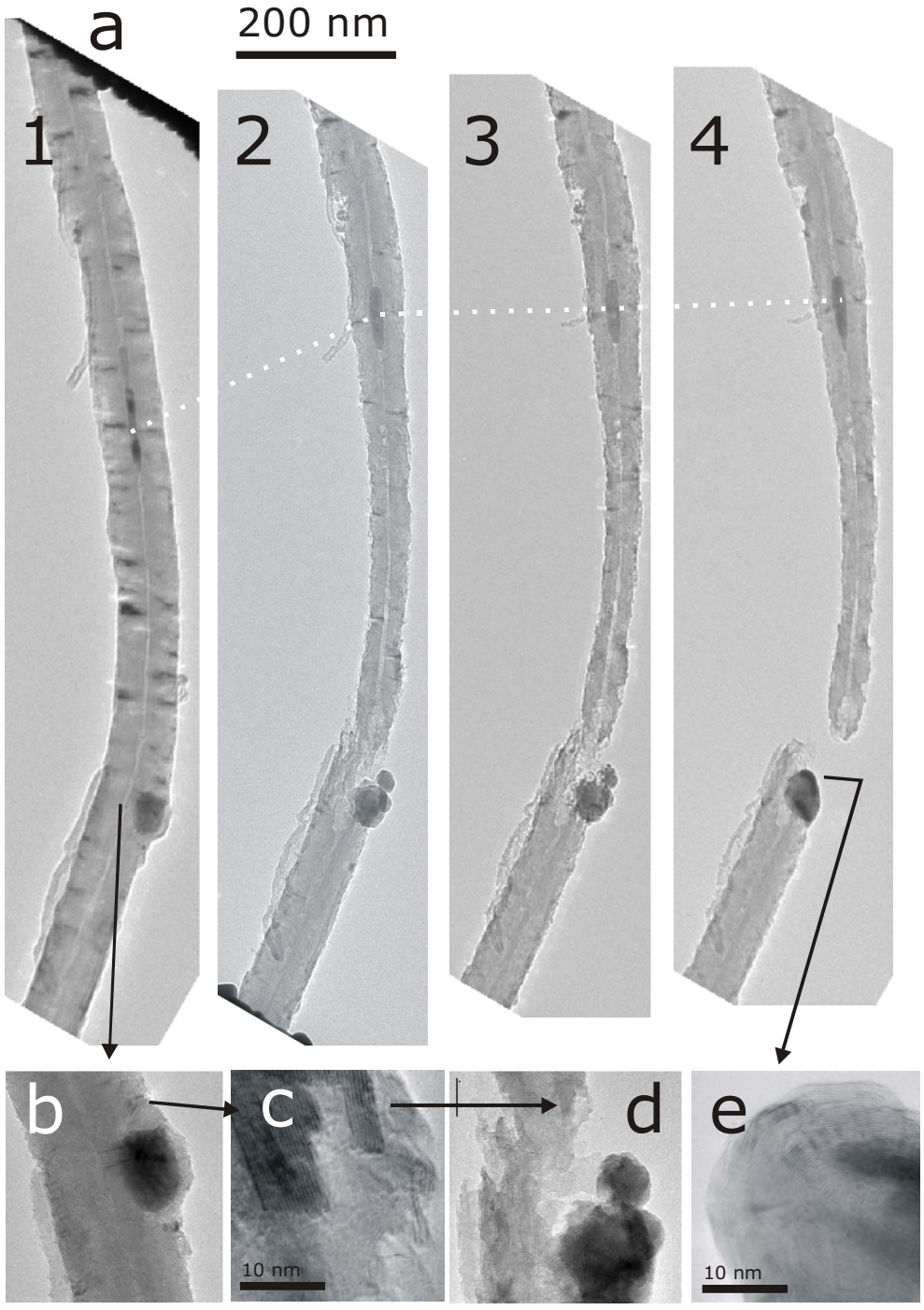

Figure 5.3: A series of TEM images of a C-MWNT, bridging two cantilevers on a TEM-Chip, and showing the progressive destruction due to shell burn experiments in air. The 3 corresponding IV and It curves recorded between the TEM images are shown in Fig 5.5. a) Overview images. The dotted white line indicates the motion of a catalytic particle within the nanotube cavity. The nanotube breakdown primarily takes place in the vicinity of a catalytic particle incorporated in the shell structure. The middle part of the tube is also considerably thinned down during the shell burn experiment. Four close-ups TEM images are shown below, each from the above image in (a): b) The largest catalytic particle with a thin carbon coating. c) The destroyed shell structure just above the catalytic particle. d) The large catalytic particle. e) A new layered carbon shell structure formed around the catalytic particle during TEM analysis.

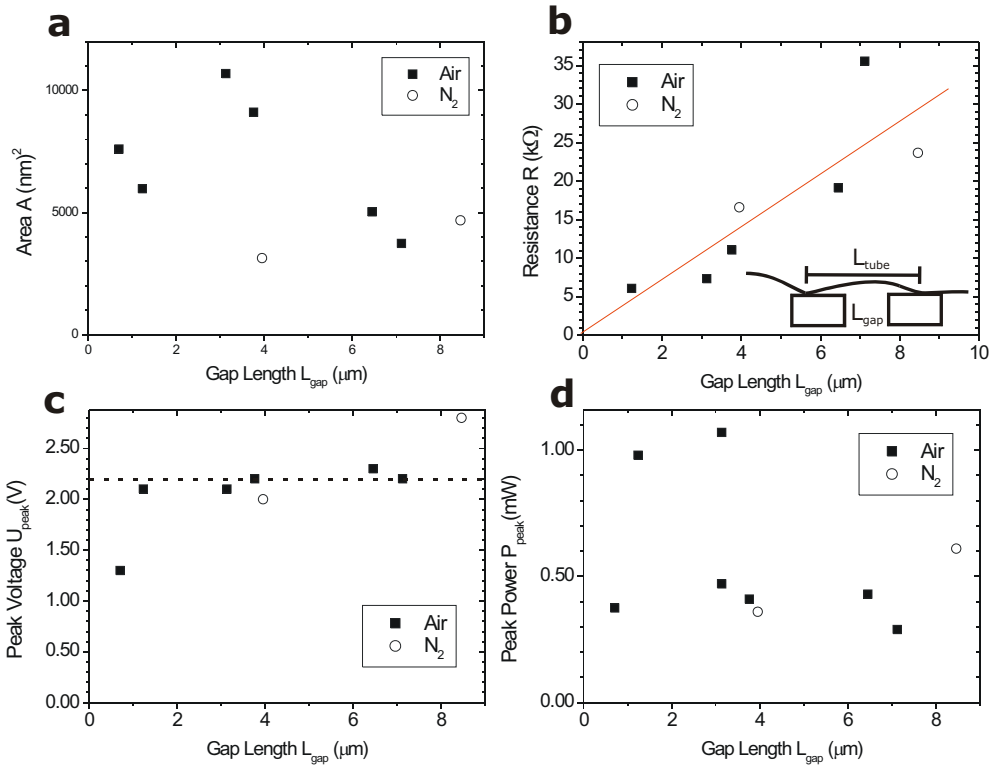

Figure 5.4: Overview of the electrical properties of those devices that achieved good contact to the MWCNT (R<50kΩ). a) There is a wide spread in both tube area and gap length. b) Measured zero bias resistance versus length show that the tubes are diffusive conductors on the micron scale and have a (almost negligible) contact resistance of the order 0.5 kΩ. The inset shows how the gap length not necessarily reflects the true length of the nanotube between contact points. c) At high bias voltages the current saturation occurs at a relatively constant voltage of about 2 V, for almost all tubes, independent of length. d) The maximum power dissipated in the bridges does not exceed 1 mW and is about 0.5 mW for most samples.

Discussion of the IV and It Curves

The following discussion is based on the data acquired for the nanotube shown in Fig 5.3, which is representative for the observed behavior of the investigated nanotube devices. Different models are briefly discussed that could explain the IV characteristics and a simple model is found that describe the IV data well.

Figure 5.5a shows the sequential IV curves measured on the nanotube shown in Fig 5.3. The voltage sweep was started at 0V, and initially every 0.2 V the sweep was stopped temporarily to observe the time dependence of the current at fixed bias. As the saturation point was approached, more stops were made in the sweep. The current dependence with time is shown in Fig 5.5b. At low bias voltages up to a bias voltages about 1.5V, the decay rate is negligible (of the order nA/s). Above 1.5 V, the decay rate increases and appears linear in time for the acquired time series for bias voltages up to about 1.7 V.

Above 1.7V the current decay with time can be fitted well with an exponential decay towards a steady state value. If only the initial 10 seconds of the exponential decay with reasonably linear behavior is considered, the decay rate of the current increases linearly with bias voltage as 16μA/s per volt bias. The logarithm to the measured decay rates are not obviously linear functions of power and it is therefore difficult to relate the decay rate to an estimated temperature (Eq. 5.3) and corresponding Arrhenius like dependence of oxidation rate (Eq. 5.4).

The periods with fixed bias voltage cause the vertical steps at high bias voltage in the IV curve Fig 5.5a. These steps conveniently indicate how the time factor is an increasingly important factor for the shape of the IV curve at high bias voltages.

The IV sweep is nonlinear, even at low bias voltages <1.5V, with conductivity increasing with voltage. This is in accordance with the published observations discussed in Sect. 5.1.1. The electrical and thermal conductivity generally depends on temperature. The joule heating of the bridge by the dissipated power can influence the measurements depending on the temperature coefficient of resistance and thermal conductivity of the nanotube (and thermal and electrical contact resistance, which will be neglected below). A simple model can estimate the effect of the self-heating of the nanotube due to the dissipated power. To first order, the linear temperature coefficient α of resistance gives

$$R = R_0(1 + \alpha\,(T - T_0)) \tag{5.5}$$

Using $\Delta T = T - T_0$ and Eq. 5.3, one can estimate the effect of the dissipated power in the nanotube resistance if the material constants are known. For carbon fibers, α has been measured to lie in the range $[-0.13;\ 0.02]$ %/K [163] and given the diffusive transport and defect density of the C-MWNT in this work, these values are probably reasonable estimates for the present sample. Measurements by Vincent et al. [152] give resistance as function of temperature as $R\ [\Omega] = 2 * 10^6 - 820\Delta T$ and hence a value of $\alpha = -0.0\,41\%/K$, which falls within the values found for carbon fibers,

although the measured resistance was rather high compared to our devices. We did attempt to do one cryogenic measurements on a MWNT on a TEM-Chip[3]. The measured temperature coefficient was in the range $[-0.2; -0.02]$ %/K. Based on these results the nanotubes studied here seem to have negative temperature coefficient of resistance within the expected range fro α. The discussion in many published works discusses the temperature dependence of resistance, but Zhou et al. [146] discussed the temperature dependence of conductance for their C-MWNT sample, which they found to be highly linear in the wide range of temperature 50-800 K. For sufficiently small $\alpha\Delta T \ll 1$ the two following equations are approximately identical

$$G = G_{0V}\left(1-\alpha\Delta T\right) = G_{0V}\left(1-\alpha\frac{L}{8\kappa A}P\right) \tag{5.6}$$

$$R = R_{0V}\left(1+\alpha\Delta T\right) = R_{0V}\left(1+\alpha\frac{L}{8\kappa A}P\right) \tag{5.7}$$

From the data presented by Zhou et al. α seems to have a value of about 0.1%, and $\alpha\Delta T$ covers a range of about 0.3. In this case the two above equations will no longer be equal at all temperatures and the results by Zhou et al. do not look linear of plotted as R vs T. To get an indication of which equation (Eq 5.6 or 5.7) that describes the present nanotube sample best, Fig 5.5 plots $R = U/I$ and $G = I/U$ vs. dissipated power $P = UI$ for the voltage sweeps. All R and G vs. P are surprisingly linear, especially when considering that the considerable tube damage from one voltage sweep curve to the next. The linearity of both R and G vs. P indicates that $\alpha\Delta T$ is small in the present case.

The curves in R vs P (Fig 5.5a) are slightly curved for all three shell burn sweeps, while the G vs P curves (Fig 5.5b) appear more linear for all three shell burn curves. For the G vs P curves at high powers, the inclination is slightly lower, but this can be explained by the shell burning taking place while the sweep is being done at high bias. The sequential shell burn curves have almost the same inclination for each individual sweep in the G vs P curves, and this is also the case for the results made by scanning four point probes in air by Søren Dohn. This make it tempting to suggest Eq. 5.6 as a phenomenological model for the MWNT conduction in the present sample. The apparent applicability of Eq. 5.6 is beyond expectations, since the nanotube behaves linearly even after several shell burns have been performed on it and has been almost broken in two pieces as shown in Fig .5.3.

The thermal conductivity of the nanotube also enters into Eq. 5.3 and cannot be assumed to be constant based the measurements reported on literature [164]. It would be interesting to verify if the better fit of Eq. 5.6 than Eq. 5.7 also holds for

[3]This experiment was done at Copenhagen University in collaboration with Jesper Nygård and Thomas Sand, to test if cryogenic measurements were at all possible. The resistance increased as the temperature was lowered and contact was eventually lost at 150 K.

tubes heated externally rather than by dissipated power. Measuring IV curves of the C-MWNT at various temperatures should provide such information. This experiment is planned to be done in the near future.

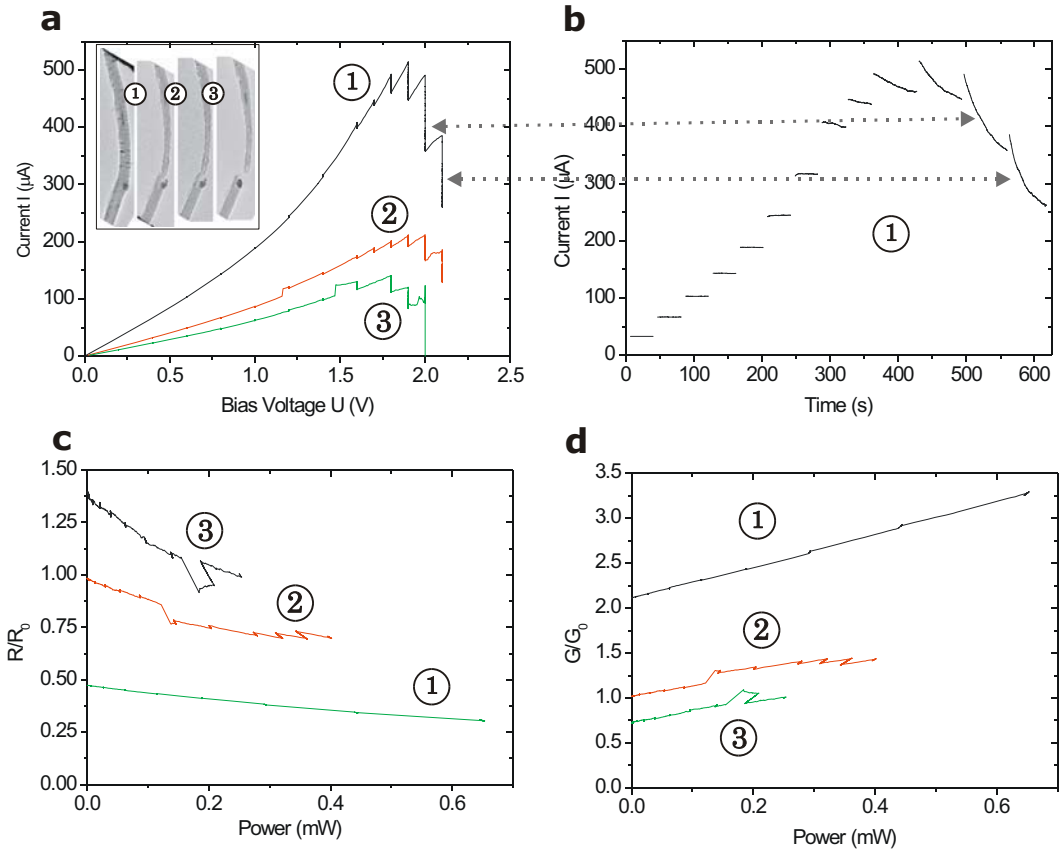

Figure 5.5: Electrical measurements on C-MWNT in air with both bias voltage scan and observation of the current as function of time for temporarily fixed bias voltages. a) IV curves showing sequential reduction of conductance after reaching the current saturation point. The inset shows the tube image sequence from Fig. 5.3. The vertical parts of the curve appears when bias has been kept fixed temporarily. b) The current as function of time during periods with temporarily fixed bias voltage. The current decreases faster as the current saturation point is reached and crossed. c) Device resistance R in units of $R_0 = G_0^{-1}$ versus disspated power $P = U \cdot I$ d) Conductance G/G_0 versus P. For fixed voltage during the time sequences, the G-P curve follows lines $G=P/U^2$.The dependence is for all voltage sweeps of the type G=aP+b (Eq. 5.6). The R vs P graph, which does not follow the linear prediction by Eq. 5.7 as well as the G vs P graph follows Eq. 5.6.

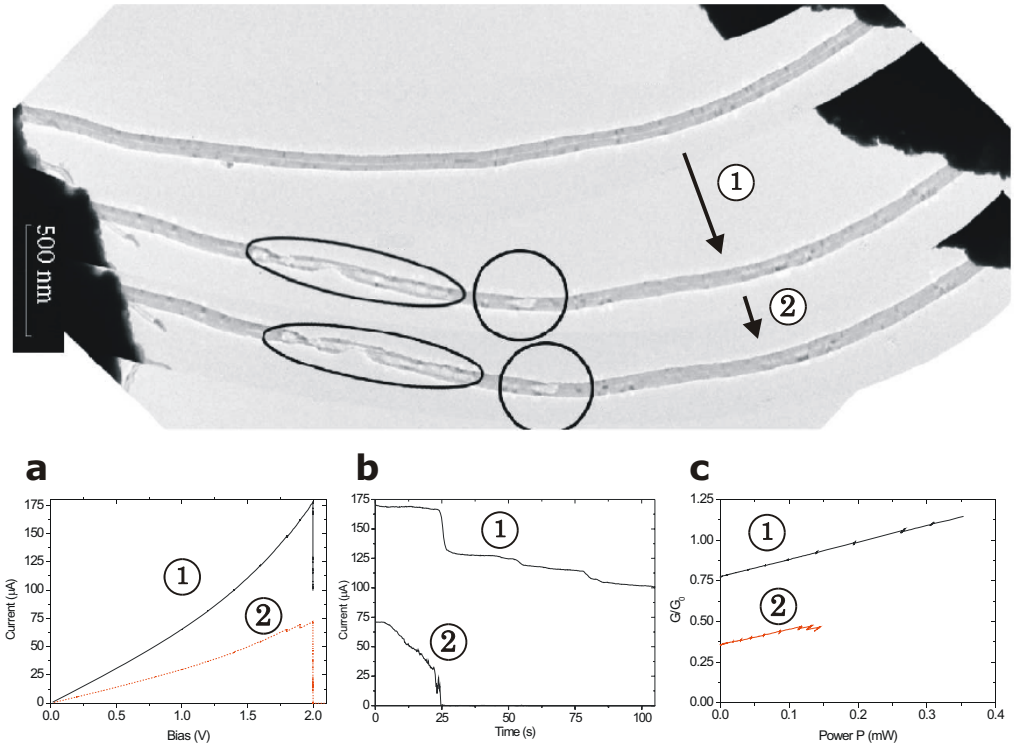

Figure 5.6: Shell-burn curves performed on a C-MWNT in nitrogen. a) IV curves. The voltage was kept fixed when saturation was reached and the current was followed as function of time. The areas with dark rings encircle the regions with most damage to the tube structure. b) The current vs time for the curves in (a). This is one of the few shell burn curves that display a resemblance to the results by Collins et al [122] with stepwise reduction of current. c) G vs P graph. The sweep follows Eq. 5.6 remarkably well for both sweeps.

Shell Burn Performed in Nitrogen

In the SEM experiments, the nanotubes were observed to fail in a single step. To study the effect of shell burn in an inert environment, shell burn experiments were done with a flow of nitrogen directed onto the nanotube. The nitrogen flow was directed onto the TEM-Chip from a handheld plastic tube. In these experiments the possibility of a spurious draft of air cannot be excluded, and the results can only be taken as an indication of what would probably happen if the experiments were performed in a truly inert environment.

Fig 5.6 show both the TEM images of the nanotube and the IV, It and G vs. P curves. This is one of the few cases where a step wise reduction in current was seen. This could be interpreted as the individual "shells" in the nanotube burning off one by one. The step size is not as constant as those reported by Collins et al. [122]. The irregular step size in the present experiment could partly be due to the nanotube

being under stress, since its a suspended nanotube not supported by a substrate as those used by Collins et al.. Figure 5.5g show the G vs P plot for the nitrogen experiment, which follows the Eq. 5.6 remarkably well for both shell burns.

5.3.3 Summary

Pristine individual C-MWNT were manipulated by etched tungsten tips to make bridges between microcantilevers on TEM-Chips for TEM investigation and electrical measurements. The contact resistance was reduced by making water condense temporarily onto the sample. The nanotube bridges had resistances increasing linearly with the length of the cantilever gap, and seemed to have a negligible contact resistance. The nanotubes were found to be diffusive conductors with a resistivity 20-50 times that of the graphite in-plane resistivity. Shell burn experiments were performed by sweeping the applied bias voltage and recording the current through the nanotube. The current increased until a saturation point would be reached at about 2 V. At the saturation point the bias voltage was kept fixed and the current was observed to decrease over time. The current decrease indicates a slow burning of the heated nanotube in air. Before and after a shell burn experiment, the nanotube was imaged in TEM. The saturation voltage of 2 V was inexplicably constant compared to the dissipated powers and estimated temperatures when shell burning was taking place. Time was found to be an important factor for the shape of the IV curve when current saturation was approached.

The simplest first order equation for the temperature dependence of resistance and conductance was compared to the results. The tubes had reasonably linear dependence of both resistance (R) and conductance (G) as function of dissipated power (P). For the described devices, plots of G vs P appeared more linear than that of R vs P. Further studies of the temperature dependence of conductance is needed to link the observations with a specific model for MWNT conduction such as those described in the beginning of the chapter.

5.4 Electron Irradiation Induced Destruction of Carbon Nanotubes

Already with the first TEM images recorded in the project, it became apparent that the carbon structures were damaged by the TEM electron beam. Several publications have described irradiation effects in carbon structures, since TEM and SEM are standard tools to image carbon nanotubes and similar structures [165]. For the present study, the TEM was operated at 100 keV. As will be discussed below, 100 keV irradiation is generally considered safe for imaging MWNT. The cause of the observed nanotube damage was hence a puzzle, and for the TEM chip measurements also a serious problem that had to be solved. Using low beam currents improved imaging conditions and resulted in lower damage rates than high beam currents. To study the damage effect we have used high current densities. The beam current has not been measured, but an upper order of magnitude estimate of the beam current

density[4] must be $j_{\max}$ =10^3A/cm^2.

Several studies of electron irradiation induced damage and the dependence on beam energy and irradiated dose have been published:

- Ajayan et al. [166] observed slow removal of carbon atoms from a SWNT at 200 keV which destroyed the nanotube in 30 min. The beam current density was about $10^{-3} j_{\max}$ corresponding to a dose of the order 10^3 C/cm^2. They explained their findings by knock-on collisions, and expected a threshold energy for the process of 120 keV.

- Smith and Luzzi [128] observed no deformation of SWNT at 80 keV at a dose of $3 * 10^4$ C/cm^2. At 100 keV they observed strong deformation of the nanotube structure at 10^4 C/cm^2. At 200 keV the nanotube turned completely into amorphous carbon at a dose of 5×10^3 C/cm^2. The disordering is attributed to $sp^2 \rightarrow sp^3$ transitions of the carbon atoms, causing cross-linking between adjacent planes in a nanotube. They discussed the difference between MWNT and SWNT and concluded that 100 keV can be used for routine imaging of MWNT while 80 keV is required for SWNT. This also indicates our experiments are performed at a safe energy level, though at $j_{\max}$ severe deformation is expected on a time scale of the order several seconds.

- Banhart [143] also observes SWNT to deform under intense 200 keV irradiation and notes that heating the samples stage to 300-700 °C has been shown to decrease the rate of defect creation since it enables broken bonds in the structure reform. Banhart [167] has also observed the slow graphitization of amorphous carbon at 80 keV irradiation, which did not influence carbon nanotube structures embedded in the amorphous carbon, in agreement with the results of Smith and Luzzi. Recently, Li and Banhart [168] have shown how a 300 kV TEM beam can be used to controllably deform MWNT and SWNT.

- Crespi el al. [169] find complete collapse and disordering of MWNT at a dose of 300 C/cm^2 at 800 keV. They observe that the knock on collisions primarily remove atoms in planes perpendicular to the beam in accordance with models of such collisions [169][128].

The reported observations of irradiation damage at 80 keV and 100 keV did not show sign of removal of material from the nanotube [128][167]. Rather amorphous carbon did appear to accumulate in the images presented by Smith and Luzzi, unlike the observations by Ajayan et al. at 200 keV where the nanotube eventually disappeared [166]. From the above observations, one should expect that MWNT irradiated with $j_{\max}$ at 100 keV should be safely below threshold, while SWNT should turn into amorphous carbon.

[4] Assuming 0.1 μA beam current at condenser lens setting "spot 2" and a beam area of $(0.1\ \mu\text{m})^2$ at high magnification.

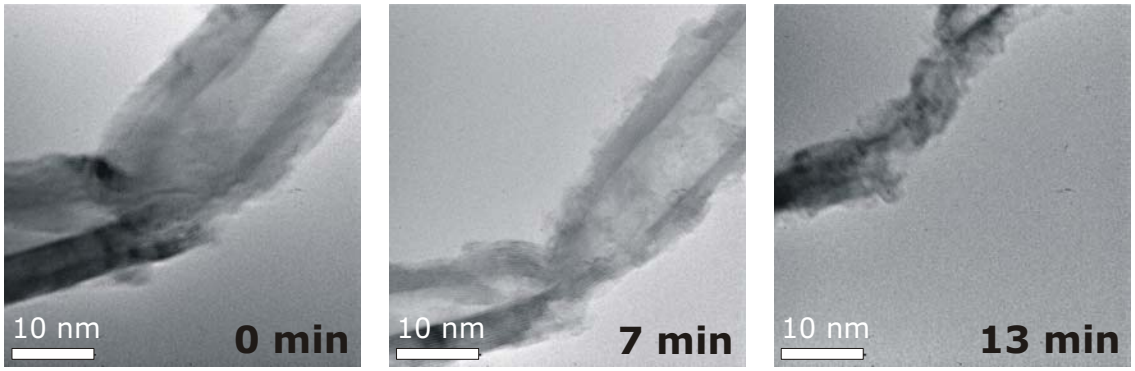

Figure 5.7: TEM image sequence showing the progessing destruction of the carbon shells structure with time under intense electron beam irradiation.

5.4.1 TEM observations of Nanotube Irradiation Damage

The TEM image sequence in Fig 5.7 shows a multiwalled carbon nanotube slowly being destroyed under the beam exposure. After 15 minutes at high beam current the nanotube structure has been completely removed. Even very large MWNT as the one shown in Fig. 5.8 can be considerably damaged by prolonged exposure to the beam.

From the cross section of both the small (Fig 5.7) and large nanotube (Fig. 5.8) it seems that a considerable fraction of the outer shells have been removed while the inner shells are less susceptible to irradiation induced damage. Irradiation induced cross-linking of the carbon bonds would be expected to appear throughout the nanotube and convert the shell structure to amorphous carbon. Knock-on collisions are expected to mainly attack graphene planes perpendicular to the beam, but the observed damage also seems to be considerable to the planes parallel to the beam on the outer shell. The nanotube does not collapse as reported in the 800 kV experiment [169]. In both nanotubes (Fig 5.7 and 5.8), the damage to the outer shells could be interpreted as the formation of pits in the structure, though one should be careful when interpreting the TEM images. Such pits are known to form by oxidation (Sect 5.1), which would also explain why material appear to be removed from the nanotube surface, and not in a uniform manner throughout the nanotube or the walls perpendicular to the beam. The question is what causes oxidation in the vacuum environment.

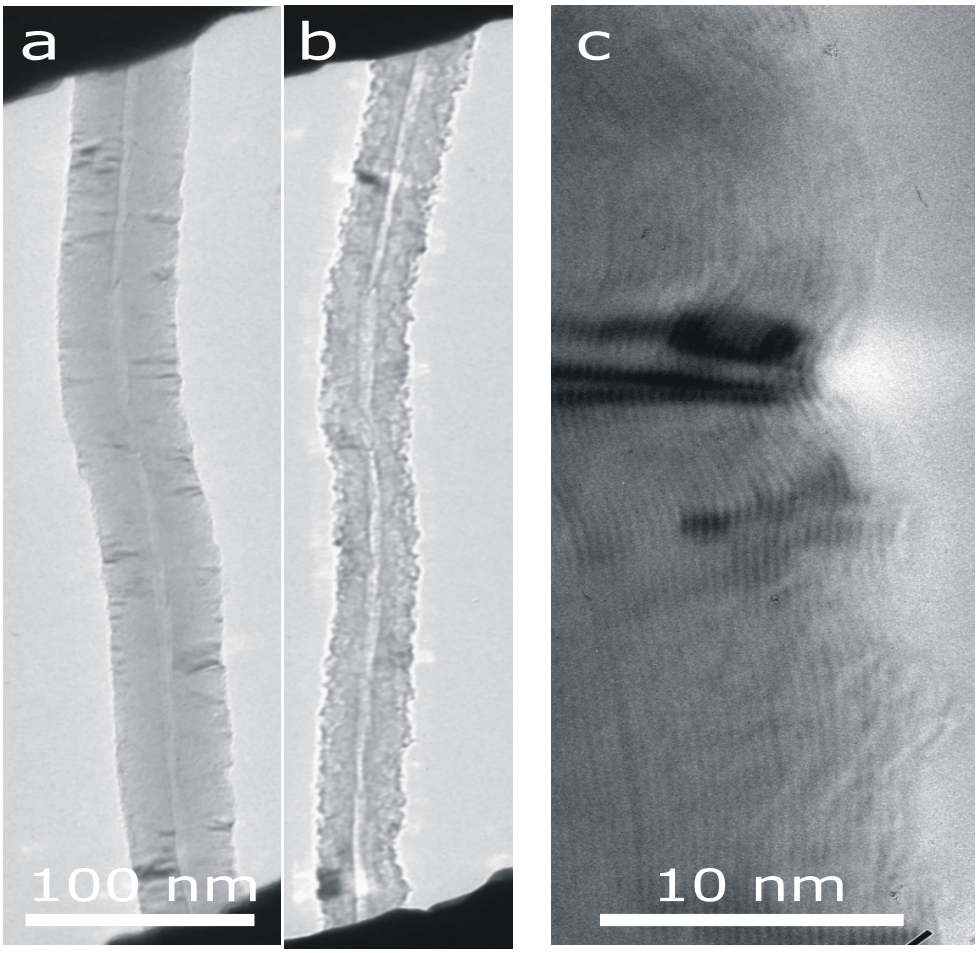

Figure 5.8: Irradiation damage on a large C-MWNT. a) The inital overview image of the suspended C-MWNT. b) The same tube after extensive imaging at high resolution with a focused beam. the inner shell structure appears relatively unaffected, vhile the outer structure has been severely damaged. c) Close-up of the outer shell structure, illustrating how regions with bent shell structure cause the dark regions visible in the overview images. The inner shells are well graphitized, while the outer shells appear relatively damaged.

5.4.2 Electron Irradiation Induced Chemical Reactions with Nanotubes

The removal of carbon by chemical reactions has been observed in other in-situ experiments with carbon nanotubes. As described in chapter 4, a carbonaceous background gas can cause deposition of amorphous carbon on irradiated structures. The effect is caused by inelastic scattering leading to ionization and dissociation, and this effect is dominant at low energies by electron-electron collisions compared to the high-energy knock-on collisions discussed above [167][165]. Depending on the type of background gas, the inelastic collisions can cause either deposition when for instance hydrocarbons are present, or etching if gasses such as water or oxygen are present [170].

For nanotubes samples, Gogotsi and co-workers [171][172] have observed that water enclosed in the nanotube interior can cause etching holes in the MWNT structure if irradiated by a sufficiently intense electron beam in TEM. The etching was believed to be caused by the reaction

$$C + 2H_2O \rightarrow CO_2 + 2H_2 \quad \Delta H = -82.4kJ/mol \tag{5.8}$$

In addition to the water reaction, carbon can be removed from the nanotube structure by the following reactions

$$C + O_2 \rightarrow CO_2 \quad \Delta H = -393.5kJ/mol \tag{5.9}$$

$$C + 2H_2 \rightarrow CH_4 \quad \Delta H = -74.81kJ/mol \tag{5.10}$$

Both oxygen and hydrogen can be present in the vacuum chamber, and also adsorbed on the nanotube (and in the case of hydrogen also released from the water reaction). Though energy is released in the reactions, an activation energy is needed to initiate the reaction (Eq. 5.4).

5.4.3 Can TEM Cause Etching of Nanotubes ?

A plausible explanation for the observed damage to the MWNT is that an oxidation is taking place on the outer shell, activated by the electron irradiation. The oxidizing agent could be oxygen (Eq. 5.9), water vapor (Eq. 5.8), hydrogen (Eq. 5.10), or unknown compounds adsorbed on, or absorbed within the MWNT. That absorbed compounds within the nanotube should cause the damage is unlikely, since the effect appear to occur at the outer surface. Nanotubes that have been used for shell-burn experiments, where the outer layers have been removed, are also damaged, so it seems likely that the predominant species that could be adsorbed on the nanotube surface must be water or oxygen from ambient air. Oxygen and water vapor are abundant and especially water could adsorb on the sample holder in air and in this way be transferred to the TEM chamber. A leak in the TEM vacuum system could

in principle also increase the water and oxygen or water vapor pressure in the TEM vacuum system, but the vacuum was in fine condition during the experiments.

The TEM is equipped with a cold finger that can be cooled by liquid nitrogen, making plates above and below the specimen holder reach temperatures low enough to condense water and carbohydrates out of the vacuum chamber. A cold finger is normally used for condensing carbohydrates to avoid electron beam deposition in the TEM. Water has a vapor pressure of 10^{-8} Pa at -100°C [173], and even lower at liquid nitrogen temperatures, while oxygen has a vapor pressure of 10^4 Pa at liquid nitrogen temperatures [173]. In the high vacuum TEM chamber, hydrogen and oxygen cannot be removed from the background gas while the water vapor pressure should be drastically reduced at liquid nitrogen temperatures.

Since the damage primarily attacks the outer shell, single wall nanotubes (SWNT) would probably be highly sensitive to the effect. This was tested experimentally: A lacy carbon grid was dipped into a sonicated isopropanol dispersion of HiPCO SWNT [174]. The grid was dried and it was attempted to acquire high resolution TEM images of the SWNT. Figure 5.9a-b shows a low resolution TEM image of the SWNT sample before and the attempt to image at high resolution. It turned out to be impossible to achieve high resolution images of the SWNT as they practically disappeared as the beam was focussed on them. This could in a way be expected considering the possibly very high current density in the beam and the damage rates reported in literature at such irradiation doses [128][166].

The cold finger was then cooled with liquid nitrogen and a new attempt was made to image another region of the SWNT sample. The SWNT were now stable even at high magnification with focused beam and high beam current. Figure 5.9 shows a small nanotube bundle extending from the sample being almost unaffected by 14 minutes imaging. The nanotube bundle did not appear to be reduced in diameter or density, but rather seemed to deform slightly, as expected since knock-on collisions will create disorder in the structure.

The observed damage to the SWNT when using a cold finger could be caused by electron irradiation induced disordering in the nanotube structure [128]. The very limited damage rate when using the cold finger indicates that the actual beam current density in the TEM is considerably lower than above estimated maximal beam current density, $j_{\max}$. The above observations seem to support the hypothesis that water is the primary cause for the etching of the nanotubes from the outer shell. By using a cold finger at liquid nitrogen temperatures, the water can be frozen out of the background gas and imaging of nanotubes can be done for tens of minutes with very limited damage to the nanotube structure. If indeed water is such an important factor for the observed irradiation damage, it could also explain the discrepancy between the observations at 200 keV of Ajayan et al. and Smith and Luzzi, where Ajayan observes loss/etch of carbon while Smith and Luzzi observe deformation of the structure and deposition of carbon.

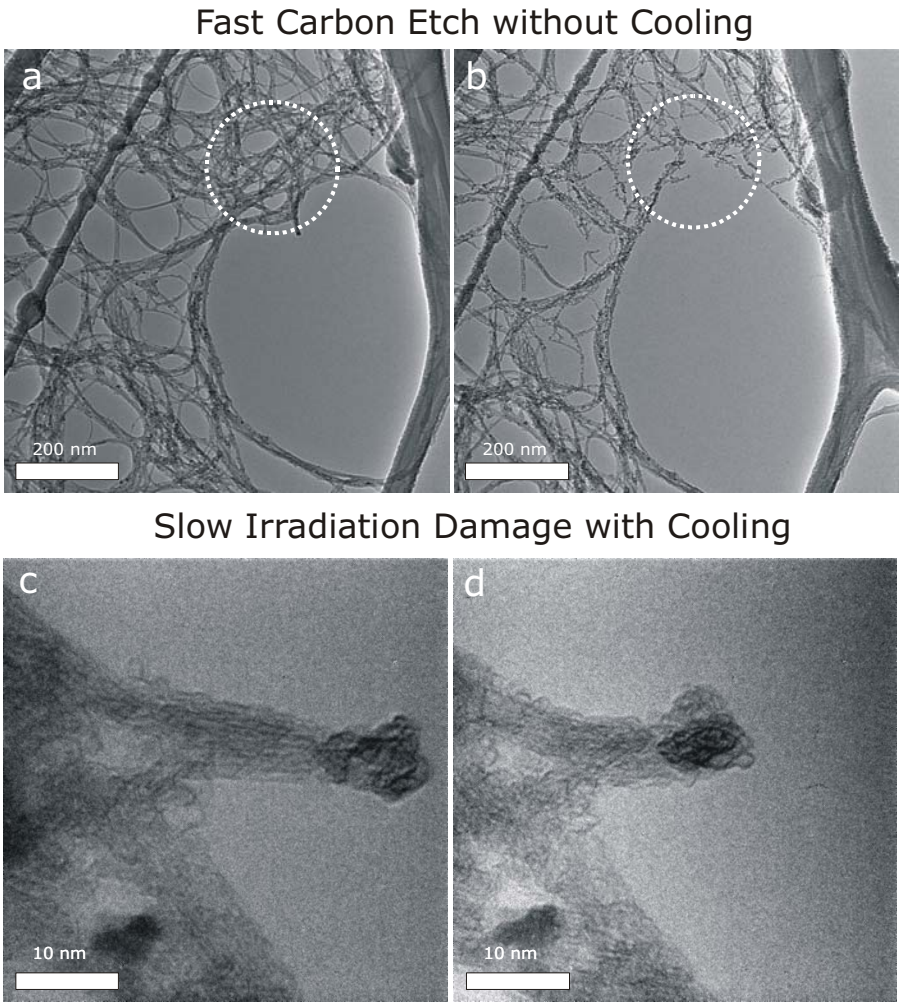

Figure 5.9: The irradiation induced damage rate and type of damage depends on the cold finger temperature. a-b) HRTEM was attempted on a lacey carbon grid with SWNT without cooling the cold finger. As the beam was focused to achieve a higher magnification the SWNTs were rapidly disappearing. About 30 minutes of irradiation mainly in the encircled region removed a large fraction of the exposed SWNT sample. c-d) Cooling the cold finger with liquid nitrogen made it possible to image at high magnification. Image (c) and (d) show the same sample before and after 14 minutes exposure to the focused beam at high magnification. Without cooling, focussing would not have been possible and such a small structure would have dissappeared in a couple of minutes. Little -if any- material is removed during the 14 minute exposure with wooling. The change in the SWCNT structure with cooling is probably mainly due to disordering rather than etching.

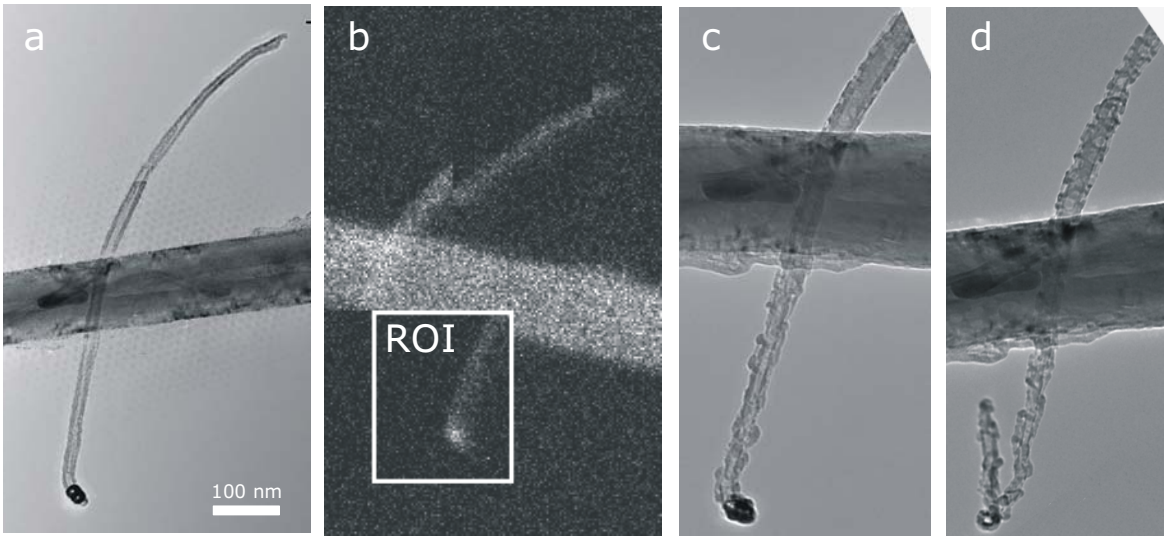

Figure 5.10: SEM induced etch of C-MWNT. a) TEM image of a small Ø22 nm C-MWNT adhering to a large C-MWNT suspended between two cantilevers. b) The lower part of the small C-MWNT was exposed to 5 keV SEM beam for 4 minutes by selecting a small region of interest (ROI). c) TEM image after the SEM exposure shows a considerable damage to the exposed part of the tube. d) Imaging in TEM without cooling eventually also damaged the tube.

5.4.4 Nanotube Damage in SEM

As discussed in Sect. , the ionization and dissociation cross sections for gas molecules are generally peaked at low energies, indicating that secondary electrons might be the main cause of irradiation induced etching. If secondary electrons are the main initiators of the etching process, SEM imaging of carbon nanotubes could also have an influence on the nanotube structure despite the beam energy being well below the above listed thresholds for TEM irradiation damage. The image sequence in Fig. 5.10 show a small C-MWNT first imaged in TEM, then transferred to the MIC SEM where a part of it was exposed for 4 min at 5 keV and then finally returned to the TEM to observe the effect of the SEM exposure. In the initial TEM image, the small C-MWNT had what appeared to be well graphitized shells. The SEM image shows a small region of interest (ROI) with area of 0.05 μm^2 that was positioned to only expose the lower part of the nanotube to the scanning beam. The electron beam current was not measured but is expected to be in the range 100-400pA from previous measurements on the MIC SEM. The accumulated dose during a 4 min exposure in the region of interest is hence of the order 1 μC/μm^2. The nanotube was then imaged in TEM again. Figure 5.10c shows that the exposed lower part of the nanotube has been severely damaged by the SEM irradiation, while the upper unexposed part is relatively unaffected. As expected, continuous exposure in the TEM further damaged the nanotube as shown in Fig. 5.10d. In the first image, the nanotube has a diameter

of about 22 nm and after the SEM exposure the diameter has at least been reduced to 17 nm, corresponding to the loss of about 7 shells. The observed etch rate is in this case of the order 10 shells per $\mu C/\mu m^2$ (or 0.1 shell per C/cm^2).

The etch rate imposes strict limits on the allowable exposure of carbon nanotubes devices if defect free nanotubes are required. For EBL the required dose for exposing the resist is normally of the order 10 $\mu C/cm^2$. The EBL exposure itself is hence orders of magnitude too low to remove an entire shell from a carbon nanotube, but would give rise to a damage probability of removing 1 per 10^6 atoms for a SWNT. A (10,10) SWNT has $2*10^5$.atoms pr μm. The EBL exposure alone could cause a defect for every 5 μm nanotube length. For EBL devices, the nanotubes are usually located by SEM to prepare the EBL pattern, before resist is spun onto the sample[5]. Such SEM imaging will expose the nanotubes to a higher irradiation dose. Two additional factors might increase the etch rate: the nanotubes supported by a surface might have a small capillary water meniscus below them, and the SE yield from the supporting surface is likely to be much higher than from the nanotube itself; finally, the chemical reactions taking place in the EBL resist might also cause nanotube damage. These considerations imply that for EBL exposure, multiwalled carbon nanotubes could be damaged in the outer layers by the process, and in the case of SWNT defects must be expected. The initial SEM imaging and EBL should probably be done in vacuum chambers with cold fingers to avoid damaging the nanotubes. It is planned to install a cold finger in the SEM to test if cooling would reduce the SEM etch rate as well. Although the question regarding the cause of the TEM and SEM irradiation induced damage may have been answered, it is still puzzling that such damaging effects have not been reported much in literature, considering the amount of work done on EBL based nanotube devices and TEM irradiation effects. If the majority of EBL devices have been made in SEM with a carbonaceous background gas, the etch rates might be lower and the deposition effect has been dominating.

[5]Though some use AFM to image the sample and prepare the pattern in order to avoid carbon deposition during SEM imaging [26].

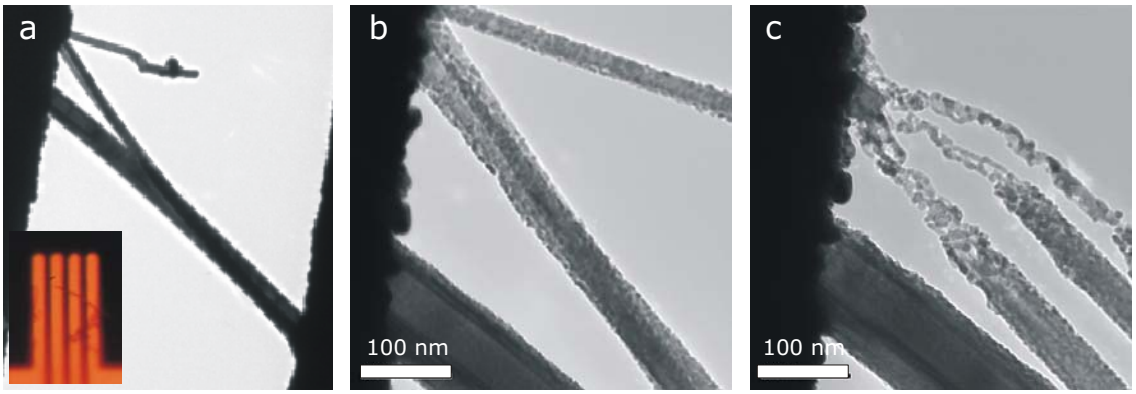

Figure 5.11: TEM damage to InP nanowires (without cooling the cold finger). a) TEM overview image of the InP nanowire bridging two cantilevers. The inset shows an optical microscope image of the device. b-c) The TEM induced etching could be used to remove the small additional nanowires by focussing the beam onto them for a couple of minutes. The small wires were almost removed by the exposure to the beam while the main wire was largely unaffected by the nearby intense electron beam.

5.4.5 InP Nanowire Damage in TEM

Apart from C-MWNT and SWNT, a few TEM-Chips were prepared with InP nanowires[6] to test if such nanowires could be studied by the TEM-Chip method as well.

The InP wires are known to be have an oxide layer on the surface [176]. The prepared devices often had resistances of the order several MΩ when the wires had been placed on the cantilevers. After the TEM investigation some bridges were observed to have a linear IV characteristic in the bias voltage range +/-100mV. The resistance was comparable to those of EBL devices made from similar InP wires, where the resistance was determined by the nanowire length L as $R = 40\ \mathrm{k\Omega} + 45\ \mathrm{k\Omega}\ L/\mu\mathrm{m}$ [176]. The TEM irradiation apparently improved the contact resistance for some devices. As shown in Fig 5.11, the TEM beam was also observed to damage the InP wires and could be used to remove small wires completely. When the wires appeared layered, especially the outer layer was susceptible to the irradiation induced damage, and this could relate to the improved contact resistance after TEM irradiation. It has not yet been tested if cooling the cold finger prevents damage on the InP. It is interesting that the TEM beam can be used to selectively remove InP nanowires from the devices, though the underlying processes and chemical composition of the layers and the remaining residues remain to be investigated.

[6]Sample supplied by Erik P. A. M. Bakkers from Philips Research Laboratories, Eindhoven [175]

5.4.6 Summary

It has been observed in TEM that the outermost shells of C-MWNT are damaged and removed by electron irradiation, while deeper layers in large diameter nanotubes appear unaffected. SWNT were observed to be very susceptible to the irradiation induced removal of carbon. The rate for irradiation induced loss of material could be reduced to a negligible level by cooling the cold finger on the TEM. With cooling, the damage effect changed to a slow deformation rather than loss of material. The deformation can be explained by the irradiation induced disordering of carbon shell structures [168].

Since cooling the cold finger can drastically reduce the loss of carbon, water seems to be an important factor causing etching of carbon structures under electron radiation. Water is the only substance readily available in the setup that can react with carbon and also be removed by cooling the cold finger. SEM irradiation of C-MWNT at 5 keV was observed to cause loss of material as well, indicating the process can take place well below the 80 keV threshold for knock-on collisions reported by [128]. The observation that the damage can even take place in SEM is important, not only for the work with nanomanipulation but also for production of carbon nanotube devices with EBL. Finally, irradiation induced material loss was observed in InP nanowire devices, and could be used to selectively remove nanowires and often improve the contact resistance of the bridging nanowires lying on cantilevers.

5.5 Conclusion and Outlook

CVD produced multiwalled carbon nanotubes (C-MWNT) were used to test scanning micro conductance probe measurements on nanotubes in air and in-situ SEM. The limited resolution of the images in the instruments and high sensitivity to vibrations and drift during the measurements led to the development of the TEM-Chip system described in Sect 2.3.3.

The TEM-chip system was used to investigate where and how the C-MWNT would burn in air and nitrogen. Reliable and stable contact could be achieved to about half the nanotubes placed onto the cantilevers by the described procedure. The nanotubes appeared to be diffusive conductors and had a resistivity 20-50 times that of in-plane graphite resistivity. The nanotubes were capable of sustaining current densities up to $10^7 \mathrm{A/cm^2}$ and dissipated powers below 1 mW. The TEM-Chips made it possible to observe the C-MWNT with atomic resolutions and follow the detailed changes in the structure of the nanotube when high bias voltages had been applied. The nanotubes primarily failed in the middle of the gap between the two cantilevers supporting the nanotube, in accordance with expectations for joule heated diffusive conductors. However, the onset of current saturation and burning of the shell structure was remarkably constant at about 2 V bias voltage for most nanotubes. TEM-

Chip measurements of the nanotube conductivity was found to be linearly dependent on the dissipated power even for nanotubes that had been subjected to several shell burn experiments. Whether this linear dependence corresponds to a highly linear dependence of conductivity on temperature remains to be investigated.

The effect of TEM irradiation on MWNT and SWNT was studied. It was found that water vapor is likely to cause etching of the outer layers of carbon structures under electron irradiation, even with beam energies that were otherwise expected to be harmless to MWNT. The etching rate could be reduced to an almost negligible level by cooling a cold finger in the TEM by liquid nitrogen. TEM irradiation was also damaging to the structure of InP nanowires.

SEM irradiation of a MWNT was found to create pits in the shell structure, just as the TEM irradiation, indicating that care must be taken when imaging nanostructures in both SEM and TEM.

5.5.1 Outlook

The reliability of the TEM chip system has been demonstrated, and the ability to use the wide variety of microfabricated probes, such as grippers, opens up unprecedented opportunities. If a nanowire is suspended between the actuators of a gripper, it should in principle be possible to study both the electrical, and mechanical properties. The experiment would resemble that of piezoresistive measurements on the soldered carbon nanotube in Sect. 4.5.3. But instead of using an tungsten tip to actuate the cantilevers, the gripper could be used (if sufficient gripping force is available). This would make it possible to perform the experiment under a wide range of conditions such a cryogenic, or various environments, and TEM analysis can be done between experiments. Its worth noting that important material constants such as the thermal conductivity can be measured by a lock-in four point conductance setup by the so-called 3ω-method [177].

Experiments are planned to do a more quantitative measurement of the beam current density and the dependence of etching on the irradiated dose. It will also be attempted to leave the sample overnight in the vacuum chamber to see if that reduces the etch rate. This simple experiment should make it possible to determine whether the water source is the limited amount of water adsorbed on the specimen holder or some other source such as a leak around the specimen holder.

Chapter 6

Summary

This Ph.D. project aimed at developing new tools for manipulation, assembly and characterization of three-dimensional nanometer-scale structures.

To achieve the high spatial resolution required to observe the objects and tools for nanomanipulation, several in-situ scanning electron microscope (SEM) nanomanipulation setups were developed. The setups were based on the stage available in the SEMs, and an additional three degree-of-freedom manipulator with sub-micron precision. The SEM systems were used for pick-and-place manipulation of nanowires while an environmental SEM system was used for electron beam deposition experiments.

A survey was presented of the forces estimated to be required for picking up nanowires. This showed that the minimum force would probably be required when peeling a nanowire extending over the edge of a surface it is adhering to. Microfabricated grippers based on electrostatic and electrothermal actuation were designed, fabricated, and characterized. The electrostatic grippers were successfully used for in-situ SEM pick-and-place manipulation of silicon nanowires. The wires were moved from suitably prepared substrates onto silicon chips and TEM grids. Successful manipulation was only achieved with wires prepared as the survey of forces had indicated. Prototypes of the electrothermally actuated grippers were used to demonstrate the possibility of acquiring a force feedback signal from the gripping forces.

To directly deposit three-dimensional nanostructures and also mechanically and electrically contact manipulated nanostructures, electron beam deposition (EBD) was studied. When the EBD was done in an environmental SEM, using water vapor as the environmental gas, it was discovered that deposited structures could contain a core of solid polycrystalline gold. The environmental EBD (EEBD) was studied in detail, and the gold core was found to be highly conductive and capable of carrying high current densities comparable to carbon nanotubes. The EEBD was also used to solder carbon nanotubes onto cantilever electrodes, and gave a low contact resistance.

A simple electron beam lithography (EBL) system was developed to control the electron beam when creating three dimensional EBD structures. A feasibility study was made of EEBD and the limits to scan rate, deposition angles, and deposition line

width. A survey was also presented of the various contamination effects that should be considered when using EBD. Despite the discussed limitations, EEBD seems to be a versatile and useful tool for a wide range of applications in a nanomanipulation setup.

To characterize the manipulated or deposited nanostructures, a "TEM-Chip" method was developed, based on chips with microcantilever electrodes. The TEM-Chips were demonstrated to enable combined electrical characterization and TEM analysis. The method was used to study the electrical properties of multiwalled carbon nanotubes and their breakdown when carrying high currents. Finally the effect of the electron beam irradiation of carbon nanotubes in SEM and TEM was investigated. It was observed that the outer shells of nanotubes were severely damaged by the electron irradiation. It was shown how cooling a cold finger in the TEM with liquid nitrogen could efficiently reduce the irradiation induced damage rate. Chemical reactions of the surface carbon atoms with water seems to be the cause of the observed nanotube etching. TEM investigation of a sample that had been irradiated in SEM, showed that SEM radiation also could cause considerable damage to the nanotube shell structure.

The methods and systems developed in this project seem to support each other. The TEM-Chip system will enable a detailed investigation of the effects of EEBD and manipulation on nanowires and tubes. The development of improved electrostatic and electrothermal grippers will not only lead to improved possibilities for pick-and-place manipulation, but also to new TEM-Chip designs for in-situ TEM experiments (and possibly also cryogenic measurements). The EEBD can both aid the pick-and-place manipulation by soldering grabbed objects to the target position and improving electrical contact, but also be used to create nanostructures such as nanotweezers tips on the grippers.

Appendix A

Article [1]
Electro-thermally Actuated Microgrippers with Integrated Force Feedback

INSTITUTE OF PHYSICS PUBLISHING JOURNAL OF MICROMECHANICS AND MICROENGINEERING

J. Micromech. Microeng. **15** (2005) 1265–1270 doi:10.1088/0960-1317/15/6/018

Electro-thermally actuated microgrippers with integrated force-feedback

Kristian Mølhave and Ole Hansen

MIC—Department of Micro and Nanotechnology, Technical University of Denmark, DK-2800 Kgs. Lyngby, Denmark

E-mail: krm@mic.dtu.dk

Received 2 December 2004, in final form 30 March 2005
Published 9 May 2005
Online at stacks.iop.org/JMM/15/1265

Abstract

Microfabricated grippers and tweezers are promising tools for manipulation of micro- and nanoscale objects. As with ordinary macroscale grippers, the ability to sense the forces involved in grabbing would be advantageous for controlling the operation as well as for measuring the mechanical properties of the grabbed object. A simple design is presented for an electro-thermally actuated microfabricated gripper capable of providing a piezoresistive read-out of the gripper deflection, which can be used to measure the forces applied to the grabbed object. Measurements of actuation of test devices are presented and found to be in reasonable agreement with expected values. Finally, piezoresistive measurements of the gripper deflection are demonstrated.

1. Introduction

The ubiquitous presence of gripping tools in everyday workshop processes makes microgrippers interesting tools for handling micro- and nanoscale objects. In recent years several designs for microfabricated grippers and tweezers have been demonstrated. These range from almost millimeter-sized grippers made from two chips bonded together with a bimetal cantilever and piezoresistive sensor cantilever [1] or electro discharge machined (EDM) grippers with optical force-feedback [2], over sub-millimeter electro-thermal [3] and electrostatic microgrippers [4, 5], to carbon nanotube tweezers for handling objects on the nanometer scale [6, 7]. Recently, microfabricated devices have become commercially available from companies such as Zyvex and Nascatec. The actuation of grippers is often based on either electrostatic attraction, such as comb drives [8] or parallel flexible beams [4], or on electro-thermal expansion of parts by resistive heating to move the actuator. Electro-thermal actuators have been made in many designs such as two- or three-beam actuators [9, 10] and even by design optimization algorithms [11].

Although adhesion forces generally make pick-and-place operations difficult on micro- and nanometer length scales, biological cells [12] as well as nanoscale objects have successfully been manipulated by tweezers [5–7].

For successful manipulation of a macroscale object, control of the gripping force is usually advantageous. For automated pick-and-place processes, force-feedback also enables a quick detection of whether an object has been grabbed. As still smaller objects are being manipulated, there is also a fundamental interest in studying the forces involved in gripping micro- and nanoscale objects, because the gripper–object interactions become increasingly complicated as the surface forces become increasingly important and the simple models of macroscale friction less correct. To make microgrippers a reliable tool for nanomanipulation, the physics of gripping on this scale has to be systematically investigated. This requires measurement of the involved forces, and today it seems that no gripper is available with force-feedback and well-defined end-effectors on the sub-micron scale to make such investigations. Force detection between a single tip and a surface is done routinely by atomic force microscopy (AFM), but AFM is usually limited to planar structures on surfaces. A microgripper with sensitive force-feedback would make force measurements possible on three-dimensional objects. To date, devices that provide such feedback signals have only been sparsely reported in the literature, such as the EDM fabricated device [1] or bonded-chip structures [2], and it will be difficult to downscale such structures with the required precision of the gripper end-effectors to the size required for manipulation of nano- and micrometer objects.

An overview of some grippers presented in the literature is shown in table 1. The actuation range seems to be highly dependent on the chosen device length, and electro-thermal

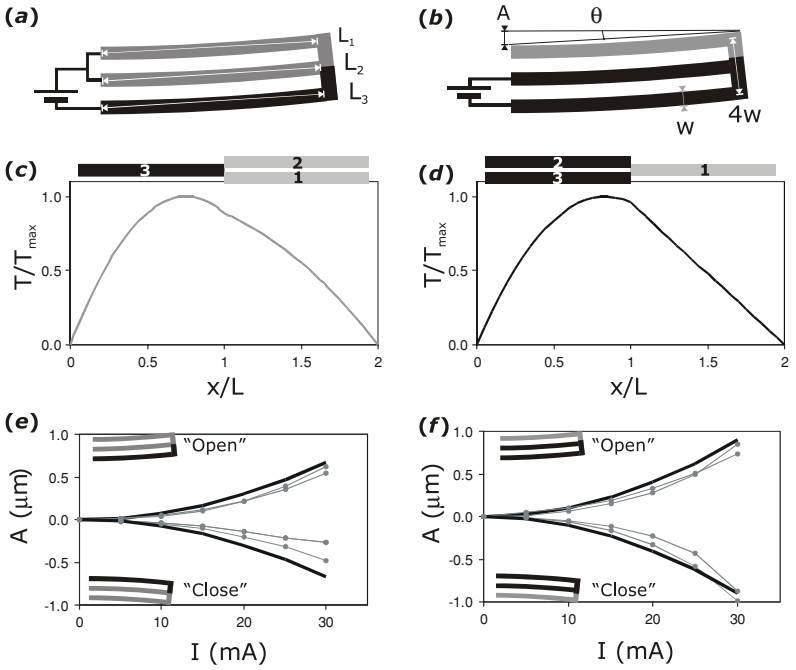

Figure 1. Actuation by resistive heating. The structure bends when two (or one) beam resistors are heated relative to the remaining beam(s). Black color indicates the higher and gray the lower temperature. (*a*) One hot and two cooler beams. (*b*) Two hot and one cooler beam. (*c*) and (*d*), respectively, show the calculated temperature profile for (*a*) and (*b*). (*e*) and (*f*), respectively, show the calculated actuation as a function of current for (*a*) and (*b*), compared to the measured actuation of two devices.

Table 1. Approximate values for gripper specifications. Grippers with force-feedback are indicated with an asterisk (*).

Actuation principle	Length (μm)	Gap (μm)	Actuation (μm) per arm	Force (μN)	Reference
Electro-thermal	500		30	15 000	[11]
Shape memory alloy	3900	1000	180	17 000	[13]
Electro-thermal	1000	18	8	210	Zyvex model SM
Electro-thermal	1000	500	25	550	Zyvex model BB
Bimetal*	1500		200	250	[1]
Electrostatic	1200	150			Nascatec
Electrostatic	500	10	10	0.013	[8]
Nanotweezer	10	2	1	0.01	[6]
Electrostatic	100	2	1	1	[4, 5]
Electro-thermal*	100	2	1	10	This work

grippers are generally capable of applying larger gripping forces than electrostatic grippers. The small size of the device makes thermal processes fast and hence the response time of the order of tens of milliseconds [9–11].

This paper presents a simple design of an electro-thermally actuated microfabricated gripper capable of providing a force-feedback signal. The design is based on a simple actuator/sensor structure consisting of three parallel beams connected by an end bar as depicted in figure 1(*a*). Three-beam actuators have been demonstrated to work with other microfabricated designs [9, 10], and recently it was demonstrated how such actuators are able to both open and close [14]. The single mask microfabrication process makes it easy to achieve a high resolution of the end-effector shape, which is essential for precise gripping of nanoscale objects.

The present grippers have been made to test the three-beam actuation and force-feedback concept, but lack the high aspect ratio (height/width) of the beams to avoid out-of-plane bending and the ability to achieve large gripping forces. We are developing a new microfabrication process capable of producing more suitable beams for useful devices.

In section 2 the basic actuation and sensor properties of the design are estimated from simple models. Section 3 presents measurements on microfabricated test devices.

2. Theory of operation

The devices presented here are all based on a fundamental actuator/sensor structure consisting of three beams connected by an end bar as shown in figures 1(*a*) and (*b*). The structure is made of a resistive material layer so that the beams can be heated by a current passed through them, making the end bar move sideways due to unequal thermal expansion of the three beams. The beams are made from a single material and can be defined by a single lithographical mask. Depending on the connection of the gripper arms, the design allows

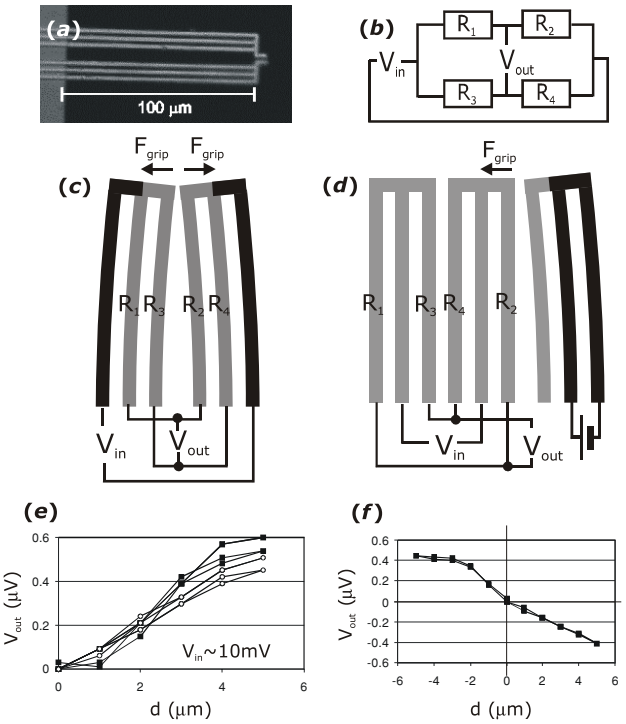

Figure 2. Piezoresistive feedback. (*a*) Optical image of the test device. (*b*) A typical Wheatstone bridge resistor configuration. (*c*) Gripper made with two actuators in the configuration from figure 1(*a*) connected as a Wheatstone bridge circuit. (*d*) Gripper configuration with three, three-beam structures connected to avoid thermal stress influencing the sensitive force detection. (*e*), (*f*) Piezoresistive measurements on the setup in (*c*) and (*d*), respectively, made by deflecting the gripper tip a distance d (in the direction of F_{grip}) while applying a voltage of about 10 mV at 1 kHz using lock-in detection. (*e*) Piezoresistive signals V_{out} as functions of deflection d when opening the gap by opening and closing each actuator repeatedly (square and circle markers indicate deflection of the left and right part). (*f*) Piezoresistive signal when deflecting the sensor in (*d*) back and forth from the neutral position.

for several sensing-actuation configurations. Current can be applied to the actuator in two ways, shown in figures 1(*a*) and (*b*), to make it bend sideways. If for instance current is sent through resistor 3 in figure 1(*a*) and led to ground through resistors 1 and 2, the actuator will bend sideways (upward in the figure). If the current is applied in a mirrored configuration, the actuator moves in the opposite direction, as shown in figure 1(*e*). Using two opposing actuators in a gripper setup as in figure 2(*a*) makes a gripper capable of both opening and closing the gap depending on how the driving current is applied. By connecting the actuator beams in a Wheatstone bridge configuration as shown in figure 2(*b*), the difference in the piezoresistive changes of the shortened and the elongated cantilevers can be measured to give a value for the actuator deflection and hence the applied gripping force when the spring constant of the structure is known.

2.1. Mechanical analysis

2.1.1. Thermal actuation. To estimate the actuation properties of the device we assume the material properties to be independent of temperature to a first approximation. As seen in figure 1, each of the three beams has initial room temperature length L, width w and height h. When forces or currents are applied to bend the actuator, the beams have lengths $L_i = L(1 + \alpha T_i) - F_i/k_{\text{beam}}$, $i = 1, 2, 3$, where T_i is the average beam temperature, α is the thermal expansion coefficient, F_i is the force applied to each beam by the end bar and k_{beam} is the tensile spring constant of the beam. For small range actuation $A \ll L$, as in figure 1(*b*), we can approximate $A = L\theta$, where $\theta = (L_1 - L_3)/4w$. With forces and moments in equilibrium, one finds that

$$A = \alpha \frac{L^2}{4w} \Delta T,$$

with the beam average temperature difference $\Delta T = T_1 - T_3$ between the hot and cold beams. For the gold structure shown in figure 2(*a*) the calculated actuation is 1.7 μm per 100 K temperature difference.

2.1.2. Actuator spring constant. The spring constant of the three-beam structure can be calculated from the actuation $A(x)$ of a single cantilever beam when applied a transverse force F_L and moment M_L at the tip $A(L) = 12(M_L L^2/2 - F_L L^3/3)/(Ehw^3)$, with Young's modulus $E = 78$ GPa for gold. Upon combining three beams into an actuator, the bending moments of the three beams will equal that of the tensile forces in the individual beams if the end bar is at an angle $\theta = A'(L) = 12(M_L L - F_L L^2/2)/(Ehw^3)$ giving $3M_L = -8w^2 k_{\text{beam}} A'(L)$, with tensile spring constant of the individual beam $k_{\text{beam}} = Ewh/L$. The spring constant, k_{act}, when pressing the actuator sideways as $F_{\text{act}} = 3F_L = -K_{\text{act}} A(L)$ can then be shown to be

$$k_{\text{act}} = \frac{11}{4} Eh \left(\frac{w}{L}\right)^3.$$

For the gripper in figure 2(*a*), $k_{\text{act}} = 2$ N m^{-1}. The thermally actuated grippers are generally more rigid than electrostatically actuated grippers with similar lengths. The presented gripper is about ten times more rigid than a correspondingly sized electrostatic gripper with a cantilever actuator with dimensions of a single beam.

2.2. Thermal distribution

The average temperature of beams 1 and 3 can be calculated from the temperature distribution, $T(x)$, found by analytically solving the steady-state heat continuity equation $T''(x) = -C(x)$, where $C(x) = J^2(x)\rho/\kappa$, with the current density $J(x)$ (constant in each beam), electrical conductance ρ, and heat conductivity κ. To estimate the properties of the gripper we will assume that convective and radiative heat losses can be neglected.

With an applied current I, we find a temperature distribution for the structure in figure 1(*a*) as shown in figure 1(*c*), as a function of distance along the structure as sketched in the graph. The maximum temperature in the beam is $T_{\max} = (9I^2\rho)/(32\kappa wh)$. The current must be limited, so $T_{\max} < T_{\text{limit}}$, where T_{limit} is typically some fraction of the material melting point to avoid damaging the structure. Naturally, one should also consider the temperature limits of the objects to be manipulated when defining T_{limit}. By averaging the temperature distribution in beams 1 and 3 we

find the average temperature difference as a function of applied current $\Delta T = (I^2\rho)/(16\kappa wh)$. The maximal temperature difference ΔT_{limit} is achieved when T_{limit} is reached and is $\Delta T_{\text{limit}} = 2T_{\text{limit}}/9$.

We can now express the actuation as a function of current for the configuration in figure 1(*a*):

$$A = \frac{\alpha\rho}{\kappa}\frac{L^2}{64w^2h}I^2.$$

The maximal actuation is $A_{\text{limit}} = (\alpha L^2 T_{\text{limit}})/(18w)$. Using the melting point of gold as T_{limit} gives an upper estimated actuation range for the test device of about 4 μm at a current $I_{\text{limit}} = 146$ mA and an actuation voltage of 230 mV.

If the heating current is applied as in figure 1(*b*) rather similar results are obtained with the maximal actuation 8% larger than in the case of figure 1(*a*). However, the maximal temperature is in this case reached in both hot beams in figure 1(*b*) whereas the two cold beams in figure 1(*a*) reach only $90\%T_{\max}$. In the following we will use the setup in figure 1(*a*) to avoid the highest temperatures in the beams used as piezoresistors.

2.3. Piezoresisitve sensitivity

The piezoresistive change in the beam resistance $\delta = \Delta R/R$ can be calculated from the gauge factor K and change in length $\Delta L/L$ due to tensile forces in the individual beams as $\delta = K\Delta L/L$. For silicon, the gauge factor can be up to >100 [15] while for gold it is about 4 [16].

Accurate measurements of the piezoresistive response can be made using a Wheatstone bridge to reduce noise by measuring the change in a resistor relative to a network of thermally similar resistors [15]. A standard Wheatstone configuration as shown in figure 2(*b*) would give a signal $V_{\text{out}} = (\delta_1 - \delta_2 - \delta_3 + \delta_4)V_{\text{in}}/4$ if all resistors have almost equal values $R_i = R(1 + \delta_i)$. In the three-beam actuator designs shown in figures 2(*c*) and (*d*), the stress induced by pushing the three-beam sensor sideways gives $V_{\text{out}} = V_{\text{in}}\delta/2$. The force sensitivity S_F of these sensor designs can be calculated from the equations in section 2.1 to give

$$S_F = \frac{V_{\text{out}}}{V_{\text{in}}F_{\text{grip}}} = \frac{2KL}{33w^2hE}.$$

For the gold device presented here the sensitivity is estimated to be 0.1 mN^{-1} or 0.1 mV per μN of gripping force per volt applied to the gripper. The position sensitivity $S_x = Kw/(6L^2) = 140\ \text{V V}^{-1}\ \text{m}^{-1}$, so moving the gripper tip 1 μm should give 0.14 mV output signal per applied volt.

The calculated sensitivity is comparable to that found in some other devices made from materials with higher piezoresisitive coefficients [1]; however, the applicable voltages are limited by the maximally allowable current to avoid reaching T_{limit}.

In the configuration of figure 2(*c*), the applied voltage will also lead to actuation and the thermally induced stress in the structure will give an additional contribution V_{add} to the measured signal from the sensor V_{meas}, which must be subtracted from the measured signal to obtain the true signal due to deflection $V_{\text{out}} = V_{\text{meas}} - V_{\text{add}}$.

V_{add} can be estimated as $V_{\text{add}} = 2KwA/L^2$. This is proportional to I^2 and can reach a voltage of order mV for the gold gripper. Thus, V_{add} can be orders of magnitude higher than the gripping force signal V_{out}. Since the error in the piezoresistive signal is expected to be proportional to V_{in}^2, this voltage should be kept as low as possible. The best method for measuring V_{out} is lock-in detection of an oscillating signal sufficiently small to avoid oscillating actuation—a dc voltage can be added for simultaneous actuation.

For a more sensitive detection of the gripping force one can use the Wheatstone bridge setup shown in figure 2(*d*), which is not influenced by thermal stress caused by the voltage applied for piezoresistive measurements in the structure—and one can then use the slightly more efficient configuration from figure 1(*b*) or other suitable actuator designs for actuation. Such a setup would make it simple to use the gripper in a closed loop control of the gripping actuation and force, while using a three-beam structure as sensor and actuator simultaneously might be more complicated due to the change in piezoresistive sensitivity with temperature.

The setup in figure 2(*c*) is sensitive to the sum of forces applied to the gap and will show the same signal if both the actuators touch an object with force F_{grip} or only one gripper touches with a force $2F_{\text{grip}}$. Interchanging the leads to the beams R_2 and R_4 will make the output voltage independent of symmetrical stress due to actuation or applied forces. The interchanged Wheatstone bridge configuration will then give a signal if the object is only in contact with one actuator, which could be useful when positioning the gripper for applications such as automated pick-and-place processes. The controlling electronic circuit could be made to alternate between the two measurement modes to give both signals while maintaining a constant actuation current.

If one increases the complexity of the device by using two conducting layers separated by an insulating layer, instead of just one conducting layer, it should also be possible to both sense and control in- and out-of-plane bending actively.

3. Experimental results

To test the design and above analysis, grippers were microfabricated in gold, with beam length $L = 100$ μm, width $w = 2$ μm and height $h = 1$ μm. The fabrication process uses a silicon nitride layer as both etch mask for release of the chip body and as insulating layer under the electrode structures that are made by electron beam evaporation of the wanted metal onto an UV-lithography defined lift-off mask. The process is described in detail by Mateiu *et al* [17]. The present devices are not suitable for manipulation since the aspect ratio (h/w) is less than 1 [11] and we observe some out-of-plane bending during actuation. For real applications, the aspect ratio should be increased to at least 3, which can be achieved by standard microfabrication methods. For increased piezosensitivity of the device, one should also consider using a different material than gold to obtain a higher resistivity and gauge factor (K). However, high K values are often combined with larger thermal variations in the piezoresistivity, thus for the present demonstration purposes gold was considered a suitable material.

3.1. Measurement of actuation

The actuation is measured by an image analysis program capable of extracting the position of the tips of the grippers with approximately 10 nm precision from live video images in a Labview controlled setup based on a 100× Navitar microscope. The applied actuation current is limited to 30 mA in order not to damage the devices, and to avoid both annealing effects/drift as well as loss of precision in the measurement precision of actuation due to out-of-plane bending at the highest temperatures. Actuation up to 3 μm has been observed when applying higher currents with the configuration in figure 1(*a*), but high currents often resulted in destruction of the devices.

Figures 1(*e*) and (*f*) show the estimated actuation as a function of applied current together with the measured values of a test device. As expected, the configuration in figure 1(*b*) does actuate more than the one in figure 1(*a*) at a fixed current. The measured actuation is consistently lower than the estimated values, which is likely due to the neglected convective and radiative heat losses in the above analysis as well as out-of-plane bending.

3.2. Piezoresistive measurements

A Stanford SR830 lock-in amplifier was used as a voltage source in figure 2(*c*) for the piezoresistive measurements and was connected in series with a 1 kΩ protective resistor to give a 1 mA current (the device resistance is calculated to be 1.6 Ω). The actuator tip was deflected by a sharp silicon wafer edge mounted on a Newport Motion Controller capable of moving the sample in 100 nm steps. The measured output voltage is shown as a function of deflection of the tip for the structure in figures 2(*c*) and (*d*) in figures 2(*e*) and (*f*), respectively. The configuration of figure 2(*c*) is sensitive to the opening of the gap and the two actuators give the same signal as they are individually deflected to open the gap. The configuration in figure 2(*d*) senses only the forces applied to one part of the gripper. At the maximal deflection of the structure, out-of-plane bending was visible in the microscope, which might cause the decrease in sensitivity at high deflections. The applied voltage over the three-beam device should be about 1 mV, giving a measured sensitivity for all tested structures about 10 μV V^{-1} μm^{-1} which is a factor of 15 less than expected. The observed out-of-plane bending during deflection is expected to be a significant source of error since it effectively reduces the tensile strain in the beams.

4. Conclusion

An analysis was presented to estimate the actuation range and piezoresistive sensitivity of an electro-thermally actuated micro fabricated gripper based on a three-beam actuator/sensor structure. Several configurations using the same three-beam structure have been analyzed to evaluate the actuation range and sensitivity (figures 1(*a*) and (*b*) and figures 2(*c*) and (*d*)). Measurements on test devices made in gold showed actuation in good accordance with theory and an actuation range sufficient to close the gap if defined by the same line width as the actuator beam structure itself. If the gap of the presented device is opened by 4 μm to grip a 4 μm object and closed by a corresponding current, the gripping force is of the order 15 μN. The device spring constant is proportional to the device height and much larger gripping forces approaching the mN range would be possible in devices with high aspect ratios achievable with ASE or RIE techniques.

The piezoresistive sensitivity was found to be about a factor of 15 lower than the calculated value. The sensitivity and reliability of the presented device is likely to be considerably improved by increasing the aspect ratio to avoid out-of-plane bending. Increased piezoresistive sensitivity must also be expected if the device is made from silicon or polysilicon rather than gold. Finally, the structure shown in figure 2(*d*) should provide a better piezoresistive signal than the structure in figure 2(*c*), since the stress caused by the current in the Wheatstone bridge should have no influence on the piezoresistive signal. If made in silicon, highly sensitive devices could be made with the presented strain sensor structure, with potential applications such as piezoresistive AFM probes, where the single mask process could be a considerable process simplification compared to previous piezoresistive AFM probes.

Acknowledgments

The authors would like to thank Peter Bøggild for reviewing the manuscript; Ramona Mateiu for processing the devices; and Ole Sigmund and Mohammad Shafique for discussions and simulations. The work was funded by the Nanohand STVF-project.

References

[1] Greitmann G and Buser R A 1996 Tactile microgripper for automated handling of microparts *Sensors Actuators* A **53** 410–5
[2] Ansel Y *et al* 2002 Development of tools for handling and assembling microcomponents *J. Micromech. Microeng.* **12** 430–7
[3] www.zyvex.com
[4] Boggild P *et al* 2001 Customizable nanotweezers for manipulation of free-standing nanostructures *IEEE-NANO 2001* (Piscataway, NJ: IEEE)
[5] Molhave K *et al* 2004 Towards pick-and-place assembly of nanostructures *J. Nanosci. Nanotechnol.* **4** 279–82
[6] Kim P and Lieber C M 1999 Nanotube nanotweezers *Science* **286** 2148–50
[7] Akita S *et al* 2001 Nanotweezers consisting of carbon nanotubes operating in an atomic force microscope *Appl. Phys. Lett.* **79** 1691–3
[8] Kim C-J *et al* 1992 Polysilicon microgripper *Sensors Actuators* A **33** 221–7
[9] Kolesar E S *et al* 2002 Single- and double-hot arm asymmetrical polysilicon surface micromachined electrothermal microactuators applied to realize a microengine *Thin Solid Films* **420–421** 530–8
[10] Hashiguchi G and Fujita H 2002 Micromachine nanoprobe and its application *Proc. IEEE Sensors* **1** 922–5
[11] Jonsmann J, Sigmund O and Bouwstra S 1999 Compliant electro-thermal microactuators *Micro Electro Mechanical Systems, 1999 MEMS '99: 12th IEEE Int. Conf.* (Piscataway, NJ: IEEE)
[12] Jericho S K *et al* 2004 Micro-electro-mechanical systems microtweezers for the manipulation of bacteria and small particles *Rev. Sci. Instrum.* **75** 1280–2

[13] Kohl M *et al* 2000 SMA microgripper with integrated antagonism *Sensors Actuators* A **83** 208–13
[14] Nguyen N-T, Ho S-S and Low C L-N 2004 A polymeric microgripper with integrated thermal actuators *J. Micromech. Microeng.* **14** 969
[15] Thaysen J *et al* 2000 Atomic force microscopy probe with piezoresistive read-out and a highly symmetrical Wheatstone bridge arrangement *Sensors Actuators* A **83** 47–53
[16] Jen S U *et al* 2003 Piezoresistance and electrical resistivity of Pd, Au, and Cu films *Thin Solid Films* **434** 316–22
[17] Mateiu R *et al* 2004 An approach to a multi-walled carbon nanotube based mass sensor *Microelectron. Eng.* **73–74** 670–4

Appendix B

Article [2]
A Simple Electron Beam Lithography System

Available online at www.sciencedirect.com
SCIENCE DIRECT®
Ultramicroscopy 102 (2005) 215–219
ultramicroscopy
www.elsevier.com/locate/ultramic

A simple electron-beam lithography system

Kristian Mølhave*, Dorte Nørgaard Madsen, Peter Bøggild

Department of Micro and Nanotechnology, Technical University of Denmark, Bldg. 345e, Lyngby 2800, Denmark

Received 6 January 2004; received in revised form 19 August 2004; accepted 28 September 2004

Abstract

A large number of applications of electron-beam lithography (EBL) systems in nanotechnology have been demonstrated in recent years. In this paper we present a simple and general-purpose EBL system constructed by insertion of an electrostatic deflector plate system at the electron-beam exit of the column of a scanning electron microscope (SEM). The system can easily be mounted on most standard SEM systems. The tested setup allows an area of up to about $50 \times 50\,\mu m$ to be scanned, if the upper limit for acceptable reduction of the SEM resolution is set to 10 nm. We demonstrate how the EBL system can be used to write three-dimensional nanostructures by electron-beam deposition.

PACS: 41.85.Ne; 81.07.−b; 85.40.Hp; 87.64.Ee

Keywords: e-Beam lithography; Electron optics; SEM; Electron-beam deposition; Electron-beam-induced deposition

1. Introduction

In recent years electron-beam lithography (EBL) has become a commonly used technique for defining nanostructures, often combined with traditional photolithography for patterning of larger surrounding structures. EBL-defined contacts to both carbon nanotubes [1,2] and semiconducting nanowires [3,4] have enabled a systematic investigation of the electrical properties and creation of high-performance field-effect transistors. Furthermore, resist-based EBL techniques have been employed in the fabrication of nanomechanical structures, such as the carbon nanotube-based rotational actuator demonstrated by Fennimore et al. [5]. In addition to the resist-based EBL technique, electron beams can be used for constructive lithography, such as electron-beam deposition (EBD). Here, organic or organometallic vapors added to the specimen chamber are decomposed by the electron beam, leading to the formation of three-dimensional nanostructures, which in some cases can be conductive. The EBD metal deposition technique has been employed for fabrication of three-dimensional devices made

*Corresponding author.
E-mail address: krm@mic.dtu.dk (K. Mølhave).

0304-3991/$ - see front matter © 2004 Elsevier B.V. All rights reserved.
doi:10.1016/j.ultramic.2004.09.011

entirely of electron-beam-deposited material [6,7], and for soldering of carbon nanotubes using nanoscale deposits with a high gold content [8,9].

Commercial EBL tools are either complete systems or additional options to an SEM. However, even an add-on system can be a significant expense in an experimental budget, which would be out of proportion if the needs are occasional, basic experimental applications.

In this paper we present a simple low-cost EBL system that meets the requirements for range and precision needed to write nanoscale contacts or interconnects between microelectrodes defined by standard lithography. The system is an electrostatic deflection system inserted into the specimen chamber above the sample. This solution is particularly convenient when the electron microscopes do not have direct external connections for beam control in the column, as is often the case. Electrostatic control of charged particle beams has proven to have several advantages over magnetic beam control in some systems [10]. Complex all-electrostatic systems have been built, such as storage rings for charged particles [11] and miniature electron microscopes [12]. Electrostatic beam deflection is also used in some EBL systems [13,14].

To obtain the highest possible resolution, defocusing and astigmatism introduced by the EBL system should be minimized. For instance, the EBL system JBX-9300FS from JEOL uses a combination of electrostatic quadrupole and octopole beam deflectors. A highly harmonic potential can be achieved by choosing an electrode geometry similar to the design of a quadrupole mass spectrometer (or linear Paul trap) [15]. This also allows a simple and short deflector design, providing a short working distance that is essential for high image quality in an SEM.

2. Theory

The SEM-based EBL system presented here is based on an electrostatic deflector plate system consisting of four electrodes placed inside the SEM specimen chamber, around the beam where it exits the column. With the SEM in "spot" mode, the deflector plate system will fully control the beam position.

An illustration of the design is shown in Fig. 1. Calculations by Denison [16] show that if the rod diameter d_e and diagonal inter-rod distance d_d are chosen to be $d_e/d_d = 1.147$, the leading term of the deviation from the harmonic potential will be of the order of $(r/d_d)^{12}$, where r is the distance from the center of the deflector plates.

If a voltage $\pm\frac{1}{2}U$ is applied to two diagonally opposed rods, while the other two are kept at ground potential, the electrical field, $E = U/d_d$, will be constant and the electron beam will be deflected a distance D from the center given by

$$D = \alpha \frac{L\left(\frac{1}{2}L + L_{\text{free}}\right)}{2d_d}\frac{U}{V} = C\frac{U}{V}, \tag{1}$$

where L is the rod electrode length, L_{free} is the length from the end of the rods to the sample, V is the electron-beam acceleration voltage, and α is a coefficient accounting for edge effects due to the finite length of the rods. The deflection distance D is seen to be proportional to U/V with C denoting the proportionality constant. The coefficient α is expected to be about 1. If needed, α and higher-order corrections can be found by simulations of

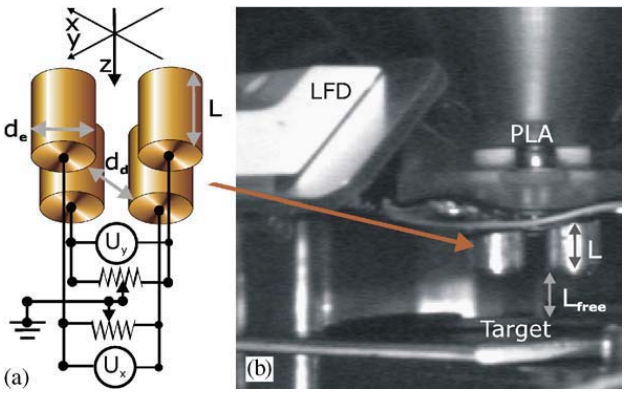

Fig. 1. The EBL setup. (a) Diagram of the four rod electrodes with the electron beam oriented along the rods. Voltages for scan in the x and y directions are applied to the electrodes through potentiometers for minimization of astigmatism. (b) Image of the deflector setup mounted in an ESEM. The system is here mounted onto the pressure limiting aperture (PLA), where the e-beam exits the column. The rod length L and distance L_{free} from the end of the rods to the target, are marked in the figure. To the left, a LFD is visible.

the electrical field in the device. Using the values $U = 10\,\mathrm{V}$, $V = 10\,\mathrm{kV}$, $d_e = 5\,\mathrm{mm}$, $d_d = 4.3\,\mathrm{mm}$, $L = L_{free} = 5\,\mathrm{mm}$, and $\alpha \approx 1$, we find $D \approx 3\,\mu\mathrm{m}$ corresponding to a $6 \times 6\,\mu\mathrm{m}$ scan area. Since standard photolithography typically has a resolution of $1\,\mu\mathrm{m}$, this scan range is sufficient for fabricating nanostructures that interface microelectrode structures, and for refining microstructures as needed in many research applications [17].

The maximum obtainable scan range is limited by the deflection voltages that can be applied to the electrodes without inducing serious astigmatism and defocusing effects. A straightforward method for verifying that such effects are not present is to observe the image resolution while applying deflection voltages. Depending on the specific setup and the detector type, there will also be different upper limits to the deflection voltages that can be applied without degradation of the image contrast, since the charged electrodes will tend to deflect the low-energy electrons away from the detection system. In preliminary tests, a standard Everhart–Thornley detector in a Leo 1550 SEM showed no significant effects on the image quality with deflection voltages up to 75 V, while the large field detector (LFD) in a Phillips XL-30 FEG Environmental SEM (ESEM) sets an upper limit for the deflection voltage of about 25 V.

3. SEM experiments

The deflector plate system shown in Fig. 1a was built using brass rod electrodes with $L = 6\,\mathrm{mm}$, $d_e = 5\,\mathrm{mm}$, and $d_d = 4.3\,\mathrm{mm}$, mounted on a polycarbonate plate. The dimensions of the system were machined to about 0.1 mm precision. The deflector system was mounted on a small rod above the sample on the stage in a LEO 1550 SEM.

The stage was used to center the deflection system around the beam. With an applied deflection voltage on the EBL system, no noticeable dependence of the image quality on the position of the system relative to the beam was observed within about 10% of d_d from the center of the system. With the deflector system centered, and the electrodes grounded in one direction, the maximum voltage that would allow proper imaging was applied in the other direction. The astigmatism was then minimized by adjusting one of the potentiometers shown in Fig. 1a, thereby compensating for slight misplacements and other imperfections in the setup. Then the same procedure was followed for the other potentiometer. The test showed a resolution of about 20 nm at $U = 0\,\mathrm{V}$. After potentiometer optimization at $U = \pm 75\,\mathrm{V}$, which gave rise to a displacement $D = \pm 90\,\mu\mathrm{m}$ (at $V = 10\,\mathrm{kV}$ and $L_{free} = 13\,\mathrm{mm}$), the resolution was about 40 nm. From the displacement the correction factor α in Eq. (1) can be estimated to $\alpha \approx 1.1$.

To compare our system with commercial EBL systems, one should consider both the resolution requirements and the achievable scan range. In resist-based EBL the resolution is often limited to roughly 10 nm. The resolution of our EBL system is limited by the inherent resolution of the SEM electron-beam, as well as by the loss of resolution of the beam due to the deflection system. The latter appeared to be roughly proportional to the deflection voltage and thereby the scan range. Based on the preliminary test, a scan range of about $90\,\mu\mathrm{m}$ ($\pm 45\,\mu\mathrm{m}$ deflection) can thus be obtained with less than 10 nm reduction of the SEM resolution.

The lithography system can be controlled via a standard DAQ card. For electron-beam exposure of resist, the dwell time precision can be as low as 10 ns per pixel in raster scans. This requires the DAQ card to sustain sampling rates up to 100 MS/s. EBD demands much higher doses and dwell times, requiring less than 100 S/s. The DAQ-card resolution must be of the order of 10 mV/bit on two channels to support 10 nm precision of the beam position in two dimensions. If a beam blanker is available in the SEM, one could use an extra DAQ-card channel to control it. We use a National Instruments 1200 DAQ card in a laptop PC. Direct driving of the system with the DAQ card limits the applicable voltage to 10 V, which is compatible with the contrast requirement of the ESEM detection system in our setup. The 16-bit resolution gives a 0.15 mV/bit corresponding to a resolution of 0.15 nm, which is much smaller than the resolution of the ESEM.

4. ESEM results and discussion

For the EBD experiment, the deflector system was mounted onto the pressure-limiting aperture of a Philips XL-30 FEG ESEM, as shown in Fig. 1B. Despite the relatively coarse manual alignment no influence on deflection and induced astigmatism was observed when the system had been removed and reinserted between the experiments. This is in accordance with our observations in the preliminary test.

The deflection as a function of voltage for the EBL system was calibrated by EBD using a source containing dimethylacetylacetonate gold(III) inserted into the specimen chamber of the XL-30 ESEM. First, a reference marker was deposited with all electrodes at ground potential. Next, a marker was deposited with an applied deflection voltage from a power supply. Such sets of markers were deposited at a series of deflection voltages, and for each set the deflected distance was measured. Fig. 2a presents the obtained deflection distance versus deflection voltage for electron-beam acceleration voltages of 5, 10 and 20 kV. A linear dependence was seen for all tested acceleration voltages. Linear fits give the proportionality factors 0.52, 0.30 and 0.16 μm/V, respectively. In Fig. 2b the proportionality factors from Fig. 2a are shown versus inverse acceleration voltage.

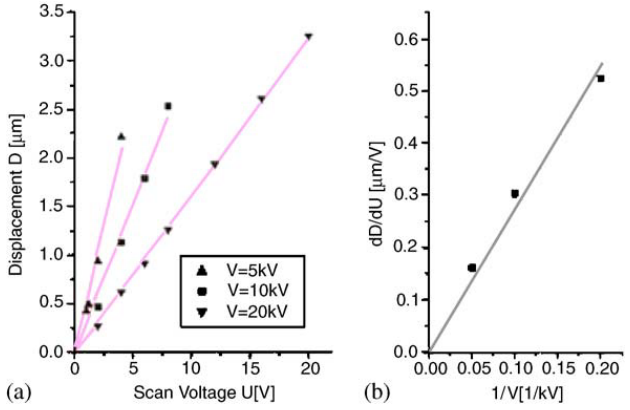

Fig. 2. Calibration of the EBL system. (a) Beam deflection versus applied voltage for electron-beam acceleration voltages of 5, 10 and 20 kV. Linear fits give the proportionality factors 0.52, 0.30 and 0.161 μm/V, respectively. (b) Proportionality factors from Fig. 2a versus reciprocal acceleration voltage, indicating a linear dependence as expected from theory.

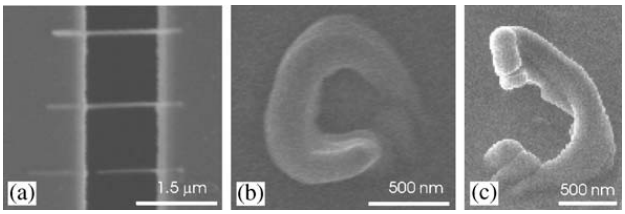

Fig. 3. (a) ESEM image showing EBD lines deposited as bridges between microcantilevers using the lithography system. (b) SEM image showing a top view and (c) side view of an electron-beam-deposited spiral structure obtained with the computer controlled x–y scan.

A linear fit gives the parameter $C = 2.7(1)$ mm in accordance with the theory if $\alpha = 0.73$.

Several three-dimensional test structures were deposited using the system, as shown in Fig. 3. Conducting interconnects making horizontal bridges between microcantilevers [18] were deposited at scan speeds of up to 30 nm/s. The line width was measured to be 60–200 nm, decreasing with scan speed, and comparable to the line width obtained for deposits fabricated without the EBL system [9]. The conductivity of the deposited material has been measured to be 1–2 orders of magnitude lower than pure bulk gold.

The spiral-like structure in Fig. 3b and c was deposited using a circular scan at a low scan speed of 10 nm/s. The structure is not perfectly circular since carbon contamination accompanying EBD in an ESEM deforms the already deposited parts of the structure, when exposed to electron radiation. A more detailed study of the environmental EBD process in three dimensions can be found in Ref. [18].

5. Conclusion

A simple EBL system can be made by inserting a small electrostatic quadrupole deflection system into a standard SEM. The reduction of the SEM resolution caused by the EBL system increases with the applied deflection voltage, and is of the order of 10 nm within a 50 μm scan range in the tested system. Although the scan range of commercial EBL systems are typically an order of magnitude larger, this combination of scan range

and resolution is adequate for many research applications, and few standard SEM-based EBL systems offer minimum precision below 50 nm. For electron-beam nanolithography, dwell times in the sub-microsecond range are often required, demanding very rapid movement of the beam. Due to the lack of inductance in the system, the deflection speeds should primarily be limited by the bandwidth of the DA converters. However, exposure of nanoscale patterns in a resist film is yet to be demonstrated.

We point out that the EBL system presented here is straightforward to construct and install, and that results competing with results from far more complex and expensive setups can be obtained. If required, the tested system could be improved considerably both in terms of shielding against electrical noise, prevention of charging of the plastic parts, and tighter tolerances on the mechanical parts.

The presented system is ideal for EBD experiments, when using LabView-controlled DAQ cards without amplification electronics for pattern generation and beam control. The setup gives a high degree of flexibility to make customized solutions for experiments where full-beam control is advantageous, besides providing a straightforward path to resist-based EBL. We expect this post-column deflection system to be valuable for both scientists and students in making full-control EBL available to a wider range of laboratories.

Acknowledgments

This project was supported by the Danish Technical Research Council (NanoHand talent project). For the generous loan of ESEM and stimulating discussions the authors wish to thank Haldor Topsøe A/S, and in particular Michael Brorson, Charlotte Clausen Appel, and Sven Ullmann.

References

[1] P. Avouris, Acc. Chem. Res. 35 (2002) 1026.
[2] P.G. Collins, M.S. Arnold, P. Avouris, Science 292 (2001) 706.
[3] Y. Cui, C.M. Lieber, Science 291 (2001) 851.
[4] Y. Huang, X. Duan, Y. Cui, L.J. Lauhon, K. Kim, C.M. Lieber, Science 294 (2001) 1313.
[5] A.M. Fennimore, T.D. Yuzvinsky, Wei-Qiang Han, M.S. Fuhrer, J. Cumings, A. Zettl, Nature 424 (2003) 408.
[6] H.W.P. Koops, J. Kretz, M. Rudolph, M. Weber, G. Dahm, K.L. Lee, Jpn. J. Appl. Phys. 33 (1994) 7099.
[7] I.W. Rangelow, T. Gotszalk, N. Abedinov, P. Grabiec, K. Edinger, Microelectron. Eng. 57–58 (2001) 737.
[8] D.N. Madsen, K. Mølhave, R. Mateiu, A.M. Rasmussen, M. Brorson, C.J.H. Jacobsen, P. Bøggild, Nano. Lett. 3 (2003) 47.
[9] K. Mølhave, D.N. Madsen, A.M. Rasmussen, A. Carlsson, C.C. Appel, M. Brorson, C.J.H. Jacobsen, P. Bøggild, Nano. Lett. 3 (2003) 1499.
[10] P.W. Hawkes, E. Kasper, Principles of Electron Optics, vol. 1, Academic Press, New York, 1989.
[11] S. Pape Møller, Nucl. Instr. Meth. In Phys. Res. A 394 (1997) 281.
[12] R.H. Roberts, M.M. El Gomati, J. Kudjoe, I.R. Barkshire, S.J. Bean, M. Prutton, Meas. Sci. Technol. 8 (1997) 536.
[13] P. Rai-Choudhury (Ed.), Handbook of Microlithography, Micromachining, and Microfabrication, vol. I, SPIE, 1997.
[14] G. Owen, Rep. Prog. Phys. 48 (1985) 795.
[15] W. Paul, Rev. Mod. Phys. 62 (1990) 531.
[16] D.R. Denison, J. Vac. Sci. Technol. 8 (1971) 266.
[17] K. Mølhave, T.M. Hansen, D.N. Madsen, P. Bøggild, J. Nanosci. Nanotechnol. 4 (2004) 279.
[18] K. Mølhave, D.N. Madsen, S. Dohn, P. Bøggild, Nanotechnology 15 (2004) 1047.

Appendix C

Article [3]
Constructing, connecting and soldering nanostructures by environmental electron beam deposition

INSTITUTE OF PHYSICS PUBLISHING NANOTECHNOLOGY

Nanotechnology **15** (2004) 1047–1053 PII: S0957-4484(04)77526-1

Constructing, connecting and soldering nanostructures by environmental electron beam deposition

Kristian Mølhave[1], **Dorte Nørgaard Madsen, Søren Dohn and Peter Bøggild**

Mikroelektronik Centret, Technical University of Denmark, DK-2800 Kgs. Lyngby, Denmark

E-mail: krm@mic.dtu.dk

Received 9 March 2004
Published 21 June 2004
Online at stacks.iop.org/Nano/15/1047
doi:10.1088/0957-4484/15/8/033

Abstract

Highly conductive nanoscale deposits with solid gold cores can be made by electron beam deposition in an environmental scanning electron microscope (ESEM), suggesting the method to be used for constructing, connecting and soldering nanostructures. This paper presents a feasibility study for such applications. We identify several issues related to contamination and unwanted deposition, relevant for deposition in both vacuum (EBD) and environmental conditions (EEBD). We study relations between scan rate, deposition rate, angle and line width for three-dimensional structures. Furthermore, we measure the conductivity of deposits containing gold cores, and find these structures to be highly conductive, approaching the conductivity of solid gold and capable of carrying high current densities. Finally, we study the use of the technique for soldering nanostructures such as carbon nanotubes. Based on the presented results we are able to estimate limits for the applicability of the method for the various applications, but also demonstrate that it is a versatile and powerful tool for nanotechnology within these limits.

M This article features online multimedia enhancements

1. Introduction

The investigation of electron beam deposition (EBD) as a technique for serial writing of three-dimensional nanostructures started in the 1980s. EBD has been used to make functional structures, such as field emission devices [1], thermal sensors [2], nanotweezers [3, 4] and tools for manipulating DNA [5]. In combination with *in situ* nanomanipulation equipment, EBD is capable of forming mechanically strong attachments of carbon nanotubes for strain measurements [6] and decreasing the contact resistance of contacts to nanotubes [7]. Conductive nanostructures are deposited by using metal-containing source gasses. The conductivity can be increased by decreasing the amount of amorphous carbon included in the structure [8, 9]. Environmental electron beam deposition (EEBD), where a background gas such as water is present in an environmental electron microscope, was demonstrated by Folch *et al* [10]. Their results indicated that a high metal content could be achieved by EEBD. Our investigations have shown that it is possible to form a core of solid gold in EEBD structures [11]. Figures 1(a) and (b) show typical apexes of tips deposited in nitrogen and water, respectively. A gold core is clearly present in the tip deposited in water, while the tip deposited in nitrogen contains nanocrystals in an amorphous carbon matrix. The solid gold structures appear to be highly conductive and EEBD can be used to solder carbon nanotubes to electrodes obtaining low contact resistances [12].

Over the last decade a range of promising three-dimensional devices have been achieved with EBD, but relatively little has been reported regarding the limitations of the technique for such structures. Koops *et al* [13] studied growth rate and inclination of free standing EBD lines versus

[1] Author to whom any correspondence should be addressed.

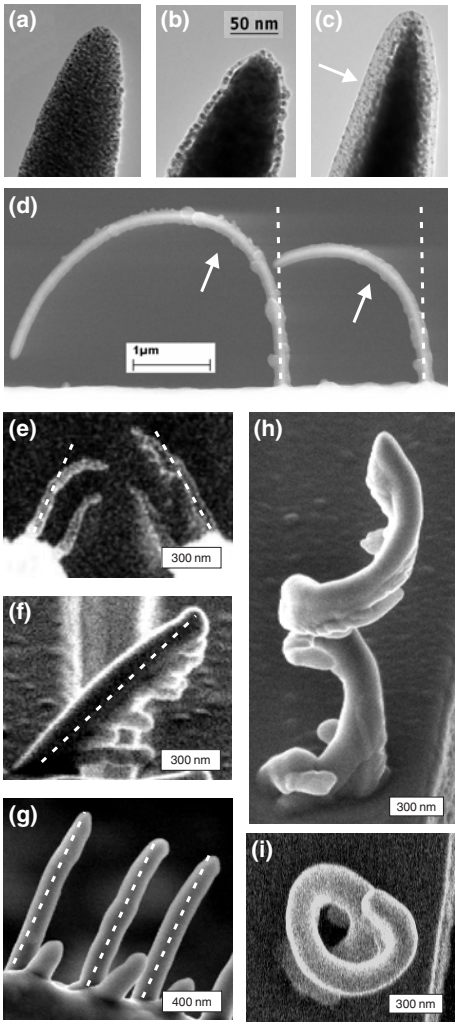

Figure 1. Three-dimensional structures made by EBD/EEBD under different deposition conditions (see footnote 3). The intended structures are indicated by dashed lines. (a) TEM image of the apex of a tip deposited in nitrogen. (b) TEM image of the tip apex with a gold core deposited in water vapour. (c) TEM image showing an asymmetric contamination layer on an EEBD tip deposited in water vapour. The thicker layer on the left-hand side (indicated by the arrow) was caused by a later deposition of a tip a few micrometres to the left. (d) SEM image of initially straight EEBD tips with asymmetric contamination layers. When the tips were exposed to electron radiation in SEM and TEM, they bent irreversibly to the side with the thickest layer (indicated by the arrow). (e) EBD tips at the end of a micro-fabricated pair of tweezers. Parallel deposits were created below the intended structures. The EBD lines on the left-hand side, which were deposited first, subsequently deformed plastically, bending away from the intended straight line towards the later deposits. (f) EEBD line structure showing pronounced branching of the deposit. (g) EEBD line structures showing another branching effect, where the intended structure is accompanied by a thick and almost horizontal line extending into free space. (h) Elaborate three-dimensional corkscrew structure made by EEBD, showing additional small branches. (i) Top view of the structure in (h).

scan rate. The minimum achievable line-width for EBD lines on surfaces and in vertical tips, which is limited by the scattering of primary and secondary electrons, has been investigated theoretically and experimentally [14, 15]. Fujita *et al* recently observed a very narrow line width limit of 5 nm for free-standing lateral carbonaceous structures [16], indicating that laterally written free-standing structures can be fabricated with very narrow line widths.

The gold containing deposits made by the EEBD technique are potentially useful for many applications such as constructing, connecting and soldering nanostructures. In this paper we investigate to what extent the EEBD method can be used for in these applications. First we focus on the application of the technique to the deposition of three-dimensional structures, investigating issues such as contamination and unwanted depositions for both EDB and EEBD. We study the maximum achievable scan rates, growth rates, deposition angle and line width for individual lines. An analysis of a series of line deposits enables us to determine these important parameters and their mutual dependency. In order to study the electrical properties of the deposit, we demonstrate the deposition of suspended micrometre-long bridges and measure how the electrical properties of the bridges depend on the environmental gas conditions. Finally, we investigate EEBD soldering by measuring the mechanical and electrical properties of carbon nanotubes soldered to two microcantilever electrodes.

2. Experimental setup

The deposition setup used for the EEBD experiments reported here, was identical to the setup described in [11]. The precursor gas dimethyl-gold-acetylacetonate (DGAA) was used in an environmental electron microscope (Philips XL-30 FEG ESEM) with a pressure of 1 Torr of the environmental gas (water vapour or nitrogen). The beam current for the experiments was kept at approximately 200 pA, which is sufficient to create a solid gold core in a water vapour environment [11]. Based on previous experiments we expect the partial pressure of the precursor gas to be approximately constant within each data series of the presented experiments. It may however fluctuate from one data series to another.

In the experiments the beam was scanned slowly by electrostatic deflection, using a quadrupole electrode structure, inserted where the beam exits the column and driven by a function generator or by a LabView® controlled DAQ card. The deflector system is described in [17].

3. Results and discussion

3.1. Additional depositions

The complete control over the beam scan offers large freedom to design EBD structures. However, during deposition of three-dimensional EBD structures, additional depositions often appear away from the intended structure. Such additional depositions could in some cases be detrimental to the intended structures. Figure 1 presents typical examples of the various types of additional depositions observed in our experiments under a wide range of deposition conditions[2]. They can be divided into two categories: contamination effects ((a), (b)) and secondary line depositions ((c), (d)):

[2] Deposition conditions for the structures in figure 1: (a) EEBD without core, using DGAA and 1 Torr N_2 environmental gas. (b, c, d, f, h, i) EEBD with core using DGAA and 0.8 Torr H_2O environmental gas. (e) EBD using carbonaceous background gas in a SEM. (g) $Mo(CO)_6$ precursor and 0.8 Torr H_2O environmental gas.

(a) *Contamination.* If EBD structures are imaged while the EBD source is present or if a second deposition is made within a radius of about 5 μm from the EBD structure, an asymmetric contamination layer will often coat the structure. In the case of EEBD with a DGAA source, the contamination layer has a much lower gold content than the rest of the deposit [11]. Figure 1(c) shows a TEM image of a tip with a gold core, which has been coated with such an asymmetric low gold-content contamination layer during a later deposition to the left of the tip shown. The contamination layer is thickest on the side facing the later deposition.

(b) *Contamination bending.* If a straight structure has been asymmetrically contaminated by a nearby deposition, it tends to deform plastically when subsequently exposed to electron radiation. Figure 1(d) shows a tip that initially was straight, but during TEM/SEM investigation was bent almost 180° to the side having the thickest contamination layer. We have observed this bending behaviour in both EEBD (figure 1(d)) and EBD (figure 1(e)).

(c) *Parallel growth.* Any protrusion in the path of the incident electron beam or the part of the electron beam that penetrates below the deposited structure can become a starting point for a second deposition, which often grows parallel to the primary structure. It has been suggested as a way to make intentionally parallel structures [5]. Figure 1(e) shows two pairs of such parallel lines deposited at the tip of a pair of micro-fabricated electrostatic tweezers [3, 4]. The lines were deposited from a SEM background gas as straight lines but exhibited signs of contamination bending during later deposition and imaging (figure 1(e)).

(d) *Branching.* When depositing three-dimensional structures, smaller secondary lines branch out from the primary structure (figures 1(f), (g)). Often, the additional lines will be deposited at a more horizontal angle than the main structure. We have not identified parameters that reliably control the creation of such branches, but note that a high source gas pressure tends to favour their creation. We have observed both multiple small branches as in figure 1(f) and, at other times, a single large branch from the base as seen in figure 1(g). Substantial branching might cause short circuits in three-dimensional structures. We have observed branching in ESEM depositions, but also in preliminary SEM deposition experiments using DGAA as the source gas.

An example of a three-dimensional corkscrew structure, made by slowly scanning the beam in a circle, is presented in figure 1(h) and a top view of the same structure is shown in figure 1(i). The spiral demonstrates fabrication of more elaborate structures, but also that branching can take place.

3.2. Three-dimensional structures

To gain control over the three-dimensional deposition, we measured the dimensions of freestanding lines deposited at various scan rates. Since the parallel deposition and branching is assumed to take place due to a large fraction of primary electrons (PEs) penetrating the structure [5], we investigated deposition at different PE energies to determine the effect

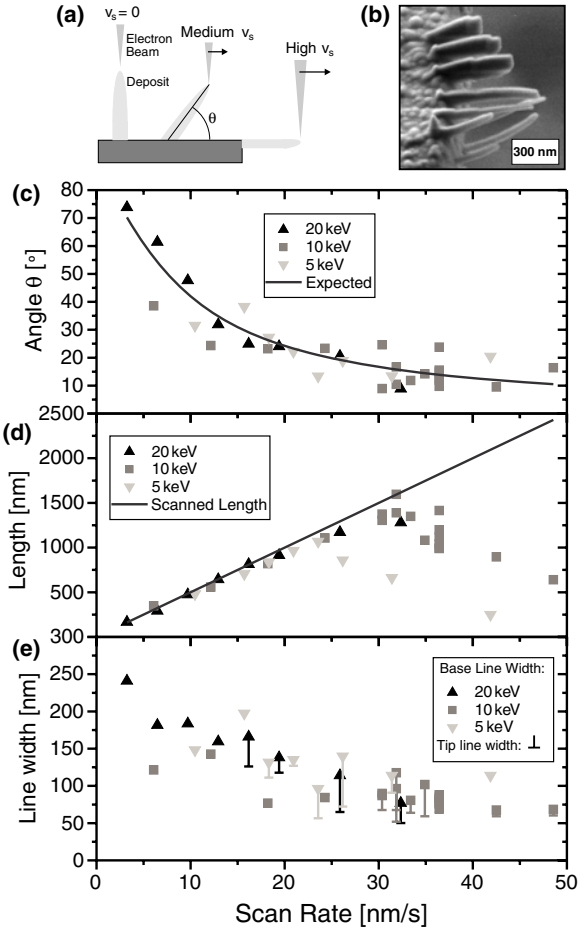

Figure 2. Effect of scan rate on the geometry of three-dimensional lines deposited in 50 s at electron beam energies of 5, 10 and 20 keV. (a) Illustration of the angle to horizontal, θ, of the deposits as function of scan rate, v_s. (b) SEM image of a series of the deposits. (c) Graph of θ as function of scan rate. The solid curve in the graph show the angle expected from a vertical growth rate of 9 nm s^{-1} and is seen to be in agreement with the measurements. (d) The length of the deposits versus scan rate. The solid curve indicates the distance scanned by the beam. Above a certain threshold scan rate, the deposits are shorter than the scanned distance. (e) Base width (filled symbols) and tip width (horizontal bars) of deposits. The base and tip width decrease with scan rate and the tip diameter also begin to narrow compared to the base value around the threshold scan rate until a minimum line width of about 60 nm is reached.

of a change of penetration depth. Lines were deposited using 0.8 Torr water vapour as environmental gas at beam acceleration voltages of 5, 10 and 20 kV. The starting points of the lines were on the edge of a 1 μm thick silicon oxide microcantilever coated with Ti/Au (100 Å/800 Å) [3]. After deposition in ESEM, the dimensions of the structures were measured using higher resolution SEM images, as the one shown in figure 2(b). The accuracy of the measurements was limited by the roughness of the cantilever surface and the factors described in section 3.1. We estimate the uncertainty to be about ± 50 nm for the dimensions corresponding to about $\pm 10°$ on the angle.

From the measured height of the deposits, the vertical growth rate, v_v, was found to be constant with a value of $v_v = 9 \pm 3$ nm s^{-1} for all acceleration voltages. Figures 2(a) and (c) show the angle (to horizontal) of the deposits versus the beam

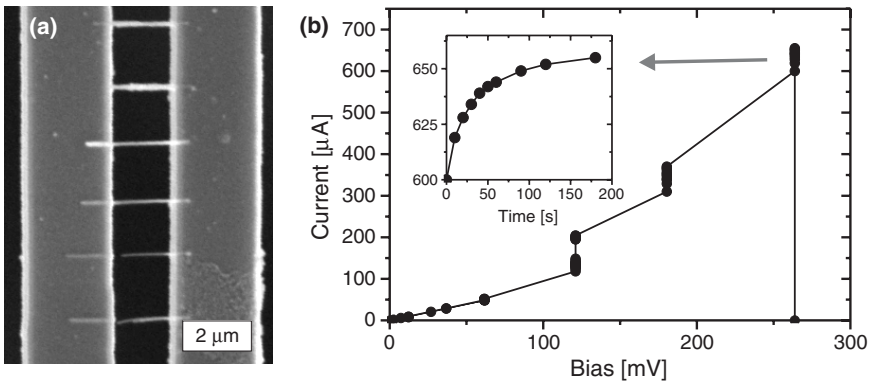

Figure 3. Measurements on conducting EEBD bridges. (a) ESEM image of bridges deposited between two cantilevers for electrical measurements. (b) I–V curve of the bridge having the highest conductivity. The bias voltage was kept constant several times to observe the time dependence of the current. In all cases the current was seen to approach a steady state after 2–3 min. The inset shows the current as function of time for the last period.

scan rate v_s. The solid curve represents the expected angle dependence $\theta = \arctan(v_v/v_s)$. The expected dependence of the angle is seen to be in good agreement with the measurements, considering the estimated uncertainty of $\pm 10°$.

The lengths of the deposits are shown in figure 2(d). All lines were deposited in 50 s. For low scan rates, the lengths of the deposited lines were identical to the scanned distance (indicated by the solid line, length $= v_s$ 50 s), but when the scan rate was increased above a certain threshold, the length of the deposit decreased, despite the increasing scanned distance. At scan rates of about 50 nm s^{-1} only very short lines were deposited. The presence of a threshold scan rate shows that the deposition process cannot keep up with the scanning electron beam, causing the deposition to terminate as the beam moves ahead of the deposited line. The value of the threshold scan rate appears to be slightly lower at a beam energy of 5 keV (approximately 25 nm s^{-1}) compared to the threshold at 10 keV (approximately 30 nm s^{-1}). We did not reach the threshold for 20 keV in this experiment.

The diameters of the deposited lines decrease with increasing scan rate, both at the base and at the tip of the lines, as shown in figure 2(d). Furthermore, the tip diameter is reduced compared to the base diameter for lines deposited around and above the threshold scan rate. The tip diameter seems to reach a lower limiting value of about 60 nm.

Since parallel deposits are supposedly being caused by primary electrons penetrating the deposited structure, it is interesting to note that at high scan rates the 5 and 10 keV deposits had an average of 3 parallel lines, while the 20 keV deposits only had 1.5 parallel lines on average. The parallel deposits are spread over the thickness of the cantilever but only 10% of the tips are in the lower 250 nm of the 1 μm thick cantilever, indicating that the finite width of the cantilever probably did not affect the observed number of parallel deposits. The number of parallel deposits also decreased with decreasing scan rate, giving a high probability for a single line at scan rates below 10 nm s^{-1}.

3.3. Electrical properties of EEBD structures

The presence of a solid gold core in the deposited material makes EEBD useful for interconnecting micro- and nanostructures [12]. The electrical properties of the deposits are ultimately tested by forming deposits bridging the gap between gold-coated micro-cantilevers. In a previous study, a solid gold core was observed only in the presence of water [11]. We here determine the effect of the gold core by comparing bridges deposited by EEBD in nitrogen as well as bridges deposited in water.

As described in the previous section, the EEBD of 1 μm long completely horizontal bridges is not immediately possible due to the threshold limiting the achievable length at low angles, see figure 2(a). However, the starting point of the bridge often lies on the side of the cantilever below the surface level and deposits with angles of 10°–20° can thus bridge the cantilever gap. The success ratio for achieving electrical contact when depositing bridges on a horizontal electrode structure is rather low, as this experiment intentionally pushes the method to the limits. It was not attempted to make counter-parallel lines meet in the middle of the gap, since the effect of possible contamination layers between the lines could make interpretations of such measurements difficult. Tilting the substrate should make it possible to make bridges with a higher success ratio.

An ESEM image of a series of deposited bridges is shown in figure 3(a). In total, 22 bridges were deposited with varying scan rates; half of these were deposited in nitrogen and the other half in water vapour. Successful electrical contact ($R < 200$ MΩ) was achieved in five cases using water vapour and in one case using nitrogen. During deposition, 13 bridges appeared to bridge the gap, but for 7 of these, later SEM inspection showed that the bridge either had too high an angle to reach the target cantilever or appeared to have broken during deposition. The resistance and the maximum current carrying capability were determined after deposition of each bridge by increasing the bias voltage and measuring the current until failure of the bridge.

Figure 3(b) shows the I–V curve of a deposited bridge. The bridge shown has the highest measured conductivity, but the behaviour is representative for bridges deposited in water vapour. At low bias voltages a linear I–V relationship was found. As the bias was raised, the resistance decreased. The increase in bias voltage was stopped several times to observe the time dependence of the current at fixed high bias. For fixed bias, the current increased with time, approaching a steady

Table 1. Electrical properties of EEBD bridges with smallest measured resistance, R_{min}, maximal current, I_{max}, maximal current density, J_{max}, and minimum resistivity, ρ_{min}. For bridges deposited in water vapour, the current density and resistivity are based on the cross-section of the gold core, which is typically 10% of the entire bridge cross-section. For comparison, the resistivity of gold is $\rho = 24 \times 10^{-9}$ Ω m.

ESEM gas	R_{min} (kΩ)	I_{max} (μA)	J_{max} (10^9 A m^{-2})	ρ_{min} (10^{-9} Ω m)
H_2O	2	5.7	9.0	732
H_2O	0.2	655	926	88
H_2O	0.2	708	2500	42
H_2O	1.7	36	[a]	[a]
H_2O	3.2	40	46	1750
N_2	2×10^3	5.5	6.5	10^6

[a] An estimate of the bridge cross-section was not possible due to the presence of several parallel bridges.

state. The observed time dependence suggests that annealing effects reduce the resistance of the bridge. The inset shows the current as function of time at a fixed bias of 260 mV, where the current approaches a steady state over 200 s until the bridge finally fails.

Table 1 lists the measured minimum resistance and maximum current through each of the approximately 1.5 μm long bridges together with the maximum current density and lowest resistivity calculated for the core as measured from SEM images. Typically the outer width of the bridges was 100 nm and the gold core diameter 30 nm. Only depositions in water vapour had cores visible in SEM images.

The single bridge deposited in nitrogen that achieved contact had a resistivity approximately three orders of magnitude higher than those deposited in water vapour, and failed at a current of just 5 μA. All bridges deposited in water contained solid gold cores and had resistances of the order of 1 kΩ. Two bridges were capable of carrying currents higher than 0.6 mA and sustained a power of about 100 μW before failure. This indicates that the gold core is highly conductive compared to the material consisting of gold nanoparticles embedded in amorphous carbon, which makes up the entire deposit when nitrogen is used as the environmental gas and is also similar to the material in the shell surrounding the gold core in water deposits (see figure 1(a)). Table 1 shows the current density and resistivity calculated with the assumption that all current is carried in the core. The highest current density reaches 10^{12} A m^{-2} and the lowest resistivity is within an order of magnitude from that of bulk gold (24×10^{-9} Ω m). This is comparable to the limits for the properties of gold nanowires described by Durkan and Welland [18] and the EBD results achieved by Utke *et al* (220×10^{-9} Ω m) [9]. If the current is assumed to flow through both core and crust, we obtain current densities a factor of 10 smaller and correspondingly higher resistivities. Even if both core and crust are carrying current at high bias, the structures are still highly conductive and capable of sustaining high current densities, comparable to, e.g. carbon nanotubes [19] and gold wires made by electron beam lithography [18].

3.4. EEBD soldering of carbon nanotubes

Highly conductive EEBD has also proven useful for soldering nanostructures, such as carbon nanotubes to microelectrodes [11, 12]. Such nanotube devices generally show resistances down to about 10 kΩ for nanotube bridges with lengths of a few micrometres, indicating that the contact resistance must be relatively low since the carbon nanotube bridge itself is expected to contribute with a resistance value of that order based on measurements obtained with scanning four point probes [20]. Hence, the method compares to lithographically defined contacts [21] and EBD-enhanced contacts [7].

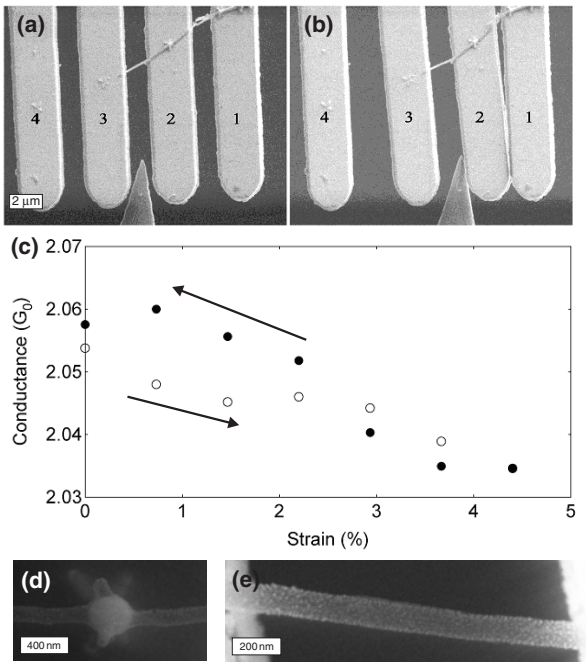

Figure 4. EEBD soldered multiwalled carbon nanotube. ((a), (b)) SEM images of a carbon nanotube bridge attached by EEBD between two microcantilevers being stretched by deflecting one microcantilever to the side. (A video sequence is available online.) (c) Conductance measured during nanotube stretching (open circles) and release (dots) showing a reversible conductance change of 1%. Conductance is stated in units of $G_0 = 2e^2/h = 6.5$ kΩ. ((d), (e)) Close-up SEM images of a solder point and a nanotube bridge.

M Multimedia for this figure is available from stacks.iop.org/Nano/15/1047

To investigate the properties of EEBD soldered nanotubes, a multiwalled carbon nanotube (MWNT) was soldered to two microcantilever electrodes, forming a bridge. The carbon nanotube could be stretched by deflecting one of the microcantilevers with an etched tungsten tip, while simultaneously measuring the resistance of the device. This measurement enables us to measure the strain-induced changes in resistance of the device as well as setting a lower estimate on the solder bond strength.

Figures 4(a) and (b) show two out of a series of SEM images of the soldered nanotube bridge being stretched. (A video sequence is available online.) It appears from the images that the nanotube was fixed all the way to the edge of the cantilever, so only the section of the nanotube suspended between the microcantilevers was stretched in the process. The strain was measured from the SEM images and the conductance versus strain is plotted in figure 4(c). The conductance

changed roughly 1% with a strain of 4%. This is a very small response compared to measurements on single-walled carbon nanotubes [22, 23]. While this could be due to the electromechanical properties of the MWNT being different from those of SWNT, other causes like high defect density and a possible initial slack of the MWNT reducing the actual stretching of the C–C bonds that leads to a change in resistance must also be considered. The image in figure 4(d) of a soldering region shows a dense gold core covered with a thin layer of carbon and in figure 4(e) the nanotube itself has apparently also been covered with a thin layer. Whether the soldering and contamination of the nanotube affect the properties of the nanotube and the measured strain-induced resistance change is not known.

A lower limit for the strength of the soldering can be estimated from the deflection of cantilever number 3, which from the image is determined to be 0.92 μm. With a spring constant of 19.7 N m^{-1}, calculated from the dimensions and materials of the cantilever, the force exerted on cantilever 3 is of the order of 20 μN. A value for the Young's modulus of the nanotube based on the full cross-section of the nanotube can hence be estimated to be 30 GPa, which is comparable to previous measurements on multiwalled carbon nanotubes by Wang [24]. With a soldering contact area to the nanotube of about 0.1 μm^2 in the deposited crosses, the shear stress of the EEBD nanotube soldering must be higher than 200 MPa, which is comparable to the yield strength of gold. That the nanotube did not move on the cantilever surface during the experiment, however, indicates that the soldered surface is larger and the yield strength could be smaller.

4. Summary and conclusion

Environmental electron beam deposition (EEBD) was employed to create three-dimensional nanostructures containing gold cores. Several issues important to consider when employing this technique have been identified: contamination effects can coat the deposited and nearby structures, which later can cause plastic deformation of the structures when exposed to electron radiation. During deposition, parallel or branching deposits can appear. Such deposits could possibly be used to create parallel structures, but might also unintentionally short-circuit structures. We have observed these effects in both SEM and ESEM experiments. The issues regarding parallel deposition and branching appear to diminish at higher primary electron energies—contrary to the expectation that increasing penetration depth would favour the creation of additional structures at high energies. When using focused ion beam for deposition, the beam penetration depth is considerably smaller than for electron beam induced deposition [24] and elaborate three dimensional structures [25] have been created in carbon material without obvious signs of the contamination and branching effects reported in this paper for electron beam deposition. However, FIB deposition can also create spurious depositions as reported by Ishida *et al* [26] using $W(CO)_6$ as precursor.

The effect of the scan rate of the electron beam on the deposited structure was investigated in detail. The growth rate of the structure in the vertical direction was found to be independent of acceleration voltage and of scan rate up to the threshold rate where deposition terminates. The angle of the deposit could be varied from about 10° above horizontal to vertical. However, deposition at angles lower than 30° to horizontal is limited by a rapid narrowing of the deposited tip structure, limiting the achievable length of such low-angle deposits. The results indicate that deposition stops at the highest scan rates when the line width of a free deposit reaches a lower limiting value of around 60 nm. Based on the presented observations, the EEBD technique appears to be most suited for deposition at high acceleration voltages of structures with angles above 30° to horizontal, where also the deposition of parallel structures at low scan rates seems to be reduced. It remains to be investigated how the observed effects and limits depend on the source gas pressure.

Nearly horizontal bridge structures making electrical contact across a 1.5 μm gap between microelectrodes were deposited with a success rate of about 1/3. The deposited bridges showed a strong dependence on the environmental deposition conditions. The resistance of bridges deposited in nitrogen was three orders of magnitude higher compared to those made using water vapour, where a gold core was formed in the deposit. This indicates that the gold core is highly conductive compared to the material of gold nanoparticles embedded in amorphous carbon, which surrounds the core and makes up the entire nitrogen deposits. Assuming that the current is carried in the gold core, a resistivity twice that of bulk gold was achieved and current densities above 10^{12} A m^{-2} were reached. The EEBD structures appear to be suitable for contacting nanostructures and have electrical properties approaching those of multiwalled carbon nanotubes.

For horizontal carbonaceous deposits, Fujita *et al* [16] recently reported minimum EBD line widths of the order 5 nm and did not observe limitations on the length. However, no conductivity measurements have yet been reported on such deposits. The possibility of graphitizing carbon structures [27] for improving the mechanical strength and potentially also the conductance is an interesting possibility. Making deposits with high gold content by EBD using carbon-free source gases also appears promising [9], but whether limitations such as those discussed above are present with this technique remains to be investigated.

By soldering carbon nanotubes to microelectrodes we have shown that EEBD can be used for highly conductive and mechanically stable soldering of carbon nanotubes in order to carry out strain measurements. Whether the soldering and contamination of the nanotube affect the measured strain-induced resistance change is not known. Preliminary experiments in our setup indicate that the contamination by EEBD soldering can be considerably reduced by using a valve system to close the organometallic source when not needed.

Acknowledgments

We would like to thank Haldor Topsøe A/S for allowing us to use the ESEM for this study and we appreciate technical assistance from and discussions with Michael Brorson, Charlotte Clausen Appel, Anna Carlsson and Sven Ullmann. We thank Richard Czerw for providing carbon nanotube samples. This research was supported by the Danish Technical Research Council through a 'Talent-Project' grant.

References

[1] Koops H W P, Schössler C, Kaya A and Weber M 1996 *J. Vac. Sci. Technol.* B **14** 4105

[2] Rangelow I W J, Gotszalk T, Abedinov N, Grabiec P and Edinger K 2001 *Microelectron. Eng.* **57/58** 737

[3] Bøggild P, Hansen T M, Tanasa C and Grey F 2001 *Nanotechnology* **12** 331

[4] Mølhave K, Hansen T M, Madsen D N and Bøggild P 2004 *J. Nanosci. Nanotechnol.* **4** 1

[5] Ooi T, Matsumoto K, Nakao M, Otsubo M, Shirakata S, Tanaka S and Hatamura Y 2000 *Proc. IEEE Micro Electro Mechanical Systems (MEMS)* pp 580–3

[6] Yu M, Lourie O, Dyer M J, Moloni K, Kelly T F and Ruoff R S 2000 *Science* **287** 637

[7] Bachtold A, Henny M, Terrier C, Strunk C, Schönenberger C, Salvetat J P, Bonard J M and Forro L 1998 *Appl. Phys. Lett.* **73** 274

[8] Koops H W P, Schössler C, Kaya A and Weber M 1996 *J. Vac. Sci. Technol.* B **14** 4105

[9] Utke I, Hoffman P, Dwir B, Leifer K, Kapon E and Doppelt P 2000 *J. Vac. Sci. Technol.* B **18** 3168

[10] Folch A, Servat J, Esteve J and Tejada J 1996 *J. Vac. Sci. Technol.* B **14** 2609

[11] Mølhave K, Madsen D N, Rasmussen A M, Carlsson A, Appel C C, Brorson M, Jacobsen C J H and Bøggild P 2003 *Nano Lett.* **3** 1499

[12] Madsen D N, Mølhave K, Mateiu R, Rasmussen A M, Brorson M, Jacobsen C J H and Bøggild P 2003 *Nano Lett.* **3** 47

[13] Koops H W P, Kretz J, Rudolph M and Weber M 1993 *J. Vac. Sci. Technol.* B **11** 2386

[14] Silvis-Cividjian N, Hagen C W, Kruit P, Stam M A J and Groen B 2003 *Appl. Phys. Lett.* **82** 3514

[15] Kohlmann-von Platen K T, Chlebek J, Weiss M, Reimer K, Oertel H and Brünger W H 1993 *J. Vac. Sci. Technol.* B **11** 2219

[16] Fujita J, Ishida M, Ichihashi T, Ochiai Y, Kaito T and Matsui S 2003 *J. Vac. Sci. Technol.* B **21** 2990

[17] Molhave K, Madsen D N and Bøggild P 2004 *Ultramicroscopy* at press

[18] Durkan C and Welland M E 2000 *Ultramicroscopy* **82** 125

[19] Collins P G, Hersam M, Arnold M, Martel R and Avouris P 2001 *Phys. Rev. Lett.* **86** 3128

[20] Bøggild P, Grey F, Hassenkam T, Greve D R and Bjørnholm T 2000 *Adv. Mater.* **12** 947

[21] Collins P G and Avouris Ph 2002 *Appl. Phys.* A **74** 329

[22] Minot E D, Yaish Y, Sazonova V, Park J Y, Brink M and McEuen P L 2003 *Phys. Rev. Lett.* **90** 156401

[23] Cao J, Wang Q and Dai H 2003 *Phys. Rev. Lett.* **90** 157601

[24] Wang Z L 2001 *J. Mater. Sci. Technol.* **17** 303
Matsui S, Kaito T, Fujita J, Komuro M, Kanda K and Haruyama Y 2000 *J. Vac. Sci. Technol.* B **18** 3181

[25] Hoshino T *et al* 2003 *J. Vac. Sci. Technol.* B **21** 2732

[26] Ishida M, Fujita J, Ichihashi T, Ochiai Y, Kaito T and Matsui S 2003 *J. Vac. Sci. Technol.* B **21** 2728

[27] Fujita J, Ishida M, Ichihashi T, Ochiai Y, Kaito T and Matsui S 2002 *J. Vac. Sci. Technol.* B **20** 2686

Appendix D

Article [4]
Solid Gold Nanostructures Fabricated by Electron Beam Deposition

NANO LETTERS

2003
Vol. 3, No. 11
1499−1503

Solid Gold Nanostructures Fabricated by Electron Beam Deposition

Kristian Mølhave,*,† Dorte Nørgaard Madsen,† Anne Marie Rasmussen,‡ Anna Carlsson,‡ Charlotte C. Appel,‡ Michael Brorson,‡ Claus J. H. Jacobsen,‡ and Peter Bøggild†

Mikroelektronik Centret, Technical University of Denmark, DK-2800 Kgs. Lyngby, Denmark and Haldor Topsøe A/S, Nymøllevej 55, DK-2800 Lyngby, Denmark

Received July 17, 2003; Revised Manuscript Received September 3, 2003

ABSTRACT

Direct writing with gold by electron beam deposition is a method for rapid fabrication of electrically conducting nanostructures. An environmental scanning electron microscope (ESEM) equipped with a source of the precursor gas dimethylacetylacetonate gold(III) was used to fabricate nanoscale tips and bridges. Transmission electron microscopy was used to study how the composition of these structures was affected when the background gas in the ESEM chamber and the electron beam parameters were varied. The nanostructures were layered composites of up to three different materials each characterized by a certain range of gold/carbon ratios. Above a certain threshold of ESEM chamber water vapor pressure and a certain threshold of electron beam current, the deposited tips contained a solid polycrystalline gold core. The deposition technique was used to fabricate free-standing nanowires and to solder free-standing carbon nanotubes to gold electrodes as well as to other carbon nanotubes.

Introduction. Electron beam deposition (EBD) is an attractive tool for rapid construction of three-dimensional nanostructures with customizable mechanical and electrical properties.[1−3] Typically, in a scanning electron microscope (SEM), a small amount of residual organic gas molecules is present in the chamber. When the electron beam is focused on a surface, the generated secondary electrons decompose the organic gas molecules and a solid carbonaceous tip will grow in the direction of the beam. By slowly scanning the electron beam during deposition, more complex three-dimensional structures can be fabricated.[4] EBD has also been used to attach nanotubes to other structures[5] and to join carbon nanotubes together.[6]

Metal-containing EBD materials can be obtained by introducing an organometallic gas in the chamber. The metal content of the EBD material can be increased by (i) heating the substrate,[7] (ii) using a precursor gas without carbon,[8] or (iii) introducing an additional gas such as water vapor while using an *environmental* scanning electron microscope (ESEM).[9,10] Recently, we demonstrated low contact resistance soldering of carbon nanotubes onto microelectrodes using organometallic EBD in an ESEM.[11] Folch et al. investigated EBD in an ESEM with dimethyl(hexafluoroacetylacetonate) gold(III) as precursor gas.[9] Using Auger electron spectroscopy they found that the gold content of tips could be increased to 50% by using 10 Torr 80%Ar/20%O_2 as chamber gas. However, Auger electron spectroscopy mainly probes the outermost atomic layers (a few nanometers) of the typically 20−200 nm wide structures.

In this article we report controlled EBD in an ESEM of nanostructures with solid gold cores. The influence of various parameters on the structure and composition of the deposited material was investigated by high-resolution TEM (HRTEM). It was found that the presence of water vapor in the ESEM chamber plays a crucial role in obtaining dense, polycrystalline gold cores.

Experimental Methods. The deposition setup was installed in a Philips XL30 ESEM equipped with a field emission electron gun. All experiments were performed at room temperature using the precursor gas dimethylacetylacetonate gold(III), [$Au(CH_3)_2(C_5H_7O_2)$]. The solid source material (vapor pressure 0.01 Torr equal to 1.3 Pa at 25 °C) was placed in a small aluminum cylinder mounted on a nozzle with a 10 mm long, 1 mm diameter bore, ending about 1 mm from the TEM grid that served as the deposition target. The cylinder was loaded with 50 mg freshly crushed [$Au(CH_3)_2(C_5H_7O_2)$] crystals before each ESEM session, but the lifetime of the source varied substantially. Thus, tip growth rates could vary as much as a factor of 2 from session to session. Each graph presented in this paper is based on data from within one single session. Without precursor gas

* Corresponding author. E-mail: krm@mic.dtu.dk.
† Mikroelektronik Centret.
‡ Haldor Topsøe A/S.

10.1021/nl034528o CCC: $25.00
Published on Web 10/01/2003

present in the chamber, the deposition rate was negligible in the high vacuum mode as well as in the gas mode of the ESEM.

The dependence of the EBD tip structure and composition on the various experimental parameters was investigated. Before deposition of a tip, the electron beam was focused to the smallest possible spot at the given experimental parameters. During deposition, the beam was kept in the same position for 120 s. The working distance was maintained at 10 mm in all experiments. The beam current was controlled by changing the strength of the condensor lens (i.e., spot size), and its magnitude was estimated by placing an electrically conducting plate in the beam path and measuring the absorbed current in high vacuum mode. This is not a strictly correct measure of the beam current but for the present purposes the method is adequate. In the experiments, gas type, pressure, working distance, and temperature were kept constant when beam current was changed. Therefore, under the given conditions the ratio I/I_0 (where I_0 is the intensity of the electron beam in a vacuum and I is the intensity of the unscattered part of the beam) is expected to be constant.[12] Analysis of the deposited tips was made by HRTEM at 200 kV in a Philips CM200 FEG UltraTwin.

Results. During a deposition session, the tip height grew with a constant rate of up to 1.5 μm/minute, which is comparable to EBD growth rates reported in the literature.[7,13] The TEM analysis showed that, depending on the ESEM parameters, the deposited tips may contain three distinct types of concentric layers, which we shall refer to as *core*, *crust*, and *contamination layers*. The apices of three tips with different morphologies, all deposited by a beam of 10 kV acceleration voltage and about 0.2 nA beam current, are presented in Figure 1. Tips deposited in 1 Torr N_2 (Figure 1a) consisted of gold nanocrystals (diameter 3−5 nm) embedded in an amorphous carbon matrix; they appear similar to tips fabricated by EBD in a traditional SEM.[14] Tips deposited using 0.9 Torr H_2O vapor as chamber gas (Figure 1b) contained a central core of dense gold surrounded by a crust resembling the material of the tip shown in Figure 1a. The tip presented in Figure 1c was made under similar conditions as the tip in Figure 1b, but in this case a second deposition was made 1.5 μm to the right of the tip shown. This led to the tip becoming covered by a contamination layer, thickest on the side facing the second deposition. The contamination layer consisted of amorphous carbon with lower gold content than the crust. When structures with asymmetric contamination layers were imaged in SEM or TEM, the tips slowly bent toward the side with the thickest contamination layer (Figure 1d).

In HRTEM images of tip cores, crystal grains can often be found over areas much larger than the typical diameter of nanocrystals in the crust, and sometimes even comparable to the core diameter. Figure 2 shows an example of such a tip structure, where lattice patterns are visible across distances much larger than the sizes of the crust nanocrystals. Estimating the upper limit of the size of the core crystal grains is not straightforward because the thicker parts of the cores block the TEM electrons. Fourier transforms of TEM

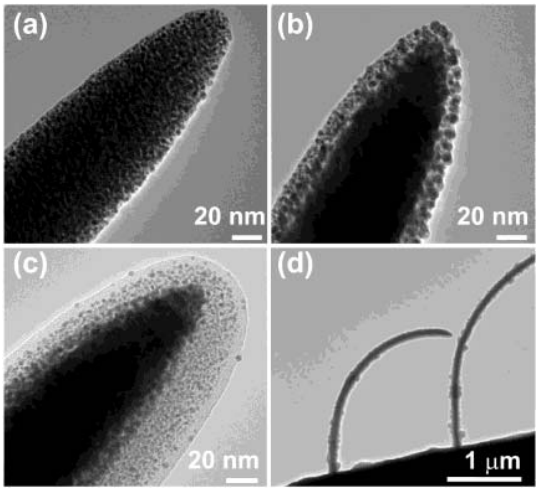

Figure 1. TEM images giving an overview of typical tip structures deposited in an ESEM. (a) Deposition in nitrogen gas; tips consist of gold nanocrystals embedded in an amorphous carbon matrix. (b) Deposition in water vapor; tips consist of a dense core of gold surrounded by a crust of gold nanocrystals in amorphous carbon, i.e., the crust material is similar to the material of the tip in (a). (c) Influence of later deposition nearby; a thick contamination layer covers the tip on the side toward the deposition a few μm to the right. Contamination layers have a lower gold content than the crust material and are thicker on the side facing the later depositions. Further, imaging of structures in ESEM with the source present results in contamination layers of almost pure carbon (the uniform outermost layer of the tip in (c)). (d) Influence on tips with contamination layers of electron radiation in SEM or TEM; irreversible deformation occurs as a bending toward the side with the thickest contamination layer.

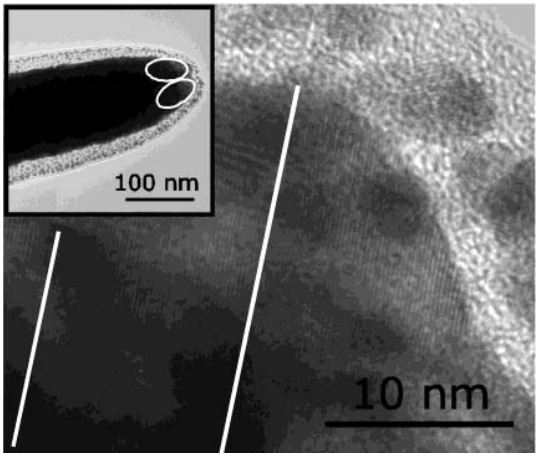

Figure 2. HRTEM image of a tip with a core. The cores often contain large crystal grains visible over distances several times the typical nanocrystal diameter. The two marked areas in the inset show the approximate size and position of two large monocrystalline grains in the tip apex. The higher magnification image show half the upper grain, with the lattice structure indicated by the white lines.

core images show lattice spacings of 2.5, 2.1, and 1.5 Å corresponding to gold lattice spacings 2.35, 2.04, and 1.44 Å, within an uncertainty of approximately 5%, which is expected since the imaging conditions were not optimized for calibrated measurements of lattice spacings. The large crystal domains together with the observed lattice spacings

and EDX spectra indicate that the core consists of solid polycrystalline gold, with grain dimensions significantly larger than the nanocrystals in the crust.

We have examined the dependence of the tip structure on beam acceleration voltage, beam current, and chamber gas pressure. These parameters were varied individually with respect to a default setting of 10 kV acceleration voltage, about 0.2 nA beam current and 0.8 Torr H_2O pressure, which was found optimal in terms of imaging. All tips were deposited in 120 s. The acceleration voltage had little effect on the layer structure except at low energies (<5 kV), where the layer structure became more diffuse. At low acceleration voltages the beam is significantly broadened due to scattering of the primary electrons on the chamber gas. The dependence of the structure on beam current and chamber gas pressure is presented in Figure 3.

The observed structural dimensions for tips deposited at different beam currents are shown in Figures 3a and 3b. Figure 3b shows an increase of the core diameter with beam current. The fit indicates that the core diameter is proportional to the square root of the current.

The type and pressure of the chamber gas used during the deposition also affects tip structure and dimensions (Figure 3c and 3d). The outer (crust) diameter is approximately constant with pressure and similar for H_2O and N_2 (Figure 3c), indicating that the beam is not significantly widened, despite the expected larger scattering of the primary beam at the highest pressures. No cores were observed in the tips deposited in N_2 at any gas pressure. Using water vapor pressures above about 0.4 Torr, the tips contained a solid core surrounded by a crust as shown in Figure 1b, while no cores were seen below this threshold pressure. Both tip height and core diameter appeared to decrease rapidly with decreasing vapor pressure when approaching the threshold. Tips were also deposited using two different gas mixtures, 60%He/40%H_2 and 80%Ar/20%O_2 (both at 2 Torr), where the amounts of O and H in the chamber corresponds to that of water vapor at 0.8 Torr. It was not possible to produce any cores in these experiments, while using water at 0.8 Torr as chamber gas resulted in a core in all experiments.

By scanning the electron beam along a line during deposition, we deposited wires on surfaces as well as from free-standing wires. Using a free-standing carbon nanotube as the starting point, a wire was deposited in the plane perpendicular to the beam by scanning the beam at a speed of a few nm/s (Figure 4a). Like the tips deposited on surfaces, these wires have a core with high gold content. The wire appears to be firmly attached to the carbon nanotube, which was noticeably deformed at the joint. Both the nanotube and the gold wire were covered by a low gold-content contamination layer that arose while imaging at high magnification in the presence of the precursor gas. Figure 4b shows a SEM image of a nanotube soldered to an electrode as reported in ref 11. The line width of such depositions can be down to 20−30 nm, and we have achieved continuous cores with line widths down to 10−20 nm for both fixed and scanned beam depositions (see Figure 3b (and inset), 4a, and 4b).

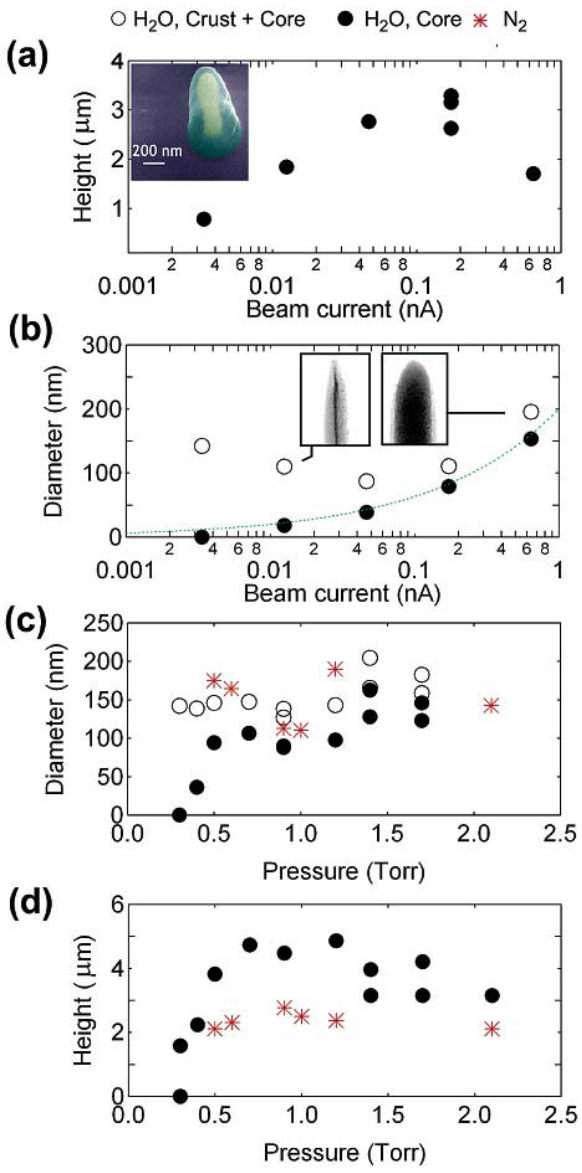

Figure 3. Tip structure as function of beam current, pressure, and type of the chamber gas. All tips were deposited in 120 s using 10 kV acceleration voltage. (a) Tip height (dots) vs beam current with 0.8 Torr H_2O as chamber gas. The inset shows a SEM image of a tip with a crust, which is transparent to the 30 kV SEM beam electrons used for imaging, and a solid core, which appears opaque. (b) Tip diameter (of core (dots) and crust + core (circles)) vs beam current also with 0.8 Torr H_2O as chamber gas. The diameter of the core was proportional to the square root of the current (cf. the curve shown). The insets show TEM images of tips deposited at different currents. (c, d) Tip diameters and heights obtained at different chamber gas types and pressures at a constant primary beam current (0.2 nA).

Discussion. The TEM analyses show that the EBD tips made in ESEM have a unique layer structure, to our knowledge not previously reported in the literature. Three distinct types of layers have been identified: a core, a crust, and carbonaceous contamination layers. From Figures 1a and 1b it is evident that the crust material consists of crystalline particles (3−5 nm diameter) separated by about 1−2 nm. The precursor gas dimethylacetylacetonate gold(III) has a

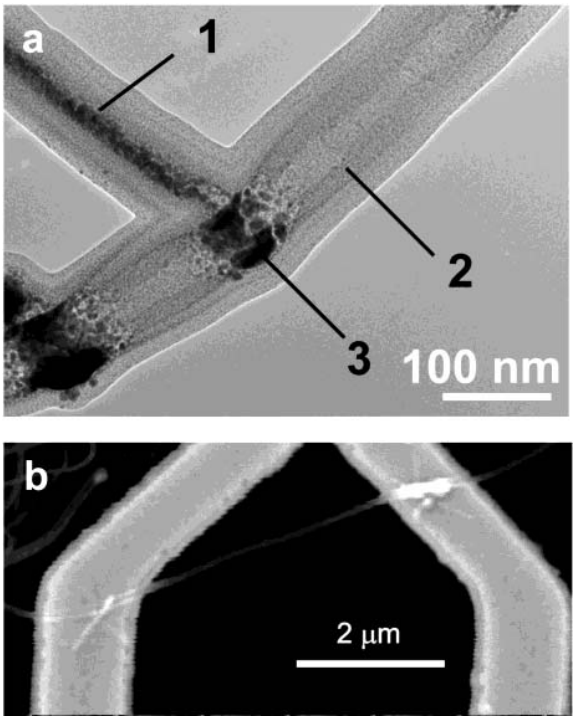

Figure 4. (a) High-resolution transmission electron microscopy image of a joint between a carbon nanotube and a deposited gold wire. The gold wire (1) was made by scanning the beam across a free-standing carbon nanotube (2). Deformation of the nanotube is seen in the joint (3). Both nanotube and gold wire are covered by a 20−30 nm thick contamination layer. (b) An ESEM image of a suspended carbon nanotube soldered onto two gold electrodes by cross-shaped gold depositions. The line width of the depositions is about 20−30 nm. The measured resistance across such bridges is typically in the 10 kΩ range.[11]

C/Au ratio of 7:1. In a solid material consisting of gold spheres with a diameter of 3 nm and graphitic carbon, the gold spheres must be spaced by 1 nm to give the C/Au ratio of the precursor gas. This spacing is consistent with our observations for tips deposited in N_2, in 60%He/40%H_2, and in 80%Ar/20%O_2.

Based on the observed lattice patterns of the cores, with crystal domains much larger than the nanometer-sized crystals commonly seen in the crusts, we find that the cores most likely consist of solid, polycrystalline gold. This is supported by the low resistivity of 10^{-4} Ωcm measured on bridges made of this material, as reported in ref 15. Further, bridges deposited using the chamber gas N_2, which gives no core structure, showed resistivities beyond the measurement sensitivity, i.e., several orders of magnitude higher than the value of ref 15. An extensive study of the mechanical and electrical properties of these structures is in progress. Solid gold cores have been observed with diameters from around 10 nm to 150 nm (Figures 3 and 4). Cores thinner than about 10 nm appear as dense regions with crystallites rather than as continuous solid cores resembling the structure of the core in Figure 4a.

The core diameter can apparently be controlled through the beam current and the water vapor pressure. Compared to deposition in N_2, deposition in the presence of water vapor leads to taller and wider tips as well as a higher gold content, since the gold core takes up a significant fraction of the tip volume. Folch et al. found by Auger electron spectroscopy that oxygen mixtures gave rise to higher gold contents than water vapor.[9] The discrepancy may be explained by the fact that Auger electron spectroscopy probes only the outermost layers of the tips. A minimum requirement for the generation of a core appears to be a water vapor pressure of about 0.4 Torr. We found that the cross-section area of the core was proportional to the beam current (Figure 3b). No gold cores were formed when N_2, O_2/Ar or H_2/He was used as chamber gas, even though the content of O and H in the gas mixtures were comparable to water vapor pressures that consistently gave dense cores. We notice that water is known to influence the diffusion of gold during deposition[16] and that irradiation is capable of affecting the diffusivity of gold clusters.[17]

The tip height appears to decrease at beam currents higher than 0.2 nA and lower than 0.04 nA (Figure 3a). The reason could be that it is difficult to focus at small and large spot sizes (low and high beam currents, respectively). From Figure 3b it seems that at beam currents higher than about 0.05 nA the increase in combined crust and core diameter follows the increase in core diameter. At beam currents lower than 0.05 nA the combined crust and core diameter increases while the core diameter decreases. An explanation may be that as the core diameter decreases, a larger amount of electrons may be able to escape the tip edges and thus cause crust deposition when decomposing precursor gas molecules.

When imaging at very high resolution and in the presence of the gold precursor gas, an outer layer of almost pure carbon, a so-called contamination layer, formed on the deposited structures. Also, when depositing groups of closely spaced tips, a similar layer with very low gold content was observed on the deposited tips at the side that had later faced the beam. The deposition rate in the absence of the precursor gas source was negligible, indicating that the formation of these contamination layers is due to the precursor gas. The contamination layers appeared to induce stress in the tip structures when exposed to electron radiation during imaging in SEM or TEM. The structures were seen to bend toward the side with the thickest contamination layer and retained the bent shape after being exposed to air. This phenomenon has not been reported in earlier work, although we have observed a similar behavior for carbonaceous tips made by EBD from the background gas in a traditional SEM. Mechanically tuning the shape of nanostructures by exposing irradiation-sensitive layers is an intriguing possibility. Preliminary experiments using a controllable source that can be closed when deposition is undesired, show that the thickness of contamination layers can be reduced drastically, thereby also reducing the deformation effect during subsequent imaging.

The EBD method provides the unique possibility of directly forming electrical and mechanical interconnections between free-standing carbon nanotubes and other micro- and nanostructures. The TEM images of nanotube soldering show that the gold connections deform or collapse the nanotube in the joint, which may damage the graphitic layer-

structure of the nanotube close to the solder material. How this affects the electrical properties of the nanotube remains to be investigated.[15] Also, depositions of material on surfaces may give rise to a different material structure, since the surface influences the generation of secondary electrons, which play an important role in the deposition process.[18]

The fast construction of three-dimensional solid gold nanostructures could find applications in many areas of nanotechnology. Apart from rapid prototyping and wiring of electrically conducting structures with potential use as wires, field emitters, strain gauges or thermal sensors (depending of composition), the method has already proven useful for soldering of nanotubes.[11] Furthermore, gold can easily be functionalized to modify the chemical properties of the surface, which may be used to make scanning probe microscopy tips with tailored friction, adhesion or conducting properties.

Acknowledgment. Technical assistance from Sven Ullmann and carbon nanotube samples fabricated by Ramona Mateiu are greatly appreciated. We thank Rodney Ruoff for valuable discussions. The research was supported by the Danish Technical Research Council through a "Talent-projekt" grant.

References

(1) Edinger, K.; Gotszalk, T.; Rangelow, I. W. *J. Vac. Sci. Technol. B* **2001**, *19*, 2856.
(2) Koops, H. W. P.; Weber; M., Schossler, C.; Kaya, A. *SPIE* 1996, *2780*, 388.
(3) Boggild, P.; Hansen, T. M.; Tanasa, C.; Grey, F. *Nanotechnology* **2001**, *12*, 331.
(4) Ooi, T.; Matsumoto, K.; Nakao, M.; Otsubo, M.; Shirakata, S.; Tanaka, S.; Hatamura, Y. *Proceedings of the IEEE Micro Electro Mechanical Systems (MEMS)* **2000**, 580.
(5) Yu, M.-F.; Lourie, O.; Dyer, M. J.; Moloni, K.; Kelly, T. F.; Ruoff, R. S. *Science* **2000**, *287*, 637.
(6) Banhart, F. *Nano Lett.* **2001**, *1*, 329.
(7) Koops, H. W. P.; Schossler, C.; Kaya, A.; Weber, M. *J. Vac. Sci. Technol. B* **1996**, *14*, 4105.
(8) Utke, I.; Hoffman, P.; Dwir, B.; Leifer, K.; Kapon, E.; Doppelt, P. *J. Vac. Sci. Technol. B* **2000**, *18*, 3168.
(9) Folch, A.; Tejada, J.; Peter, C. H.; Wrighton, M. S. *Appl. Phys. Lett.* **1995**, *66*, 2080.
(10) Folch, A.; Servat, J.; Esteve, J.; Tejada, J. *J. Vac. Sci. Technol. B* **1996**, *14*, 2609.
(11) Madsen, D. N.; Molhave, K.; Mateiu, R.; Rasmussen, A. M.; Brorson, M.; Jacobsen, C. J. H.; Boggild, P. *Nano Lett.* **2003**, *3*, 47.
(12) Danilatos, G. D. *Mikrochim. Acta* **1994**, *114/115*, 143−155.
(13) Koops, H. W. P.; Kaya, A.; Weber, M. *J. Vac. Sci. Technol. B* **1995**, *13*, 2400.
(14) Kretz, J.; Rudolph, M.; Weber, M.; Koops, H. W. P. *Microelectron. Eng.* **1994**, *23*, 477.
(15) Madsen, D. N.; Molhave, K.; Mateiu, R.; Boggild, P.; Rasmussen, A. M.; Appel, C. C.; Brorson, M.; Jacobsen, C. J. H., to appear in *Proceedings of the 2003 Third Conference on Nanotechnology* **2003**.
(16) Harsdorff, M. *Thin Solid Films* **1984**, *116*, 55.
(17) Xue, B.; Chen, P.; Hong, Q.; Lin, J.; Tan, K. L. *Mater. Chem.* **2001**, *11*, 2378.
(18) Silvis-Cividjian, N.; Hagen, C. W.; Leunissen, L. H. A.; Kruit, P. *Microelectronic Engineering* **2002**, *61*−*62*, 693−699.

NL034528O

Appendix E

Article [5]
Soldering of nanotubes onto microelectrodes

NANO LETTERS

2003
Vol. 3, No. 1
47−49

Soldering of Nanotubes onto **Microelectrodes**

Dorte Nørgaard Madsen,[†] Kristian Mølhave,[†] Ramona Mateiu,[†] Anne Marie Rasmussen,[‡] Michael Brorson,[‡] Claus J. H. Jacobsen,[‡] and Peter Bøggild*,[†]

Mikroelektronik Centret, Technical University of Denmark, DK-2800 Kgs. Lyngby, Denmark, and Haldor Topsøe A/S, Nymøllevej 55, DK-2800 Lyngby, Denmark

Received September 17, 2002; Revised Manuscript Received November 6, 2002

ABSTRACT

Suspended bridges of individual multiwalled carbon nanotubes were fabricated inside a scanning electron microscope by soldering the nanotube onto microelectrodes with highly conducting gold–carbon material. By the decomposition of organometallic vapor with the electron beam, metal-containing solder bonds were formed at the intersection of the nanotube and the electrodes. Current–voltage curves indicated metallic conduction of the nanotubes, with resistances in the range of 9–29 kΩ. Bridges made entirely of the soldering material exhibited resistances on the order of 100 Ω, and the solder bonds were consistently found to be mechanically stronger than the carbon nanotubes.

Carbon nanotubes have been proposed as prototypical nanoscale building blocks because of their unique mechanical and electrical properties.[1] To explore their potential in physics, chemistry, and biology, a number of methods have been employed to form electrical and mechanical connections to devices and nanostructures.[2−5] We present an in situ method for the highly conductive attachment of nanoscale components by the use of a gold−carbon composite soldering material deposited by a focused electron beam. This method does not require electrical contact to the electrodes or the component and allows for the assembly of 3D structures.

We used a Philips XL30 ESEM-FEG environmental scanning electron microscope, operating at a water vapor pressure of 100 Pa. Dimethylacetylacetonate gold(III), which has a vapor pressure of 1 Pa at 25 °C, was placed in a container with a narrow bore tube to control the diffusion of organometallic vapor onto the sample. The electron beam locally decomposes the organometallic compound and thereby deposits a material with metallic content.[6] Using a 2-mm-long tube with a diameter of 0.8 mm, we obtained a growth rate of 500 nm/min. Tips with lengths of more than 10 μm could be grown without a significant decrease in the growth rate. All depositions were made at room temperature. A nanomanipulator stage inside the chamber was used to move a silicon chip with two cantilever microelectrodes.[7] The electrodes were connected to a DC voltage source, and the current was monitored continuously (see Figure 1a). Samples of free-standing multiwalled carbon nanotubes (MWNTs) were prepared[8] and characterized by transmission electron

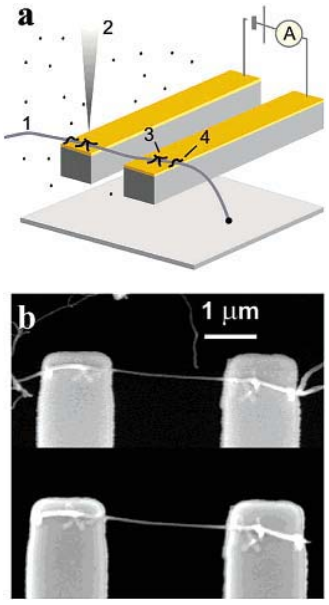

Figure 1. (a) Illustration of two microelectrodes positioned close to a multiwalled nanotube (1) extending from a catalyst particle on a substrate. Organometallic molecules decomposed by the electron beam (2) are deposited to form a cross-shaped solder bond (3) and a protective bond (4) near the edge of the electrode. (b) ESEM image of a carbon nanotube across two electrodes, connected by soldering bonds and protective bonds (top). When the electrode pair is withdrawn, the nanotube breaks at the protective bonds (bottom).

* Corresponding author. E-mail: pb@mic.dtu.dk.
[†] Technical University of Denmark.
[‡] Haldor Topsøe A/S.

10.1021/nl0257972 CCC: $25.00
Published on Web 11/27/2002

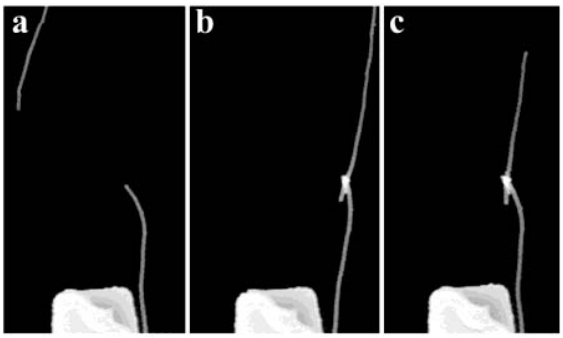

Figure 2. SEM image sequence of tube-to-tube soldering showing the approach of a nanotube soldered to a microelectrode toward a MWNT extending from the substrate (a) and subsequent soldering of the tube ends (b). Withdrawal of the electrode broke the nanotube and not the bond (c).

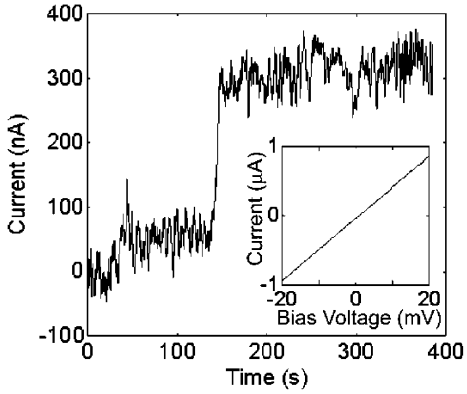

Figure 3. Current vs time during soldering of the MWNT using the electron beam. A fixed voltage of 10 mV is applied across the microelectrodes. During the formation of the second soldering bond, the current suddenly increased to a stable 300 nA. The IV characteristic (inset) was found to be linear.

microscopy (TEM), which revealed the presence of more than 20-μm-long, 80−120-nm-wide MWNTs. In the ESEM, a microelectrode pair was aligned to a nanotube extending from the sample so that both electrodes touched the nanotube. By slowly scanning the beam across the nanotube at the point of contact to the first electrode, two cross-shaped gold−carbon soldering bonds were formed.

The deposition of a set of protective bonds near the edge of the microelectrodes allowed us mechanically to break off the MWNT parts extending beyond the electrodes without damaging the soldering bonds (see Figure 1b, lower panel). We consistently observed the MWNTs to break rather than the protective bonds, both for tube−electrode bonds (Figure 1) and for tube−tube bonds, as shown in Figure 2. To avoid unwanted contamination of the nanotubes by soldering material, we avoided imaging the suspended part of the nanotubes at high magnification.

For all of the examined bridges, electrical contact was established during the soldering procedure at the second electrode. In the example shown in Figure 3, the current increased in two steps, first from 0 to 60 nA and then abruptly to 300 nA, at a bias voltage of 10 mV. A linear current−voltage curve was measured, indicating metallic

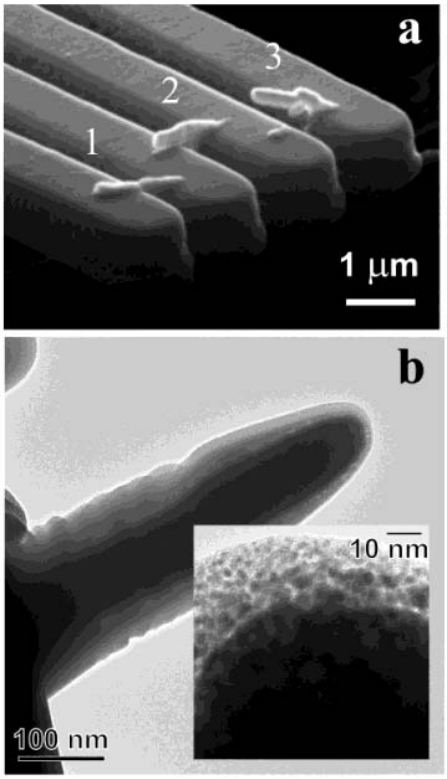

Figure 4. (a) SEM image of three bridges of soldering material deposited between microelectrodes by scanning the electron beam across the gaps at different speeds (fastest for bridge 1). The resistances were 127 Ω for bridge 1 and 520 Ω for bridge 2. Bridge 3 did not connect to both electrodes. (b) TEM image of a beam of soldering material, showing a dense core encapsulated in a porous crust. In the inset, the porous crust structure with 3−5-nm nanoparticles can be seen.

conduction (Figure 3, inset), and the resistance was 27 kΩ. We connected four nanotubes and every time obtained reliable ohmic contacts upon soldering to the second electrode, with resistances of 9, 11, 27, and 29 kΩ, with no clear correlation to the length of the MWNT bridge. The resistances of the nanotube bridges were unaffected by the breaking of the nanotube extensions and by the deposition of the protective bonds and were found to be constant in air for days.

We verified that the soldering material itself was conducting by depositing gold−carbon bridges between microelectrode pairs (Figure 4a) and measuring the IV characteristics. All of the bridges that connected properly to both microelectrodes, such as bridges 1 and 2 in Figure 4a, showed ohmic resistances between 80 and 520 Ω. By estimating the cross section of the bridges from SEM images and taking a serial resistance of roughly 60 Ω into account, we obtained resistivities down to 10^{-4} Ω cm. TEM analysis of the soldering material revealed a gold−carbon composite structure with a porous crust of 3−5-nm nanoparticles around a dense core (Figure 4).

We also attached MWNTs to microelectrodes by means of nonmetallic carbonaceous material; these devices showed electrical conduction in the megaohm range. This strongly

indicates that the metal content of the soldering material is necessary for good electrical contact.

The question regarding the contribution of individual shells in MWNTs to the conductivity of the tube is still not resolved. Frank et al.[9] observed a consistent resistance of 13 kΩ for nearly defect-free arc-discharge-grown MWNTs, whereas Collins and co-workers[10] found lower values (5−15 kΩ) and evidence of several contributing shells at low bias. Chemical-vapor-deposited nanotubes generally contain more structural defects than arc-discharge-grown nanotubes, which leads to a curving of the nanotubes (see Figure 1). The reason for the relatively small resistances (compared to those in ref 9 and 10) observed in our CVD-grown nanotubes is not clear. It has been proposed that structural defects may decrease the intershell resistivity. In our case, this could lead to more shells contributing to the transport, thus partially compensating for the reduced resistance of each shell.

The resistivity of the soldering material is slightly larger than the value of 1.3×10^{-5} Ω cm reported by Bietsch et al. for microcontact-printed pure-gold nanowires of similar dimensions[11] and 2 orders of magnitude larger than that of bulk gold. For electron-beam-deposited nanowires, resistances as small as ours have been obtained by heating the sample to 80 °C during deposition to increase the relative content of gold.[6] These values were obtained only after annealing at 180 °C, which further reduced the resistivity by 2−3 orders of magnitude. One possible explanation for the high conductivity of our material achieved at room temperature without annealing could be that the presence of H_2O in the sample chamber reduces the relative amount of carbon, as suggested by Folch and co-workers.[12] This could be clarified by analyzing the chemical composition of the soldering material deposited at different vapor pressures.

The method of nanosoldering presented here does not depend on the particular nanocomponent or on the electrodes. It involves no lithographic steps or electrical connections such as in spot welding,[5] and it is straightforward to achieve accurate alignment. The soldering bonds were found to be mechanically strong compared to the MWNTs. To investigate this quantitatively, a piezo-resistive force sensor will be integrated in the setup. We anticipate automated electron-beam nanosoldering to be useful for quickly connecting complex circuitry consisting of nanoscale components in a way similar to the soldering of electronic components on the macroscale.

Acknowledgment. We acknowledge financial support from the Danish Technical Research Council (NANOHAND talent project).

References

(1) Collins, P. G.; Avouris, P. *Sci. Am.* **2000**, *283*, 38.
(2) Williams, P. A.; Papadakis, S. J.; Falvo, M. R.; Patel, A. M.; Sinclair, M.; Seeger, A.; Helser, A.; Taylor, R. M.; Washburn, S.; Superfine, R. *Appl. Phys. Lett.* **2002**, *80*, 2574.
(3) Yu, M. F.; Dyer, M. J.; Skidmore, G. D.; Rohrs, H. W.; Lu, X. K.; Ausman, K. D.; Von Ehr, J. R.; Ruoff, R. S. *Nanotechnology* **1999**, *10*, 244.
(4) Banhart, F. *Nano Lett.* **2001**, *1*, 329.
(5) Cumings, J.; Zettl, A. *Science (Washington, D.C.)* **2000**, *289*, 602.
(6) Koops, H. W. P.; Schossler, C.; Kaya, A.; Weber, M. *J. Vac. Sci. Technol., B* **1996**, *14*, 4105.
(7) Bøggild, P.; Hansen, T. M.; Tanasa, C.; Grey, F. *Nanotechnology* **2001**, *12*, 331.
(8) Wang, X. B.; Liu, Y. Q.; Zhu, D. B. *Chem. Commun.* **2001**, 751.
(9) Franks, S.; Poncharal, P.; Wang, Z. L.; Heer, W. A. *Science (Washington, D.C.)* **1998**, *280*, 1744
(10) Collins, P. G.; Avouris, P. *Appl. Phys. A* **2002,** *74*, 329
(11) Bietsch, A.; Michel, B. *Appl. Phys. Lett.* **2002**, *80*, 3346
(12) Folch, A.; Tejada, J.; Peter, C. H.; Wrighton, M. S. *Appl. Phys. Lett.* **1995**, *66*, 2080.

NL0257972

Appendix F

Article [6]
Towards pick-and-place assembly of nanostructures

Towards Pick-and-Place Assembly of Nanostructures

Kristian Mølhave, Torben Mikael Hansen, Dorte Nørgaard Madsen, and Peter Bøggild

Department of Micro and Nanotechnology, Technical University of Denmark, DK-2800 Lyngby, Denmark

We examine an approach to three-dimensional pick-and-place assembly of wire-like nanoscale components, such as carbon nanotubes and silicon nanowires, on microstructures inside a scanning electron microscope. In this article we demonstrate that microfabricated electrostatically actuated tweezers can pick up silicon nanowires and show how electron beam deposition of carbon residues can be used to assemble carbon nanotubes on microelectrodes.

Keywords: Nanomanipulation; Nanowire; Nanotube; Tweezers; Electron Beam Deposition or Electron Beam Induced Deposition.

1. INTRODUCTION

Since the discovery of carbon nanotubes a decade ago, the fascinating properties of these and other wire-like nanostructures have been the subjects of intense study. To realize the potential of nanotubes and nanowires as active components in electronic devices, methods for reliable integration with microstructures are required.

Scanning probe microscopes have been widely used for manipulation of nanotubes on planar surfaces to measure rolling, sliding, and bending properties of single-walled nanotubes (SWNTs),[1, 2] construction of field-effect transistors,[3] and detailed studies of nanotube junctions.[4] In these experiments, tube-surface adhesion often plays a dominating role. It has also been shown that the electrical properties of SWNTs can be considerably affected by direct contact to a surface.[5]

Common strategies for three-dimensional integration include directed growth of nanostructures on microelectrodes,[6, 7] assembly in liquid solution using flow alignment,[8] and direct mechanical assembly using sharp tips.[9, 10] Opening and closing of nanotweezers designed for nanomanipulation have been demonstrated in a scanning electron microscope (SEM),[11–13] and nanotweezers have also been used to pick up nanoscale objects in ambient conditions.[11, 13]

So far, approaches to reliable pick-and-place assembly of nanowires and nanotubes have not been reported. The key issue is to control the balance between the sum of forces acting between the object and the surface, F_{surface}, and the forces acting between the object and the tool, F_{tool}. Although picking up an object requires F_{tool} to overcome F_{surface}, the balance must be reversed to place and release the object. On the nanoscale, controlling this balance is particularly difficult due to the presence of forces such as van der Waals and electrostatic forces. The snap-in and sticking effects arising from these forces are among the main challenges of micro- and nanoscale pick-and-place manipulation.

In this work we examine an approach to pick-and-place integration of nanowires and nanotubes on microstructures inside a SEM. We use microfabricated, electrostatically actuated tweezers capable of applying an adjustable force to an object. When the tweezers are opened to release an object, electrostatic forces may still prevent well-controlled placement. To secure precise placing of the object, electron beam deposition (EBD) may be used *in situ* to "solder" the nanotube/nanowire onto the desired location and thereby increase the surface adhesion. Electron beam deposits are formed through a decomposition of gas molecules by localized electron irradiation inside a SEM. The gas source can be the carbonaceous background gas present in the SEM, which has been used to attach carbon nanotubes to other objects[14, 15] or a selected organometallic precursor gas, which can result in deposits with high metal contents[16] and can form highly conductive connections to carbon nanotubes.[17]

In this article we first describe the design of tweezers and manipulation of silicon nanowires using these tweezers. Then we demonstrate that EBD provides a convenient tool for accurately placing nanocomponents, by soldering with deposits smaller than 50 nm.

2. EXPERIMENTAL DETAILS

The microtweezers consist of three to five cantilevers. Figure 1 shows a SEM image of a five-electrode tweezers chip, fabricated in a silicon microfabrication process.[12, 18] The process allows any planar miltielectrode geometry with a linewidth down to 750 nm and cantilever lengths up

*Author to whom correspondence should be addressed.

RESEARCH ARTICLE

  1533-4880/2004/04/279/554/$17.00+.25 doi:10.1166/jnn.2004.025

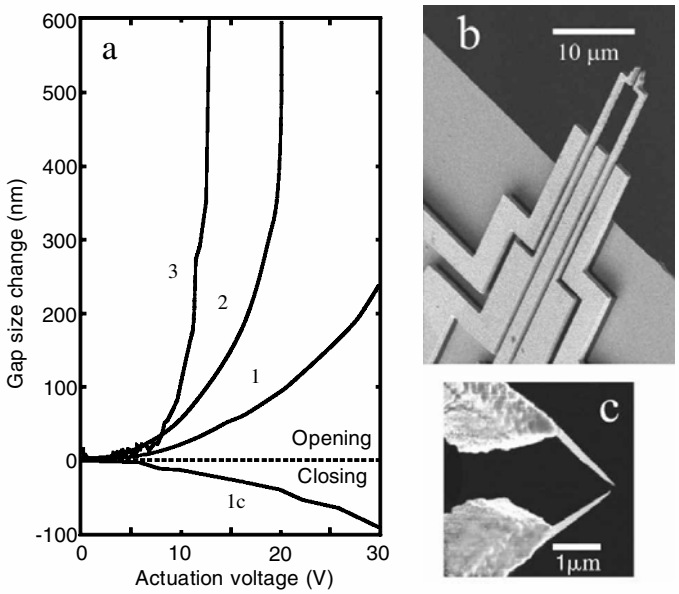

Fig. 1. (a) Actuation curves for three different microtweezer arms, showing the change in gap size relative to the neutral position as a function of applied voltage. Curves 1 and 1c are opening (1) and closing (1c) actuation curves from the same device. In both cases, the actuation curves exhibit a nearly parabolic behavior at low voltages. Curve 2 shows two consecutive actuation curves for a 50-μm-long microtweezer arm, where the arms snapped in between the first and the second measurement. The negligible difference demonstrates the reproducibility of the actuation. Curve 3 shows an actuation range of 400 nm at 14 V obtained using a 60-μm-long pair of tweezers. (b) SEM image of a pair of microtweezers with three wide driver electrodes and two long flexible tweezers electrodes. (c) SEM image showing the apex of a pair of microtweezers with EBD tips deposited using the SEM background gas. The deposited tips reduce the size of the gap to 100 nm.

to 80 μm. The cantilevers are made of a 1-μm-thick silicon oxide layer covered with a thin layer of metal (100 Å Ti/1000 Å Au). By applying a voltage between the narrow flexible tweezers electrodes and the wide "driver" electrodes (Fig. 1b), the electrostatic attraction causes the tweezers gap to open or close, depending on whether the inner or the outer driver electrodes are biased. Because no voltage difference has to be applied between the tweezers arms, the electrostatic fields near the grabbed object can be made insignificant, reducing the risk of unwanted electrostatic forces on the object. EBD can be used to add tips with diameters in the 100 nm range at the apex of the microcantilevers (Fig. 1c), which should make it possible to manipulate objects much smaller than the micron-sized cantilevers. With this technique we achieve a considerable reduction of the contact area, thereby reducing the tip–object adhesion forces. The minimum stable gap obtained with this technique is 25 nm.[12]

The change in gap size as a function of applied voltage is shown in Figure 1a for three devices with varying lengths of tweezers arms. The bottom curves demonstrate opening (1) and closing (1c) of one 40-μm-long tweezer arm. The longer devices (50- and 60-μm arms) exhibit steeper actuation curves (2 and 3). The maximal gripping forces are in the sub-μN range. In the experiments described below, these nanotweezers devices were used as tools for manipulation of nanowires and for support for suspended nanotube bridges attached using EBD.

The manipulation setup consists of two platforms that can be positioned in three dimensions with nanometer precision using joystick-controlled PC interfaces. One platform is placed on the 5 dF stage of a LEO 1550 SEM and is capable of supporting several substrates and tools, such as microtweezers and four-point probes. The other platform is mounted on a xyz-manipulator from Klocke Nanotechnik and holds a single pair of microtweezers.

3. RESULTS

The image sequence in Figure 2a–c shows a pair of microtweezers grabbing a silicon nanowire. The tweezers have an actuation range of 300 nm at a voltage of 30 V. The silicon nanowire has a diameter less than 100 nm and is initially lying on a gold-coated Si substrate. To confirm that the applied force and *not* the adhesion of the wire to the tweezers is dominating the pick-up process, the microtweezers were first closed around the wire (Fig. 2a) and subsequently reopened (Fig. 2b). Although the nanowire adhered to the tweezers, the adhesion forces were not sufficient to pull the wire off. Closing the tweezers again (Fig. 2c) allowed the wire to be picked up.

The silicon nanowires require much less force for released from the substrate than the carbon nanotube samples available for the study. While modifications of the nanotweezer shape to facilitate picking up of carbon nanotubes are in progress, we have explored the possibilities of controlled placing of nanotubes using EBD.

We first investigated the mechanical strength of the EBD-grown tweezers tips and a multiwalled carbon nanotube (MWNT) extending from a disordered bundle. They were brought in contact and soldered together using a 30-s exposure to a 5 kV beam, illustrated by the triangle in Figure 3a. When the microtweezers were retracted, the

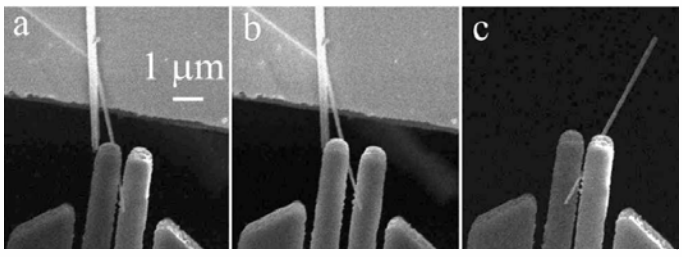

Fig. 2. SEM images of microtweezers gripping a silicon nanowire, which is less than 100 nm wide. (a) The nanowire is gripped at an actuation voltage of 30 V applied between the inner electrodes. (b) The wire is released to verify that adhesion forces alone are not sufficient to pull the wire off the substrate. (c) Finally, the tweezers are closed again using a 30 V bias voltage, enabling the nanowire to be gripped and pulled off the substrate.

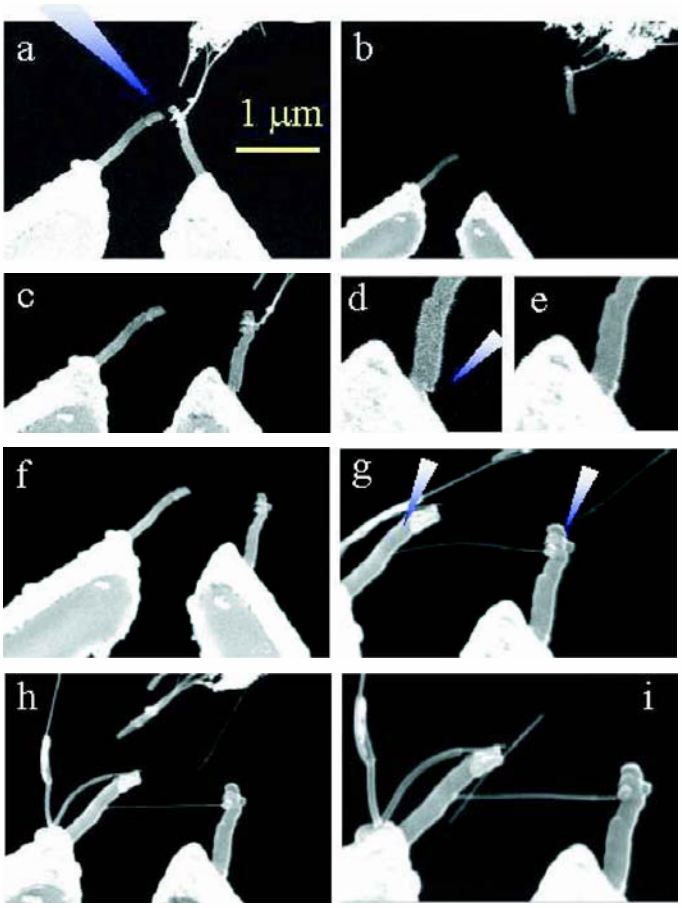

Fig. 3. Electron beam soldering of nanostructures. (a) A multiwalled carbon nanotube extending from an entangled bundle of nanotubes was bonded to the electrode using an electron beam. (b) The tweezers were retracted, whereby the nanotip broke off. (c) The nanotip was then placed in a new position near the electrode. (d) The electron beam spot was directed toward the gap between the tip and the electrode. (e) The sub-50 nm gap was filled with carbonaceous material by a 30-s exposure. (f) Retracting the nanotube broke it off and left the tip in the new position. (g) A multiwalled carbon nanotube was dragged across the two tips and bonded. The bonding fixed the nanotube so that it could be broken off the electrode. (h and i) A second, shorter nanotube was positioned and bonded to the bridging nanotube. Charging of the carbon tips by the electron beam deflected the nanotube and prevented it from being positioned in the middle of the gap.

nanotip eventually broke off at the microelectrode (Fig. 3b). By measuring the bending of the tweezers electrode, the tensile strength was estimated to be on the order of 0.1 μN. The nanotip was subsequently brought in contact with the electrode close to its original position (Fig. 3c). Another 30-s EBD exposure filled the gap between the dangling tip and the electrode, establishing a firm connection at the base of the tip (Fig. 3d–e). The deposit was less than 50 nm in size. By retracting the tweezers a second time, the nanotube broke off, leaving the tip in its new position.

In a subsequent experiment, we connected a MWNT with a diameter of 20–30 nm between the thin EBD tips by first soldering the tube to the left tip (Fig. 3g), dragging it across to the second tip, and finally soldering at the point of contact on the second tip (Fig. 3h). The second bond was strong enough to allow the excess tube to be broken off, while leaving the bridge intact. The EBD tips produced from the background gas in these experiments were not conducting and we measured no electrical conduction (<1 nA at 100 mV bias) in these devices, which sustained bias voltages of several volts.

4. DISCUSSION

We have demonstrated that silicon nanowires can be picked up by electrostatically actuated microtweezers provided that $F_{\text{tool}} > F_{\text{surface}}$ and that carbon nanostructures can be interconnected and integrated on microelectrodes using EBD. Although the two experiments show the feasibility of pick-and-place integration of nanoobjects using tweezers, the results also show the efficiency of EBD for performing nanomanipulation even for materials adhering so strongly to the substrate that they cannot be picked up by the tweezers ($F_{\text{tool}} < F_{\text{surface}}$).

Compared to manipulation using a sharp tip, grabbing of a nanowire with tweezers ideally prevents the nanowire from being misoriented by electrostatic forces in the SEM caused by charging, without the need for contamination of the wire by electron beam deposition. Compared with nanotube nanotweezers,[11, 13] the micrometer-wide arms seem efficient in limiting the freedom of movement of the gripped object. However, with the present setup and microtweezers designs, careful optimization of the accelerating voltage for the electron microscope is necessary to minimize charging of the gripped object and surroundings. Improved tweezers designs, capable of applying larger forces, are under development to widen the range of applications.

The source gas for EBD in the results presented was the background gas present in the electron microscope. The presence of the carbon nanotube sample appeared to contribute to the amount of carbonaceous gas near the electron beam, because the deposition rate was generally higher with carbon nanotube samples.

In the presence of the carbonaceous background gas, the electron beam also deposited material on the nanotubes by EBD when the nanotube was imaged over a long time and/or at high magnification. Using a clean sample reduced the contamination rate significantly. EBD soldering with negligible contamination should be possible by using an EBD gas source with a controllable flow rate. Such a system is under construction.

Compared with pick-and-place integration, methods such as dielectrophoretic integration and *in situ* growth are typically faster, simpler, and scaleable to large production quantities. However, control of the individual components is not easily accomplished with such processes, partly due to the randomness inherent to the assembly process.

We have shown how microfabricated tweezers are capable of picking up silicon nanowires and demonstrated that electron beam deposition is a versatile *in situ* method for making strong connections between nanostructures and microelectrodes. The proposed scheme is similar to automated pick-and-place of macroscopic electronic components onto printed circuit boards, only in this case the objects are 10000 times smaller. For large-scale production of nanotube/nanowire-based devices, self-assembly methods in principle offer a much higher throughput than the nanoscale pick-and-place. Provided that precise control of the positioning of the components can be obtained, such methods would be of great importance for nanocomponent production. We believe electron beam-assisted pick-and-place assembly could become a routine method available for a range of nanotechnology research and prototyping applications.

Acknowledgments: We thank J. Nygård and E. Bakkers for providing us with sample, and F. Grey for fruitful discussions. We are greatly indebted to L. Montelius for use of the SEM. We acknowledge financial support from STVF (Nanohand Talent Projekt).

References and Notes

1. M. R. Falvo, J. Steele, R. M. Taylor, and R. Superfine, *Phys. Rev. B* 62, R10665 **(2000)**.
2. M. R. Falvo, G. T. Clary, R. M. Taylor, V. Chi, F. P. Brooks, S. Washburn, and R. Superfine, *Nature* 389, 582 **(1997)**.
3. P. Avouris, T. Hertel, R. Martel, T. Schmidt, H. R. Shea, and R. E. Walkup, *Appl. Surf. Sci.* 141, 201 **(1999)**.
4. C. Thelander, M. H. Magnusson, K. Deppert, L. Samuelson, P. R. Poulsen, J. Nygard, and J. Borggreen, *Appl. Phys. Lett.* 79, 2106 **(2001)**.
5. J. Nygard and D. H., Cobden, *Appl. Phys. Lett.* 79, 4216 **(2001)**.
6. Y. G. Zhang, A. L. Chang, J. Cao, Q. Wang, W. Kim, Y. M. Li, N. Morris, E. Yenilmez, J. Kong, and H. J., Dai, *Appl. Phys. Lett.* 79, 3155 **(2001)**.
7. H. J. Dai, J. Kong, C. W. Zhou, N. Franklin, T. Tombler, A. Cassell, S. S. Fan, and M. Chapline, *J. Phys. Chem. B* 103, 11246 **(1999)**.
8. Y. Huang, X. F. Duan, Q. Q. Wei, and C. M. Lieber, *Science* 291, 630 **(2001)**.
9. M. F. Yu, M. J. Dyer, G. D. Skidmore, H. W. Rohrs, X. K. Lu, K. D. Ausman, J. R. Von Ehr, and R. S. Ruoff, *Nanotechnology* 10, 244 **(1999)**.
10. W. S. Yun, J. Kim, K. H. Park, J. S. Ha, Y. J. Ko, K. Park, S. K. Kim, Y. J. Doh, H. J. Lee, J. P. Salvetat, and L. Forro, *J. Vac. Sci. Technol. A* 18, 1329 **(2000)**.
11. P. Kim and C. M. Lieber, *Science* 286, 2148 **(1999)**.
12. P. Boggild, T. M. Hansen, C. Tanasa, and F. Grey, *Nanotechnology* 12, 331 **(2001)**.
13. S. Akita, Y. Nakayama, S. Mizooka, Y. Takano, T. Okawa, Y. Miyatake, S. Yamanaka, M. Tsuji, and T. Nosaka, *Appl. Phys. Lett.* 79, 1691 **(2001)**.
14. P. A. Williams, S. J. Papadakis, M. R. Falvo, A. M. Patel, M. Sinclair, A. Seeger, A. Helser, R. M. Taylor, S. Washburn, and R. Superfine *Appl. Phys. Lett.* 80, 2574 **(2002)**.
15. L. Dong, F. Arai, and T. Fukuda, in *IEEE-NANO 2001. Proceedings of the 1st IEEE Conference on Nanotechnology, 2001*, Maui, IEEE 93-98 **(2001)**.
16. H. W. P. Koops, J. Kretz, M. Rudolph, and M. Weber, *J. Vac. Sci. Technol. B* 11, 2386 **(1993)**.
17. D. N. Madsen, K. Mølhave, R. Mateiu, A. M. Rasmussen, M. Brorson, C. H. J. Jacobsen, and P. Boggild, *NanoLetters* 3, 47 **(2003)**.
18. C. L. Petersen, T. M. Hansen, P. Boggild, A. Boisen, O. Hansen, T. Hassenkam, and F. Grey, *Sens. Actuator Phys.* 96, 53 **(2002)**.

Received: 10 January 2003. Revised/Accepted: 28 May 2003.

Appendix G

Article
Pick-and-place nanomanipulation using microfabricated grippers

INSTITUTE OF PHYSICS PUBLISHING NANOTECHNOLOGY

Nanotechnology **17** (2006) 2434–2441 doi:10.1088/0957-4484/17/10/002

Pick-and-place nanomanipulation using microfabricated grippers

Kristian Mølhave[1,3], Thomas Wich[2], Axel Kortschack[2] and Peter Bøggild[1]

[1] MIC, Department of Micro and Nanotechnology, Technical University of Denmark, DK-2800 Kongens Lyngby, Denmark

[2] Abteilung für Mikrorobotik und Regelungstechnik, Universität Oldenburg, 26129 Oldenburg, Germany

E-mail: krm@mic.dtu.dk

Received 9 February 2006, in final form 5 March 2006
Published 24 April 2006
Online at stacks.iop.org/Nano/17/2434

Abstract

Microfabricated grippers could be useful for the manipulation of nanoscopic and microscopic samples. A survey is presented of the force requirements for a microgripper to complete pick-and-place nanomanipulation tasks. We then demonstrate *in situ* pick-and-place operations of nanowires inside a scanning electron microscope using microfabricated electrostatically actuated grippers, and compare the theoretically estimated force requirements with the results of experimental tests of picking up nanowires to evaluate how grippers and strategies for nanomanipulation can be optimized.

M This article features online multimedia enhancements

(Some figures in this article are in colour only in the electronic version)

1. Introduction

While micromanipulation with tools such as micropipettes or lasers is a mature technique for handling microscopic samples in liquids [1, 2], micro- and nanomanipulation in dry environments is still a challenging task due to the absence of liquids to reduce the often strong adhesion forces. In dry environments, scanning probe microscopy (SPM) equipment has been used to push, slide, and roll nanostructures in two dimensions across surfaces. In this way proof-of-principle devices such as field effect transistors have been constructed [3]. Furthermore, numerous nanomechanical investigations have been carried out using nanomanipulation, for instance on carbon nanotubes [4, 5]. Compared to SPM nanomanipulation, few examples have been published with three-dimensional nanomanipulation in dry environments, and this has to date mainly been done with one or more individual SPM tips mounted on a manipulation unit, often in combination with electron beam deposition for local gluing and bonding [6, 7]. Apart from standard SPM tips, more advanced tips such as nanotube brushes [8] or similarly functionalized microstructures could also be used for nanomanipulation.

Compared to manipulation using 'single ended' tools such as SPM tips, a microfabricated gripper could provide better control over the applied forces, as well as a more well-defined mechanical grip on the object since rotation will be limited by the gripper geometry. It is also possible to make direct electrical and mechanical measurements on the grabbed object if the gripper arms are made of conducting material or can provide a force feedback signal. Over the last few years, several research groups have been developing grippers for micromanipulation and they have also become commercially available from companies such as Nascatec and Zyvex. Many different gripper actuation principles and designs have already been explored, but often only to the point of proving the actuation capability of the device, rather than actual testing of the device on real samples. Of manipulation on the submicron scale there have been few demonstrations. For instance, gripper structures have been used to manipulate nanoparticle samples both under ambient conditions [9], *in situ* SEM [10], and in liquids: DNA [11, 12] and cells [13].

It appears that grippers could find a wide variety of applications provided there is further development and specialization of the gripper functionality for the various environmental conditions. With grippers, one could imagine

[3] Author to whom any correspondence should be addressed.

the development of a nanoscale workshop where individual nanocomponents could be picked up, characterized and tested, in a way not unlike how millimetre sized components are normally handled with tweezers in an electronic workshop. Common tasks would then be to transport an individual nanostructure from the original substrate onto a transmission electron microscope (TEM) grid for initial examination, and then to mount it in a prototype electronic or mechanical nanoscale device, or to mount it in ways that cannot easily be achieved by direct growth or deposition.

One typical nanomanipulation task where a gripper is a relevant tool is handling of TEM samples which, due to the limitations of transmission electron microscopy, generally have a thickness smaller than 200 nm, such as TEM lamellae or nanotubes/wires. TEM lamellae are slices cut out of a larger sample by focused ion beam milling and they are usually some micrometres wide and long. Depending on the material and fabrication process, nanowires and nanotubes may have lengths of a few hundred nanometres to several hundreds of micrometres. A nanomanipulation system, including the environmental chamber, actuators, and grippers, should at least be capable of handling these types of component. The focus in this work is on *in situ* SEM manipulation, which compared to optical microscopy [9] allows nanostructures to be monitored and handled with nanometre-scale image precision, but not to observe their internal structure with atomic resolution as is possible with *in situ* TEM equipment [14].

The development of tools capable of such three-dimensional *in situ* SEM and TEM nanomanipulation could hopefully pave the way for new experimental methods in nanoscience, in the same way the development of the STM and AFM techniques initiated completely new types of physical investigations by allowing the experimenter to not only observe but also interact mechanically with planar surfaces and nanostructures supported on them. Rational optimization of gripper tools requires investigations of the underlying physics of gripping. However, apart from the rather few examples of pick-up operations with grippers such as those mentioned previously, there has been little systematic investigation of the basic requirements for the grippers to successfully complete pick-and-place operations, such as the forces actually required for nanomanipulation with grippers (figure 1). With the aim of making a quantitative foundation for pick-and-place nanomanipulation experiments, this paper presents an analysis of the fundamental strategies for pick-and-place operations on a nanoscale object and the corresponding force requirements for the gripper (figure 2). We present illustrative examples of *in situ* SEM pick-and-place operations of nanowires to demonstrate the possibilities and limitations for the technique. A video sequence of real time nanomanipulation is available at stacks.iop.org/Nano/17/2434. Both experiments and calculations are based on scenarios of manipulation of relatively stiff, elongated structures such as nanowires/tubes or TEM lamellae. Finally we discuss the implications the results have for gripper design and the pick-and-place procedures.

It is important to remember the ubiquitous pick-and-place processes met everyday on the macroscale, where a wealth of specialized gripper designs have been developed, each for their own application. For these initial calculations and experiments

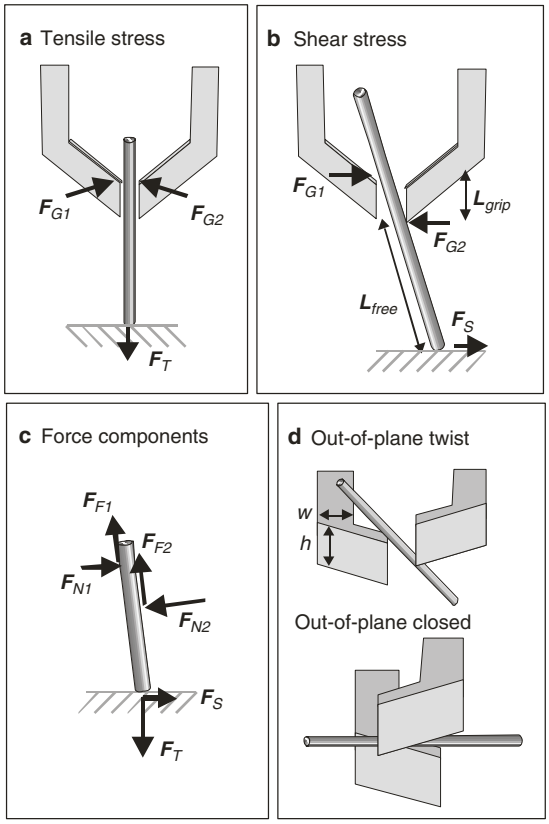

Figure 1. Gripper forces on a nanowire. By pulling (a), a gripper can apply a tensile force F_T, perpendicular to the substrate; and by moving sideways (b), a shear force F_S parallel to the substrate. (c) The gripper force $F_{G1,2}$ can be decomposed into a component $F_{N1,2}$ normal to the nanowire surface, which can cause a friction force $F_{F1,2}$, and the sum of these forces and moments must be balanced by the tensile and shear forces from the substrate surface F_T and F_S. (d) Applying excessive shear or gripping forces can result in the grippers twisting out of the plane if the gripper spring constant in the out-of-plane direction is not large compared to the in-plane direction (if $w > h$).

with nanoscale gripping, only simple representative cases are investigated. As suitable grippers with integrated force feedback become available for nanomanipulation [15], and enable quantitative comparison of experiment and theory, we expect that further analysis and tests such as presented here will facilitate the development of a wider range of effective three-dimensional nanomanipulation tools.

2. Pick-and-place manipulation of nanowires

Substrates with nanowires/tubes accessible for pick-and-place manipulation can be prepared in various ways, such as growth directly on the substrate by CVD/PECVD [16], MOVPE [17] or similar methods, or deposited from liquid dispersions, to provide substrate structures as illustrated in figures 2(a)–(c). Generally, we distinguish between three samples that pose different possibilities and limitations for the nanomanipulation of nanowires: vertical (free standing), supported (fixed on planar substrate), and suspended (with an unsupported section). Depending on the specific sample, figures 2(d)–(h) show the fundamental pick operations a gripper can perform

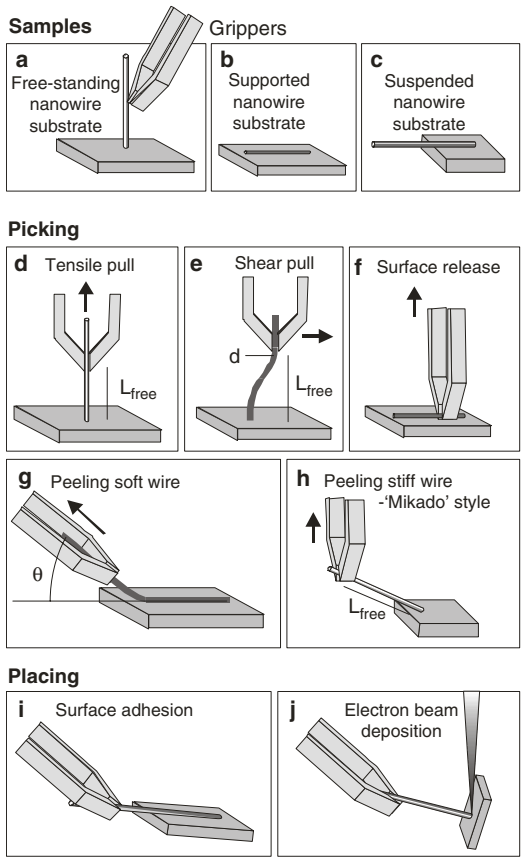

Figure 2. Samples and strategies for picking and placing a nanowire. Samples with nanowires (a) vertical, fixed nanowires standing up from the substrate, (b) suspended on planar surface, or (c) suspended/extended over an edge. Picking nanowires can be done by pulling along (d) or sideways (e) to the axis of a standing wire. Wires lying flat on substrates can be lifted perpendicularly (f) or peeled (g) off the substrate. Wires extending over an edge make it possible to use several strategies ((f)–(h)). Placing a nanowire on a surface (i) requires stronger adhesion of the wire to the surface than the grippers. Placing a wire in a mechanically unstable position (j) requires electron beam deposition or some other method to fix the wire to remain in the position when opening the gripper.

on such samples. Below, we will estimate the required forces and demands for successful completion of each pick operation and subsequent placing of the wire.

2.1. Force requirements for picking up nanowires

For any pick-and-place operation, it is essential to control the balance of the forces between the object and the substrate, F_T and F_S in figure 1, and the gripping forces acting between the object and the gripper $F_{G1,2}$ [10]. The gripping forces can be decomposed in a normal force component perpendicular to the nanowire surface and a component parallel to the surface with a contribution from the static friction force preventing the wire from sliding at the end-effector surfaces (figures 1(a) and (c)). With the assumption that friction can be regarded as roughly macroscopic, the static friction force F_F is proportional to the normal component F_N of the gripping force F_G, $F_F = \mu F_N$, implying that it is essential to control the gripping force during pick-and-place operations as in macroscale gripping. Assuming surfaces that are smooth on the scale of the nanowire dimensions, i.e. 50 nm, we will in the following calculations use an estimated friction static coefficient $\mu = 0.1$ [18, 19]. One should remember that effects such as surface roughness, contamination, and charging of the nanowire and gripper surfaces must be expected to contribute with considerable adhesive and pull-off forces of the nanowire to nearby surfaces unless care is taken to reduce such effects [19] and possibly influence the value of μ. The following calculations provide order-of-magnitude estimates for the involved forces giving an overview of the demands set by the various pick operations based on a silicon nanowire with a radius $r_{nw} = 50$ nm, comparable to those considered in [9, 10], and a gripper with two flat 1 μm × 1 μm gripper end-effector surfaces contacting the wire.

Tensile gripping (figure 2(d)). The force required to release a nanowire from the substrate by pulling in the direction parallel to the axis without sliding (figures 1(a) and (b)) is determined by the lowest yield strength of the nanowire or substrate material as $F_T = \sigma_{yield}\pi r_{nw}^2$. The lowest yield stress, σ_{yield}, of either the substrate or the nanowire should be used. For a silicon nanowire, $\sigma_{yield,Si} = 7$ GPa [20], giving $F_S = 55$ μN. The force will have to be applied through the static friction force, requiring a gripping force of the order $F_G = 0.5$ mN, a high value for most available microgripper designs [15].

Shear gripping (figure 2(e)). By bending a wire it is possible to break it at the base where the stress will be largest and eventually can reach the yield stress. The minimum radius of curvature, r_{curv}, a nanowire can withstand can be calculated as $r_{curv} = r_{nw}Y/\sigma_{yield}$ [20], which is about 1 μm for a 50 nm nanowire. If it is long enough, the nanowire can almost be curled around the micrometre sized grippers considered here without breaking. Considering the nanowire as a clamped–clamped cantilever structure (gripped in one end, fixed in the other) with no tension, the flexure formula gives the maximal bending moment $M_{max} = \sigma_{yield}I/R$ as a function of the yield stress, the maximal distance from the beam neutral axis $R = r_{nw}$, and the moment of inertia $I = \pi r_{nw}^4/4$. To break off the nanowire through shear stress, the gripper must be able to apply the required moment $M_{max} = \pi r_{nw}^3\sigma_{yield}/4$, which in this case is $\sim 10^{-12}$ N m. Applying such a moment requires the two grippers to press the wire with a gripping force $F_G = M_{max}/L_{grip} = 1$ μN, where L_{grip} is the 1 μm length of the gripper contact surface with the nanowire (figure 1(b)). In addition to applying a moment, the gripper must also apply a force F_S to create the sideways deflection, that can be calculated from the distance d the wire tip has been moved sideways by the gripper, and the spring constant of a double-clamped circular beam as $F_S = 3\pi r_{nw}dY/L_{free}^3 = 0.1$ μN, where we have used $L_{free} = 5$ μm for a typical estimate and $d_{max} = L_{free}^2\sigma_{max}/(12Yr_{nw}) = 2$ μm for a silicon nanowire with $Y = 160$ GPa [20]. Hence the gripper must in addition to the moment be capable of applying a deflection force which is increasing the requirements on the gripping force capabilities if the gripper is to remain closed during the operation.

By shear gripping we have reduced the required force to detach a nanowire roughly two orders of magnitude compared to tensile gripping. However, the gripper must be mechanically

rigid to prevent in-plane and out-of-plane deflection when applying M_{max} and F_S, as shown in figures 1(b) and (c).

Scrape lift (figure 2(f)). When attempting to lift a nanowire lying flat on a surface, while pulling in the direction *perpendicular* to the surface, it is necessary to overcome the strong adhesive surface forces. The maximal force is required when the entire wire must be lifted up simultaneously at the very beginning of the picking operation. A wide variety of surface forces can be expected to influence the process, making the required force difficult to estimate [21]. For a dry substrate with electrical contact between the wire and substrate, the major attractive force must be the van der Waals force (vdW) which per unit length of a cylindrical rod can be written as $f_{vdW} = -A_H(r_{nw}/8\sqrt{2}D^{5/2})^{1/2}$ [22] with Hamaker constant, A_H, usually in the range 10^{-19}–10^{-20} J [22]. For the distance between the object and the surface, D, we can use the typical Lennard-Jones distance of roughly 0.2 nm [23], giving 2 μN per μm length of nanowire. Based on these assumptions, the vdW force for a rigid 5 μm nanowire will be of order 10 μN, requiring a 100 μN gripping force to achieve a high enough friction force. However, when capable of applying the required force, the gripper will have to be equipped with extremely sharp end-effectors or well-defined edges in order to grab the thin wire in such close contact with the surface without touching the surface. From these considerations as well as from experimental experience, nanowires lying on flat surfaces hence seem to be very difficult to pick up with grippers. The vdW force is reduced if the substrate is corrugated. It is likely that structured substrates, such as nanotube forests [16], could effectively lower the adhesion force as well as give the gripper space to operate.

Peeling (figure 2(g)). Peeling a flexible nanowire lying on a surface can reduce the required steady state gripping force considerable compared to the scrape lift. If the wire is assumed to be unable to slide or stretch, but able to bend, the tensile force required to peel at an angle θ to horizontal is given by $F_{peel} = \Delta U/\Delta x(1 - \cos\theta)$, with the adhesion energy per unit length of wire $\Delta U/\Delta x = -A_H(r_{nw}/12\sqrt{2}D^{3/2})$ [22]. Using the same constants as above, we estimate $\Delta U/\Delta x = 0.2$ nN. The peeling force is reduced to half $\Delta U/\Delta x$ when the wire is peeled to make a U-bend at $\theta = 180°$. The gripping force can be as low as a few nN if we assume the nanowire is flexible like a chain with negligible spring constant for bending. For elastically bending nanowires, an additional orthogonal force will be required to bend the nanowire.

'Mikado' peeling (figure 2(d)). If the wire is rigid and extending over the edge of the substrate, lifting in the direction normal to the surface can considerably reduce the required force to release the wire. We call this operation 'Mikado' peeling (after the game Pick-up Sticks). The required force becomes $F_{mikado} = L^2_{surface} f_{vdW}/2L_{free}$. As an example, if $L_{free} = 5 \times L_{surface} = 5$ μm and using the above vdW force, $F_{rigid} = 0.2$ μN and the gripping force is only 2 μN.

The above estimates of the required forces show a strong dependence on the nanowire and gripper dimensions. In the calculated examples, shear gripping, peeling and Mikado peeling offer by far the lowest requirements for gripping force. Mikado peeling also makes the nanowire easily accessible on the edge of a substrate, unlike attempting to peel wires lying on a flat surface. Depending on the design of the gripper and nanowire properties, one should carefully consider what pick operation will provide the best chances for successful manipulation: shear gripping, for instance, increases with the nanowire diameter as r^3_{nw}, while Mikado peeling is relatively independent of the diameter.

2.2. The place procedure

Moving and placing a grabbed object also imposes certain requirements.

Moving. When gripped, the electrostatic forces due to charging in the SEM can result in movement or even loss of the wire or increased electrostatic attraction between the gripper and nanowire, all of which is normally undesired. The gripper end-effectors, the sample, and the target substrate should all be electrically grounded and the wire should be in electrical contact with the grounded grippers to avoid excessive charging. The manipulator should transport the nanowire from the sample to the target substrate with low vibrational noise, since vibrations may excite resonances in the grippers and thus result in loss of the grabbed object. Deliberate excitation of mechanical resonances in the grippers have even been used to release adhering objects [11].

Releasing. Depending on which configuration the wire is to be placed in on the target substrate, different methods could be employed to release it in the correct position. If the wire is to be placed on a surface as shown in figure 2(i), a successful release requires the surface energy of the wire–substrate interface to be high compared to the wire–gripper interface. This can in many cases be achieved if the part of the wire in contact with the substrate is much longer than the part in contact with the gripper end-effectors and possibly aided by exciting mechanical resonances [11]. If the wire is being placed on conducting electrodes, applying a bias voltage to attract it electrostatically might assist in placing the wire successfully [24].

To place a wire in a mechanically unstable position, such as standing up perpendicular to the substrate (figure 2(j)), fixing the wire to the substrate in the correct position before releasing it is commonly needed [25]. Electron beam deposition is one possibility, though it has some limitations [26], while curable glue added to the surface is another option [9], or soldering by heating with a focused laser [24]. Preparing the substrate with narrow holes or edges to enhance the surface adhesion could also improve the stability.

3. The nanomanipulation system

To demonstrate *in situ* SEM pick-and-place operations, we have constructed a robot-based nanomanipulation setup.

3.1. Experimental setup

To avoid excessive demands on the mounting alignment for SEM-mounted systems, the required manipulation range must be several millimetres.

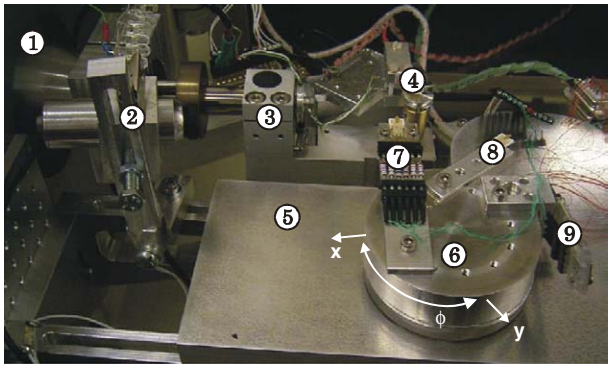

Figure 3. Example of a nanomanipulation setup mounted on an SEM chamber door. (1) The chamber door. (2) Camera with IR diode light source to follow the robot motion. (3) SEM sample stage with sample (4). (5) Table for '*R*2–*D*2' (rotational/translational) robot (6) with mounted gripper (7) and other tools ((8), (9)).

For *in situ* SEM nanomanipulation, at least two actuation units are required to position the tool and the sample in the region with high SEM resolution. One unit can be a coarse position manipulation stage to bring either the tool or the sample into the imaging region, if the other unit then has sufficient precision to complete the actual manipulation procedure. Recently, commercial manipulation systems have become available from companies such as Kleindiek and Zyvex. Several research groups have also pursued the development of such systems [24, 27, 25].

In one of our setups, shown in figure 3, we use the manual SEM stage as one actuator and for the other actuator a recently developed actuator colloquially called *R*2–*D*2, which is able to move in both x–y directions and rotate [28]. Unlike many commercial xyz actuators, the *R*2–*D*2 design makes it possible to mount many different tools extending over the edge of the unit and then to select the appropriate tool by rotating it to towards the target. The Zeiss DSM 950 SEM sample stage was controlled manually. Another similar setup used for some of the presented experiments has been described previously [10].

The grippers were microfabricated by a process described elsewhere [29]. The gripper arms are made of silicon dioxide and coated with a layer of 10 nm titanium and 100 nm gold to make them electrically conducting. The gripper arms are 1–2 μm wide, 1 μm thick, and 20–100 μm long. Unlike the carbon nanotube tweezers [9] and microfabricated grippers described in [10], the microgrippers used in the present work are operated by indirect electrostatic actuation, in which the actuation voltage is applied to a nearby actuator electrode, while the gripper arms can be held at ground potential. In this way, actuation is independent of the voltage applied to the gripper end-effectors, which in principle allows electrical measurements to be done on the sample independently of the actuation. The maximal gripping force is estimated to be of the order 1 μN [30]. Compared to the above analysis these grippers should be able to pick up nanowires extending over the edge of a grounded substrate by peeling or Mikado peeling, while shear gripping could be problematic because of the low aspect ratio giving low spring constants for out-of-plane bending.

4. Picking results

The various pick operations described in section 2.1 were attempted on silicon nanowires with roughly 100 nm diameter made by etching a Si substrate [31]. When attempting tensile gripping, the gripper would slide along the nanowire, and for shear gripping it was twisted open. Scrape lift and peeling were generally not possible since the wires lying on top of surfaces were too narrow to get a firm grip on with the rounded edges of the gripper, and having the gripper in contact with the substrate obstructed its operation.

The image sequence in figures 4(a)–(f) shows a gripper using Mikado peeling to pick up a silicon nanowire extending from the gold surface of the chip. The substrate was prepared by pushing the edge of a gold-coated silicon chip into a sample with vertically standing silicon nanowires which would then break off and adhere to the chip edge. The nanowires lying on the surface of the chip exposed to the electron beam could not be picked up with the gripper by scrape lift, as the wire adhered very strongly to the substrate. This could be due to electron beam deposited contamination on the top surface which fixed the nanowires to the surface during imaging [26]. Mounting the gold-coated surface facing downwards as shown in figure 4(a), so it was not directly exposed to the electron beam, efficiently reduced the adhesion of the wires to the substrate, making Mikado peeling possible.

To investigate whether the applied gripping force or the adhesion between the wire and the grippers is dominating the picking process, the grippers were first moved while just touching the wire (figures 4(b) and (c)), confirming that the wire–substrate adhesion was low enough to allow the nanowire to be moved around. Then the gripper was closed around the wire (figure 4(d)) by applying 20 V to the central actuation electrode while the gripper arms were kept grounded and subsequently opened again (figure 4(e)) and moved to see whether the adhesion would be enough to remove the wire. Although the nanowire did adhere to the grippers, the adhesive forces were not sufficiently strong to remove the wire. It was only when the gripper was firmly closed and pulled away that the nanowire could be picked up (figure 4(f)), demonstrating that control of the friction force by the gripping force is essential.

As demonstrated by the online video sequence, the pick-and-place procedure is a relatively fast operation comparable to, for instance, SPM imaging and manipulation because of the fast frame rate offered by the SEM. These observations for the pick operations were reproduced on several occasions in our two experimental setups, and qualitatively confirm the prediction of the low gripping force required to accomplish the Mikado peeling procedure and the problems anticipated with the other picking operations for grippers with relatively low maximal available gripping force.

5. Placement results

The observation that the nanowires supported by the upper silicon surface of the substrate in figure 4 adhered strongly made it obvious to try placing a grabbed nanowire on this surface (figure 5). A nanowire was picked up, and in the process, the gripper twisted and closed around the nanowire

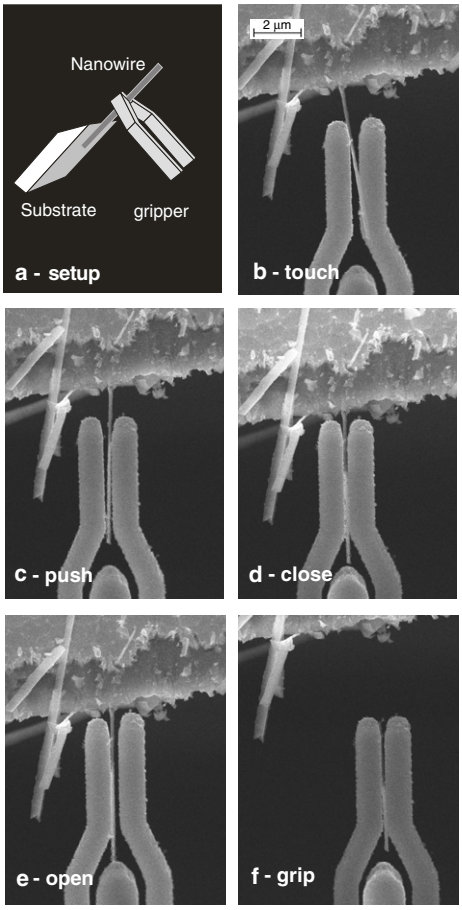

Figure 4. Picking up a silicon nanowire extending over the edge of a substrate. (a) Illustration of a part of the configuration as seen from the side—the SEM images view the gripper surface from the top. The nanowires located on the upper silicon surface of the substrate were usually adhering too strongly to be moved. Wires extending from the edge of the gold surface were generally much easier to move and some of these were possible to pick up. (b) The gripper was moved into contact with the wire. (c) Moving the wire and sliding the gripper along it could not release the wire. (d) The gripper was closed around the wire and reopened (e) without removing the wire. (f) The wire could only be peeled from the substrate when the gripper was kept closed and pulled away.

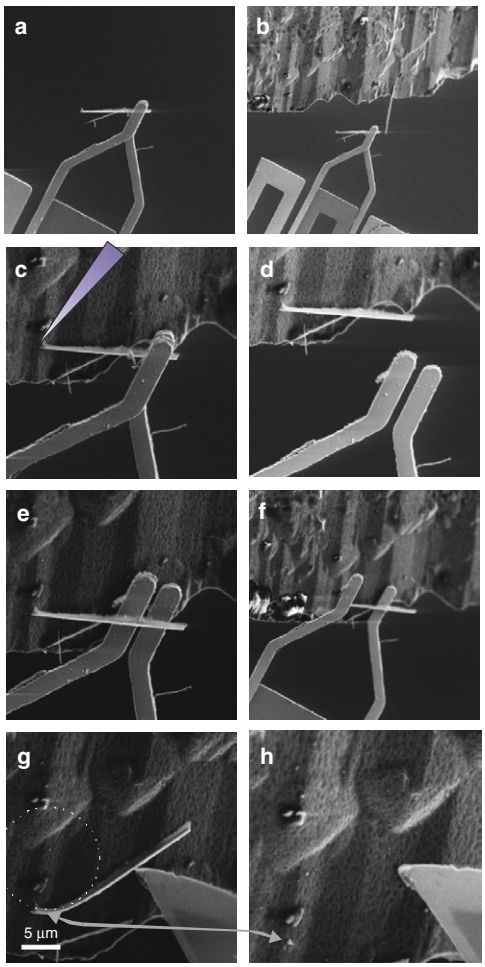

Figure 5. SEM image sequence of placing a nanowire on an adhesive surface ((a)–(d)) and subsequent test of the yield strength of the nanowire attachment to the substrate ((e)–(h)). (a) The nanowire was picked up and moved to a new substrate (b) to be placed on the upper surface with strong adhesion. The substrate was inclined with the height in the left-hand side of the image higher than that of the gripper. Once contact was achieved, the contact point was irradiated (c) to solder it by electron beam deposition as indicated by the triangle. Though practically no change was visible at the soldering point, the nanowire appear well fixed to the substrate upon release (d) and seemed impossible to remove again with the grippers ((e), (f)). A larger AFM cantilever was able to remove the wire, which only yielded after considerable bending, where r_{curv} is indicated by the circle (g), and left a small residue on the substrate (h).

(figure 1(d)) but still appeared to have a firm grip on the wire (figure 5(a)). The free end of the nanowire was moved to contact the inclined substrate surface (figure 5(c)). The wire–substrate contact point was exposed to the electron beam for 60 s to solder it by electron beam deposition. The deposition rate is, however, very low in this setup, and there was no obviously visible deposit. The nanowire release from the gripper was immediately successful upon opening it, and the nanowire remained at the position it was placed (figure 5(d)). The grippers could be moved in under the wire (figure 5(e)), indicating that it was standing out from the surface and not supported along the entire length.

To investigate the strength of the nanowire's mechanical connection to the substrate, it was attempted to break the nanowire free from the substrate again. The wire did not seem to move at all, even when lifting the gripper up with one end-effector stuck under the wire as in figure 5(f). It seemed that the wire was so well attached to the substrate that attempts to break it off would probably do more damage to the gripper than the wire. The $R2$–$D2$ robot was rotated to use a more robust AFM cantilever capable of applying larger forces. In figure 5(g), taken just before the nanowire broke, the radius of curvature at the fixed end of the nanowire is about $r_{\mathrm{curv}} = 6$–$7\ \mu$m. With a nanowire radius of about $r_{\mathrm{nw}} = 0.27\ \mu$m and the Young's modulus $Y = 160$ GPa of single crystalline silicon this gives an approximate yield stress [20] $\sigma_{\mathrm{yield}} = Y r_{\mathrm{nw}}/r_{\mathrm{curv}}$ of about 7 GPa, which is indeed the yield stress of bulk silicon.

In figure 5(g), the nanowire itself is bending, rather than rotating as a rigid rod around the point where it is fixed to the substrate. This indicates that the point contact to the substrate is as strong as the wire material itself. The small soldering

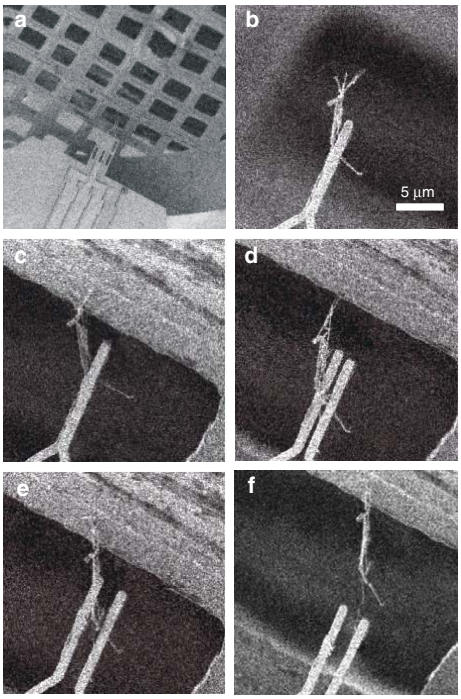

Figure 6. Placing a nanowire on a non-sticking surface. Frames ((a)–(f)) are from an SEM video sequence of a nanowire bundle being placed on a TEM grid.

joint of the nanowire to the substrate (figure 3(h)) in this case resulted in a mechanically very strong solder joint with a yield stress comparable to that of the nanowire. The radii used in the calculations are visual estimates and emphasize the need for better force and size metrology to make quantitative measurements of the forces involved in nanomanipulation.

In the SEM image sequence shown in figure 6, a grabbed bundle of silicon nanowires is placed onto a copper TEM grid. The nanowires were slowly moved into contact with the TEM grid (figures 6(a)–(c)). As in the previous experiment, when one of the wires touched the grid, the contact point was irradiated for 60 s, to increase the adhesion to the grid. The actuation voltage was then turned off, and the grippers were withdrawn (figure 6(d)). This was not sufficient to completely release the wires from the gripper. In figure 6(e) the grippers were opened further up by applying a bias voltage to a pair of outer driver electrodes, and this apparently altered the force balance enough to release the wires (figure 6(f)). It is worth noting that in this case electron beam deposition was initially not strong enough to make the wires stick to the grid, and it was not used when the wires got stuck. The adhesion of the wires to the grid was strong enough for the grid to be handled by a pair of tweezers by hand when removed from the SEM and observed under an optical microscope at later times.

6. Conclusion

Estimates of the force requirements for pick-and-place operations with microgrippers have been calculated. Several *in situ* SEM pick-and-place operations of silicon nanowires were compared to the estimates. Successful picking of the nanowires required the sample to be prepared with wires extending from the edge of a substrate where they could be peeled off by Mikado peeling, figure 4, which offers both low requirements on the gripping force and makes the wires easily accessible. Placing of nanowires onto silicon substrates and TEM grids was demonstrated. To help make mechanically strong contacts to the target substrate when placing a grabbed object, electron beam deposition can be a useful tool for local fixation.

With a suitable model for the possible pick-and-place processes, more effective grippers and substrates can be developed for the various tasks. Our current efforts concentrate on increasing the applicable gripping force and gripper aspect ratio by making the gripper arms taller to avoid out-of-plane bending, and increase the gripping force. Grippers with force feedback [15] should also make pick-and-place manipulation a measurable and optimizable process rather than the presented trial and error investigation to test whether the force balance in pick-and-place operations can be controlled at all. The successful demonstrations of pick-and-place operations of nanostructures indicate that properly optimized SEM-based nanomanipulation systems could be useful for the characterization of nanocomponents and in the fabrication of prototype devices. Some techniques for integration of nanocomponents in microsystems offer better throughput [32], however the flexibility and short turn-around time of manual nanoassembly makes gripper manipulation attractive for fast prototyping of individual devices.

Acknowledgments

We thank Erik Bakkers for providing the nanowire sample and Maria Dimaki, MIC, and Danchip for processing the microgrippers. We are grateful to the Nanohand STVF talent project and ASSEMIC EU-project for funding. We thank Ole Hansen for valuable discussions and for reviewing the manuscript.

References

[1] Kenneth T and Brown D G F 1987 *Advanced Micropipette Techniques for Cell Physiology* (New York: Wiley)
[2] Grier D G 2003 A revolution in optical manipulation *Nature* **424** 810–6
[3] Avouris P *et al* 1999 Carbon nanotubes: nanomechanics, manipulation, and electronic devices *Appl. Surf. Sci.* **141** 201–9
[4] Falvo M R *et al* 1998 Nanomanipulation experiments exploring frictional and mechanical properties of carbon nanotubes *Microsc. Microanal.* **4** 504–12
[5] Thelander C *et al* 2001 Gold nanoparticle single-electron transistor with carbon nanotube leads *Appl. Phys. Lett.* **79** 2106–8
[6] Yu M F *et al* 2000 Strength and breaking mechanism of multiwalled carbon nanotubes under tensile load *Science* **287** 637–40
[7] Nakayama Y and Akita S 2003 Nanoengineering of carbon nanotubes for nanotools *New J. Phys.* **5** 128
[8] Cao A Y *et al* 2005 Multifunctional brushes made from carbon nanotubes *Nat. Mater.* **4** 540–5
[9] Kim P and Lieber C M 1999 Nanotube nanotweezers *Science* **286** 2148–50
[10] Molhave K *et al* 2004 Towards pick-and-place assembly of nanostructures *J. Nanosci. Nanotechnol.* **4** 279–82

[11] Watanabe H *et al* 2001 Single molecule DNA device measured with triple-probe atomic force microscope *Appl. Phys. Lett.* **79** 2462–4
[12] Hashiguchi G *et al* 2003 DNA manipulation and retrieval from an aqueous solution with micromachined nanotweezers *Anal. Chem.* **75** 4347–50
[13] Chronis N and Lee L P 2005 Electrothermally activated SU-8 microgripper for single cell manipulation in solution *J. Microelectromech. Syst.* **14** 857–63
[14] Svensson K *et al* 2004 Nanopipettes for metal transport *Phys. Rev. Lett.* **93** (14)
[15] Molhave K and Hansen O 2005 Electro-thermally actuated microgrippers with integrated force-feedback *J. Micromech. Microeng.* **15** 1265–70
[16] Teo K B K *et al* 2001 Uniform patterned growth of carbon nanotubes without surface carbon *Appl. Phys. Lett.* **79** 1534–6
[17] Samuelson L *et al* 2004 Semiconductor nanowires for novel one-dimensional devices *Physica* E **21** 560–7
[18] Bhushan B 2003 Review articles-adhesion and stiction: mechanisms, measurement techniques, and methods for reduction *J. Vac. Sci. Technol.* B **21** 2262–96
[19] Ando Y 2004 Friction and pull-off forces on submicron-size asperities measured in high-vacuum and in both dry and humid nitrogen at atmospheric pressure *Japan. J. Appl. Phys.* 1 **43** 4506–10
[20] Senturia S D 2001 *Microsystem Design* (Massachusetts: Kluwer–Academic)
[21] Burnham N A *et al* 1993 Interpretation of force curves in force microscopy *Nanotechnology* **4** 64
[22] Bhushan B E 2004 *Springer Handbook of Nanotechnology* (Berlin: Springer)
[23] Yu M-F *et al* 2001 Structural analysis of collapsed, and twisted and collapsed, multiwalled carbon nanotubes by atomic force microscopy *Phys. Rev. Lett.* **86** 87–90
[24] Tsuchiya K *et al* 1999 Micro assembly and micro bonding in nano manufacturing world *Proc. SPIE-Int. Soc. Opt. Eng.* **3834** 132–40
[25] Williams P A *et al* 2002 Controlled placement of an individual carbon nanotube onto a microelectromechanical structure *Appl. Phys. Lett.* **80** 2574–6
[26] Molhave K *et al* 2004 Constructing, connecting and soldering nanostructures by environmental electron beam deposition *Nanotechnology* **15** 1047–53
[27] Yu M *et al* 1999 Three-dimensional manipulation of carbon nanotubes under a scanning electron microscope *Nanotechnology* **10** 244–52
[28] Kortschack A *et al* 2003 Driving principles of mobile microrobots for micro-and nanohandling *IROS 2003: Intelligent Robots and Systems, 2003. Proc. 2003 IEEE/RSJ Int. Conf.* vol 2, pp 1895–900
[29] Boggild P *et al* 2001 Customizable nanotweezers for manipulation of free-standing nanostructures *IEEE-NANO 2001* (Piscataway, NJ: IEEE)
[30] Mølhave K 2004 Tools for *in situ* manipulation and characterization of nanostructures *PhD Thesis* Department of Micro and Nanotechnology, Technical University of Denmark, Copenhagen
[31] van den Meerakker J E A M *et al* 2000 etching of deep macropores in 6 in. Si wafers *J. Electrochem. Soc.* **147** 2757–61
[32] Huang Y *et al* 2001 Directed assembly of one-dimensional nanostructures into functional networks *Science* **291** 630–3

Appendix H

Article
Transmission Electron Microscopy Study of Individual Carbon Nanotube Breakdown Caused by Joule Heating in Air

NANO
LETTERS

xxxx
Vol. 0, No. 0
A−F

Transmission Electron Microscopy Study of Individual Carbon Nanotube Breakdown Caused by Joule Heating in Air

Kristian Mølhave,*,† Sven Bjarke Gudnason,† Anders Tegtmeier Pedersen,† Casper Hyttel Clausen,† Andy Horsewell,‡ and Peter Bøggild†

NanoDTU, Department of Micro and Nanotechnology (MIC) and Department of Manufacturing Engineering and Management (IPL), Technical University of Denmark, DK-2800 Kgs. Lyngby, Denmark

Received April 11, 2006; Revised Manuscript Received June 15, 2006

ABSTRACT

We present repeated structural and electrical measurements on individual multiwalled carbon nanotubes, alternating between electrical measurements under ambient conditions and transmission electron microscopy (TEM). The multiwalled carbon nanotubes made by chemical vapor deposition were manipulated onto cantilever electrodes extending from a specially designed microfabricated chip. Repeated TEM investigations were then made of the progressive destruction of the nanotube structure induced by Joule heating in air. The electrical measurements indicate that the studied nanotubes behave as diffusive conductors with remarkably predictable electrical properties despite extensive structural damage.

1. Introduction. Carbon nanotubes have long been regarded as suitable candidates for active and passive components in future electronic devices. Both single-walled (SWNT) and multiwalled (MWNT) carbon nanotubes have been investigated for many such applications. The MWNTs used for the majority of electrical measurements reported in the literature have been fabricated by arc discharge (A-MWNT),[1−3] and such nanotubes are known to have a much lower defect density than carbon nanotubes fabricated with chemical vapor deposition (CVD), C-MWNT, which are typically regarded as diffusive conductors.[4,5] Defects can be of a variety of types, such as pentagon−heptagon pairs (Stone-Walls defect), vacancies and domains of graphite, corrugations, bamboo-like walls, and residues of catalysis particles.[6] However, from a practical perspective, the C-MWNTs are interesting, since they can easily be integrated in microsystems by methods such as CVD or plasma-enhanced CVD (PECVD) from prepositioned catalytic particles,[7−9] while A-MWNTs needs to be integrated into microsystems from liquid dispersions of the nanotube powder or by similar methods with little control over the placement of the individual nanotube. Despite the high defect density, C-MWNTs are also promising for electrical devices and have been shown to sustain high current densities above 10^7 A/cm^2.[10] In addition, high-density (10^{11} cm^2) transistor arrays have been made with highly defective C-MWNTs.[11]

Recently, transmission electron microscopy (TEM) compatible chips have received increased attention, as TEM allows detailed study of the structure of nanodevices. To create nanodevices accessible to the TEM electron beam, various methods have been used, such as lithographically defined contacts to nanotubes dispersed on a TEM transparent silicon nitride thin film,[12,13] or direct CVD growth of nanotubes or peapods in slits etched into chips.[14,15] The underlying substrate of planar devices has also been etched out to leave the planar nanostructure freely suspended for TEM inspection.[16] Earlier work has used a focused ion beam to mill slits for creation of individual devices for TEM investigation.[17]

In this paper, repeated TEM measurements are used to investigate how C-MWNTs change under repeated Joule heating in air to study the durability of these nanoscale structures under conditions likely to be encountered in high power devices in an ambient environment, such as interconnects in computer chips.[9]

To perform such an investigation on individual nanotubes, we have developed microfabricated cantilever chips adapted to be mounted in a TEM specimen holder. Combined electrical and TEM characterization is done by manipulating

* Corresponding author. E-mail: krm@mic.dtu.dk.
† Department of Micro and Nanotechnology.
‡ Department of Manufacturing Engineering and Management.

10.1021/nl060821n CCC: $33.50
Published on Web 07/06/2006

a nanotube to bridge two cantilever electrodes for electrical contact with the suspended part of the nanotube accessible for the TEM electron beam. In this way, we ensure that the electrical measurements are done on one specifically selected tube. Hence, suspended nanotube devices can be made without the need for chemical processing of the nanotube to create dispersions or underetching of the substrate.[16] The method also avoids using thin films for suspending the structure thus leaving the nanostructure entirely freely suspended and in pristine condition.

2. Theory. To provide a basis for understanding the Joule heating experiments, we will briefly review the conductive properties of carbon nanotubes as a function of temperature and bias voltage, as well as the oxidation effects and structural changes taking place as the nanotube is Joule heated in air.

Dai and co-workers[4] found the transport mechanism of C-MWNT to be diffusive rather than ballistic, with a resistivity of the order 10−100 $\mu\Omega$m. Although there is some variation in the current−voltage (*IV*) curves reported and in the explanations for the behavior in the literature, the *IV* measurements on C-MWNT generally show nonlinearly increasing conductance as function of low bias voltages.[10,18,19] In air, a lasting decrease of conductance will be observed if the bias voltage is increased beyond the point where a saturation effect eventually limits the current at high bias voltages in the range 1−10 V.[10,18] Oxidation of the outer shells due to Joule heating of the nanotube at the high bias voltage is mentioned as a possible explanation for the current limit. The Joule heating temperature rise at the center of the nanotube bridge, ΔT, can be estimated by solving the heat continuity equation $AT'' = -R'I^2$ for a cylindrical rod clamped at both ends with a fixed temperature,[20] giving $\Delta T = (L/(8\ A))P$, where L is the bridge length, A the cross-sectional area, the thermal conductivity and $P = UI$ the dissipated power in the bridge with bias voltage U and current I. The thermal conductivity of MWNTs has been measured to be in the wide range 25−3000 W/mK[20] and for C-MWNTs the conductivity has been found in the range 25−200 W/mK.[21,22] For a 1 μm long 100 nm diameter nanotube with a dissipated power of 1 mW, the temperature increase could be in the range 50−500 K given the wide range reported for the thermal conductivity of C-MWNTs.

The change in resistance with respect to temperature has been investigated by several groups with quite different results. To first order, the linear temperature coefficient α of resistance gives $R_2 = R_1(1 + \alpha\ \Delta T)$, where $\Delta T = T_2 - T_1$ is the temperature change. For carbon fibers, α has been measured to be in the range [−0.13;0.02] %/K.[23] For A-MWCNT, $\alpha = -0.041$%/K has been reported.[24] C-MWNT samples have also been measured to have highly linear conductance dependence on temperature $G_2 = G_1(1 + \beta\Delta T)$ in the wide range of temperatures 50−800 K,[25] while another study found both positive and negative temperature coefficients depending on the degree of disorder in the shell structure.[26] Given the wide variety of defect types and their different effects on the electrical properties of an individual nanotube shell, it seems difficult to predict the properties of an individual C-MWNT without extensive structural studies. The method presented here allows for investigations of these issues in detail on the individual nanotube.

In air, amorphous graphite begins to oxidize at around 350 °C, while carbon nanotubes generally have higher oxidation temperatures, starting around 600 °C.[27] This is often explained by the absence of dangling bonds and the protection of inner shells by the outermost one. When nanotubes are heated in air, TEM studies have shown that pits tend to form in the shell structure.[28] Oxidation occurs faster at kinks, corrugations, and at points under a state of stress due to bending.[29] In addition, when high currents are passed through a nanotube, electron scattering near defects may cause local heating effects.[30]

3. Experimental Setup. Microfabricated chips with gold-coated (10 nm Cr/100 nm Au) silicon oxide microcantilevers were made with a "O" or "U" chip shape (inset in Figure 1), adapted to fit into a standard TEM grid holder. The microfabrication process has been described previously.[31] The present work has focused on studying a C-MWNT sample produced by a ferrocene/xylene CVD process,[32] and the nanotube structure appears comparable to those used by others.[33] Individual C-MWNTs bridging the microcantilevers were positioned on the TEM chip by manipulation using a an optical microscope and a manual *xyz*-stage fitted with an etched tungsten tip. For smaller nanotubes and nanostructures, an in situ SEM manipulation setup for nanoscale resolution can be used to place the nanostructure on the cantilevers.[34]

The achieved bridge resistance was often of the order of 100 kΩ when the nanotube was initially placed on the cantilevers. Temporary condensation of water onto the chip surface resulted in a stable reduction of the bridge resistances to below 50 kΩ in about half of the investigated samples, suggesting that adhesive capillary forces pull the nanotube into close contact with the cantilever surface to provide a more stable and reliable electrical contact. The method has been used to efficiently make electrical contact to both carbon nanotubes of different types and InP nanowires.

The TEM investigation was carried out in a Philips EM 430 operating at 100 keV. Using a liquid nitrogen cooled coldfinger, low beam currents, and relatively short beam exposure times (<2 min) ensured that no significant influence on the electrical properties of the nanotubes could be attributed to the TEM observations.

The electrical measurements were made using a Keithley 2400 sourcemeter. The control program allows the voltage sweep (*IV* curve) to be paused during the experiment when predefined voltages are reached or when current saturation occurs ($dI/dV = 0$) to record the current as function of time (*It* curve) until the bias voltage sweep is continued or the experiment stopped. For convenience, conductance will be given in units of the conductance quantum, G_0, keeping in mind that the transport mechanism is not expected to be ballistic at room temperature on the μm length scales investigated here.

4. Results. A TEM image sequence of the progressive oxidation of a nanotube in air is shown in Figure 1, where

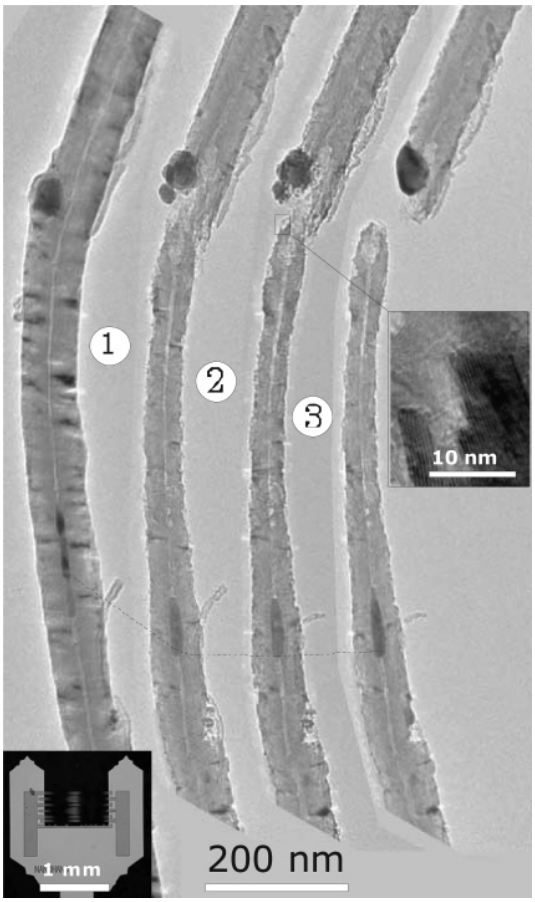

Figure 1. A series of TEM images of a C-MWNT, bridging two cantilevers on a TEM chip. The progressive destruction due to three consecutive Joule heating experiments (1−3) in air is clearly visible. The three corresponding *IV* and *It* curves recorded between the TEM images are shown in Figure 3. The dotted line indicates the motion of a catalytic particle within the nanotube central cavity. The nanotube breakdown primarily takes place in the vicinity of a particle incorporated into the shell structure, but also the middle part of the tube is considerably thinned down as a result of the Joule heating. The close-up shows the destroyed shell structure close to the catalytic particle where the termination of individual shells is clearly visible. The inset shows a U-shaped TEM compatible chip.

a Joule heating experiment has been performed between each TEM image was recorded. The nanotube clearly becomes thinner in the central part of the bridge with extensive damage in the vicinity of a large catalytic particle. The particles in the nanotube interior were generally observed to move and change shape, similar to the behavior reported by refs 33 and 35.

The C-MWNTs tested in these experiments had estimated initial cross-sectional area, A, in the range (3−10) 10^3 nm^2 (neglecting the narrow inner hole) and the length of the cantilever gap, L_{gap}, spans the range 0.7−9 μm. However, the distance between contact points of the nanotube located on top of the cantilevers, L_{tube}, may well be larger than the measured gap size as shown in the inset in Figure 2. The rough linearity of the measured resistance versus gap size indicates that this effect is only moderately important. A linear fit of the measured resistance as a function of length

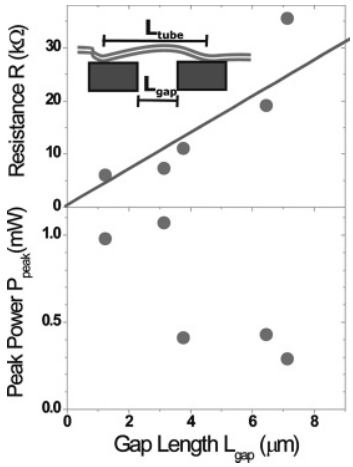

Figure 2. Overview of the electrical properties of the devices that achieved good contact to the C-MWNT (R < 50 kΩ). (a) The measured low bias resistance roughly scales with the gap length, showing that the tubes can be regarded as diffusive conductors on the micrometer scale and have a low contact resistance of the order of 0.5 kΩ. The inset illustrates that the nanotube section between contact points can be larger than the cantilever gap and that the length measurements therefore should be regarded with caution. (b) The maximum power dissipated in the bridges is around 1 mW for the shortest nanotubes and decreases with increasing gap length.

indicates an average contact resistance around 0.5 kΩ, which is less than 10% of the measured resistance for most nanotubes. The resistance through the microchip leads is only 90 Ω, hence the nanotubes may be regarded as diffusive conductors with resistance $R = \rho L/A$. The measured resistivity, ρ, is a factor 20−100 larger than the in-plane resistivity of graphite, 5 10^{-5} Ω cm[36] and thus comparable to the results by Dai et al.[4] The peak current density reaches 10^6−10^7 A/cm^2 for all nanotubes, which compares to previous studies of C-MWNT.[10] The peak power dissipated in the nanotube is quite different for the various C-MWNTs but seems to be limited to about 0.5−1 mW, as shown in Figure 2 and decreases with increasing gap length. This behavior may be expected for a heated bridging nanotube reaching the largest temperatures in the suspended part farthest away from the electrode heat sinks. All nanotubes were observed to be affected most in the middle of the gap between the electrodes, indicating that Joule heating is mainly taking place in the suspended part of the nanotube rather than at the contact points as expected for a diffusive conductor with low contact resistance.[37]

The electrical measurements on the nanotube observed in TEM in Figure 1 are shown in Figure 3 and are representative for the investigated nanotubes. Figure 3a shows the sequential *IV* curves indicated by the numbers in Figure 1. The voltage sweep was started at 0 V, and initially the sweep was stopped temporarily every 0.2 V, to observe the time dependence of the current at fixed bias, plotted in Figure 3b. As the saturation point was approached, pauses were made with smaller voltage intervals. At low bias voltages up to a bias voltage about 1.5 V, the current decay rate dI/dt is of order nA/s, which can be regarded as negligible. Above 1.5 V, dI/dt increases. Figure 3d plots the initial dI/dt at the beginning of each pause in the voltage sweep, as a function

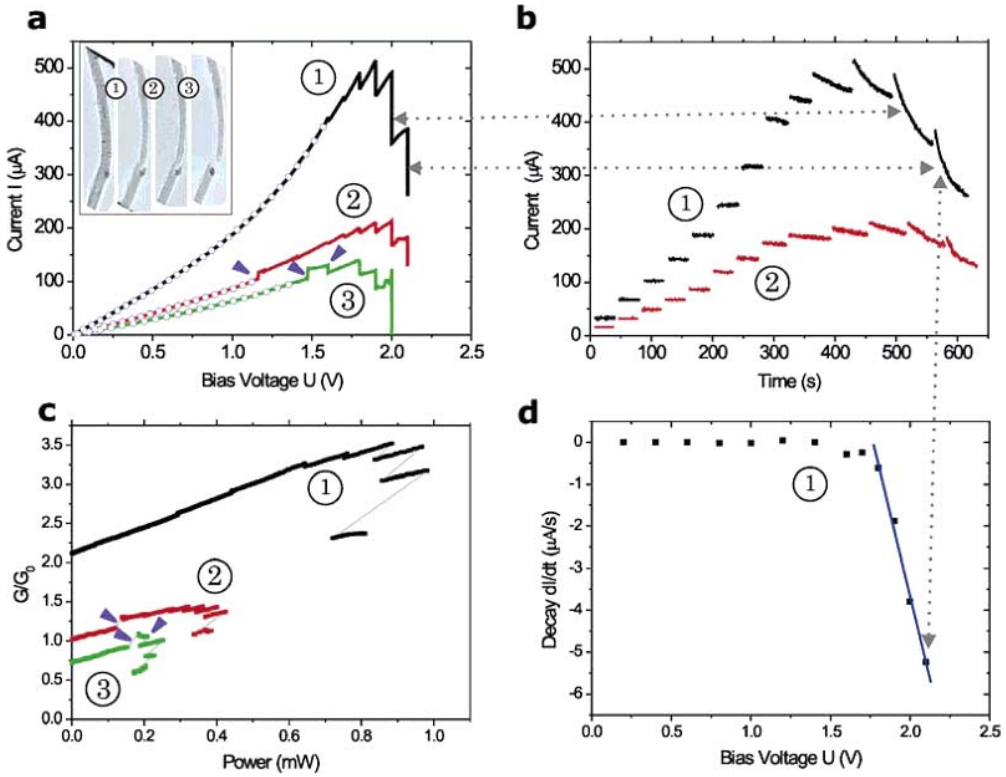

Figure 3. (a) Current through an individual C-MWNT as a function of bias voltage measured three successive times (1−3). The inset shows the TEM image sequence, also seen in Figure 1. The vertical parts of the curve appear in the intervals where the bias voltage was kept fixed, showing an increasingly strong time dependence at high bias voltages. The circles at low bias are nonlinear fits of the Joule heating *IV* dependence $I = U/(r + cU^2)$. (b) The current as a function of time at certain temporarily fixed bias voltages (correlations between the graphs are indicated with arrows). The current decreases faster with time above the threshold voltage, which is clear from the plot of dI/dt vs V in (d). (c) Normalized conductance G/G_0 versus dissipated power P. At fixed bias voltage, i.e., during the time sequences, the $G-P$ curve follows the gray lines ($G = P/U^2$). During the voltage sweep a dependence of the type $G = cP + 1/r$ is found for all samples with a fairly constant factor c. The small arrows in parts a and c indicate a glitch in the current source at 100 μA due to an automatic range shift.

of the fixed bias voltage. From 1.5 V the time dependence of the current increases dramatically.

As seen in Figure 3b, at high bias voltage the current as function of time resembles an exponential decay towards a steady-state value. The logarithm to the measured decay rates are not obviously linear functions of dissipated power and it is therefore difficult to relate the decay rate to an estimated temperature and corresponding Arrhenius-like dependence of oxidation rate similar to the thermal oxidation experiment by ref 29. We do not observe instantaneous drops in the current as function of time, as reported in experiments on A-MWNTs[1] or small C-MWNTs,[5] since the nanotubes in the present sample contain numerous shells and kinks, where the contribution from rupture of a single shell or merely a section of a shell will only give a minor contribution to the overall electrical behavior of the nanotube.

The onset of decay at the threshold voltage can be taken as an indication of beginning oxidation of the amorphous carbon in the C-MWNT, which should begin at 350 °C. From the dissipated power at the threshold and the nanotube dimensions, the formula $= LP/(8A\Delta T)$ with $\Delta T = 350$ °C provides an estimate of the thermal conductivity for the different tubes. From the measurements we find to be in the range 50−200 W/mK, in agreement with previously reported results.[21,22]

5. Discussion. In accordance with observations by other groups, the *IV* curves of the nanotube devices are nonlinear, with the conductivity increasing with respect to bias voltage lower than 1.5 V. The fixed bias voltage intervals cause the vertical steps at high bias voltage in the *IV* curves Figure 3a. These steps conveniently indicate how time becomes an increasingly important factor for the shape of the *IV* curves at high bias voltages. The time dependence should largely account for the saturation behavior of the measured *IV* curves that is often observed if the bias voltage is continuously increased without temporary stops.

The nonlinearity of the *IV* curves at low bias voltages, where no time dependence is observed, could be caused by thermal effects in the nanotube bridge. The conductance $G = I/U$ in units of the conductance quantum G_0 vs dissipated power $P = UI$ for the voltage sweeps is surprisingly linear, especially considering the extensive tube damage during each voltage sweep. This indicates a linear dependence on temperature $G_2 = G_1(1 + \beta\Delta T)$ with the temperature proportional to the dissipated power, $\Delta T = (L/(8\ A))P$. Combining these equations and expressing them in terms of voltage and current gives a conductivity $I/U = 1/r + cUI$,

with $r = 1/G_1$ and $c = \beta L/(8\ A)$, leading to a current−voltage relation $I = U/(r + cU^2)$. The linear conductance-power dependence $G = cP + 1/r$, gives a good fit to the low bias *IV* curve with fitting parameters r and c for each curve, as shown with circles in Figure 3a. For the G vs P curves at high power, the slope is slightly lower and can be explained by oxidation and the accompanying decaying current as function of time. Despite the very extensive damage of the nanotube structure, the sequential Joule heating curves have almost the same slopes for each individual sweep in the G vs P curves (we also find a linear G vs P dependence in our previous results obtained by scanning four point probes on nanotubes in air).[38]

The model of linear temperature dependence of nanotube conductance for the MWNT conduction seems to describe the present sample best, even after several current-induced oxidations of the outer shells have been performed on it, and even when it is nearly broken in two pieces after the second *IV* sweep (see Figure 1).

6. Conclusion and Outlook. The measurements on carbon nanotubes demonstrate the onset of nanotube damage in ambient conditions, with accelerated rate at higher bias voltages. The low bias *IV* curve is reasonably well described by a simple, phenomenological model based on linear dependence of conductivity on temperature and Joule heating. At high bias, the gradual oxidation of the nanotube shells is essential in describing the irreversible conductance change over time. On the basis of the decaying current with respect to time, the oxidation is likely to be the main factor causing the saturation of the *IV* curve for the studied C-MWNT. From the dissipated power at the threshold voltage, where the current begins to decay as function of time, an estimate can be made of the thermal conductivity of the nanotubes, giving reasonable values in the range 50−200 W/mK. Future work comparing different types of multiwalled nanotubes and independent measurements of the dependence of their properties with temperature should be essential for making better models of these interesting nanostructures' properties and evaluating their possible applications in devices.

The presented study also demonstrates the ability to use microcantilever electrodes for combining TEM with other characterization methods to provide unprecedented opportunities for characterizing a pristine individual nanostructure with several techniques. The microfabricated TEM chips (inset in Figure 1) offer good flexibility in terms of varying the design of the cantilevers, facilitating for instance multipoint conductance measurements or even integrated MEMS actuators and sensors for characterization of nano-electromechanical systems. If a nanostructure is suspended between the actuators of a cantilever-based actuator and force sensor[39] or between cantilevers with heaters and microbolometers[40] it should in principle be possible to study the electrical, thermal, and mechanical properties of the pristine nanostructures under a wide range of conditions with the option of performing TEM analysis in situ or between the experiments.

Acknowledgment. We thank Richard Czerw for supplying the nanotube samples.

References

(1) Collins, P. G.; et al. Current saturation and electrical breakdown in multiwalled carbon nanotubes. *Phys. Rev. Lett.* **2001**, *86* (14), 3128−3131.
(2) Nakayama, Y.; Akita, S. Nanoengineering of carbon nanotubes for nanotools. *New J. Phys.* **2003**, *5*.
(3) Poncharal, P.; et al. Room-temperature ballistic conduction in carbon nanotubes. *J. Phys. Chem. B* **2002**, *106* (47), 12104−12118.
(4) Dai, H. J.; Wong, E. W.; Lieber, C. M. Probing electrical transport in nanomaterials: Conductivity of individual carbon nanotubes. *Science* **1996**, *272* (5261), 523−526.
(5) Huang, J. Y.; et al. Atomic-scale imaging of wall-by-wall breakdown and concurrent transport measurements in multiwall carbon nanotubes. *Phys. Rev. Lett*. **2005**, *94* (23).
(6) *Carbon Nanotubes—Synthesis, Structure, Properties and Applications*; Dresselhaus, M. S., Dresselhaus, G., Avouris, P., Eds.; Topics in Applied Physics; Springer-Verlag: New York, 2003; Vol. 80.
(7) Teo, K. B. K.; et al. Uniform patterned growth of carbon nanotubes without surface carbon. *Appl. Phys. Lett*. **2001**, *79* (10), 1534−1536.
(8) Moser, J.; et al. Individual free-standing carbon nanofibers addressable on the 50 nm scale. *J. Vacuum Sci. Technol., B* **2003**, *21* (3), 1004−1007.
(9) Graham, A. P.; et al. Carbon nanotubes for microelectronics? *Small* **2005**, *1* (4), 382−390.
(10) Lee, S. B.; et al. Study of multiwalled carbon nanotube structures fabricated by PMMA suspended dispersion. *Microelectron. Eng.* **2002**, *61−2*, 475−483.
(11) Choi, W. B.; et al. Ultrahigh-density nanotransistors by using selectively grown vertical carbon nanotubes. *Appl. Phys. Lett*. **2001**, *79* (22), 3696−3698.
(12) Yuzvinsky, T. D.; et al. Imaging the life story of nanotube devices. *Appl. Phys. Lett*. **2005**, *87* (8).
(13) Xu, S. Y.; Xu, J.; Tian, M. L. A low cost platform for linking transport properties to the structure of nanomaterials. *Nanotechnology* **2006**, *17* (5), 1470.
(14) Kim, T.; et al. Imaging suspended carbon nanotubes in field-effect transistors configured with microfabricated slits for transmission electron microscopy. *Appl. Phys. Lett*. **2005**, *87* (17).
(15) Chikkannanavar, S. B.; et al. Synthesis of peapods using substrate-grown SWNTs and DWNTs: An enabling step toward peapod devices. *Nano Lett.* **2005**, *5* (1), 151−155.
(16) Meyer, J. C.; et al. Transmission electron microscopy and transistor characteristics of the same carbon nanotube. *Appl. Phys. Lett.* **2004**, *85* (14), 2911−2913.
(17) Kasumov, A. Y.; et al. Conductivity and atomic structure of isolated multiwalled carbon nanotubes. *Europhys. Lett.* **1998**, *43* (1), 89−94.
(18) Lee, S. B.; et al. Characteristics of multiwalled carbon nanotube nanobridges fabricated by poly(methyl methacrylate) suspended dispersion. *J. Vacuum Sci. Technol., B* **2002**, *20* (6), 2773−2776.
(19) Li, Q. H.; Wang, T. H. Shell coupling through a single multiwall carbon nanotube. *Chinese Phys. Lett.* **2003**, *20* (9), 1558−1560.
(20) Purcell, S. T.; et al. Hot nanotubes: Stable heating of individual multiwall carbon nanotubes to 2000 K induced by the field-emission current. *Phys. Rev. Lett.* **2002**, *88* (10).
(21) Yi, W.; et al. Linear specific heat of carbon nanotubes. *Phys. Rev. B* **1999**, *59* (14), R9015−R9018.
(22) Yang, D. J.; et al. Thermal and electrical transport in multiwalled carbon nanotubes. *Phys. Lett. A* **2004**, *329* (3), 207−213.
(23) Blazewicz, S.; Patalita, B.; Touzain, P. Study of piezoresistance effect in carbon fibers. *Carbon* **1997**, *35* (10−11), 1613−1618.
(24) Vincent, P.; et al. Modelization of resistive heating of carbon nanotubes during field emission. *Phys. Rev. B* **2002**, *66* (7).
(25) Zhou, F.; et al. Linear conductance of multiwalled carbon nanotubes at high temperatures. *Solid State Commun.* **2004**, *129* (6), 407−410.
(26) Jang, J. W.; et al. Conduction mechanism of the bamboo-shaped multiwalled carbon nanotubes. *J. Korean Phys. Soc.* **2003**, *42*, S985−S988.
(27) Sekar, C.; Subramanian, C. Purification and characterization of buckminsterfullerene, nanotubes and their byproducts. *Vacuum* **1996**, *47* (11), 1289−1292.
(28) Morishita, K.; Takarada, T. Gasification behavior of carbon nanotubes. *Carbon* **1997**, *35* (7), 977−981.
(29) Lu, X. K.; et al. Scanning electron microscopy study of carbon nanotubes heated at high temperatures in air. *J. Appl. Phys.* **1999**, *86* (1), 186−189.

(30) de Pablo, P. J., et al. Correlating the location of structural defects with the electrical failure of multiwalled carbon nanotubes. *Appl. Phys. Lett.* **1999**, *75* (25), 3941−3943.
(31) Boggild, P.; et al. Fabrication and actuation of customized nanotweezers with a 25 nm gap. *Nanotechnology* **2001**, *12* (3), 331−335.
(32) Andrews, R.; et al. Continuous production of aligned carbon nanotubes: a step closer to commercial realization. *Chem. Phys. Lett.* **1999**, *303* (5−6), 467−474.
(33) Kim, H.; Kaufman, M. J.; Sigmund, W. M. Phase transition of iron inside carbon nanotubes under electron irradiation. *J. Mater. Res.* **2004**, *19* (6), 1835−1839.
(34) Mølhave, K.; Wich, T.; Kortschack, A.; Bøggild, P. Pick-and-place nanomanipulation using microfabricated grippers. *Nanotechnology* **2006**, *17*, 2434−2441.
(35) Svensson, K.; Olin, H.; Olsson, E. Nanopipets for metal transport. *Phys. Rev. Lett.* **2004**, *93* (14).
(36) Matsubara, K.; Sugihara, K.; Tsuzuku, T. Electrical-Resistance in the C-Direction of Graphite. *Phys. Rev. B* **1990**, *41* (2), 969−974.
(37) Shi, L.; et al. Scanning thermal microscopy study of dissipation in current-carrying carbon nanotubes. *Am. Soc. Mech. Eng., Heat Transfer Div., (Publ.) HTD* 2001, *369* (7), 247−252.
(38) Dohn, S.; Molhave, K; Boggild, P. Direct measurement of resistance of multiwalled carbon nanotubes using micro four-point probes. *Sens. Lett.* **2005**, *3* (4), 300−303.
(39) Molhave, K.; Hansen, O. Electro-thermally actuated microgrippers with integrated force-feedback. *J. Micromech. Microeng.* **2005**, *15* (6), 1265−1270.
(40) Shi, L.; Majumdar, A.; McEuen, P. L. Thermal transport measurements of individual multiwalled nanotubes. *Phys. Rev. Lett.* **2001**, APS. 215502/1−4.

NL060821N

Bibliography

[1] Kristian Mølhave and Ole Hansen. Electro-thermally actuated microgrippers with integrated force feedback. *Journal of Micromechanics and Microengineering*, 15:1265–1270, 2005.

[2] Kristian Mølhave, Dorte Nørgaard Madsen, , and Peter Bøggild. A simple electron beam lithography system. *Ultramicroscopy*, 102:215–219, 2005.

[3] Kristian Mølhave, Dorte Nørgaard Madsen, Søren Dohn, and Peter Bøggild. Constructing, connecting and soldering nanostructures by environmental electron beam deposition. *Nanotechnology*, 15:1047–1053, 2004.

[4] K. Mølhave, D.N. Madsen, A.M. Rasmussen, A. Carlsson, C.C. Appel, M. Brorson, C.J.H. Jacobsen, and P. Bøggild. Solid gold nanostructures fabricated by electron beam deposition. *Nano Letters*, 3:1499–1503, 2003.

[5] D.N. Madsen, K. Mølhave, R. Mateiu, A.M. Rasmussen, M. Brorson, C.J.H. Jacobsen, and P. Bøggild. Soldering of nanotubes onto microelectrodes. *Nano Letters*, 3:47–49, 2003.

[6] K. Mølhave, T.M. Hansen, D.N. Madsen, and P. Bøggild. Towards pick-and-place assembly of nanostructures. *Journal of Nanoscience and Nanotechnology*, 4:279–282, 2004.

[7] Søren Dohn, Peter Bøggild, and Kristian Mølhave. Direct measurement of resistance of multiwalled carbon nanotubes using micro four-point probes. *Sensor Letters*, 3:300–303, 2004.

[8] R. Mateiu, Z.J. Davis, D.N. Madsen, K. Molhave, P. Boggild, A.-M. Rassmusen, M. Brorson, C.J.H. Jacobsen, and A. Boisen. An approach to a multi-walled carbon nanotube based mass sensor. *Microelectronic Engineering*, 73-74:670–674, 2004.

[9] G. E. Moore. Cramming more components onto integrated circuits. *Electronics*, 38:–, 1965.

[10] G. Binnig and H. Rohrer. In touch with atoms. *Reviews of Modern Physics*, 71(2):S324–30, 1999.

[11] G. Binnig, C.F. Quate, and C. Gerber. Atomic force microscope. *Physical Review Letters*, 56(9):930–3, 1986.

[12] E. Ruska. The development of the electron microscope and of electron microscopy. *Reviews of Modern Physics*, 59(31):627–38, 1987.

[13] C. W. Oatley. The early history of the scanning electron microscope. *Journal of Applied Physics*, 53(2):R1–R13, 1982.

[14] Robert F. Curl and Richard E. Smalley. Probing c_{60}. *Science*, 3.242(4881):1017–1022, 1988.

[15] S. Iijima. Helical microtubules of graphitic carbon. *Nature*, 354(6348):56–8, 1991.

[16] C.M. Lieber. Nanowires as building blocks for nanoelectronics and nanophotonics. *Electron Devices Meeting, 2003. IEDM '03 Technical Digest. IEEE International*, page 12.3.1, 2003.

[17] L. Samuelson. Self-forming nanoscale devices. *Materials Today*, 6(10):22–31, 2003.

[18] Y. Cui and C.M. Lieber. Functional nanoscale electronic devices assembled using silicon nanowire building blocks. *Science*, 291(5505):851–853*, 2001.

[19] Mark S. Gudiksen, Lincoln J. Lauhon, Jianfang Wang, David C. Smith, and Charles M. Lieber. Growth of nanowire superlattice structures for nanoscale photonics and electronics. *Nature*, 415(6872):617–620, 2002.

[20] Yi Cui, Qingqiao Wei, Hongkun Park, and C.M. Lieber. Nanowire nanosensors for highly sensitive and selective detection of biological and chemical species. *Science*, 293(5533):1289–92, 2001.

[21] L. Samuelson, M.T. Bjork, K. Deppert, M. Larsson, B.J. Ohlsson, N. Panev, A.I. Persson, N. Skold, C. Thelander, and L.R. Wallenberg. Semiconductor nanowires for novel one-dimensional devices. *Physica E*, 21(2-4):560–567, 2004.

[22] D.H. Gracias, J. Tien, T.L. Breen, C. Hsu, and G.M. Whitesides. Forming electrical networks in three dimensions by self-assembly. *Science*, 289(5482):1170–2, 2000.

[23] Yuegang Zhang, Aileen Chang, Jien Cao, Qian Wang, Woong Kim, Yiming Li, N. Morris, E. Yenilmez, Jing Kong, and Hongjie Dai. Electric-field-directed growth of aligned single-walled carbon nanotubes. *Applied Physics Letters*, 79(19):3155–7, 2001.

[24] M. Saif Islam, S. Sharma, T.I. Kamins, and R. Stanley Williams. Ultrahigh-density silicon nanobridges formed between two vertical silicon surfaces. *Nanotechnology*, 15(5):L5–L8, 2004.

[25] K.B.K. Teo, M. Chhowalla, G.A.J. Amaratunga, W.I. Milne, D.G. Hasko, G. Pirio, P. Legagneux, F. Wyczisk, and D. Pribat. Uniform patterned growth of carbon nanotubes without surface carbon. *Applied Physics Letters*, 79(10):1534–6, 2001.

[26] B. Bourlon, D.C. Glattli, B. Placais, J.M. Berroir, C. Miko, L. Forro, and A. Bachtold. Geometrical dependence of high-bias current in multiwalled carbon nanotubes. *Physical Review Letters*, 92(2):026804/1–4, 2004.

[27] Y. Huang, X. Duan, Q. Wei, and C.M. Lieber. Directed assembly of one-dimensional nanostructures into functional networks. *Science*, 291(5504):630–633*, 2001.

[28] Phaedon Avouris. Carbon nanotube electronics. *Chemical Physics*, 281(2-3):429–445, 2002.

[29] A.M. Fennimore, T.D. Yuzvinsky, Wei-Qiang Han, M.S. Fuhrer, J. Cumings, and A. Zetti. Rotational actuators based on carbon nanotubes. *Nature*, 424(6947):408–410, 2003.

[30] M.R. Falvo, G. Clary, A. Helser, S. Paulson, R.M. Taylor II, V. Chi, F.P. Brooks, Jr., S. Washburn, and R. Superfine. Nanomanipulation experiments exploring frictional and mechanical properties of carbon nanotubes. *Microscopy and Microanalysis*, 4(5):504–512, 1998.

[31] C. Thelander, M.H. Magnusson, K. Deppert, L. Samuelson, P.R. Poulsen, J. Nygard, and J. Borggreen. Gold nanoparticle single-electron transistor with carbon nanotube leads. *Applied Physics Letters*, 79(13):2106–8, 2001.

[32] Ph. Avouris, R. Martel, and H.R. Shea. Carbon nanotubes: nanomechanics, manipulation, and electronic devices. *Applied Surface Science*, 141(3-4):201–209, 1999.

[33] Stefan Hembacher, Franz J. Giessibl, and Jochen Mannhart. Force Microscopy with Light-Atom Probes. *Science*, 305(5682):380–383, 2004.

[34] Zyvex. http://zyvex.com.

[35] Kensuke Tsuchiya, Akihiro Murakami, Gustavo Fortmann, Masayuki Nakao, and Yotaro Hatamura. Micro assembly and micro bonding in nano manufacturing world. *Proceedings of SPIE - The International Society for Optical Engineering*, 3834:132–140, 1999.

[36] MinFeng Yu, Mark J. Dyer, George D. Skidmore, Henry W. Rohrs, XueKun Lu, Kevin D. Ausman, James R. Von Ehr, and Rodney S. Ruoff. Three-dimensional manipulation of carbon nanotubes under a scanning electron microscope. *Nanotechnology*, 10(3):244–252, 1999.

[37] T. Fukuda, F. Arai, and L. Dong. Fabrication and property analysis of mwnt junctions through nanorobotic manipulations. *International Journal of Nonlinear Sciences and Numerical Simulation*, 3(3-4):753–8, 2002.

[38] P. Kim and C.M. Lieber. Nanotube nanotweezers. *Science*, 286(5447):2148–50, 1999.

[39] H. Watanabe, K. Shimotani, T. Shigematu, and C. Manabe. Electric measurements of nanoscaled devices. *Thin Solid Films*, 438-439:462–466, 2003.

[40] O. S. Heavens and R. W. Ditchburn. *Insight Into Optics*. John Wiley & Sons, Inc., 1987.

[41] J. Goldstein, D. Newbury, P. Echlin, D. C. Joy, A. D. Romig, C. E. Lyman, C. Fiori, and E. Lifshin. *Scanning Electron Microscopy and X-Ray Microanalysis, 2nd Ed.* Plenum Press, 1992.

[42] P. J. Goodhew and F. J. Humphreys. *Electron Microscopy and Analysis, 2rd Ed.* Taylor and Francis, 1988.

[43] S. Humphries. *Charged Particle Beams*. John Wiley and Sons, 1990. PDF version available at http://www.fieldp.com/cpb/cpb.html.

[44] P. W. Hawkes and E. Kasper. *Principles Of Electron Optics*. Academic Press, 1989.

[45] L. Reimer. *Transmission electron microscopy: Physics of image formation and microanalysis, 3rd Ed.* Springer-Verlag, 1993.

[46] FEI/Philips Ole Mariager. Private communication.

[47] Brock & Michelsen A/S Thorkild Hansen. Private communication.

[48] P. W. Milonni and J. H. Eberly. *Lasers*. John Wiley & Sons, Inc., 1988.

[49] Nanofactory Instruments. http://www.nanofactory.com.

[50] David G. Grier. A revolution in optical manipulation. *Nature*, 424(6950):810–816, 2003.

[51] P.A. Williams, S.J. Papadakis, M.R. Falvo, A.M. Patel, M. Sinclair, A. Seeger, A. Helser, R.M. Taylor, S. Washburn, and R. Superfine. Controlled placement of an individual carbon nanotube onto a microelectromechanical structure. *Applied Physics Letters*, 80(14):2574–6, 2002.

[52] Min-Feng Yu, O. Lourie, M.J. Dyer, K. Moloni, T.F. Kelly, and R.S. Ruoff. Strength and breaking mechanism of multiwalled carbon nanotubes under tensile load. *Science*, 287(5453):637–40, 2000.

[53] Keun Soo Kim, Seong Chu Lim, Im Bok Lee, Key Heyok An, Dong Jae Bae, Shinje Choi, Jae-Eun Yoo, and Young Hee Lee. In situ manipulation and characterizations using nanomanipulators inside a field emission-scanning electron microscope. *Review of Scientific Instruments*, 74(9):4021–4025, 2003.

[54] Min-Feng Yu, Bradley S. Files, Sivaram Arepalli, and Rodney S. Ruoff. Tensile loading of ropes of single wall carbon nanotubes and their mechanical properties. *Physical Review Letters*, 84(24):5552–5555, 2000.

[55] Inger Ekvall, Erik Wahlstrom, Dan Claesson, Hakan Olin, and Eva Olsson. Preparation and characterization of electrochemically etched w tips for stm. *Measurement Science and Technology*, 10(1):11–18, 1999.

[56] Lixin Dong, F. Arai, and T. Fukuda. 3d nanorobotic manipulation of nano-order objects inside sem. *Micromechatronics and Human Science, 2000. MHS 2000. Proceedings of 2000 International Symposium on*, pages 151 –156, 2000.

[57] Cedric Clevy, Arnaud Hubert, and Nicolas Chaillet. A new micro-tools exchange principle for micromanipulation. *Proc. IROS 2004*, 2004.

[58] Torben M. Hansen. *Tools for Nanoscale Conductivity Measurements*. PhD thesis, MIC-Department of Micro and Nanotechnology, Technical University of Denmark, 2003.

[59] CAPRES A/S. http://www.capres.com.

[60] P. Boggild, T.M. Hansen, C. Tanasa, and F. Grey. Fabrication and actuation of customized nanotweezers with a 25 nm gap. *Nanotechnology*, 12(3):331–335, 2001.

[61] Peter Andreas Rasmussen. *Cantilever-based Sensors for Surface Stress Measurements*. PhD thesis, MIC- Department of Micro and Nanotechnology, Technical University of Denmark, 2003.

[62] J. Thaysen, A. Boisen, O. Hansen, and S. Bouwstra. Atomic force microscopy probe with piezoresistive read-out and a highly symmetrical wheatstone bridge arrangement. *Sensors and Actuators A: Physical*, 83(1-3):47–53, 2000.

[63] Wolfgang Zesch. *Multi-Degree-of-Freedom Micropositioning Using Stepping Principles*. PhD thesis, Swiss Federal Institute of Technology, ETH, Zurich, 1997.

[64] Klocke Nanotechnik. http://www.nanomotor.de.

[65] Kleindiek Nanotechnik. http://www.nanotechnik.com.

[66] A. Kortschack, O.C. Hanbler, C. Rass, and S. Fatikow. Driving principles of mobile microrobots for micro- and nanohandling. *Intelligent Robots and Systems, 2003. (IROS 2003). Proceedings. 2003 IEEE/RSJ International Conference on*, 2:1895–1900 vol.2, 2003.

[67] V. Klocke. Engineering in the nanocosmos: Nanorobotics moves kilograms of mass. *Journal of Nanoscience and Nanotechnology*, 2(3-4):435–40, 2002.

[68] Roland Buechi, Wolfgang Zesch, Alain Codourey, and Roland Siegwart. Inertial drives for micro- and nanorobots: analytical study. *Proceedings of SPIE - The International Society for Optical Engineering*, 2593:89–97, 1995.

[69] Shuji Hasegawa, Ichiro Shiraki, Fuhito Tanabe, and Rei Hobara. Transport at surface nanostructures measured by four-tip stm. *Current Applied Physics*, 2(6):465–471, 2002.

[70] G.D. Danilatos. Foundations of environmental scanning electron microscopy. *Advances in electronics and electron physics. Vol.71*, pages 109–250, 1988.

[71] G.D. Danilatos. Equations of charge distribution in the environmental scanning electron microscope (esem). *Scanning Microscopy*, 4(4):799–823, 1990.

[72] Point Electronics. http://www.pointelectronic.de.

[73] A.Yu. Kasumov, H. Bouchiat, B. Reulet, O. Stephan, I.I. Khodos, Yu.B. Gorbatov, and C. Colliex. Conductivity and atomic structure of isolated multiwalled carbon nanotubes. *Europhysics Letters*, 43(1):89–94, 1998.

[74] Gen Hashiguchi, Takushi Goda, Maho Hosogi, Ken Hirano, Noritada Kaji, Yoshinobu Baba, Kuniyuki Kakushima, and Hiroyuki Fujita. Dna manipulation and retrieval from an aqueous solution with micromachined nanotweezers. *Analytical Chemistry*, 75(17):4347–4350, 2003.

[75] H. Watanabe, C. Manabe, T. Shigematsu, K. Shimotani, and M. Shimizu. Single molecule dna device measured with triple-probe atomic force microscope. *Applied Physics Letters*, 79(15):2462–4, 2001.

[76] S K Jericho, M H Jericho, T Hubbard, and M Kujath. Micro-electro-mechanical systems microtweezers for the manipulation of bacteria and small particles. *Review of Scientific Instruments*, 75(5):1280–1282, 2004.

[77] J. Jonsmann, O. Sigmund, and S. Bouwstra. Compliant electro-thermal microactuators. *Micro Electro Mechanical Systems, 1999. MEMS '99. Twelfth IEEE International Conference on*, pages 588 –593, 1999.

[78] G. Greitmann and R.A. Buser. Tactile microgripper for automated handling of microparts. *Sensors and Actuators A: Physical*, 53(1-3):410–415, 1996.

[79] M. Kohl, E. Just, W. Pfleging, and S. Miyazaki. Sma microgripper with integrated antagonism. *Sensors and Actuators A: Physical*, 83(1-3):208–213, 2000.

[80] Chang-Jin Kim, Albert P. Pisano, Richard S. Muller, and Martin G. Lim. Polysilicon microgripper. *Sensors and Actuators, A: Physical*, 33(3):221–227, 1992.

[81] S. Akita, Y. Nakayama, S. Mizooka, Y. Takano, T. Okawa, Y. Miyatake, S. Yamanaka, M. Tsuji, and T. Nosaka. Nanotweezers consisting of carbon nanotubes operating in an atomic force microscope. *Applied Physics Letters*, 79(11):1691–3, 2001.

[82] Christine Meyer, Heribert Lorenz, and Khaled Karrai. Optical detection of quasi-static actuation of nanoelectromechanical systems. *Applied Physics Letters*, 83(12):2420–2422, 2003.

[83] Bharat Bhushan. Review articles - adhesion and stiction: Mechanisms, measurement techniques, and methods for reduction. *Journal of Vacuum Science and Technology - Section B*, 21(6):2262–2296, 2003.

[84] S. D. Senturia. *Microsystem Design*. Kluwer Academic Publishers, 2001.

[85] Bharat (Ed.) Bhushan. *Springer Handbook of Nanotechnology*. Springer-Verlag, 2004.

[86] Min-Feng Yu, Tomasz Kowalewski, and Rodney S. Ruoff. Structural analysis of collapsed, and twisted and collapsed, multiwalled carbon nanotubes by atomic force microscopy. *Physical Review Letters*, 86(1):87–90, 2001.

[87] D. H. Kaelble. Theory and analysis of peel adhesion: Mechanisms and mechanics. *Transactions of the Society of Rheology*, 3:161–189, 1959.

[88] C.-J. Kim, A.P. Pisano, R.S. Muller, and M.G. Lim. Polysilicon microgripper. *Solid-State Sensor and Actuator Workshop, 1990. 4th Technical Digest., IEEE*, pages 48 –51, 1990.

[89] I. S. Grant and W. R. Philips. *Electromagnetism*. John Wiley & Sons, Inc., 1990.

[90] Sayanu Pamidighantam, Robert Puers, Kris Baert, and Harrie A C Tilmans. Pull-in voltage analysis of electrostatically actuated beam structures with fixed–fixed and fixed–free end conditions. *Journal of Micromechanics and Microengineering*, 12(4):458–464, 2002.

[91] P.M. Osterberg, R.K. Gupta, J.R. Gilbert, and S.D. Senturia. Quantitative models for the measurement of residual stress, poisson ratio and young's modulus using electrostatic pull-in of beams and diaphragms. *Technical Digest. Solid-State Sensor and Actuator Workshop*, pages 184–8, 1994.

[92] E.S. Kolesar, M.D. Ruff, W.E. Odom, J.A. Jayachadran, J.B. McAllister, S.Y. Ko, J.T. Howard, P.B. Allen, J.M. Wilken, N.C. Boydston, J.E. Bosch, and R.J. Wilks. Single- and double-hot arm asymmetrical polysilicon surface micromachined electrothermal microactuators applied to realize a microengine. *Thin Solid Films*, 420-421:530–538, 2002.

[93] R. Lariviere Stewart. Insulating films formed under electron and ion bombardment. *Phys. Rev.*, 45:488Ű490, 1934.

[94] J. J. Hren. *Barriers to AEM: contamination and etching. In: Introduction to Analytical Electron Microscopy.* Plenum, New York, 1979.

[95] Shuji Kiyohara, Hideaki Takamatsu, and Katsumi Mori. Microfabrication of diamond films by localized electron beam chemical vapour deposition. *Semiconductor Science and Technology*, 17(10):1096–1100, 2002.

[96] T. Ooi, K. Matsumoto, M. Nakao, M. Otsubo, S. Shirakata, S. Tanaka, and Y. Hatamura. 3d nano wire-frame for handling and observing a single dna fiber. *Micro Electro Mechanical Systems, 2000. MEMS 2000. The Thirteenth Annual International Conference on*, pages 580 –583, 2000.

[97] H.W.P. Koops, O.E. Hoinkis, M.E.W. Honsberg, R. Schmidt, R. Blum, G. Bottger, A. Kuligk, C. Liguda, and M. Eich. Two-dimensional photonic crystals produced by additive nanolithography with electron beam-induced deposition act as filters in the infrared. *Microelectronic Engineering*, 57-58:995–1001, 2001.

[98] Hans W. Koops, M. Weber, C. Schossler, and A. Kaja. Three-dimensional additive electron beam lithography. *Proceedings of SPIE - The International Society for Optical Engineering*, 2780:388–395, 1996.

[99] K. Edinger, T. Gotszalk, and I.W. Rangelow. Novel high resolution scanning thermal probe. *Journal of Vacuum Science and Technology B: Microelectronics and Nanometer Structures*, 19(6):2856–2860, 2001.

[100] Natalia Silvis-Cividjian. *Electron Beam Induced Nanometer Scale Deposition.* PhD thesis, Technical University in Delft, Faculty of applied Physics, 2002.

[101] M. Wendel, H. Lorenz, and J.P. Kotthaus. Sharpened electron beam deposited tips for high resolution atomic force microscope lithography and imaging. *Applied Physics Letters*, 67(25):3732–4, 1995.

[102] H.W.P. Koops, R. Weiel, D.P. Kern, and T.H. Baum. High-resolution electron-beam induced deposition. *Journal of Vacuum Science and Technology B (Microelectronics Processing and Phenomena)*, 6(1):477–81, 1988.

[103] S. Matsui and K. Mori. In situ observation on electron beam induced chemical vapor deposition by auger electron spectroscopy. *Applied Physics Letters*, 51(9):646–8, 1987.

[104] Y.M. Lau, P.C. Chee, J.T.L. Thong, and V. Ng. Properties and applications of cobalt-based material produced by electron-beam-induced deposition. *Journal of Vacuum Science and Technology A: Vacuum, Surfaces and Films*, 20(4):1295–1302, 2002.

[105] H.W.P. Koops, C. Schoessler, A. Kaya, and M. Weber. Conductive dots, wires, and supertips for field electron emitters produced by electron-beam induced deposition on samples having increased temperature. *Journal of Vacuum Science and Technology B: Microelectronics Processing and Phenomena*, 14(6):4105–4109, 1996.

[106] P. Hoffmann, I. Utke, F. Cicoira, B. Dwir, K. Leifer, E. Kapon, and P. Doppelt. Focused electron beam induced deposition of gold and rhodium. *Materials Development for Direct Write Technologies. Symposium (Materials Research Society Symposium Proceedings Vol.624)*, pages 171–7, 2000.

[107] A. Folch, J. Servat, J. Esteve, J. Tejada, and M. Seco. High-vacuum versus environmental electron beam deposition. *Journal of Vacuum Science and Technology B (Microelectronics and Nanometer Structures)*, 14(4):2609–14, 1996.

[108] P. Boggild, T.M. Hansen, K. Molhave, A. Hyldgard, M.O. Jensen, J. Richter, L. Montelius, and F. Grey. Customizable nanotweezers for manipulation of free-standing nanostructures. *Nanotechnology, 2001. IEEE-NANO 2001. Proceedings of the 2001 1st IEEE Conference on*, pages 87–92, 2001.

[109] V. Scheuer, H. Koops, and T. Tschudi. Electron beam decomposition of carbonyls on silicon. *Microelectronic Engineering*, 5(1-4):423–30, 1986.

[110] Inc. Strem Chemicals. http://www.strem.com.

[111] W. Paul. Electromagnetic traps for charged and neutral particles. *Reviews of Modern Physics*, 62(3):531–40, 1990.

[112] H.W.P. Koops, A. Kaya, and M. Weber. Fabrication and characterization of platinum nanocrystalline material grown by electron-beam induced deposition. *Journal of Vacuum Science and Technology B (Microelectronics and Nanometer Structures)*, 13(6):2400–3, 1995.

[113] I. Utke, T. Bret, D. Laub, P. Buffat, L. Scandella, and P. Hoffmann. Thermal effects during focused electron beam induced deposition of nanocomposite magnetic-cobalt-containing tips. *Microelectronic Engineering*, 73-74:553–558, 2004.

[114] Bin Xue, Ping Chen, Qi Hong, Jianyi Lin, and Kuang Lee Tan. Growth of pd, pt, ag and au nanoparticles on carbon nanotubes. *Journal of Materials Chemistry*, 11(9):2378–2382, 2001.

[115] M. Harsdorff. The influence of charged point defects and contamination of substrate surfaces on nucleation. *Thin Solid Films*, 116(1-3):55–74, 1984.

[116] H.W.P. Koops, J. Kretz, M. Rudolph, and M. Weber. Constructive three-dimensional lithography with electron-beam induced deposition for quantum effect devices. *Journal of Vacuum Science and Technology B (Microelectronics Processing and Phenomena)*, 11(6):2386–9, 1993.

[117] M. Ishida, J. Fujita, T. Ichihashi, Y. Ochiai, T. Kaito, and S. Matsui. Focused ion beam-induced fabrication of tungsten structures. *Journal of Vacuum Science and Technology B: Microelectronics and Nanometer Structures*, 21(6):2728–2731, 2003.

[118] M. Shimojo, K. Mitsuishi, M. Tanaka, M. Han, and K. Furuya. Application of transmission electron microscopes to nanometre-sized fabrication by means of electron beam-induced deposition. *Journal of Microscopy*, 214(1):76–79, 2004.

[119] J. Fujita, M. Ishida, T. Ichihashi, Y. Ochiai, T. Kaito, and S. Matsui. Carbon nanopillar laterally grown with electron beam-induced chemical vapor deposition. *Journal of Vacuum Science and Technology B: Microelectronics and Nanometer Structures*, 21(6):2990–2993, 2003.

[120] C. Durkan and M.E. Welland. Analysis of failure mechanisms in electrically stressed gold nanowires. *Ultramicroscopy*, 82(1-4):125–133, 2000.

[121] I. Utke, P. Hoffmann, B. Dwir, K. Leifer, E. Kapon, and P. Doppelt. Focused electron beam induced deposition of gold. *Journal of Vacuum Science and Technology B: Microelectronics and Nanometer Structures*, 18(6):3168–3171, 2000.

[122] P.G. Collins, M. Hersam, M. Arnold, R. Martel, and Ph. Avouris. Current saturation and electrical breakdown in multiwalled carbon nanotubes. *Physical Review Letters*, 86(14):3128–3131, 2001.

[123] Z.L. Wang. Nanomechanics of fiber-like nanomaterials. *Journal of Materials Science and Technology*, 17(3):303–305, 2001.

[124] Jien Cao, Qian Wang, and Hongjie Dai. Electromechanical properties of metallic, quasi-metallic, and semiconducting carbon nanotubes under stretching. *Physical Review Letters*, 90(15):157601/1–157601/4, 2003.

[125] E.D. Minot, Y. Yaish, V. Sazonova, J. Park, M. Brink, and P.L. McEuen. Tuning carbon nanotube band gaps with strain. *Physical Review Letters*, 90(15):156401/1–156401/4, 2003.

[126] S. Blazewicz, B. Patalita, and Ph. Touzain. Study of piezoresistance effect in carbon fibers. *Carbon*, 35(10-11):1613–1618, 1997.

[127] Søren Dohn. Investigation of mechano-electrical properties of multi-walled carbon nanotubes. Master's thesis, MIC- Department of Micro and Nanotechnology, Technical University of Denmark, 2003.

[128] B.W. Smith and D.E. Luzzi. Electron irradiation effects in single wall carbon nanotubes. *Journal of Applied Physics*, 90(7):3509–15, 2001.

[129] Hongjie Dai, Eric W. Wong, and Charles M. Liebert. Probing electrical transport in nanomaterials: conductivity of individual carbon nanotubes. *Science*, 272(5261):523–526, 1996.

[130] C. Berger, P. Poncharal, Yan Yi, and W. de Heer. Ballistic conduction in multiwalled carbon nanotubes. *Journal of Nanoscience and Nanotechnology*, 3(1-2):171–7, 2003.

[131] B.Q. Wei, R. Vajtai, and P.M. Ajayan. Reliability and current carrying capacity of carbon nanotubes. *Applied Physics Letters*, 79(8):1172–4, 2001.

[132] J. Moser, R. Panepucci, Z.P. Huang, W.Z. Li, Z.F. Ren, A. Usheva, and M.J. Naughton. Individual free-standing carbon nanofibers addressable on the 50 nm scale. *Journal of Vacuum Science and Technology B: Microelectronics and Nanometer Structures*, 21(3):1004–1007, 2003.

[133] S.-B. Lee, K.B.K. Teo, M. Chhowalla, D.G. Hasko, G.A.J. Amaratunga, W.I. Milne, and H. Ahmed. Study of multi-walled carbon nanotube structures fabricated by pmma suspended dispersion. *Microelectronic Engineering*, 61-62:475–483, 2002.

[134] Won Bong Choi, Jae Uk Chu, Kwang Seok Jeong, E.J. Bae, Jo-Won Lee, Ju-Jin Kim, and Jeong-O Lee. Ultrahigh-density nanotransistors by using selectively grown vertical carbon nanotubes. *Applied Physics Letters*, 79(22):3696–8, 2001.

[135] P.J. de Pablo, S. Howell, S. Crittenden, B. Walsh, E. Graugnard, and R. Reifenberger. Correlating the location of structural defects with the electrical failure of multiwalled carbon nanotubes. *Applied Physics Letters*, 75(25):3941–3, 1999.

[136] Yoshikazu Nakayama and Seiji Akita. Nanoengineering of carbon nanotubes for nanotools. *New Journal of Physics*, 5(1):128, 2003.

[137] Philippe Poncharal, Claire Berger, Yan Yi, Walt A. De Heer, and Z.L. Wang. Room temperature ballistic conduction in carbon nanotubes. *Journal of Physical Chemistry B*, 106(47):12104–12118, 2002.

[138] R. Andrews, A.M. Rao, D. Qian, and E.C. Dickey. Continuous production of aligned carbon nanotubes: a step closer to commercial realization. *Chemical Physics Letters*, 303(5-6):467–474, 1999.

[139] K. Matsubara, K. Sugihara, and T. Tsuzuku. Electrical resistance in the c direction of graphite. *Physical Review B (Condensed Matter)*, 41(2):969–74, 1990.

[140] M. S. Dresselhaus, Gene Dresselhaus, and Phaedon Avouris. *Carbon nanotubes : synthesis, structure, properties, and applications*. Springer-Verlag, 2001.

[141] J.W. Ding, X.H. Yan, and J.X. Cao. Analytical relation of band gaps to both chirality and diameter of single-wall carbon nanotubes. *Physical Review B (Condensed Matter and Materials Physics)*, 66(7):073401/1–4, 2002.

[142] Supriyo Datta. Electrical resistance: an atomistic view. *Nanotechnology*, 15(7):S433, 2004.

[143] F. Banhart. Irradiation effects in carbon nanostructures. *Reports on Progress in Physics*, 62(8):1181–221, 1999.

[144] Bingqing Wei, Ralph Spolenak, Philipp Kohler-Redlich, Manfred Ruhle, and Eduard Arzt. Electrical transport in pure and boron-doped carbon nanotubes. *Applied Physics Letters*, 74(21):3149–3151, 1999.

[145] P.G. Collins, K. Bradley, M. Ishigami, and A. Zett. Extreme oxygen sensitivity of electronic properties of carbon nanotubes. *Science*, 287(5459):1801–4, 2000.

[146] F. Zhou, L. Lu, D.L. Zhang, Z.W. Pan, and S.S. Xie. Linear conductance of multiwalled carbon nanotubes at high temperatures. *Solid State Communications*, 129(6):407–410, 2004.

[147] J.W. Jang, S.H. Kim, C.E. Lee, T.J. Lee, C.J. Lee, H.S. Kim, E.H. Kim, and S.J. Noh. Conduction mechanism of the bamboo-shaped multiwalled carbon nanotubes. *Journal of the Korean Physical Society*, 42(2):S985–8, 2003.

[148] A. Rakitin, C. Papadopoulos, and J.M. Xu. Electronic properties of amorphous carbon nanotubes. *Physical Review B (Condensed Matter)*, 61(8):5793–6, 2000.

[149] S-B Lee, K B K Teo, L A W Robinson, A S Teh, M Chhowalla, D G Hasko, G A J Amaratunga, W I Milne, and H Ahmed. Nano- and microfabrication - characteristics of multiwalled carbon nanotube nanobridges fabricated by poly(methylmethacrylate) suspended dispersion. *Journal of Vacuum Science and Technology - Section B - Microelectronics Nanometer Structur*, 20(6):2773–2776, 2002.

[150] Li Qiu-Hong and Wang Tai-Hong. Shell coupling through a single multiwall carbon nanotube. *Chinese Physics Letters*, 20(9):1558–60, 2003.

[151] S.T. Purcell, Vu Thien Binh, P. Vincent, and C. Journet. Hot nanotubes: Stable heating of individual multiwall carbon nanotubes to 2000 k induced by the field-emission current. *Physical Review Letters*, 88(10):1055021–1055024, 2002.

[152] P. Vincent, S.T. Purcell, C. Journet, and V.T. Binh. Modelization of resistive heating of carbon nanotubes during field emission. *Physical Review B (Condensed Matter and Materials Physics)*, 66(7):075406/1–5, 2002.

[153] C. Sekar and C. Subramanian. Purification and characterization of buckminsterfullerene, nanotubes and their by-products. *Vacuum*, 47(11):1289–1292, 1996.

[154] K. Morishita and T. Takarada. Gasification behavior of carbon nanotubes. *Carbon*, 35(7):977–981, 1997.

[155] Xuekun Lu, K.D. Ausman, R.D. Piner, and R.S. Ruoff. Scanning electron microscopy study of carbon nanotubes heated at high temperatures in air. *Journal of Applied Physics*, 86(1):186–9, 1999.

[156] R. A. Alberty and R. J. Silbey. *Physical Chemistry, 1st Ed.* John Wiley & Sons, Inc., 1992.

[157] W. Huang, Y. Wang, G. Luo, and F. Wei. 99.9annealing. *Carbon*, 41(13):2585–2590, 2003.

[158] Y.A. Kim, T. Hayashi, K. Osawa, M.S. Dresselhaus, and M. Endo. Annealing effect on disordered multi-wall carbon nanotubes. *Chemical Physics Letters*, 380(3-4):319–324, 2003.

[159] T. Ichihashi, Jun ichi Fujita, M. Ishida, and Y. Ochiai. In situ observation of carbon-nanopillar tubulization caused by liquidlike iron particles. *Physical Review Letters*, 92(21):215702/1–4, 2004.

[160] B.C. Regan, S. Aloni, R.O. Ritchie, U. Dahmen, and A. Zetti. Carbon nanotubes as nanoscale mass conveyors. *Nature*, 428(6986):924–927, 2004.

[161] Hansoo Kim, Michael J Kaufman, and Wolfgang M Sigmund. Phase transition of iron inside carbon nanotubes under electron irradiation. *Journal of Materials Research*, 19(6):1835–1839, 2004.

[162] L. Shi, P. Kim, S. Plyasunov, A. Bachtold, P.L. McEuen, and A. Majumdar. Scanning thermal microscopy study of dissipation in current-carrying carbon nanotubes. *American Society of Mechanical Engineers, Heat Transfer Division, (Publication) HTD*, 369(7):247–252, 2001.

[163] S. Blazewicz, B. Patalita, and Ph. Touzain. Study of piezoresistance effect in carbon fibers. *Carbon*, 35(10-11):1613–1618, 1997.

[164] P. Kim, L. Shi, A. Majumdar, and P.L. McEuen. Thermal transport measurements of individual multiwalled nanotubes. *Physical Review Letters*, 87(21):2155021–2155024, 2001.

[165] R.F. Egerton, P. Li, and M. Malac. Radiation damage in the tem and sem. *Micron*, 35(6):399–409, 2004.

[166] P.M. Ajayan, V. Ravikumar, and J.-C. Charlier. Surface reconstructions and dimensional changes in single-walled carbon nanotubes. *Physical Review Letters*, 81(7):1437–40, 1998.

[167] F. Banhart. The formation of a connection between carbon nanotubes in an electron beam. *Nano Letters*, 1(6):329–32, 2001.

[168] Jixue Li and Florian Banhart. The engineering of hot carbon nanotubes with a focused electron beam. *Nano Letters*, 4(6):1143–1146, 2001.

[169] V.H. Crespi, N.G. Chopra, M.L. Cohen, A. Zettl, and S.G. Louie. Anisotropic electron-beam damage and the collapse of carbon nanotubes. *Physical Review B (Condensed Matter)*, 54(8):5927–31, 1996.

[170] D. Wang, P.C. Hoyle, J.R.A. Cleaver, G.A. Porkolab, and N.C. MacDonald. Lithography using electron beam induced etching of a carbon film. *Journal of Vacuum Science and Technology B: Microelectronics Processing and Phenomena*, 13(5):1984–1987, 1995.

[171] Y. Gogotsi, N. Naguib, and J.A. Libera. In situ chemical experiments in carbon nanotubes. *Chemical Physics Letters*, 365(3-4):354–360, 2002.

[172] Y. Gogotsi H. Ye, N. Naguib. Opening multiwall carbon nanotubes with electron beam. In *Nanoengineered Nanofibrous Materials, NATO Science Series NATO-ASI*, pages 415–422. Kluwer Academic Book Publishers, Dordrecht, Netherlands, 2004.

[173] Ed. R. C. Weast. *Handbook of Chemistry and Physics*. Chemical Rubber Publishing Company, 1978.

[174] CNI. Carbon nanotubes incorporated. http://cnanotech.com/.

[175] E P A M Bakkers and M A Verheijen. Synthesis of InP nanotubes. *Journal of the American Chemical Society*, 125(12):3440–3441, 2003.

[176] S. De Franceschi, J.A. Van Dam, E.P.A.M. Bakkers, L.F. Feiner, L. Gurevich, and L.P. Kouwenhoven. Single-electron tunneling in inp nanowires. *Applied Physics Letters*, 83(2):344–346, 2003.

[177] W. Yi, L. Lu, Zhang Dian-lin, Z.W. Pan, and S.S. Xie. Linear specific heat of carbon nanotubes. *Physical Review B (Condensed Matter)*, 59(14):R9015–18, 1999.